Doctoral theses at NTNU, 2019:252

Emil Christiansen

Nanoscale Characterisation of Deformed Aluminium Alloys

ISBN 978-82-326-4100-0 (printed ver.)
ISBN 978-82-326-4101-7 (electronic ver.)
ISSN 1503-8181

NTNU
Norwegian University of
Science and Technology

NTNU
Norwegian University of Science and Technology
Thesis for the Degree of
Philosophiae Doctor
Faculty of Natural Sciences
Department of Physics

Doctoral theses at NTNU, 2019:252

NTNU
Norwegian University of
Science and Technology

Emil Christiansen

Nanoscale Characterisation of Deformed Aluminium Alloys

Thesis for the Degree of Philosophiae Doctor

Trondheim, September 2019

Norwegian University of Science and Technology
Faculty of Natural Sciences
Department of Physics

NTNU
Norwegian University of
Science and Technology

NTNU
Norwegian University of Science and Technology

Thesis for the Degree of Philosophiae Doctor

Faculty of Natural Sciences
Department of Physics

© Emil Christiansen

ISBN 978-82-326-4100-0 (printed ver.)
ISBN 978-82-326-4101-7 (electronic ver.)
ISSN 1503-8181

Doctoral theses at NTNU, 2019:252

Printed by NTNU Grafisk senter

Abstract

Understanding deformation of structures made from aluminium alloys is important for a range of industries. Aluminium producers must know what affects the properties of the alloys in order to develop and design new and improved alloy compositions, automotive industries must be able to model their products to limit prototype tests, and oil, gas, and construction industry must understand limitations and behaviour of applied materials to predict and prevent failure. If e.g. the automotive industry is unable to use an aluminium alloy instead of other materials such as steel, the result will be a car that potentially pollute more than necessary, or an electrical vehicle with reduced range. Hence, developing models of deformation and fracture of aluminium alloys can also have an environmental impact. However, to develop models that apply to a range of alloys in different geometries and under various loads, it is important to have a physical understanding and foundation of the models. In this regard, it is important to characterise and understand the physical processes that occurs in this kind of materials during deformation down to the nanoscale. One of the most powerful tools for studying materials at the nanoscale is transmission electron microscopy (TEM). This has been the main characterisation instrument used in this thesis, and part of the work has been to develop TEM methods for studying deformed aluminium alloys.

This thesis contains four papers:

Paper 1 investigates the microstructural changes that may occur in soft precipitate free zones (PFZs) in an Al-Mg-Si alloy in peak hardness, when it is deformed. It is shown that very small subgrains ($\sim 200\ \mathrm{nm}$ in diameter) can form when strain localises in the PFZs. These subgrains will likely strengthen the PFZ by a Hall-Petch mechanism and might halt further strain localisation. However, it is still unclear whether the sub-grain boundaries themselves will be able to serve as new nuclei for voids, and the net effect on ductility is still unknown. This paper also shows that overall dislocation storage in PFZs of this width ($\sim 200\ \mathrm{nm}$) is limited, but that dislocations may accumulate in the transition region between the PFZ and grain interior in some cases. This accumulation results in small misorienta-

tion gradients between the PFZ as a whole and the grain interior. In other PFZs however, there are no misorientations between the PFZ and the grain interior, and the few dislocations that are observed in these PFZs tend to span the PFZ almost perpendicularly and have similar Burgers vectors.

Paper 2 investigates how the needle-like β" precipitates that form in Al-Mg-Si alloys in peak hardness are sheared by dislocations. This paper is an important part of the thesis, as the results are directly related to the plastic flow of peak aged Al-Mg-Si alloys. It is found that β" precipitates are sheared by dislocations, mainly in one direction, and that this shearing introduces planar defects inside the precipitates. These planar defects arise because the precipitate structure differs from the matrix so that the matrix Burgers vectors are not compatible with the precipitate phase. The study also found evidence that dislocations might cross-slip to nearby planes and shear previously non-sheared regions rather than shearing successively in a single plane. This suggests that the planar defects might locally strengthen the precipitates. In addition to the results regarding shearing of β" precipitates, the paper also demonstrates the complementary and powerful combination of advanced TEM techniques such as high-resolution TEM, atomic resolution scanning TEM, and scanning precession electron diffraction.

Paper 3 provides further details regarding the shearing of β" precipitates through multislice TEM image simulations. In this paper, images of various model structures of sheared precipitates were simulated and compared with the experimental images in Paper 2. It is found that, if precipitates are sheared in mostly one direction, the spacing between the shearing events (along their lengths) must be ~ 10 nm. For a given local strain, this spacing means that only a limited number of dislocations may have passed on each glide plane. While this paper does not provide certain evidence that dislocations shear precipitates in single steps, it shows that large local strain is required to do so in order to produce precipitates that are capable of producing the experimental results shown in Paper 2. Both the information regarding number of spacing of shearing events, and the probable shearing distribution are important inputs for models of strength and work hardening.

Paper 4 considers how the quench rate from solution heat treatment influences precipitation and mechanical properties of three different Al-Mg-Si alloys with different texture and grain structure. This study shows how dense alloys (AA6082 type) containing dispersoids may become very quench sensitive due to various PFZ effects. If the dispersoid density is high and the grain or subgrain sizes are small, PFZs around grain boundaries (GBs) and dispersoids can overlap and lead to a total suppression of precipitation in the alloy when it is air cooled rather than water quenched from solution heat treatment. However, if the dispersoid density is moderate, and the grains are large, the microstructure in the air cooled state be-

comes very inhomogeneous and consists of a mix of very dense precipitation and wide PFZs around dispersoids. Air cooling from solution heat treatment reduces the strength and increases the ductility of most of the alloys. The low strength in the dense alloy with high dispersoid content is due to the complete suppression of precipitation, while the low strength of the dense alloy with moderate dispersoid content is probably due to a combination of inhomogeneous precipitation and wide PFZs around GBs and dispersoids. In the lean alloy (AA6060 type) that was studied, the quench sensitivity is less and results in a sparser precipitation of slightly larger precipitates as well as much wider PFZs. Accordingly, the strength of this alloy decreases, but not as dramatically as for the other two alloys. The changes in strength of the alloys as a result of air-cooling is captured by the nanostructure model NaMo. However, for the dense alloy with large grains, there is a discrepancy between the predicted and experimentally observed precipitation. NaMo underestimates the precipitate number density and thus predicts a too low strength contribution. However, NaMo does not capture the detrimental effect of the inhomogeneous precipitation and the PFZs around dispersoids. These two effects appear to cancel each other, and the net effect fits well with the experimental results. Finally, this paper shows that, despite a lower yield strength, the ductility of alloys may decrease as a result of wider GB PFZs (due to slower cooling rates) that promotes intercrystalline ductile fracture.

The thesis is built up by a general introduction, the four papers, and the conclusions that may be drawn by the work and further outlook. The introduction establishes the motivation, objectives, and scope for the work, and presents necessary background on aluminium alloys and TEM to put the work in context. A thorough understanding of TEM is important in order to understand the experimental results and their limitations. The papers represent the main research that has been done. One of the four papers have been published (Paper 1), one is submitted for peer review in an international journal (Paper 2), and two papers are awaiting submission (Paper 3 and 4). The conclusions and outlook at the end of this thesis draw conclusions from both the introduction and the papers, and suggest further work that may be done.

Preface

This thesis is the result of scientific work conducted between 2015 and 2019 at the Centre for advanced structural analysis (CASA) at the Norwegian University of Science and Technology – NTNU, Trondheim. It is submitted to NTNU as part of the application for the degree of Philosophiae Doctor (PhD). CASA is a centre for research based innovation headed by Professor Magnus Langseth and is funded by the Research Council of Norway and a number partners. The partners consists of several industrial companies and research institutions, including the Department of Physics at NTNU, where most of the work has been done. A quarter of the work has been devoted to duty work; four months of teaching duties at the Department of Physics, and eight months of various tasks for CASA. The duty work for CASA has included work for Hydro Aluminium at Sunndalsøra, and supervising and helping visiting researchers at NTNU.

The work is mostly related to transmission electron microscopy (TEM) and has been performed at the TEM Gemini Centre in Trondheim. Professor Randi Holmestad, Dr. Calin Daniel Marioara, and Professor Odd Sture Hopperstad have supervised the work. The work has been conducted as part of the Lower Scale programme of SFI CASA, which consists of many research activities related to processes occurring on the nanoscale in metals and alloys during deformation. The programme is an important part of CASAs vision for a physically based multi-scale simulation framework. CASA applies a top-down/bottom-up approach, and the Lower Scale programme is closely related to the Metallic Materials programme. The need for experimental input is determined in the Metallic Materials programme, while the Lower Scale programme performs investigations in order to provide this input. This thesis should therefore be considered as part of a larger multidisciplinary and multiscale research activity.

This thesis consists of a collection of papers, in addition to some unpublished work that has been incorporated into the introduction. The papers are either accepted, submitted, or ready to be submitted to peer-review journals of international standards. In particular, Paper 3: "Multislice image simulations of sheared needle-like

precipitates in an Al-Mg-Si alloy" is in reality a draft that has not been reviewed by the co-authors in detail at the moment of submitting this thesis, as most of the authors are currently on holiday. This paper will be submitted to the Journal of Microscopy as part of a conference special issue during August, and should be finalised well before the defence of this thesis. The introduction contains most of the necessary information required to understand the context of the thesis. It has been written with the aim of bridging engineering, materials science and physics. During the PhD work, *in situ* experiments conducted in collaboration with Professor Malgorzata Lewandowska and Dr. Witold Chrominskí at the Faculty of Materials Science and Engineering, Warsaw University of Technology, Poland, have been useful and educational, although they have not resulted in any publications. Some of the results from this research stay have been incorporated into the section concerning precipitate free zones in the introduction. Furthermore, research on hot deformation and creep of cast Al-Si-Mg-Cu-Hf alloys in collaboration with Dr. Petter Åsholt and Dr. Takeshi Saito at Hydro Research and Technology Development, Sunndalsøra, Norway, is ongoing. Some of these results are incorporated into the introduction of dislocations given in this thesis.

Papers Included in the Thesis

1

Lattice rotations in precipitate free zones in an Al-Mg-Si alloy

E. Christiansen, C. D. Marioara, K. Marthinsen, O. S. Hopperstad, R. Holmestad.

Materials Characterisation **144** (2018) 522–531.

2

Nano-scale characterisation of sheared β" precipitates in a deformed aluminium alloy

E. Christiansen, C. D. Marioara, B. Holmedal, O. S. Hopperstad, R. Holmestad.

Submitted to *Scientific Reports*.

3

Multislice image simulations of sheared needle-like precipitates in an Al-Mg-Si alloy

E. Christiansen, I. G. Ringdalen, R. Bjørge, C. D. Marioara, R. Holmestad.

Presented at EMAG Manchester, UK, 2019 and to be submitted for publication in *Journal of Microscopy*, EMAG and MMC special issue.

4

The role of quench rate on the plastic flow and fracture of three aluminium alloys with different grain structure and texture

B. H. Frodal, E. Christiansen, O. R. Myhr, O. S. Hopperstad.

To be submitted for journal publication.

Statement of Author Contributions

Paper 1

The experiment and idea were designed by O.S. Hopperstad, R. Holmestad, C.D. Marioara, and E. Christiansen. EC heat treated specimens in collaboration with Bjørn Håkon Frodal (NTNU, not author) under supervision of Birgitte Karlsen (SINTEF Industry, not author). Trond Auestad (NTNU, not author) performed compression tests. CDM performed TEM investigations of reference specimens, specifically; BF images and thin foil thickness for precipitate distributions, and TEM BF images of PFZs. EC calculated precipitate statistics, and performed TEM characterisation of deformed specimens, specifically; TEM BF of PFZs, WBDF, and SPED. EC also characterised all SPED results, and prepared all figures for the manuscript. EC wrote the manuscript with comments from all co-authors. All authors contributed in discussions regarding the results and interpretations.

Paper 2

The experiment and idea were designed by R. Holmestad, C.D. Marioara, and E. Christiansen. Specimens from Paper 1 were re-used, please see the corresponding author statement for details, while new thin foils were prepared by EC. CDM and EC performed HRTEM of undeformed specimens, while EC performed HRTEM of deformed specimens. EC performed STEM experiments, with assistance from CDM. EC performed all SPED experiments. Analysis of all TEM results was done solely by EC. All authors contributed to discussions and interpretation of the results. EC prepared all figures for the manuscript, and wrote the manuscript with comments from all co-authors.

Paper 3

E. Christiansen conceived the idea, performed simulations, and analysed the results. R. Bjørge assisted in choice of simulation tools, and in interpretations of results. I.G. Ringdalen constructed the atomic models. R. Holmestad and RB advised EC on simulation parameters. EC made all figures and wrote the manuscript with comments from all co-authors. RB, RH, and EC discussed and interpreted the results.

Paper 4

B. Frodal, O.S. Hopperstad, E. Christiansen, and Sondre Sævareid (NTNU, not author) conceived the idea and experiment. B.H. Frodal wrote the manuscript, performed all simulations (except NaMo), and analysed mechanical test data. Trond Auestad (NTNU, not author) performed the Kahn Tear tests, while Tor André

Kristensen (SINTEF Industry, not author) performed tensile tests. SS measured Kahn test geometries. EC heat treated the materials, prepared TEM thin foils, performed TEM imaging, and SEM fractography, and calculated precipitate statistics. O.R. Myhr performed NaMo simulations and interpreted precipitation data. All authors contributed to discussions and interpretations of the data and results. BHF, EC, and ORM made the figures.

Other Scientific Contributions

- "TEM image simulations of overlapping phases - a case study of sheared β" precipitates in Al-Mg-Si alloys", *EMAG2019*, Manchester UK, 1st–4th July, 2019. [Talk]
- "Nano-scale characterisation of deformed aluminium alloys", *Digitalisation for smart processes and product design*, Trondheim Norway, 12th–13th June 2019. [Poster]
- "Lattice rotations in precipitate free zones in an Al-Mg-Si alloy", *Topics in ductile fracture of metals*, Trondheim Norway, 17th–18th October, 2018. [Talk]
- "Precipitate free zones and crack cropagation in Al-Mg-Si alloys", *16th International Conference on Aluminium Alloys (ICAA16)*, Montréal Canada, 17th June – 21st July, 2018. [Talk]
- "Precipitate free zones in deformed Al-Mg-Si alloys", *SCANDEM2017*, Reykjavik Iceland, 5th–9th June, 2017. [Talk]
- "Deformation induced subgrains in PFZs of AA6060 alloy subjected to uniaxial compression", *2nd INTPART Workshop*, Toyama Japan, 12th October, 2016. [Talk]
- "Subgrain-formation in precipitate free zones in aluminium alloys subjected to uniaxial compression", *Nasjonal konferanse for Materialteknologi 2016*, Trondheim Norway, 24th–25th August, 2016. [Talk]
- "Transmission electron microscopy of precipitate free zones in aluminium alloys subjected to uniaxial compression", *SCANDEM2016*, Trondheim Norway, 7th–10th June, 2016. [Talk]

Trondheim, September 2019

Emil Christiansen

Acknowledgements

This thesis is the product of many hours and the effort of a great many people, both directly and indirectly. The person that has been most important in this regard is my main supervisor Professor Randi Holmestad at NTNU. Randi, who was also the supervisor of my Masters thesis back in 2013-2015, has played a very important part in my time as a PhD candidate at NTNU in many ways. She has supported my ideas and work with enthusiasm, interest and great advice, and has pushed me to become a better scientist in the process. Without her guidance, this thesis would not have been possible. Indeed, without Randis belief in me, I would have been able to finish this work and thesis at all. Thank you for your optimism, helpfulness, and understanding, Randi. You have really meant a lot to me.

Without the funding for SFI CASA from the Research Council of Norway, none of this work could have happened. The research council is also greatly appreciated for supporting the NORTEM project that made all the TEMs I have used available. The partners of CASA are also acknowledged for their contribution and participation in the SFI. Being part of a centre funded by advanced and international industry has been an important and rewarding experience.

I must also thank my co-supervisors Dr. Calin Daniel Marioara from SINTEF and Professor Odd Sture Hopperstad from NTNU for all of their help as well. Without Calin, I would probably still be figuring out what a precipitate was and how to align an aberration corrected microscope. His advice and suggestions on data analysis, papers, manuscripts, posters, and presentations have been invaluable. Without Odd Sture, I would definitely still be lost on the nano-scale and live in a world where strain and stress is something that people writing PhD theses experience. Having a brilliant scientist as Odd Sture right next door to my office has been incredibly helpful, both in terms of science, but also as a great motivation.

During my PhD, I have collaborated closely with several people. First of all, I thank Dr. Per Erik Vullum for training me on the ARM, and to always have an answer for my questions regarding TEM and sample preparation. It seems his

knowledge is unending and he is a very important person for all PhD candidates working with TEM at NTNU. I also wish to thank all the co-authors of my papers; Professor Knut Marthinsen at NTNU, Professor Bjørn Holmedal at NTNU, Dr. Takeshi Saito at Hydro Aluminium, Dr. Ole Runar Myhr at Hydro Aluminium, Dr. Ruben Bjørge at SINTEF, Dr. Inga Gudem Ringdalen at SINTEF, and Bjørn Håkon Frodal at NTNU, for collaborating on my research papers and for fruitful discussions on a wide variety of topics.

I have belonged to two large and incredible research groups during my time as a PhD candidate at NTNU. I started out with many friends and colleagues in the TEM group at the physics department from my masters degree, and got a warm and embracing welcome in the SIMLab family when I started my PhD. There are too many people involved in these groups to mention all by name. However, I wish to thank the excellent engineers at the TEM Gemini Centre; Bjørn Gunnar Soleim and Dr. Ragnhild Sæterli for keeping the microscopes in excellent condition in a very efficient manner. I also want to thank Professor Antonius Von Helvoort for pushing all users of the TEM Gemini Centre to perform their best, and to pose interesting and challenging questions. From CASA and SIMLab, I want to thank all the Professors that have worked to establish a thriving research group of world leading class. It has been a privilege to work at CASA for the last four years. Current and former colleagues have also played an important part for me during my PhD. The kind, positive, and fun social atmosphere in both research groups have helped a great deal. In particular, I want to thank Julie, Aleksander, Adrian, Jonas, Jonas, Tina, and Elisabeth from the TEM group for valuable conversations regarding everything from TEM to the hardships of being a PhD candidate. I also want to thank the PhD candidates of CASA, whom are too many to mention by name, for welcoming me to their little corner of NTNU the way they did. Bjørn Håkon has played a very important role as a close collaborator and has saved me from many mechanical blunders. I also want to thank my "neighbour" Ole for lifting the spirits at the office during early and late office hours.

Finally, I wish to thank the most important people in my life, which is best done in Norwegian, I think. Mamma og Pappa har vært en enorm stor støtte gjennom hele livet, og særlig under min tid som student og under doktorgraden. Dere har alltid støttet meg og målene jeg har satt meg, og kanskje viktigst av alt; medmenneskligheten og omtaken dere har vist meg og lært meg å vise andre er uvurderlig. Som forsker ser jeg på dette som ekstremt viktig, og noe jeg setter enormt stor pris på. Brødrene mine, Martin og Simon, har også vært støttende, men samtidig utfordrende – slik brødre skal være. Jeg er utrolig glad og stolt over å være broren deres. Middagsdiskusjonene våre - som gjerne dreies mot et eller annet eksistensiellt spørsmål, uavhengig av hva utgangspunktet for diskusjonen var, er

veldig viktig for meg. Det er veldig stas å få selskap av Simon i Trondheim, og jeg ønsker han lykke til med studiene. Det er også veldig stas å komme på besøk til Martin og Elisabeth i Kongsvinger og å være onkel til Amanda og Maja. Jeg setter også veldig pris på å være en del av familien Frang, og takker Dina og Herman, Hans Wilhelm, og Helene, Daniel, Wilhelm, og Henrik for veldig mange hyggelige stunder både i Trondheim og i Romedal. Hjelpen og gavmildheten til Dina og Herman settes ekstremt stor pris på. Jeg vil også takke vennene mine fra "heme"; Odd Jørgen, Martin, David og Fredrik, jeg håper jeg både får bedre tid og blir flinkere til å ta meg tid til dere fremover. Dette gjelder også vennene fra studietiden, Joakim, Jonas, Monica, Thor Olaf, Arvind, Sverre, og Marius.

Til sist vil jeg takke Lisbet. Uten deg hadde jeg aldri i verden klart å ta en doktorgrad, for ikke å snakke om å ta vare på meg selv underveis! Takk for din forståelse og tolmodighet, din støtte og kjærlighet, og sist men ikke minst, din fantastiske personlighet.

Contents

PART I

INTRODUCTION

Chapter 1

Motivation

Aluminium is a relatively abundant element in the earths crust, which consists of about 8 weight % (wt%) aluminium [1]. However, the extraction of pure Al from its various ores is much more challenging than other engineering materials such as steels. To produce 1 tonne of pure Al metal from bauxite, a total of about 23000 kWh of electricity is necessary [1]. This is almost five times the energy required to produce an equivalent amount of steel. Nevertheless, the world production of aluminium is increasing year by year. There are good reasons for this increase, and the most important reason is the strength to weight ratio of aluminium. Pure aluminium is relatively soft with a yield strength of about $7 - 11$ MPa, but its alloys can be processed to achieve strengths as high as $700\ \mathrm{MPa}$ in some cases. Most common aluminium alloys have strengths of $240\ \mathrm{MPa}$, however. The density of the alloy does not change drastically compared to the pure metal, which has a density of $2.7\ \mathrm{g\,cm^{-3}}$. The resulting specific strength of pure aluminium is therefore $2.6\ \mathrm{N\,m\,g^{-1}}$, while its alloys can have specific strengths of $\sim 90 - 260$ $\mathrm{N\,m\,g^{-1}}$. These values are slightly higher than for steels, which have densities of $\sim 8\ \mathrm{g\,cm^{-3}}$ and strengths between $200 - 2000\ \mathrm{MPa}$, and thus specific strengths between $25 - 250\ \mathrm{N\,m\,g^{-1}}$. Of course, these numbers vary greatly between different alloys and steels, but the main point is that aluminium alloys offer light weight alternatives to steels. This is particularly important in transportation and packaging industries, but construction industries also benefit from this aspect of aluminium alloys. For example, development of electric vehicles depends heavily on parallel development of lightweight alternatives to traditional materials, and lightweight aluminium alloys play an important role [2]. In addition to their high specific strengths, aluminium alloys exhibit other important and useful properties, such as good formability, weldability, electrical conductivity, and corrosion resistance. These properties are strongly linked to alloy composition, and to processing

parameters. Because of this strong link, aluminium alloys are researched and studied in great detail in order to find the best alloy composition for a given application. However, the parameter space of many aluminium alloys is very large because of the many processing steps and compositional variants.

For industries to be able to utilise aluminium alloys in their products, they require trustworthy models on the continuum level that they can apply to model their product, in order to limit prototype testing and development cost. These models usually require extensive calibration by materials testing, which is very costly and time consuming. In addition, certain industries, such as construction and petroleum industries rely heavily on simulations, as large scale tests are impossible. It is therefore a need for physically based modelling frameworks where the amount of testing is reduced as much as possible. One way to do this is to create a through-scale modelling chain that covers several length scales. Aluminium producers will also benefit from such modelling frameworks, as it enables more competitive alloy development. However, development of such through-scale modelling chains requires detailed knowledge of the physical processes that occur on every length scale, and determining the relevant parameters and processes is challenging. An iterative circle of simulation and testing on various length-scales is one way to isolate and understand the different processes.

Many aluminium alloys are designed to age harden based on thermo-mechanical processing that produce strengthening precipitates. Plastic deformation of aluminium alloys usually occurs by dislocation glide, and the physical basis for the materials strength is how these dislocations interact with precipitates. These interactions occur on the nano-metre scale and determine many of the large-scale mechanical properties of the material. A continuum model cannot capture these processes directly, but by employing a through-scale modelling chain, where models operating on various length scales can be used to calibrate models further up in scale, it is possible to transfer knowledge from the nanoscale to the macro-scale and the continuum models employed by industry. However, understanding nanoscale interactions is an iterative process, as the interactions must first be identified, and then their importance of influence must be tested. This thesis concerns one of these parts, namely characterising some of the nanoscale interactions occurring in aluminium alloys. This characterisation has mostly been done by transmission electron microscopy (TEM), supported by scanning electron microscopy when needed.

TEM is the natural choice for characterising and understanding the nanoscale of a material. This choice is clear from the extensive use of TEM in alloy development and nanotechnology [3]–[7]. Indeed, the development of metallurgy and plasticity of crystals has historically depended on TEM as an essential tool [5], [8]–

[12]. TEM is an important tool because of its incredible resolving power and the large number of different characterisation techniques available in a single instrument. The magnifications in TEM can easily exceed over one million, allowing for investigations of a material in great detail. To put this resolving power in perspective, an object the size of a handball would be magnified to the size of the earth, if it could fit in the instrument. It is obvious that the amount of detail one would observe on the surface of the handball would be immense. This resolving power comes at a cost of precision and statistics, however, as it is impossible to inspect large areas of material. Considering the example of the magnified handball, investigating the entire ball would be comparable to investigating the entire surface of the earth. For the same reasons why it is not necessary to "scour the earth" for every detail in order to understand e.g. plate tectonics, it is not necessary to investigate every detail of a material by TEM in order to understand the processes of interest. While the processes occurring in metals and alloys can be complex, they may be understood by inspecting small parts of the material, and the behaviour of the macroscopic material may be explained by a series of such inspections. TEM allows for observing dislocations, particles, and grain rotations amongst other aspects of aluminium alloys and deformation, and is therefore an important part in understanding the underlying physics of plasticity and fracture on the nanoscale. As an example, strain gradients can originate from storage of dislocations around inhomogeneities in the material [13]–[15], and only by observing how these dislocations are arranged can physically accurate models of work hardening be established.

Chapter 2

Objectives and Scope

2.1 Objectives

One of the main objectives of CASA is to develop a "*physical and experimentally validated multi-scale framework providing constitutive models for microstructure evolution, strength and work hardening, crystal and continuum plasticity and damage and fracture for metallic materials*"[16]. The overall objective of this thesis is to provide experimental results from the nanoscale that can be used to further develop the multi-scale modelling framework. This overall objective is divided into two main objectives: increasing understanding of the role of precipitate free zones (PFZs) during deformation and ductile failure, and to better understand the shearing of precipitates in precipitate strengthened alloys.

2.2 Scope

Several limitations apply to the work in this thesis. First of all, the work is almost entirely experimentally oriented, with the exception of some TEM image simulations required to understand and interpret experimental results. This experimental work is mostly limited to TEM experiments. Secondly, development of models for strength, work hardening, and fracture is out of the scope for this thesis, as the objective is to obtain experimental information regarding processes relevant to ductile failure of materials. Thirdly, the materials have been limited to the wrought Al-Mg-Si alloy system (with the exception of some duty work related to cast Al-Si-Mg-Cu-Hf alloys). There are several reasons for this limitation. The most important reasons are that these alloys are industrially relevant, and that the exact same alloys have been studied in other research activities related to CASA. Fourthly, the alloys have been mostly studied in the peak-aged condition, although underaged and overaged states would also have been of interest.

It can be challenging to use a site-specific tool like TEM to study dislocation interactions and plasticity, which are somewhat stochastic processes. This challenge is most prominent when studying PFZs in deformed aluminium specimens, as plasticity in close proximity to GBs is a very complex problem. Hence, the purpose of the TEM study is not to develop or establish a theory for plasticity on the nanoscale, but rather to provide information regarding the various processes that may occur on the nanoscale. There are numerous such processes, and a selections must be made. In this thesis, the processes have been limited to investigating the microstructural features that may develop in PFZs during deformation, and to establish the shearing/looping mechanism of β" precipitates in deformed Al-Mg-Si alloys. The role of PFZs has also been studied by characterising undeformed Al-Mg-Si alloys in order to validate and aid in interpretation of macroscopic deformation experiments and simulations.

Chapter 3

Aluminium Alloys and Deformation on the Nanoscale

By alloying aluminium with various elements, the properties of the final material can be changed quite drastically [1]. This has already been motivated by the dramatic increase in specific strengths (see Chapter 1), but alloying can also improve formability, castability, weldability, conductivity, ductility, corrosion resistance, and various surface properties. In addition, alloying will also affect the recycleability of the material. Most of the properties of an aluminium alloy are linked. For example, good formability require good ductility, which in turn usually require a low strength. Surface properties, on the other hand, is linked to both formability and corrosion resistance. This wide range of properties has given rise to many different alloying systems, each optimized for a certain set of properties. There are two main classes of aluminium alloys; cast and wrought alloys. Cast alloys are cast into their final shape directly from the melt, while wrought alloys are cast into billets and subsequently shaped into a final product at a later stage, for example by rolling or extrusion. The main reason for this distinction is that cast alloys can be alloyed without taking formability into consideration, while wrought alloys must be optimized for both their forming stage as well as their service life. However, cast alloys must be additionally alloyed to improve castability.

3.1 Mechanical Properties

The mechanical properties of aluminium alloys are best described by considering the schematic stress-strain curves in Figure 3.1. This figure illustrates how a specimen elongates when it is strained due to an applied stress. For low stresses, there is a linear relationship between stress and strain. This region is called the elastic

region, and unloading the specimen will return it to its original shape. However, the material will yield at a certain stress, called the yield stress σ_0, after which it deforms plastically and will no longer return to its original shape if unloaded. In the plastic region, the material will work harden and the stress continues to increase with strain. There are several ways of measuring stress and strain, and the shape of stress-strain curves will depend on the chosen measure. For instance, the engineering strain is given by $e = \Delta L/L_0$, where ΔL is the change in specimen gauge length, and L_0 is the initial gauge length. The engineering stress σ_e is given by the applied load F divided by the initial load bearing area A_0. However, the engineering values does not account for the specimen change of a material during deformation. The true strain of a specimen is given by

$$\varepsilon = \int_{L_0}^{L} \frac{dl}{l} = \ln\left(\frac{L}{L_0}\right) = \ln\left(\frac{L_0 + \Delta L}{L_0}\right) = \ln\left(1 + e\right), \tag{3.1}$$

while the true stress is given by

$$\sigma = \frac{F}{A} = \frac{F}{A}\frac{A_0}{A_0} = \sigma_e \frac{L}{L_0} = \sigma_e \frac{L_0 + \Delta L}{L_0} = \sigma_e\left(1 + e\right). \tag{3.2}$$

In Equation (3.1), L is the instantaneous gauge length, while A in Equation (3.2) is the instantaneous load bearing area. The differences between engineering stress-strain and true stress-strain curves are shown in Figure 3.1 as well. In the engineering stress-strain curve, the material apparently softens after reaching a maximum stress, while in the true stress-strain curves the material work harden all the way until right before it fails. This is because tensile specimens usually develop a neck when pulled in tension. This is the result of a geometrical instability that localises deformation to a narrow region. The longer a material can be strained after necking until it fails, the more ductile it is.

For ductile metals and alloys, the yield stress, work hardening and fracture processes are determined by a combination of nanoscale and continuum processes. The physical mechanisms of plasticity in ductile metals and alloys, such as aluminium alloys, are based on the interaction of dislocations with the alloys microstructure. In precipitate strengthened alloys for instance, the yield stress is related to the onset of macroscopic slip of dislocations, which is determined by the interaction of dislocations and precipitates [3], [17]. Work hardening in such alloys can be a complex mixture of several processes, including dislocation storage [1], [3], [13]–[15], and ductile failure is usually the result of voids that nucleate around inclusions and subsequently grow and coalesce [3]. In order to study and understand strength, work hardening, and ductile failure of aluminium alloys, it is therefore important to understand the fundamental mechanisms responsible for plastic flow in aluminium alloys.

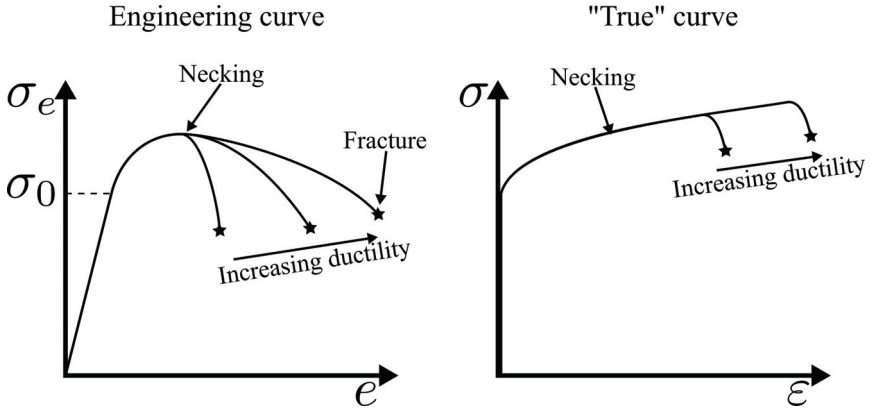

Figure 3.1: Schematic illustration of engineering stress-strain curves and true stress-strain curves of a ductile elastic-plastic material.

3.2 Strengthening Mechanisms in Aluminium Alloys

The mechanical properties of aluminium alloys originate from various features in their microstructure and how these features interact with dislocations during deformation [1]. The most important features for strength are grain boundaries, solute in solid solution, precipitates, and other dislocations. Other features can also inhibit dislocation glide, and some work suggests that even voids can interact with dislocations and inhibit their motion [18]. When discussing strengthening mechanisms, it is common to consider various additions to the critically resolved stress (CRSS) τ. This value is connected to the flow stress of the material by the Taylor factor M as $\sigma = M\tau$ [19]. This factor is related to the crystallographic texture of the material, and the average Taylor factor for an aluminium polycrystal with random texture is 2.23, 2.6 or 3.06, depending on the theory one applies [20]. As such, each strengthening contribution can be related to the flow stress of a polycrystal by an appropriate value of M. Texture (i.e. different values of M) will therefore influence the strength of an alloy, but this is not considered in the present thesis. In the following, a brief introduction to the various processing steps of aluminium alloys is given, before a short introduction to dislocations, and subsequently the four main features responsible for strengthening aluminium alloys, are described.

3.2.1 Thermo-mechanical processing of aluminium alloys

The strength of an aluminium alloy depends on its thermo-mechanical history and its chemical composition. A typical thermo-mechanical history is illustrated in Figure 3.2. The alloy is first cast into billets if it is a wrought alloy or its final

shape if it is a foundry alloy. The alloying, that was done before the alloy was cast, determines whether the alloy is a wrought or foundry alloy by affecting its formability. After casting, elements with low solubility (such as iron) will have formed particles (called primary particles), while elements with high or moderate solubility (such as silicon or magnesium) are mostly dissolved in the aluminium matrix [3]. Directly cast aluminium will consist of dendritic grains with an increasing concentration of these "soluble" elements toward the grain boundaries (GB), with the primary particles usually sitting in between the grains on the GBs. The first step of the thermo-mechanical treatment is therefore to even out the concentration gradients in the grains. This is done by heating the alloy to a high temperature (but below the melting point), and is called homogenisation. By heating the material, elements are allowed to diffuse and the chemical gradients are evened out. However, this also cause new particles to form, called dispersoids or secondary particles (in contrast to the primary particles that lie on GBs, these secondary particles are dispersed throughout the grains), that contain various elements such as Cr, Zr, or Mn [3]. After homogenisation, the alloy is usually formed into its final shape if it is a wrought alloy. The most common forming processes are rolling and extrusion, both of which involve large stresses and strains.

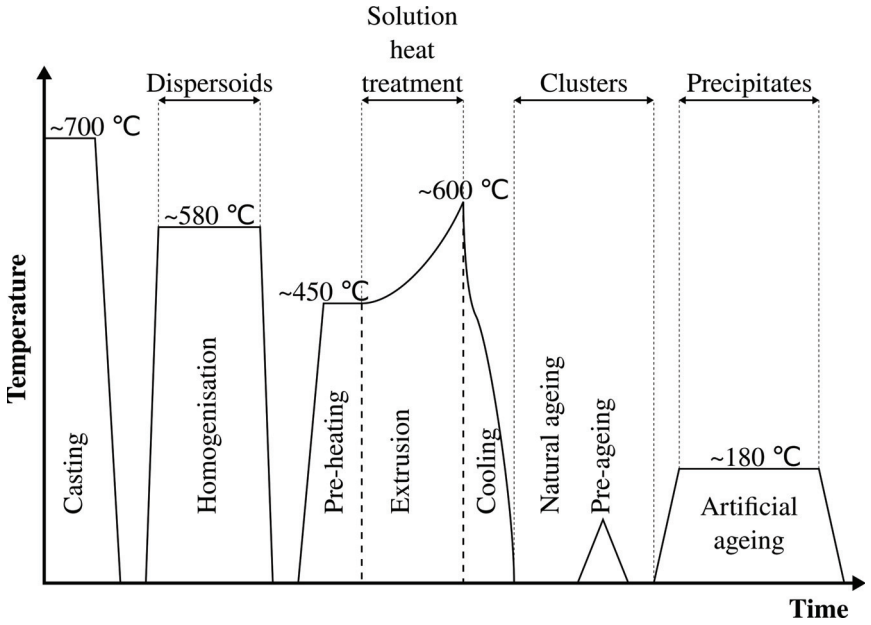

Figure 3.2: Illustration of a typical thermo-mechanical treament of an extrusion alloy. Adapted from Polmear [1].

The mechanical processing steps serve to both produce a product of desired shape,

and to break up the primary particles into smaller pieces and to reshape the dendritic grains. During extrusion for instance, where the alloy is pressed through a die of desired shape, the grains become elongated into long fibres, with the primary particles breaking up into smaller pieces that are distributed along these "new" GBs. During this process, grains will rotate by an angle determined by their crystallographic orientation and the global deformation. Because some grain orientations are more susceptible for orientation change (more "efficient" slip systems are activated, causing a more rapid rotation into a stable orientation), a crystallographic texture will appear. If the texture is strong, most of the grains have a preferred orientation relative to the specimen coordinate system, and the material will have a strong anisotropy. However, after the large deformations imposed by the forming process, the dislocation density will be incredibly high and large amounts of energy will be stored in the material. By heating the processed alloy, this energy can be released to provide a driving force for recrystallisation, a process in which some grains grow at the expense of others. The dispersoids that form during homogenisation can retard grain boundary migration (and thus retard recrystallisation), or they can stimulate recrystallisation by providing zones of high local deformation [21]. These particles are therefore wanted from a forming-perspective, but will impact the fracture processes of the material as well. Recovery and recrystallisation is a research field in its own right, and out of scope for the current thesis. However, the various grain shapes and crystallographic textures that result from these structures influence many of the properties of the aluminium alloys, and are therefore important to have in mind.

After the forming step (for wrought alloys), the alloy is heat treated. In the case of foundry alloys which are directly cast into their final shape, the concentration of solute can be very high, while for wrought alloys, the concentration of solute is kept low in order to maintain formability. The heat treatment process aims to precipitate new phases, referred to as precipitates, that increase the strength of the alloy compared to its state where the solute elements are dispersed throughout the matrix. The various phases that form depend greatly on the chemical composition of the alloy, and on the temperature that is applied [1]. To precipitate beneficial phases, solute must first be homogeneously distributed in the matrix. This is done by heating the material to very high temperatures for a short time and is called solution heat treatment (SHT). Sometimes, the homogenisation step or the forming step is used as a SHT, but this can also be a separate step that is performed right before ageing. The quench rate from SHT is incredibly important for subsequent precipitation. This is because the concentration of vacancies at the SHT temperature is much higher than at lower temperatures, and a fast quench will lock more vacancies than a slower quench. The vacancies play a two-fold role in later precipitation steps. They will both increase the diffusion speed of solute elements, and they

are important for nucleation [22] and growth of precipitates as a building block [23]. After the quench, the equilibrium state that existed at the SHT temperature is retained to a certain degree. However, at the lower temperature (usually room temperature), this is a non-equilibrium state called a super saturated solid solution (SSSS). Different ageing processes may be applied to the SSSS state to precipitate strengthening phases. Letting the material rest in room temperature is called natural ageing (NA), where solute atoms may cluster together. This clustering can improve the strength of the alloy somewhat, but its most important influence is on subsequent artificial ageing (AA). Depending on the chemical composition of the alloy, the clusters form nucleation sites for precipitates that grow, transform, and coarsen during AA. These precipitates are beneficial for strength, and there is usually an optimum phase and size distribution that result in a peak-strengthened material [1], [3], [17]. Hence, the AA temperature and time are usually tuned to produce an optimum precipitate distribution. This optimum temperature and time depends on the precipitation sequence of the particular alloy.

In the Al-Mg-Si wrought alloy system, the precipitation sequence is usually [23], [24]

$$\begin{aligned} \text{SSSS} &\rightarrow \text{Guinier-Preston zones (pre-}\beta\text{”)} \\ &\rightarrow \beta\text{”} \\ &\rightarrow \beta\text{'}, \mathrm{U}_1, \mathrm{U}_2, \text{B'} \\ &\rightarrow \beta, \text{Si (stable).} \end{aligned} \tag{3.3}$$

Table 3.1 provides an overview of the various phases in Equation (3.3). All the phases, except the stable ones, are coherent with the aluminium matrix along at least one crystallographic direction and usually assume a needle-like shape in the matrix. The different phases form at various temperatures and after certain times. By adding other solute species, the precipitation sequence can be altered. For instance, in Al-Mg-Si-Cu alloys, precipitation of lath-like L and plate-like C along with β” precipitates can occur simultaneously [23]. While precipitation sequences are not the focus of this thesis, they have serious implications on the strength, work hardening and fracture of aluminium alloys [1], [3], [17]

After typical thermo-mechanical processing, a wrought alloy usually consists of relatively small grains with hard dispersoids (~ 100 – $1000\ \mathrm{nm}$ [3]) homogeneously scattered through the microstructure. Along the "old" GBs, pieces of primary particles are distributed as stringers and can be many times larger than the dispersoids [1], [21]. If the alloy is under-aged, very small precipitates will be homogeneously distributed through the grain interiors. Peak-aged alloys will have a slightly less dense distribution of slightly larger precipitates, while over-aged alloys will have a sparse distribution of considerably larger precipitates. In addition, PFZs

Table 3.1: Relevant precipitate phases in the Al-Mg-Si system and their composition and structure.

Phase	Composition	Space group*	Lattice parameters*
GP-zones [25]–[27]	$Mg_{2+x}Al_{7-x-y}Si_{2+y}$	C2/m	$a = 14.8$ Å $b = 4.05$ Å $c = 6.48$ Å $\beta = 105.3°$
β" [28], [29]	Mg_8Si_8Al6	C2/m	$a = 15.16$ Å $b = 4.05$ Å $c = 6.74$ Å $\beta = 105.3°$
β' [30]	$Mg_{1.8}Si$	$P6_3$	$a = b = 7.15$ Å $c = 4.05$ Å $\beta = 120°$
U_1 [31]	$MgAl_2Si_2$	$P\bar{3}m1$	$a = b = 4.05$ Å $c = 6.74$ Å $\beta = 120°$
U_2 [32]	MgAlSi	Pnma	$a = 6.75$ Å $b = 4.05$ Å $c = 7.94$ Å
B' [33]	$\sim Mg_9Al_3Si_7$	Hexagonal	$a = b = 10.4$ Å $c = 4.05$ Å $\beta = 120°$
β	Mg_2Si	$Fm\bar{3}m$	$a = 6.35$ Å

* Please see [34] for details.

may have formed along GBs and around other particles. This is then the microstructure that dislocations must overcome during deformation, and that dictates many of the physical processes for strength, work hardening and fracture.

3.2.2 Dislocations

Before describing the various strengthening contributions in age-hardenable aluminium alloys, it is important to introduce the concept of dislocations. Plastic flow in crystals occurs by propagation of small displacements. The crystal structure restricts both the magnitude and direction of the displacements, and the planes in which they propagate. These slips are called dislocations, the lines separating unslipped and slipped regions are called dislocation lines, the displacements are called Burgers vectors, and the propagation planes are called glide planes. As such, a dislocation is defined by its line vector $\vec{t}$, which may vary along its length, and its Burgers vector $\vec{b}$ that must be constant along its length. When $\vec{t} \perp \vec{b}$, the dislocation is called an edge dislocation, and crystallographically it is equivalent to inserting or removing a half-plane of atoms in the crystal. As such, $\vec{b}$ must be given by the crystal structure, and plastic flow in crystals occurs by propagation of this quantised displacement on some crystallographic plane. Aluminium has a face-centerd cubic (fcc) crystal structure, and slip will usually propagate with Burgers vectors $\vec{b} = \frac{1}{2}\langle 110 \rangle$ on the close-packed $\{111\}$ planes [3], [17], [19], [35]. Given the symmetry of fcc materials, there are 12 different combinations of these vectors and planes, so that there are in total 12 different slip systems, and any global plastic deformation must be achieved by a combination of these 12 systems.

Figure 3.3 shows a schematic of an edge dislocation. The figure also shows how the Burgers vector is defined through the Burgers loop around the dislocation line. Other types of dislocations exist as well, the most important being the screw dislocation which has $\vec{t} \parallel \vec{b}$. The glide plane of a dislocation is given by $\vec{t} \times \vec{b}$, i.e. it is the plane that contains both vectors. This means that edge dislocations are more limited in terms of glide than screw dislocations. In practise however, dislocations in ductile metals curve and bend, as seen in Figure 3.4. This means that $\vec{t}$ will vary along the dislocation lines, and so will its type. This is important not only because it changes how dislocations may glide, but also because the stress field around different parts of the dislocation will be different. Figure 3.5 shows elastic stress fields around edge and screw dislocations. These stress fields are important when it comes to determining how dislocations interact with obstacles in the crystal, such as foreign atom species or inclusions. When a shear stress τ actos on the glode plane of a dislocation, the dislocation will experience a force $F = \tau b$ [19], [35]. This force acts perpendicularly along the entire dislocation, which will make the dislocation curve if it is pinned by obstacles. The line tension Γ, which acts along $\vec{t}$ against any attempt at bending the dislocation, will therefore exert a force

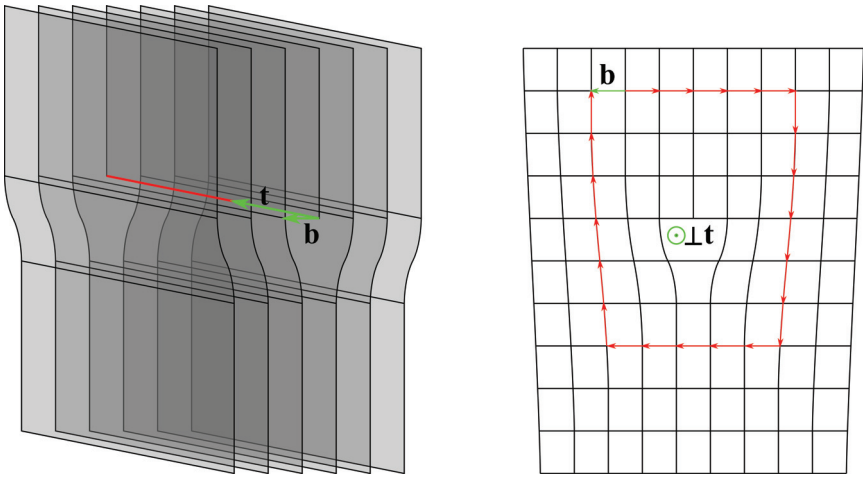

Figure 3.3: Schematic of an edge dislocation.

on the obstruction. In principle, the value of Γ depends on the angle between $\vec{b}$ and $\vec{t}$ (which will vary along dislocations subjected to stresses) [36], but it is sometimes approximated as $\frac{1}{2}Gb^2$, where G is the shear modulus of the crystal [3], [37]. The force with which a dislocation exerts on obstacles is treated in a while. First, the effects of GBs on dislocation slip is discussed.

3.2.3 Grain boundary strengthening

Grain boundaries may strengthen a material because of the incompatibility between grains [19], [38]. This incompatibility means that dislocations in one grain have no or few close slip systems in the neighbouring grain, given by the difference in crystallographic orientation between the two grains. Thus, for slip to be transmitted across a grain boundary, dislocations may have to be "reflected" as well as stored in the grain boundary in order for a new dislocation to be emitted. These extra dislocations require additional energy, and it is often necessary for dislocations to pile-up in order to reach sufficient shear stresses. The stress in front of a dislocation pile-up consisting of n dislocations is [19]

$$\tau_n = n\tau, \tag{3.4}$$

where τ is the applied shear stress. The shear stress at the front of a dislocation pile-up given by Equation (3.4) can become large enough to initiate slip across a grain boundary in commercial alloys because the grain size is large and relatively many dislocations can pile-up against grain boundaries [39]. However, in ultra-fine grain materials, the grain size is so small that dislocation activity is modified [40]. A popular approach to explain the dependence of strength on the grain size

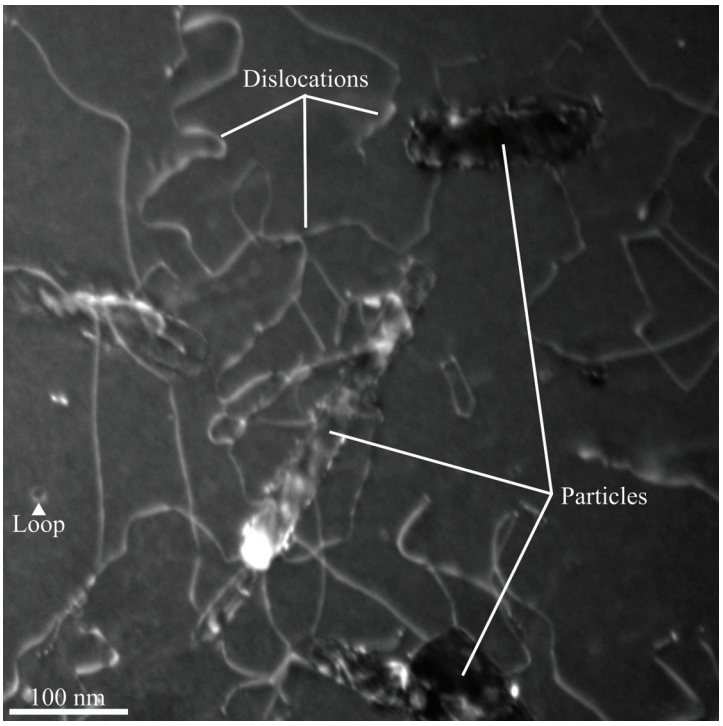

Figure 3.4: TEM weak-beam dark field image of dislocations in a Al-Si-Mg-Cu-Hf cast alloy creep (300 °C) specimen, taken far from the fracture surface.

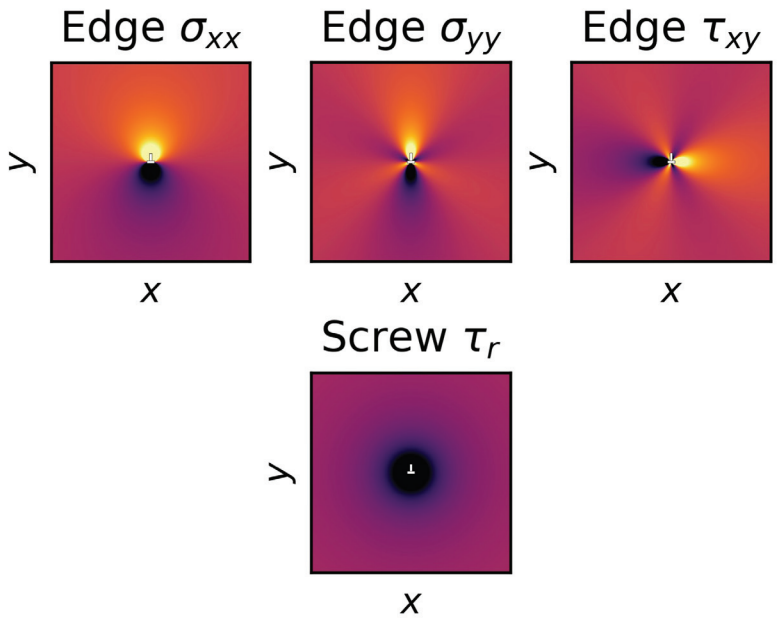

Figure 3.5: Elastic stress fields around dislocations. Dark and bright regions represent negative and positive values, respectively. Calculated based on Cottrell [19] and Hull and Bacon [35].

of a material is to relate the length of dislocation pile-ups to the grain size [19], [35], [38]. The number of dislocations in a pile-up of length L is

$$n = \frac{\tau L}{A}, A = \frac{Gb}{\pi} \left\{ \begin{array}{ll} 1, & \text{screws} \\ \frac{1}{1-\nu}, & \text{edge} \end{array} \right\}, \tag{3.5}$$

where ν is Poisson's ratio. At the front of such a pile-up, the shear stress will be

$$\tau_n = n\tau = \frac{L}{A}\tau^2. \tag{3.6}$$

If a critical shear stress of τ^* is required for slip to spread across a grain boundary, then $\tau_n = \tau^*$ at the onset of slip transmission across the GBs. A shear stress of

$$\tau = \sqrt{\frac{\tau^* A}{L}} = kL^{-1/2} \tag{3.7}$$

is required to fit the required n dislocations into a pile-up of length L and achieve $\tau_n = \tau^*$ at its tip. Equation (3.7) is the strength increment due to grain boundaries, and by adding the friction stress τ_0 of the material, the well-known Hall-Petch relation is achieved [41], [42]

$$\tau_{HP} = \tau_0 + kL^{-1/2}. \tag{3.8}$$

It is usual to put $L = d$ in Equation (3.8), where d is the grain diameter of the material, because this is the maximum length of a pile-up in a grain. However, by keeping L it is emphasized that the strength is dependent on the length of the dislocation pile-up. This distinction is important because Equations (3.5) and (3.6) are only valid for pile-ups with relatively large values of n [38]. It is also worth noting that the friction stress τ_0 in very small grains should be interpreted as the stress required to both generate and move dislocations. For very small grains, there will be very few initial dislocations in each grain and, in addition, dislocation sources might not have enough space to operate. In such cases, the dislocation pile-up model is not valid. This usually affects the power of d in the Hall-Petch equation [43], [44]. In the absence of dislocation pile-ups, plastic deformation might not occur by slip, but by grain boundary sliding or grain boundary dislocations instead [45], [46]. In other words, plastic flow is changed from intergranular to intragranular [44]. At extremely small grain sizes, grain boundary deformation mechanisms may dominate and lead to a decrease in material strength, and may be the reason for the so-called inverse Hall-Petch relationship [47]. Nevertheless, the Hall-Petch relationship is usually found to give good results for quite small grain diameters in processed aluminium alloys with ultra-fine grains [48]–[50] .

3.2.4 Dislocation strengthening

Dislocations contribute to the strength of alloys by [3], [13]

$$\tau_D = 2CG\sqrt{\rho^T}, \tag{3.9}$$

where $C \approx 0.3$, and ρ^T is the total dislocation density in the material. This is because additional stress is required to force dislocations through each other, and that the resulting steps on the dislocation lines will not glide as easily. During deformation, dislocations may multiply and lead to an increased strengthening given by Equation (3.9). It is often useful to divide the total dislocation density into two parts, the statistically stored dislocations and the geometrically necessary dislocations (GNDs). Statistically stored dislocations are the result of random encounters between dislocations and are important for work hardening of pure crystals [8], [14], but are very difficult to predict accurately. GNDs, on the other hand, are possible to determine as they are the result of strain gradients in the material [13]–[15]. These strain gradients appear in multi-phase materials where at least one of the phases deform differently than the others because dislocations must be stored to maintain compatibility between the deforming and the non-deforming phases. The simplest case is perhaps dispersion strengthened alloys, where hard particles are dispersed in a relatively soft matrix [3], [13]–[15], [17]. When the material yields and macroscopic slip occurs, the hard particles do not deform with the matrix. Instead, GNDs form around the particles. This leads to dislocation storage which inhibits dislocation glide and cause the material to work harden. At low strains, dislocation shear loops [51] around the particles are stable (i.e. the local stress in their vicinity does not exceed the local yield stress) and lead to some work hardening. As strain increases, more and more loops are necessary to accommodate the increasing mismatch between the particle and the matrix. Because these dislocations form pile-ups, the stress exerted on the particle increases roughly linearly with the number of shear loops n, which also increases linearly with the shear strain γ of the slip system of the loops. For a particle of size r, the shear stress goes roughly as $nGb/2r \approx G\gamma$, and the shear loops become unstable at around 1% strain [13]. At this strain, dislocations may cross-slip and form prismatic loops instead of the shear loops. Prismatic loops are dislocation loops where the Burgers vector points out of the loop-plane, while the Burgers vector of the shear loops lie in the loop-plane. In terms of compatibility between a non-deformable particle and the matrix, prismatic loops may be punched out from the particle in order to maintain compatibility. Because the Burgers vectors of the loops point out of their plane, they are stable and cannot collapse, but are free to move. They can be considered to be of either interstitial or vacancy character, where an extra "disk" of atoms are added or removed, respectively. The density of these loops depends on the geometry of the particles, or more precisely: by the distance between the

particles on the active slip planes. Given an inter-particle spacing λ^G, the density of GNDs is [13]

$$\rho^G = \frac{1}{\lambda^G}\frac{4\gamma}{b}. \tag{3.10}$$

For pure metals, λ^G can be interpreted as the grain size instead. The major point with Equation (3.10) is that the dislocation density in a dispersion-strengthened alloy may become quite large relatively quickly if the distance between particles is small, and the strengthening contribution given by Equation (3.9) will increase correspondingly. At a certain strain however, the back stress from the prismatic loops (if they are held up at other obstacles) will make it increasingly difficult to generate new loops. This may enable more shear loops to form around the particles, and eventually the shear stress exerted on the particle will reach the theoretical shear stress of the particle. At a certain point, the particles responsible for the GNDs will therefore break or detach from the matrix - removing their ability to generate new geometrically necessary dislocations. In fact, once these particles break or detach, voids will form around them and the GNDs may empty into these voids and lead to a softening [52]. Other mechanisms may occur as well, depending on how the stresses around the particle is relaxed. One way to relax these stresses, is for secondary (i.e. not lying on the original glide plane of slip) prismatic dislocation loops of opposite sign (i.e. one set of interstitial loops and another set of vacancy loops) to form on inclined planes around the particle [3]. This will result in two quadrants of the particle being subjected to compressive stresses, while the two remaining quadrants will experience tensile stresses. Once enough of these loops have formed, the tensile stress may open a void at the particle-matrix interface, and further generation of loops will open up the void [3]. The growth and coalescence of these voids will result in ductile fracture, and it is clear that ductile failure is closely linked to microstructure and local phenomena such as work hardening.

3.2.5 Solid solution strengthening

Solute dispersed in the aluminium matrix will slow down dislocations and strengthen the material [53], [54]. The stress field around dispersed solute atoms exerts a force on dislocations that must be overcome for plastic flow to occur. This force arises from four main elementary interactions [54]: size misfit, modulus misfit, "electrostatic" interaction, and stacking-fault interaction. Various models exist, but a power law of the solute concentration is most common [53], [54]. If more than one solute species is present in the alloy, the total strengthening contribution from each different solute species is usually added in a linear sum, where the concentrations of each species, c_i, are weighted by different "drag-coefficients" k_i [53]

$$\sigma_{ss} = \sum_i k_i c_i^r. \tag{3.11}$$

The power r in Equation (3.11) lies between $1/2$ and 1 and depends on how the dislocations intersect various solute atoms [53], [54]. The most common theories, Fleischer's and Labusch's give $r = 1/2$ and $r = 2/3$, respectively [54]. Labusch's theory tends to give better results, and several models apply Equation (3.11) with $r = 2/3$ with great success [54]–[58]. The theory of solid solution strengthening is not complete, and the effects of clustering, strain rate, and temperature is not fully understood [54]. As a final point, it should also be mentioned that how the sum in Equation (3.11) is performed can be investigated further. Labusch's theory can be applied summing the concentrations and their weights before taking the total sum to the power of $r = 2/3$ [54] (p. 167). It might also be possible to sum each strengthening contribution $k_i c^r$ from the different solute species and add them in a Pythagorean sum. As such, solid solution strengthening remains an important effect that can be modelled successfully, but not necessarily with a complete understanding. The physical mechanisms behind solid solution strengthening are of relatively little relevance to the present work, however, although they may play a role in strengthening of PFZs, which are of particular interest to this thesis.

3.2.6 Precipitation strengthening

There are two main types of theory for precipitation hardening. One of them has already been introduced when discussing the work hardening by GNDs, namely strengthening by impenetrable particles. In the context of dislocation strengthening, the focus was on how the increase in GND as a function of strain related to the impenetrable particles. Now the focus is on the stress required for the first dislocations to bypass the impenetrable particles. The other strengthening theory is similar to the solid solution strengthening theory, and considers weaker obstacles that are sheared by dislocations. Both processes are illustrated in Figure 3.6, and different parameters are important for the different cases, as will be shown in this section.

As already mentioned, the stress required for dislocations to form Orowan loops around impenetrable particles is $\tau \propto 2G/b$ [51], while Nabarro [59] proposed that strengthening from shearable particles should go as $\tau \propto \sqrt{r}$. Both of these theories are useful in their respective regimes, which are determined by the size of the particles. However, what is important for precipitation strengthening is which theory applies to the various phases that form during the ageing of the alloy. As such, when discussing precipitation strengthening, it is usually understood that the particles in question are precipitates, and possibly dispersoids. During ageing, precipitates typically start out as small and coherent phases in the aluminium matrix and gradually evolve into larger and coarser phases with increasing incoherency. Because small and coherent precipitates are expected to be shearable, while larger and more incoherent particles are expected to be bypassed, there is a transition

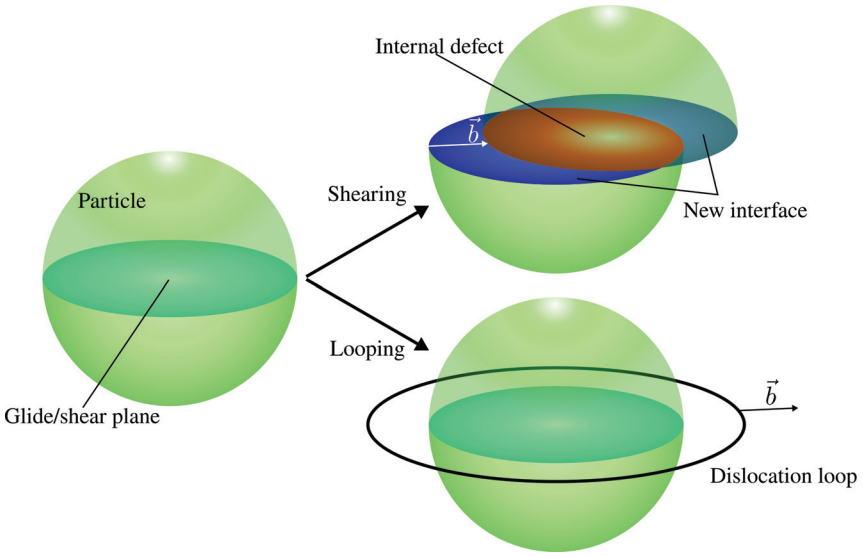

Figure 3.6: Schematic shearing or looping of a particle by a dislocation $\vec{b}$. When particles are sheared, two new interfaces and an internal defect are created, while a single dislocation loop is formed if the particle is bypassed by the Orowan mechanism.

regime centred at a critical radius r_c [51]. In the original ideas worked out in the works by Nabarro [59] and Orowan [51] (during the discussions at the symposium on Internal Stresses in Metals and Alloys in 1948) it was made quite clear that it is uncertain what happens in the transition region. Nevertheless, it is common to take r_c as the radius where the two theories coincide, as shown in Figure 3.7.

Forces acting on a dislocation pinned by obstacles

The classic case of precipitation strengthening is shown in Figure 3.8, where a schematic dislocation is pinned by a series of obstacles. Under the influence of an applied shear stress τ, the dislocation curves into an arc with radius $R = \frac{\Gamma}{\tau b}$ and angular span of 2θ [37], [59]. Each of the dislocation segments on either side an obstacle exerts a force $\vec{\Gamma}$ that acts along the tangent of the segment, and the angle between the line tensions, ϕ, depends on the radius R. Force balance then requires that the obstacle exerts a force $\vec{F} = \vec{\Gamma}_1 + \vec{\Gamma}_2$ back on the dislocation. The fundamental equation for precipitation strengthening is that this force is [3], [17], [37]

$$\vec{F} = 2|\vec{\Gamma}|\cos(\phi/2)\,, \tag{3.12}$$

and cannot become greater than $2|\vec{\Gamma}| = 2\Gamma$. Because the curvature of the pinned dislocation is related to both the applied stress and the angle ϕ, the stress required

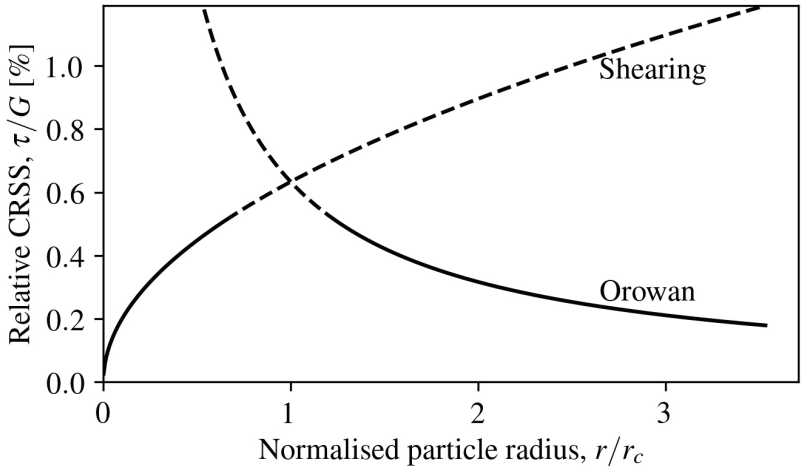

Figure 3.7: Transition between precipitate shearing to precipitate looping at constant precipitate volume fraction. Below the transition precipitate size r_c, precipitates are sheared by dislocations and the critically resolved shear stress increases as $\tau \propto \sqrt{r}$. Above r_c, the precipitates are bypassed by dislocations, and the critically resolved shear stress is given by the Orowan equation (Equation (3.14)) so that $\tau \propto 1/\lambda^G$, where λ^G is the interparticle spacing. Here, $r_c = 5.66$ nm, $G = 25.5$ GPa, $f = 0.42\%$, and $\lambda^G = \sqrt[3]{1/\rho} - 2r$, with $\rho = \frac{3}{4\pi}\frac{f}{r^3}$ as the number density of precipitates.

to produce a force given by Equation (3.12) is [3], [17], [37]

$$\tau = \frac{2\Gamma \sin(\theta)}{\lambda^G b} = \frac{2\Gamma \cos(\phi/2)}{\lambda^G b}. \tag{3.13}$$

It is clear that both the force and the stress given by Equations (3.12) and (3.13) have maxima for $\phi = 0$. It is also clear that a higher applied stress is required to reach the same pinning force when λ^G is reduced. At some critical $\tau = \tau_c$, the obstacles are either sheared or looped. If τ_c is achieved for $\phi < 0$, the maximum angle between the two line tension forces has some finite value ϕ_c and the maximum force F_i is the intrinsic strength of the obstacle. The problem of precipitation strengthening thus depends on two factors; the critical angle ϕ_c (or the intrinsic strength of the particle), and the spacing of particles along the dislocation lines λ^G. It turns out that these two factors are far from independent, and the problem can become quite complex when the particles have a size and shape distribution [3], [17], [37].

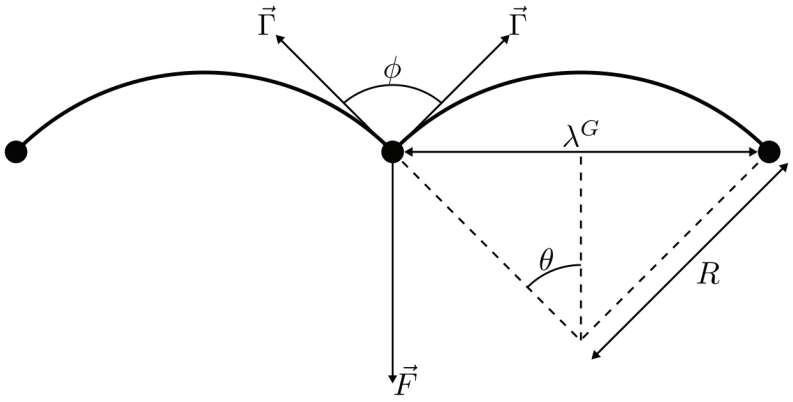

Figure 3.8: Force acting on a pinned dislocation.

Bypassing: $\phi_c = 0$

In the special case where $\phi_c = 0$, Equation (3.13) is independent on the intrinsic strength of the obstacles and depends only on the line tension and Burgers vector of the dislocation. This occurs for impenetrable particles, where the two dislocation segments that bows around the obstacle meet with two opposing line vectors, but equal Burgers vectors. These parts of the dislocation segments will annihilate, leaving an Orowan loop [51] around the particle, while the dislocation is free to move away (or to the next obstacle). Thus, for impenetrable particles, the required

stress to overcome obstacles is

$$\tau_O = \frac{2\Gamma}{\lambda^G b}, \tag{3.14}$$

which is the famous Orowan equation [51]. The Orowan stress is the stress required to both initiate plastic flow and to start the work-hardening mechanisms by impenetrable particles. Equation (3.14) is a very useful equation because it only depends on λ^G, but this single parameter may be challenging to estimate. Various statistical methods can be used to relate λ^G to θ and thus also the applied stress [36]. As a first approximation, the obstacles can be considered to lie on a square grid so that $\lambda^G \sim \sqrt[3]{1/\rho}$, where ρ is the number density of impenetrable particles. This relation gives the average spacing between centres of the obstacles and should, in principle, be corrected for the size of the particles.

Shearing: $\phi_c > 0$

If the dislocations break away from the obstacles at $\phi_c > 0$, the spacing λ^G will depend on both the density and arrangement of obstacles, and the breaking angle. Friedel statistics, which are also used for solid solution strengthening, can be used for weak obstacles (large ϕ_c) [3], [17], [37]. Assuming that the average spacing of obstacles in the slip plane is λ_l, and that the obstacles lie on a square grid so that $\lambda_l = 1/\sqrt{N_s}$, where N_s is the area density of obstacles in this plane, then [3]

$$\tau_P = \frac{|\vec{F}|^{3/2}}{bl(2\Gamma)^2} = \frac{2\Gamma \cos^{\frac{2}{3}}(\phi/2)}{bl}. \tag{3.15}$$

Equation (3.15) depends quite heavily on the assumption about how obstacles are distributed in the material. An empirical equation motivated from computer simulations gives [3]

$$\tau_P = \frac{2\Gamma \left(0.8 + \frac{\phi}{5\pi}\right) \cos^{\frac{2}{3}}(\phi/2)}{bl}, \tag{3.16}$$

for arrays of randomly distributed obstacles. From both Equation (3.15) and (3.16) it is clear that the strength of an obstacle (the critical breaking angle ϕ_c) has an important influence on yield stress of the alloy. However, how this breaking angle depends on the size, shape, and phase of the obstacle is very difficult to predict, as it will depend on a number of complex processes within the obstacle phase. As such, the phase (internal structure) of the obstacles becomes important for both strength and work hardening [60]. Ardell [36] and Martin [3] define five different processes that contribute to the strength of shearable obstacles (i.e. the breaking angle ϕ_c and corresponding F_i):

- chemical/surface strengthening

- stacking-fault strengthening
- modulus strengthening
- coherency strengthening
- order strengthening

Chemical strengthening arises from the extra energy required to form new surfaces between the precipitate and the matrix, shown as blue regions in Figure 3.6. This strengthening mechanism depends on the specific energy γ_s of the new interfaces, and of course on the shape of the particle. For spherical particles, the contribution from surface strengthening is [36]

$$\tau_{surface} = \sqrt{\frac{6\gamma_s^3 bf}{\pi\Gamma}}\frac{1}{r}, \tag{3.17}$$

where f is the volume fraction of precipitates. Equation (3.17) shows that surface strengthening decreases with particle size, which is at odds with experimental observations and Nabarro's prediction [59]. Stacking-fault strengthening, on the other hand, depends on the difference between the stacking-fault energies of the matrix and the precipitate, $\Delta\gamma = |\gamma_{sfM} - \gamma_{sfP}|$, and shows a $\tau \propto \sqrt{r}$ dependency. This strengthening mechanism considers how a dislocation dissociates into two partials with a stacking-fault between them. If the stacking-fault energies of the precipitate and the matrix are different, a force $F = \Delta\gamma l$ will act to minimize (or maximize) the stacking-fault area between the partials within the precipitate, where l is the length of dislocation residing inside the precipitate at the breaking point. Again, Friedel statistics is needed to solve the problem and yields [36]

$$\tau_{SF} = \sqrt{\Delta\gamma^3 \frac{3\pi^2 rf}{32\Gamma b^2}}, \tag{3.18}$$

for weak and small precipitates, i.e. for underaged alloys. Other estimates of l exist that will give different results than the one in (3.18), some which predict that Equation (3.18) is an overestimate for large particles [36]. Modulus strengthening is very complex to predict and is not very well understood [36]. The equations become quite complex and specialised for different cases and out of scope for this thesis, but the results are usually close to the prediction by Nabarro that $\tau_{modulus} \propto \sqrt{r}$, with various corrections [36].

Coherency strengthening is related to the original theory by Nabarro [59]. For underaged alloys, the result of coherency hardening is [36]

$$\tau_{coherency} = \chi\sqrt{(\varepsilon_P G)^3 \frac{rfb}{\Gamma}}, \tag{3.19}$$

where χ depends on the theories behind the derivation and lies somewhere between 2 and 3. The misfit parameter

$$\varepsilon_P = |\delta| \left[1 + \frac{2G\,(1 - 2\nu_p)}{G_p\,(1 + \nu_p)} \right], \tag{3.20}$$

where ν_p and G_p are Poisson's ratio and the shear modulus of the precipitate, respectively, and δ is the lattice mismatch parameter of the precipitate and the matrix. Equation (3.20) represents the strain field around the precipitate, which in reality should be a function of the aspect ratio, shape, and size of the precipitate, in addition to the lattice mismatch. Donnadieu, Dirras and Douin [61] measured the strain fields around two types of precipitates in an Al-Mg-Si alloy and simulated how a screw dislocation would interact with these. The researchers found that some of the precipitates were looped, while others were sheared, even though the precipitates were of similar size. Later works by Misumi *et al.* [62] showed experimentally that the looped precipitates were most likely sheared, however, illustrating that estimating the influence of precipitate stress/strain fields on dislocation motion can be more complex than the theory behind of Equation (3.19).

The final strengthening mechanism is order strengthening. The classical picture of this mechanism is that an anti-phase boundary forms as the upper and lower part of a precipitate are shifted relative to each other by a Burgers vector, shown as the red area in Figure 3.6. This mechanism arose as a suggestion because dislocations were observed to travel in pairs in alloys with ordered precipitates, and it was suggested that the first dislocation created an anti-phase boundary, while the trailing one repaired it. The maximum force a dislocation will experience as it creates an anti-phase boundary with energy γ_{APB} is $F = 2\gamma_{APB}r$, so that order strengthening for one dislocation becomes [36]

$$\tau_{order} = \sqrt{\gamma_{APB}^3 \frac{3\pi^2 r f}{32\Gamma b^2}}. \tag{3.21}$$

How the second dislocation influences τ_{order} is difficult to determine, as it depends on how far the second dislocation trails behind the first one, but it will usually reduce the contribution from order strengthening predicted by Equation (3.21) by more than a factor 2 [36]. Order strengthening may not be as simple as the creation and annihilation of anti-phase boundaries, however. If the precipitates are "semi-coherent", as they usually are in peak-aged Al-Mg-Si alloys, the Burgers vector shift does not necessarily match that of the atomic positions inside the precipitate. This means that the atoms in the shearing plane must reorganize in a less energetically favourable way. Furthermore, it means that the next dislocation that shears the precipitate in the same slip plane might not repair the defect. In fact,

subsequent dislocations may see an increasingly disordered structure that is less easy to glide through. Indeed, for "semi-coherent" precipitates it does not make sense to think of a dislocation slipping through the crystal structure, as the structure is incompatible with the Burgers vector. In principle, the precipitate may slip collectively (requiring the shear limit of the phase) instead. Conversely, the precipitate may shear by it's own Burgers vector $\vec{B}$ that differs from the matrix Burgers vector. This does not create an internal defect, but the mismatch between $\vec{B}$ and $\vec{b}$ must be accommodated by a modified elastic strain field around the precipitate or by interface-defects (e.g. the residue from $\vec{B} - \vec{b}$). If any of these mechanisms are possible is not known, and investigating them is an incredibly complex task. It will involve calculating the energies required to shear precipitates in various directions and magnitudes, and comparing these to the energies of other mechanisms. For instance, as Paper 2 in this thesis discusses [63], it may be possible that dislocations avoid shearing β" precipitates in previously sheared planes, and cross-slip to nearby planes in order to shear an undisturbed structure instead.

The effect of multiple shears should also be mentioned for the other strengthening mechanisms. It is obvious from Figure 3.6 that as a precipitate is sheared, its cross-section in the shearing plane is reduced. The next dislocation thus sees a different precipitate, and this may affect the strength of the alloy. For instance, when a precipitate is sheared, the next dislocation does not create as big a step as the previous one, but it must pass through a modified elastic field and slip across the previously introduced faces and the planar defect left by the first dislocation. Hence, if surface strengthening is dominating initially, it will weaken during deformation. This will in turn localise slip to this plane, and can lead to early failure and low ductility. Conversely, the localised slip may also lead to localised work hardening that causes slip to even out after some time, and the effect of shearing when it is dominated by chemical strengthening is in fact quite complex. The same can be said about the various other mechanisms. Predicting how the evolution of the global slip will change based on changes in each precipitate strengthening contribution is a problem that is very difficult to solve.

In conclusion, the various strengthening contributions from precipitates vary from quite simple (large and strong particles) to complex and challenging (small and weak particles). A commonality between the theories however, is that they depend quite strongly on the size of the precipitates, if the volume fraction of precipitates is kept constant. This can be seen by assuming spherical precipitates on a square grid so that their centre-to-centre distance $\lambda^C \approx \sqrt[3]{1/\rho}$, where ρ is the number density of particles per volume equal to

$$\rho = f \frac{3}{4\pi \langle r \rangle^3}. \tag{3.22}$$

Hence, all of the shearing theories predict that τ_P has a size-dependency. For age-hardenable aluminium alloys this is important, because the volume fraction of precipitates does not necessarily change much, while the precipitate sizes do. As an alloy is heat treated from its SSSS state, its strength increases with the precipitates size until the transition point between shearing and looping, after which it decreases again. This is the traditional under-, peak-, and over ageing stages of alloy heat treatment. However, what is important is that the rate $d\tau_P/dr$ depends on the precipitate internal structure in the shearing regime, while it does not depend on it in the bypassing regime. Hence, it is important to establish how different phases are sheared in order to increase and utilise our understanding of precipitation hardening when an alloy contains shearable precipitates. This is especially true when considering localisation of slip in alloys.

3.3 Precipitate Free Zones

It is of special interest to this thesis to investigate PFZs that form around GBs and particles (secondary and primary) in age-hardenable aluminium alloys. A PFZ forms because both vacancies and solute are drained away at GBs and particles, thus reducing or eliminating the precipitation potential in their vicinity [64], [65]. The process is illustrated in Figure 3.9. PFZs have a two-fold impact on the ductility of aluminium alloys. First, the drained solute form large grain boundary precipitates that are nucleation sites for voids during plastic deformation [69]. Second, the absence of strengthening precipitates causes these zones to become much softer than the grain interior [66]–[68] and may lead to either strain localisation or stress relaxation in the PFZ during deformation [69]. Figure 3.10 illustrates the main ideas behind the effect of varying PFZ width on ductility. By relaxing the stresses ahead of slip bands that propagate from the grain interior, PFZs may delay void nucleation and growth at the GB precipitates and thus increase ductility. On the other hand, if deformation localise in PFZs, the local strains can accelerate void growth and reduce ductility instead. Which of these processes that occur depends on both the PFZ width and the slip mechanisms in the grain interior (stress relaxation in PFZs is only a benefit if planar slip is prominent and if there are many GB precipitates for example). Hence, the role of PFZs is closely linked to other microstructural features, such as GB precipitates and precipitates in the grain interior. There is therefore little agreement on whether PFZs are beneficial [70]–[72], detrimental [73]–[75], or unimportant [76] to ductility. If preferential deformation occurs in the PFZs, and the zones are wide enough for dislocations to pile-up against the precipitates of the grain interior, PFZs may also cause softening of the material, even if the total volume fraction of them is low [71], [76], [77]. It has also been suggested that dislocation interactions themselves may nucleate voids [9], [78] and that dislocation tangles in the confined PFZ may lead to intergranular

ductile failure [73], [79], [80].

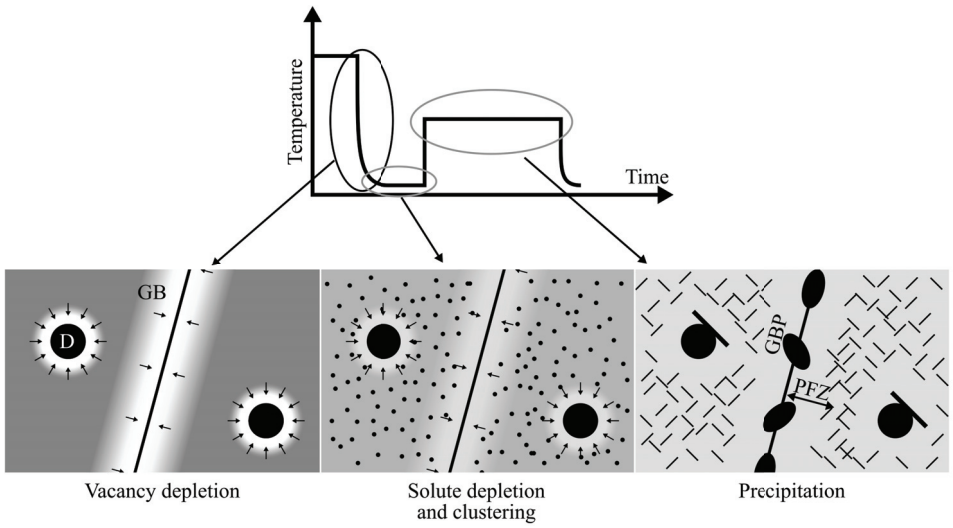

Figure 3.9: Illustration of PFZ formation. GBs and dispersoids (D) drain their surroundings of vacancies (during quenching) and solute (during ageing), reducing clustering and subsequent precipitation in these regions. Drained solute form large grain boundary precipitates (GBPs) and "overaged" phases on dispersoids that do not contribute to strength. Concentration of solute in solid solution is indicated by the background colour, and the vacancy and solute depletion gradients are illustrated in each case.

There have been several attempts to model the effect of PFZs on strength and ductility [81]–[85]. These models usually assume that the PFZs work harden much faster than the grain interiors, but start out with a much lower flow stress. This is usually a well-founded assumption, as dislocations have been shown to originate at GB sources and tangle in the PFZs at low strains [86], [87]. However, at larger strains, substructures develop in the PFZ, which complicate the work-hardening process [80], [87]. This makes sense because strain localisation in the soft PFZs effectively drives an orientation change relative to the grain interior. However, exactly how these orientation changes occur, what their magnitude are, and how they affect nucleation of voids are uncertain. Because soft zones along grain boundaries seem to be important for plasticity and fracture [85], more detailed characterisation of their deformation mechanisms is important. This was the motivation for Paper 1 [88]. In addition, understanding the deformation mechanisms inside the grain interior is also important, and this was the motivation for Paper 2 and 3 [63], [122]. Finally, Paper 4 [129] investigates the importance of PFZs around both GBs and dispersoids.

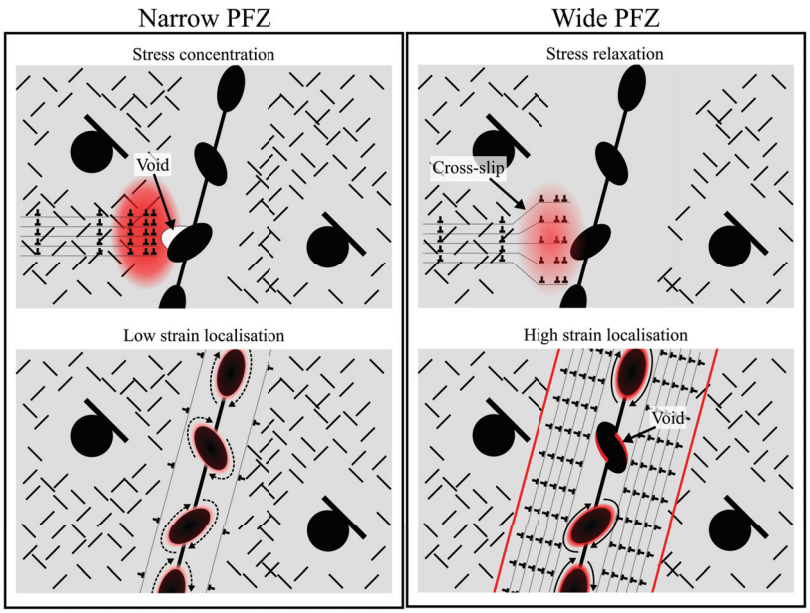

Figure 3.10: Illustration of different PFZ deformation mechanisms. A narrow PFZ is unable to relax stresses ahead of slip bands and may reduce ductility, but is less susceptible to strain localisation and may increase ductility instead. A wide PFZ can relax stresses ahead of slip bands by allowing dislocations to cross-slip more easily and can increase ductility. On the other hand, a wide PFZ is more susceptible to strain localisation that may lead to incompatibilities at the GB and GB precipitates, and thus reduce ductility.

As an example of deformation processes that may occur in PFZs, Figure 3.11 shows a time-series of an *in situ* tensile experiment performed in a TEM by the author. The specimen was a conventionally electropolished thin foil of the Al-Mg-Si alloy AA6060 in T6 temper, that was attached to two steel grips by conductive epoxy and pulled in tension. The straining initiates a crack that propagates through the specimen, and the stress in front of this crack tip initiates slip that subsequently drives dislocation activities in the field of view (away from the crack tip). The figure shows the evolution of one particular dislocation that has been emitted from a GB source. It starts out by bowing into the PFZ. Because it is anchored to the GB on one end, with its other end apparently free to move, it propagates down along the GB inside the PFZ, and eventually piles up against two dislocations that were already present in the PFZ when the moving dislocation was emitted. An interesting observation, that is not shown in the figure, is that there are relatively few dislocations inside the PFZ, while dislocations tangle and move within the precipitate strengthened grain. This experiment shows that the theories developed by numerous works [70]–[76] might not be valid for this particular alloy, which has a relatively wide PFZ for industrial Al-Mg-Si alloys (≈ 170 nm).

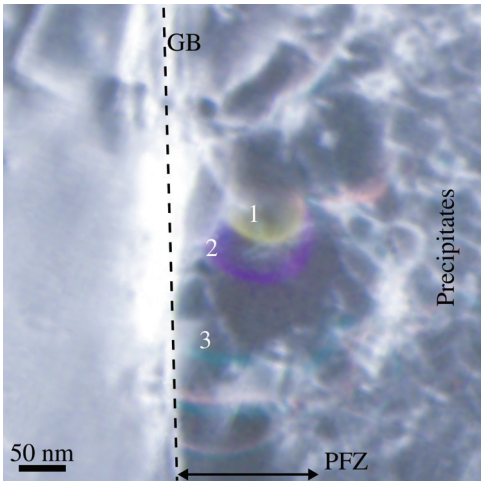

Figure 3.11: Dislocation motion within a PFZ in AA6060 during *in situ* straining in a TEM. The image shows three snapshots of an *in situ* straining experiment where each snap shot has been tinted a different colour and then been overlaid to produce a time-series. Two dislocations are already present in the PFZ initially, and the first snapshot shows a dislocation at "1" that has just been emitted from a GB source. After some time, the dislocation moves to position "2", and then finally ends up at position "3". At this position, it piles up against the already present dislocations and shift them slightly down (pink to teal positions).

Chapter 4

Transmission Electron Microscopy

The transmission electron microscope (TEM) is an important tool for nanoscale characterisation. In many ways, it is comparable to a regular visible light microscope, in that the mathematics and physical processes behind its operation are similar. However, while visible light microscopes bends photons using glass lenses of fixed power, but variable positions, a TEM bends fast-moving electrons using electromagnetic lenses of varying power but with fixed positions. In addition, because electrons carry electrical charge, the beam can be manipulated in many more ways than what a beam of photons can. The reason why the optics in a TEM is similar to that of visible light microscopes, is the wave-particle duality of electrons. De Broglie theorised in 1925 that fast-moving electrons behave as waves with a wavelength that depends on their energy. With relativistic corrections, electrons accelerated by a potential V will behave as a wave with wavelength [6]

$$\lambda = \frac{h}{\sqrt{2m_0eV\left(1+\frac{eV}{2m_0c^2}\right)}}, \tag{4.1}$$

where h, m_0, e, and c, are Planck's constant, the electron rest mass, the electron charge, and the speed of light in vacuum, respectively. For an accelerating potential of $V = 200$ kV, Equation (4.1) gives $\lambda = 0.0251$ Å, which is several orders of magnitudes less than that of visible light. For a visible light microscope, the resolution is limited by the Rayleigh criterion

$$\delta = \frac{0.61\lambda}{\mu \sin\beta}, \tag{4.2}$$

where λ, μ, and β are the wavelength of the photons, the refractive index, and the semi-angle of the magnifying lens, respectively [6]. A similar relationship exists

for electrons, where $\delta \sim 1.22\lambda/\beta$ [6], and it is thus clear that a much higher resolution can be achieved by an electron microscope compared to a visible light microscope. However, aberrations in the electromagnetic lenses dramatically reduce the resolving power of TEM, and these aberrations will be discussed in Section 4.4. With the advent of aberration corrected TEMs, spatial resolution is rarely an issue with modern TEMs, however. Hence, a TEM can be used to image materials with extraordinary magnification and to study crystal structures and symmetries. In addition, because the electrons interact differently with various atom species, a TEM can also investigate the chemistry, bandgaps, and electronic structure of materials. The strength of TEM compared to other characterisation techniques is its ability to perform many experiments from the same nanoscale area of a specimen with very high resolution. However, one of the most limiting factor of TEMs is that specimens must be thin to allow electrons to pass through, and it can be challenging to relate the experiments back to the bulk material. Another challenge is the fact that the resulting images are 2D projections of a 3D object, although this challenge can sometimes be solved by performing tomography experiments or through-focus series. In addition, because the electrons must have a high kinetic energy to achieve the high resolution, electrons can damage and change the material, and beam sensitive materials have long been impossible to study in detail using TEM. Recent advances in detector technologies and scanning techniques have made it possible to limit the dose and beam damage, however, and beam sensitive materials are becoming an increasing field of research for TEM. For this thesis, the purpose of this chapter is to introduce the technique of TEM and relate it to aluminium and how it can provide useful information relating to deformation processes occurring on the nanoscale in aluminium. It starts by introducing the single-most important aspect of TEM, namely diffraction, before showing how conventional TEM images and high-resolution TEM (HRTEM) images are formed. Next, it presents some important scanning techniques that have been used in this thesis. Finally, some data analysis approaches are described and presented. This chapter is heavily based on the books by Williams and Carter [6] and Erni [89], and more details can be found in e.g. Hirsch, Howie, Nicholson, Pashley and Whelan [5], Humphreys [90], Nellist and Pennycook [91], and Kirkland [92] .

4.1 The Instrument

Figure 4.1 shows a schematic drawing of a TEM column. The column is kept under high- to ultra-high vacuum ($\sim 10^{-4} - 10^{-9}$ Pa), and consists of a stack of electromagnetic lenses, mechanical apertures, and deflector coils. In reality, several more components and lenses are present in the microscope in order to provide flexibility and corrections, but for clarity, only some are included in the figure. High-speed electrons are emitted from the electron gun and are formed into a beam by

the illumination system, that consists of several condenser lenses and a condenser aperture. The condenser aperture is used to remove electrons that are emitted with high angles from the gun, as these have less spatial coherency than other electrons. This aperture will also reduce the size of the area in the specimen-plane that can be illuminated with a parallel beam. Changing the power of the lenses in the illumination system can be used to converge or spread the electron beam to form a focused or parallel probe/beam, respectively. When operating the instrument in scanning mode, the beam can be made small by either inserting a small condenser aperture and/or by focusing the beam using the condenser lenses. The deflector coils can be used to both tilt and shift the beam before it reaches the specimen, thus providing a way of both scanning the beam and tilting or precessing it. This is important when it comes to e.g. scanning precession electron diffraction (SPED) or when doing diffraction experiments such as weak-beam dark field imaging of dislocations.

The imaging system consists of the specimen, objective lenses, and two apertures. The specimen sits very narrowly between two pole-pieces in the objective lens, in order to be close to its very short focal point. After the electron beam passes through the specimen, some electrons will have changed their direction. This means that wave vector transfers have occurred within the specimen, which can happen in numerous ways. The most common way this occurs in typical crystalline TEM specimens is by diffraction, which will be discussed in greater detail later. In terms of instrumentation, the important point is that electrons scattered to the same angle (i.e. having undergone the same transfer of wave vectors inside the specimen), will converge in the back focal plane of the objective aperture. It is therefore possible to block electrons that have experienced certain scattering events with the objective aperture, and only keep electrons that have a certain wave vector. The most typical application of this is to either select electrons with very small wave vector transfers, which will then create an image that contain electrons that have not experienced any considerable scattering. This includes the direct beam, and such images will typically consist of a bright background (due to the direct beam) and darker features that have scattered the incoming electrons out of the collection angle of the image. Therefore, such images are called bright field images. Alternatively, other wave vector transfers can be selected, which will then create an image of regions that produce the selected transfer on a dark background. These images are called dark field images, and are useful to map regions of e.g. similar crystal orientations. Sometimes, especially when doing parallel beam electron diffraction, the beam will be much larger than the regions of interest. In these cases, a selected area aperture can be inserted in the back image plane of the objective lens to block electrons that came from regions outside of the regions of interest.

Below the imaging system, the projection system magnifies either the image plane of the objective lens or its back focal plane and brings it to the detector plane. In addition, a pair of deflector coils can be used to tilt or shift the image to align it with various detectors. This is especially important when performing electron diffraction experiments, but can also be useful for shifting regions of interest onto specific parts of the detector.

There are usually several detectors available in a TEM. Before the evolution of modern charge-coupled devices (CCDs), analogue film was used to acquire images. While providing excellent contrast and precision, film is very cumbersome and limiting, however. With modern CCD cameras, acquiring images is much more efficient and allows for direct inspection without the need for developing negatives. However, these cameras are only indirectly registering electrons by first converting them to detectable photons before converting these to electrical charges again. Recent advances in direct electron detection have enabled both faster and more accurate ways of acquiring electron images, and are especially useful when performing scanning TEM (STEM) experiments [93]–[100].

4.2 Diffraction

Diffraction is the basis for traditional imaging techniques and is still one of the most powerful tools in the TEM. Diffraction is the process where a wave interacts with an object, aperture, or slit. This will typically lead to the wave interacting with itself and resulting in interference, as shown in Figure 4.2. In general, a planar wave $e^{2\pi i\left(\vec{k}_0\vec{r}-\omega t\right)}$ propagating along its wave vector $\vec{k}_0$ of magnitude $1/\lambda$ will elastically scatter on a periodic array of objects and result in new planar waves of the type $e^{2\pi i\left(\vec{k}'\vec{r}-\omega t\right)}$ travelling along new wave vectors $\vec{k}'$ of the same magnitude as the incoming wave vector [5], [6]. When scattering on a single object, an even distribution of $\vec{k}'$ will lead to a spherical wavefront, but depending on the interaction between the object and the wave, the intensity travelling in the different directions will vary. When a periodic array of objects scatter the incoming wave, the scattered waves will interfere and lead to a new set of planar wavefronts. The interference depends on the distance between the scatterers and the incident wave vector. It requires that the path difference between the waves scattered at two different objects equals an integer of the wavelength. The general case is illustrated in Figure 4.3, where two objects separated a distance $\vec{R}$ scatter an incoming wave. When the path difference $\Delta = \vec{R}\cdot\hat{k}' - \vec{R}\hat{k}$ equals an integer $2n$, the scattered waves may interfere constructively. Equivalently, the scattered waves will interfere constructively if $e^{2\pi i\left(\vec{k}'-\vec{k}_0\right)\cdot\vec{R}} = e^{2\pi i\left(\Delta\vec{k}\right)\cdot\vec{R}} = 1$. For an array of obstacles, this must apply for all the objects. In the case of a crystal, there will be exceptionally many objects that are spaced by $\vec{R}$ and integer multiples of $\vec{R}$. By the same

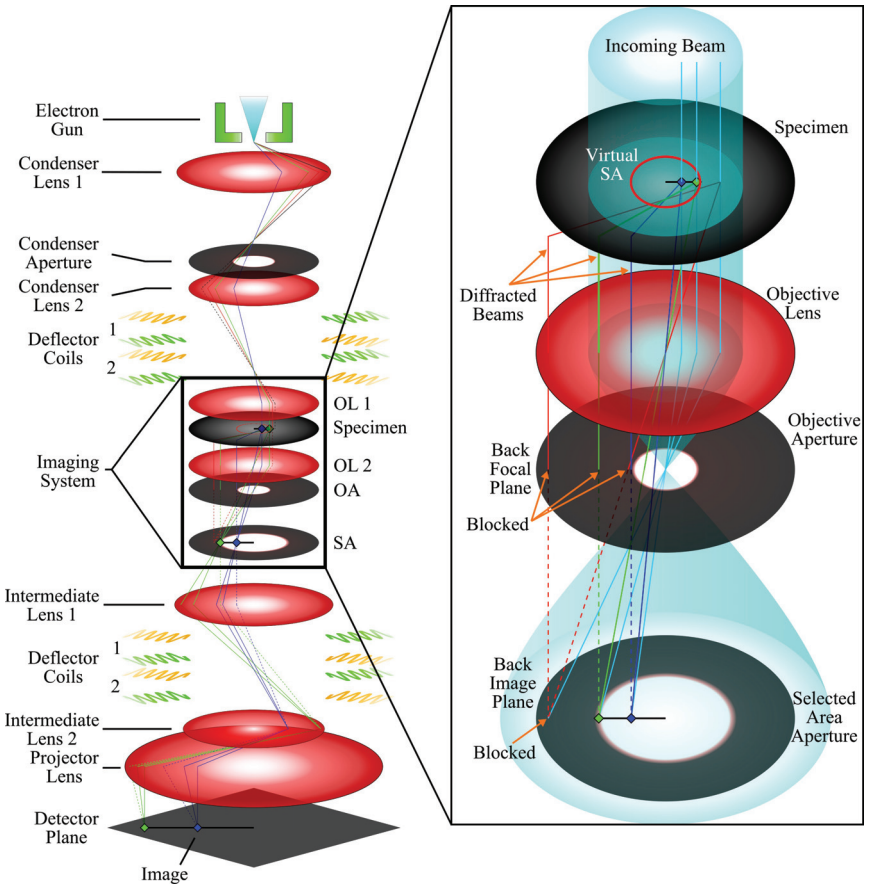

Figure 4.1: Schematic of the various lenses, apertures, and deflectors in a TEM column. All the lenses are shown to the left, while a close-up of the imaging system is shown to the right. The illumination system forms a beam from high-speed electrons emitted from the electron gun, and shines it on the specimen. The specimen sits between two objective lens (OL) pole-pieces, and will scatter beams from the incoming beam into various angles, and the objective aperture (OA) can be used to block selected beams. As this aperture sits in the back focal plane, this is equivalent to removing beams scattered to specific angles. A selected area (SA) aperture can be inserted in the back image plane to block beams originating from certain areas of the specimen-plane, as this is equivalent to inserting a virtual aperture in the specimen-plane. The intermediate lenses and projector lens brings the image from the imaging system to the detector plane.

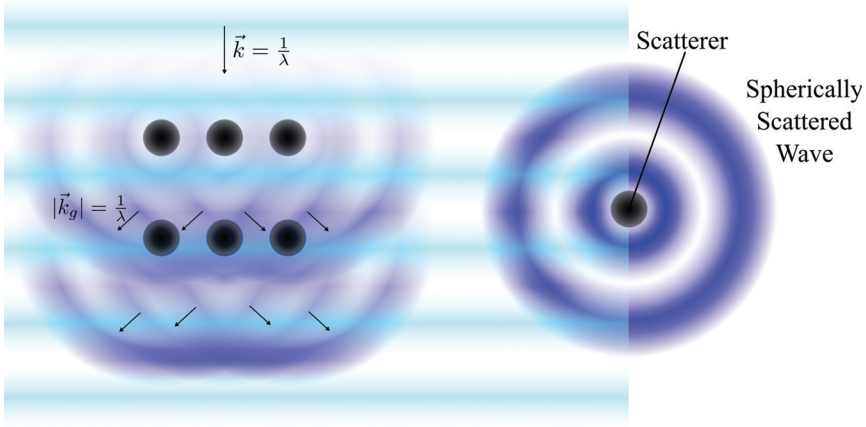

Figure 4.2: Principle of scattering and diffraction. An incoming plane wave (light blue) with wave vector $\vec{k} = \frac{1}{\lambda}$ is incident on an array of scatterers. Each individual scatterer diffracts the beam and acts as a new source of a spherically scattered wave (dark blue) with the same wavelength (elastic scattering), as shown to the right. In the array of scatterers, these spherically scattered waves interfere and give rise to new planar waves with wave vector $\vec{k}_g$ (only one is indicated, but several new planar waves are formed). Only a small number of scatterers is shown for clarity, but with increasing number of scatterers, the interference pattern will become clearer and sharper.

reasoning as before, the waves scattered from all pairs of objects spaced by $\vec{R}$ must also differ by an integer number of wavelengths. If the crystal lattice is spanned by the vectors $\vec{a}_i$, then $\vec{R}$ must be $\vec{R} = \sum n_i \vec{a}_i$. This means that objects lying on the crystal lattice will interfere if $\sum n_i \vec{a}_i \cdot \Delta\vec{k} = 2$. This occurs if and only if $\sum \vec{a}_i \cdot \Delta\vec{k} = n$. Since the crystal is a periodic structure, its real space lattice given by the vectors $\vec{a}_i$, can equivalently be represented by the reciprocal lattice spanned by the vectors $\vec{a}_i^*$, where $\vec{a}_i^* = \frac{\vec{a}_j \times \vec{a}_k}{\vec{a}_i \cdot \vec{a}_j \times \vec{a}_k}$ [5], [6]. Any reciprocal lattice point is thus given by the reciprocal lattice vector $\vec{g} = \sum n_i \vec{a}_i^* = h\vec{a}_1^* + k\vec{a}_2^* + l\vec{a}_3^*$, which will be perpendicular to a set of lattice planes (hkl) that intersects the crystal unit cell in $1/h$, $1/k$, and $1/l$ along each $\vec{a}_i$, respectively. Furthermore, $\vec{a}_i^* \cdot \vec{a}_j = \delta_{ij}$ because the basis vectors of the reciprocal lattice are perpendicular to two of the real space lattice vectors. This means that $\vec{g} \cdot \vec{R} = n \forall \left(\vec{g}, \vec{R}\right)$. Comparing this to the interference criterion, it is clear that interference occurs if

$$\Delta\vec{k} = \vec{g}, \tag{4.3}$$

which is the Laue condition for interference [5], [6]. Hence, only wave vector transfers equal to a reciprocal lattice vector will interfere constructively for a crystal. Any given elastic wave vector transfer will therefore be related to a reciprocal

lattice vector $\vec{g} = h\vec{a}_1^* + k\vec{a}_2^* + l\vec{a}_3^*$, where h, k, and l are the Miller indices of the lattice plane. This means that any elastically scattered wave will correspond to a unique set of lattice planes. Several different combinations of the lattice vec-

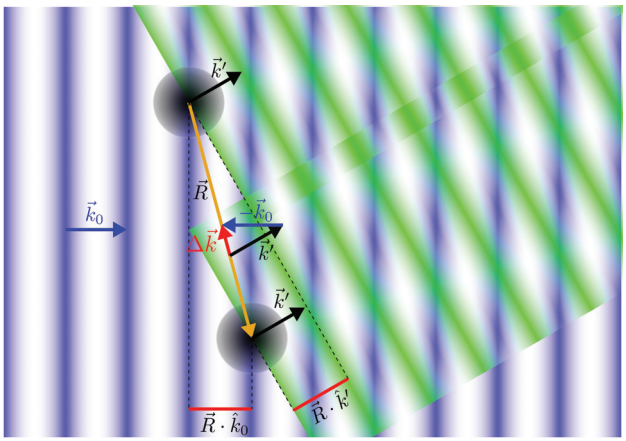

Figure 4.3: Illustration of the path difference between waves scattered from $\vec{k}_0$ to $\vec{k}'$ at two objects separated a distance $\vec{R}$. The incident beam hits the upper object first, and the incident wave will travel an extra distance $\vec{R}\cdot\hat{k}_0$, where $\hat{k}_0 = \frac{\vec{k}_0}{|\vec{k}_0|}$, before hitting the other object and scattering. The wave scattered at the upper object travels a distance $\vec{R}\cdot\hat{k}'$ before the other object scatters. The wave vector transfer $\Delta\vec{k}$ is indicated.

tors may correspond to constructive interference simultaneously, and it is useful to visualise the Laue condition graphically. The Ewald sphere construction is one way to show how a parallel beam will satisfy Equation (4.3) for a given crystal orientation and incident wave direction [5], [6]. It is a sphere of radius $|\vec{k}_0|$ and is drawn together with the reciprocal lattice of a hypothetical crystal in Figure 4.4. The Laue condition is satisfied whenever the sphere intersects a reciprocal lattice point, and elastic scattering by these wave vector transfers can occur. Because the wavelength of electrons used in TEM is several orders of magnitude less than the lattice spacings in crystals, the curvature of the Ewald sphere will be very flat compared to the reciprocal lattice vectors. Hence, very many lattice points may fall on the Ewald sphere at the same time. In addition, the macroscopic shape of the crystal causes the reciprocal lattice points to become distorted into three-dimensional objects, usually rods oriented along the specimen surface normal (referred to as rel-rods). This relaxes the Laue condition of the crystal, and enables additional wave vector transfers. This can be considered to be an effect where there are not enough scattering objects along the path of the beam to fully eliminate all beams except the ones satisfying the Laue condition exactly. In practical aspects, the Ewald sphere itself will also have finite thickness $\delta\lambda$ given by the energy spread in

the beam, and will further relax the interference criterion. The result of this is that a crystal oriented in a zone axis (i.e. with $\vec{k}_0$ aligned with some reciprocal lattice vector) will scatter near-parallel beams in a large number of directions. Each of these beams is called a reflection, as they resemble scattering from mirrors (reflection by Snell's law). The angle, θ_g with which they are scattered is also called the Bragg angle from Bragg's law $2d \sin \theta_g = n\lambda$, where d is the distance between lattice planes causing a specific reflection [5], [6]. Of course, for this interference to occur, the objects that sits on the crystal lattice must be able to scatter to the wave vectors in question. This is determined by the structure factor of the objects [5], [6]. A single atom will scatter a spherical wave, with a modulated intensity. This modulation is given by the form factor, $f(\theta)$ of the atom, and is a function of the scattering angle θ. However, in a crystal, the objects associated with each lattice point is not necessarily single atoms, but a collection of them called a basis. In this case, the structure factor for a wave vector transfer $\Delta\vec{k} = \vec{g}_{hkl}$ becomes [5], [6]

$$F_{hkl} = \sum_i f_i(\theta)\, e^{2\pi i(hx_i + ky_i + lz_i)}, \tag{4.4}$$

where x_i, y_i, and z_i are coordinates of atom number i in the basis/unit cell. The sum in Equation (4.4) can sometimes become zero for specific combinations of h, k, and l for a given atomic structure. In the case of fcc aluminium for example, there are Al atoms in $(0,0,0)$, $\left(\frac{1}{2},\frac{1}{2},0\right)$, $\left(\frac{1}{2},0,\frac{1}{2}\right)$, and $\left(0,\frac{1}{2},\frac{1}{2}\right)$, so that $F = 4f_{Al}(\theta)$ when h, k, and l are all even or all odd, and zero otherwise. Hence, some of the lattice planes in the structure scatter out of phase with other lattice planes and become forbidden [5], [6].

Because the average distance an electron travels between scattering events is low in most materials, dynamical scattering may occur [5], [6]. This complicates matters significantly because the intensity of a scattered beam is no longer given by kinematic equations, and depends non-linearly on the thickness, t, of the specimen. In a two-beam condition, i.e. a situation where only a single reciprocal lattice point lies close to the Ewald sphere in addition to the direct beam, $\vec{0}$, the intensity of the scattered beam beam varies as [5], [6]

$$|\phi_{hkl}|^2 = \left(\frac{\pi t}{\xi_{hkl}}\right)^2 \frac{\sin^2(\pi t s_{eff})}{(\pi t s_{eff})}, \tag{4.5}$$

where $\xi_{hkl} = \frac{\pi V_c \cos\theta_{hkl}}{\lambda F_{hkl}}$, with V_c as the volume of the crystal unit cell, is the extinction distance, and $s_{eff} = \sqrt{s^2 + \frac{1}{\xi_{hkl}}}$ is the effective excitation error where s is the distance from the centre of the relrod to the Ewald sphere. The intensity in the direct beam will be $1 - |\phi_{hkl}|^2$. It is clear that for the relatively simple two-beam case, there is a strong coupling between the two diffracted beams. In

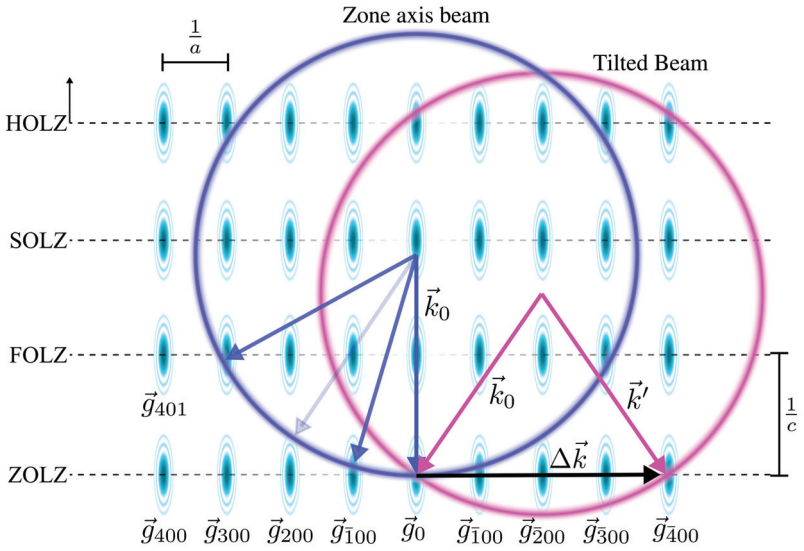

Figure 4.4: The Ewald sphere construction for elastic diffraction. Two Ewald spheres are shown (with very small incident wave vectors for clarity), each corresponding to different incident beam directions relative to the crystal. Elastic scattering requires that $|\vec{k}_0| = |\vec{k}|$, and the spheres show all possible solutions to this requirement (in 2D). The reciprocal lattice of a thin crystal is also shown, where each lattice point has a structure determined by the macroscopic shape of the crystal (in this case they are illustrated as elongated ellipses, where the major axis aligns with the thickness-direction of the TEM specimen). The Laue condition is satisfied wherever the Ewald sphere intersects one of these reciprocal lattice points. A crystal is in a zone axis if the incoming beam direction $\vec{k}_0$ aligns with one of the reciprocal lattice vectors (in this case $\vec{k}_0 || \vec{c}* = \vec{g}_{001}$ for the blue sphere). In TEM, the high velocity of the electrons makes $\vec{k}$ very large compared to the reciprocal lattice vectors (typically two orders of magnitude), which will reduce the curvature of the Ewald sphere and make it intersect close to the centres of many reciprocal lattice points in the zeroth order Laue zone (ZOLZ) when in a zone axis configuration. The tilted beam shows a two-beam condition (a symmetrical Laue case) where the sphere intersects the middle of one of the reciprocal lattice points and $\Delta\vec{k} = \vec{g}_{\bar{4}00}$ which will enable many electrons to elastically scatter to $\vec{k}'$. The Ewald sphere intersects reciprocal lattice points in the first, second and higher order Laue zones (ZOLZ, SOLZ, and HOLZs, respectively) along circles (in 3D).

addition, Equation (4.5) shows that the intensity of the scattered electron beam is a strong function of the specimen thickness, and the scattered become extinct with a periodicity of s_{eff} that depends on the extinction distance ξ_{hkl}. This dynamical transfer of intensity between the direct beam and the scattered beam become increasingly difficult to predict for increasing number of excited beams (i.e. for more reciprocal lattice points close to the Ewald sphere), as each scattered beam will also interact dynamically with each other. The problem therefore becomes impossible to solve analytically, and numerical approximations must be used instead [5], [6]. However, these methods usually require considerable computing resources, and the result will depend quite strongly on the thickness of the specimen. It is therefore quite complex to determine the thickness effects of an experimental TEM diffraction pattern. While dynamical effects might dominate in a single selected area electron diffraction pattern, they will be reduced if several selected area electron diffraction patterns acquired under different diffraction conditions are considered. One way to achieve this is to reconstruct the reciprocal space of a crystal from a tomography series of electron diffraction data [101]. Another possibility is to average the intensities in a single pattern through a series of incident beam directions, which is the basis behind precession electron diffraction (PED) which will be discussed later. Because dynamical scattering only affects the scattered intensities, the geometry of diffraction patterns is still given by kinematical theory, which enables crystallographic orientation determination from experimental patterns, even if dynamical scattering occurs.

In the TEM, a beam that is scattered an angle θ_g by the specimen will enter the objective lens with the same angle. In the back focal plane of the objective lens, this beam will be focused to a spot a distance $\propto \theta_g$ from the optical axis. If a parallel illumination is used, beams scattered by a single set of lattice planes in the crystal will give rise to a single sharp spot in this pattern, and its position in the pattern depends on the orientation of the lattice planes relative to the incoming beam direction. This is a typical situation for a selected area electron diffraction pattern, where the illuminated area is limited by a selected area aperture, as described previously. If, instead a converged beam is used, several incident $\vec{k}_0$ vectors will be superimposed and make the spot into a disk with a radius that varies with the convergence angle of the beam. If the convergence angle is made large enough, disks will overlap (their centre-to-centre distance is determined by the crystal structure). This overlap means that electrons can be scattered by several planes simultaneously, and leads to increased dynamical effects. By varying this overlap, a TEM diffraction experiment can be fine-tuned to be very sensitive to specific signals, and this is one of the strengths of TEM. In atomic resolution STEM, the resolution is determined by this overlap [89].

4.3 Precession Electron Diffraction (PED)

PED is a technique where the beam is tilted off the optical axis before the specimen in order to probe the crystal with different incident wave vectors [102]. This is done because it effectively integrates the intensities of reflections through a range of incident wave vectors and can reduce the influence of dynamic effects. Thus it enables a variety of algorithms to be applied to analyse the patterns, which would have been much more challenging if dynamic effects were strong. If the beam is scanned across the specimen in addition to being precessed, a PED pattern can be acquired for each probe position and a scanning PED (SPED) data cube can be acquired. This has several advantages and applications, where orientation and phase mapping are the most common ones [103], [104]. It can also be used to study crystallographic variations in general, such as density of GNDs, defects and strain [105]–[108]. However, before this data can be acquired, various lenses and deflector coils in the TEM must be aligned and carefully synchronised [109].

To make the electron beam precess about the optical axis of the microscope, the pre-specimen deflector coils must be synchronised. When a current is passed through one of these coils, the resulting magnetic field will bend the beam by the Lorentz force. When a current is passed through the first set of pre-specimen deflector coils ("Deflector Coils 1" in the upper part of Figure 4.1), the beam is tilted by an azimuthal angle $-\phi$ off the optical axis toward a polar angle θ, as shown in Figure 4.5. θ can be varied by changing the relative currents that pass through the two pairs of orthogonal coils ("X" and "Y" coils in the same plane), while ϕ is given by the absolute magnitude of the current. A second set of coils below ("Deflector Coils 2" in the upper part of Figure 4.1) counteracts the tilt by an azimuthal angle 2ϕ so that the beam enters the specimen with an angle ϕ relative to the optical axis. A precessing beam is achieved by changing the relative currents in the coils and synchronising all of them so that ϕ is kept constant with a varying θ. Very simply put, this can be done by passing a current $I(\phi, \theta) = I_0(\phi) \sin(\theta + \vartheta)$ through the coils, with $\vartheta = 0$ for the "X" coils and $\vartheta = \pi/2$ for the "Y" coils. The current that passes through the first set of coils is half of the current that pass through the second set, and of opposite sign. Hence, the probe will precess about the optical axis by the synchronised currents that pass through the deflector coils. In addition, if a constant bias current is passed through the coils, the beam will enter the specimen with the same angle ϕ, but at a different position. The beam can therefore be made to both precess, and scan across the specimen, by the same coils.

After the tilted beam passes through the specimen, it will enter the objective lens with an angle ϕ and hence trace a circle with radius $\propto \phi$ around the optical axis

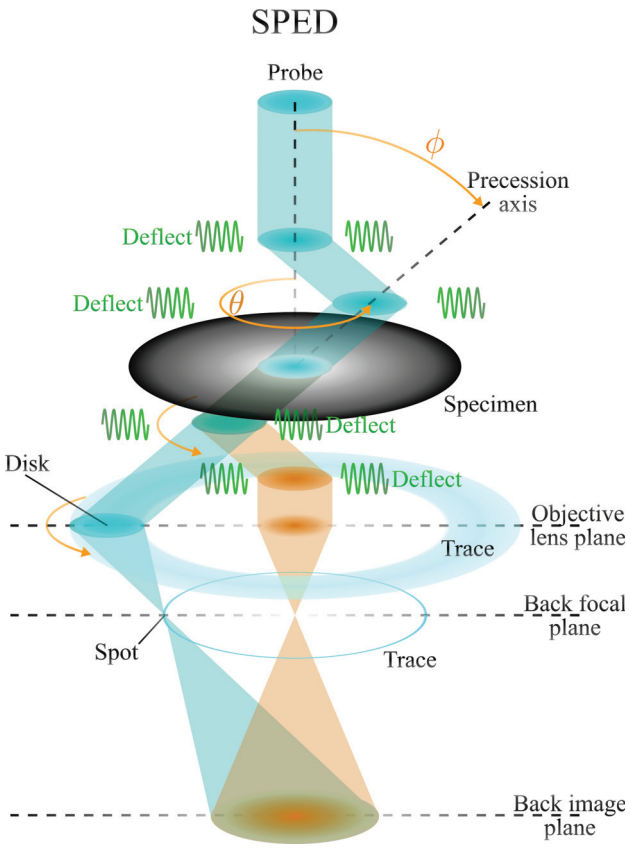

Figure 4.5: Illustration of PED operation. A probe is tilted ϕ degrees off axis and precessed around the optical axis through an angle θ. If not counteracted below the specimen, the beam traces a circle as it enters the objective lens (objective lens) with an angle ϕ and is focused to a spot ϕ degrees out from the optical axis in the back focal plane of the objective lens. If the precession is counteracted by post-specimen deflector coils, the direct beam can be tilted back on the optical axis and appear as a single spot in the back focal plane (orange beams). In reality, the post-specimen deflector coils are situated further down the column than what is illustrated, and operates on the beam as it passes through the projection system.

in its back focal plane. Eventual diffracted beams will trace circles with the same radius, but centred on their respective Bragg angles instead. The back focal plane of the objective lens is brought to the detector plane by the projection system and a precession electron diffraction (PED) pattern is acquired. If the acquisition frequency is f and the precession frequency is $\dot{\theta}$, the acquired PED pattern will consist of parts of the complete circle, corresponding to $\dot{\theta}/f$. If f is synced to $\dot{\theta}$ so that $\dot{\theta}/f = n\pi$, an integer number of precession periods are added together during acquisition.

Treating circular patterns is cumbersome and not very useful, however. By using the post-specimen deflector coils situated in the projection system to counteract the precession from the pre-specimen coils (essentially passing through identical currents, excluding the constant bias needed to scan the beam, with opposite sign), a spot-pattern is brought to the detector instead. It is still important to sync the acquisition frequency to the precession frequency so that each θ is given the same acquisition time. Each spot in this pattern will therefore be time-averages of the corresponding circle, or, equivalently, angular averages of the circles. In essence, PED allows for angular averaging of the Bragg-reflections of a crystal. It is equivalent to precessing the Ewald sphere through the reciprocal space of the crystal, as shown in Figure 4.6. The Ewald sphere intersects the zero order Laue zone and traces a circle. As the beam is precessed, θ varies, and the intersection is swept across the zero order Laue zone. The radius of the intersection is $r = 2|\vec{k}^0(\phi,\theta)|\sin\phi = \frac{2\sin\phi}{\lambda}$, and is of the order of 1.39 Å^{-1} for $\phi = 1^\circ$ and $E_0 = 200$ keV. Most crystals have lattice spacings of a few Ångströms, and many of the inner reciprocal lattice points will lie within the area swept by the Ewald sphere if it is precessed about a zone axis. In addition to averaging the intensities in these reflections, PED patterns will show excited reflections further out in reciprocal space, providing additional information.

Precessing the electron beam will reduce the spatial resolution compared to a stationary probe incident along the optical axis. First of all, this is due to an increased interaction volume due to the effectively conical beam. Secondly, if the beam is simultaneously scanned while it is being precessed, the shot noise in the coils due to the current needed to precess the beam will reduce the accuracy of the shift and limit the resolution to at least $\propto \sqrt{\phi}$ [109]. Thirdly, the tilted beam will enter the objective lens at a slanted angle which will increase the effect of lens aberrations.

4.4 Lens Aberrations

Aberrations in the objective lens is the limiting factor for most modern TEMs and advanced techniques such as SPED, HRTEM, and STEM. Indeed, imperfect

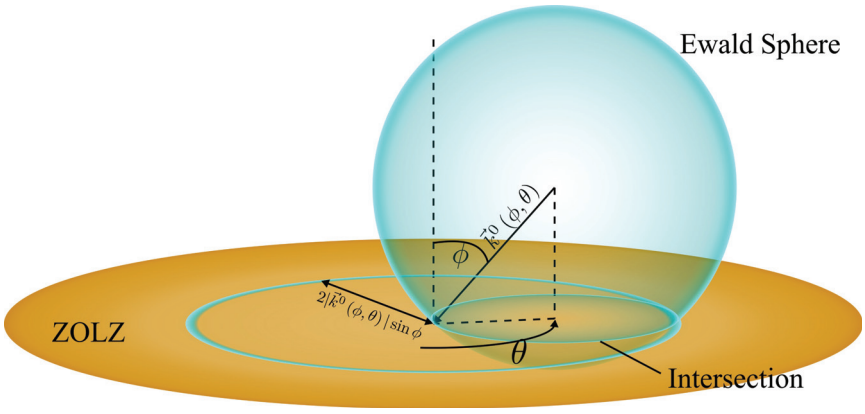

Figure 4.6: Illustration of the Ewald sphere for a tilted beam. The incoming wavevector $\vec{k}_0$ is a function of the azimuthal angle ϕ, and the polar angle θ. The Ewald sphere intersect with the first order Laue zone traces a cirlce. With ϕ constant, the intersection between the Ewald sphere and the first order Laue zone will swipe over an area if θ is varied. For a full revolution around the optical axis, the Ewald sphere intersection has spanned over a disk of radius $2|\vec{k}^0\,(\phi,\theta)\,|\sin\phi = \frac{2\sin\phi}{\lambda}$, and passed through the Bragg condition for all reciprocal lattice points inside the disk exactly twice.

electromagnetic lenses are the reason why the resolution given by the Rayleigh criterion in Equation (4.2) has not been achieved experimentally yet [6], [89]. The simplest lens aberrations to consider are spherical and chromatic aberrations. Spherical aberrations bring beams that have entered different positions of the lens to either a premature or a delayed focus. Chromatic aberrations are similar, except that the strength of the lens is a function of the wavelength rather than where the beams enter the lens. In both cases, a disk of least confusion where the object will appear the smallest lies above the image plane. Defocusing the lens to bring this plane to the image plane will improve resolution.

Lens aberrations cause an originally spherical wave front S^0 to become distorted into an irregular wavefront S [89]. The distortions $W = S^0 - S$ can be divided into a sum of various deviations of various symmetry and sensitivity to the ray path. With sensitivity, it is meant how W changes depending on where the ray originated from in the object plane, w_o, and where it intersects the back focal plane, ω. The effect of an aberration is that the ray will end up at position w_i' instead of the correct position w_i. In other words, the ray is brought to the image plane with an error $\Delta w = w_i' - w_i$. Defining the positions as complex numbers, $w_o = x_o + iy_o$ and $\omega = \theta_x + i\theta_y$, the aberrations of various symmetry and dependence on w_o and ω can be derived. In principle, there are infinitely many possible aberrations, but only the most important ones are relevant for this discussion. With aberration

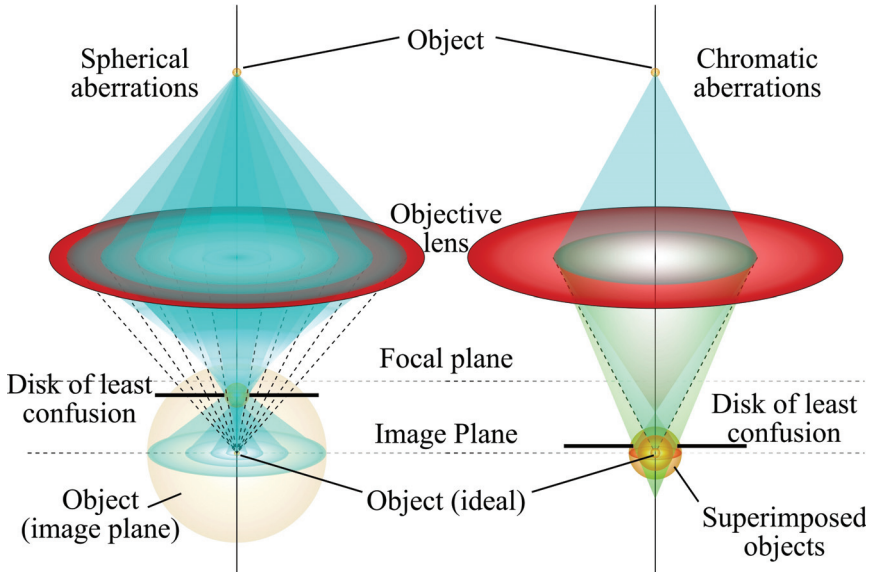

Figure 4.7: Illustration of spherical and chromatic aberrations. The imaged object will appear as a superposition of differently magnified images in the image plane. Spherical aberrations cause beams entering the lens at different positions to be focused at different positions (dashed lines show the paths of a perfect lens), while chromatic aberrations cause beams with different wave lengths to be focused differently. In both cases, a disk of least confusion appears above the image plane, where the object will appear the smallest.

corrected microscopes, it is possible to correct for some aberrations by applying an opposite aberration $W_c \approx -W$ to the beam, which will make higher order aberrations increasingly important. In any event, aberrations in TEM are most important for high-resolution imaging (HRTEM or atomic resolution STEM), where the beams originate from roughly the same area so that the effect of w_o can often be neglected. Hence, only axial aberrations are usually considered in TEM imaging. These are aberrations that depend only on ω, and $\chi \approx W\,(w_o \approx 0, \omega)$ is used as the aberration function. When Taylor expanded in terms of ω, and including 5 orders, the geometrical (i.e. excluding chromatic aberrations) aberration function reads [89]

$$\begin{aligned}\chi(\omega) = \Re\Big\{ & A_0\bar{\omega} + \frac{1}{2}C_1\omega\bar{\omega} + \frac{1}{2}A_1\bar{\omega}^2 + B_2\omega^2\bar{\omega} + \frac{1}{3}A_2\bar{\omega}^3 + \frac{1}{4}C_3\left(\omega\bar{\omega}\right)^2 \\ & + S_3\omega^3\bar{\omega} + \frac{1}{4}A_3\bar{\omega}^4 + B_4\omega^3\bar{\omega}^2 + D_4\omega^4\bar{\omega} + \frac{1}{5}A_4\bar{\omega}^5 + \frac{1}{5}C_5\left(\omega\bar{\omega}\right)^3 \\ & + S_5\omega^4\bar{\omega}^2 + R_5\omega^5\bar{\omega} + \frac{1}{6}A_5\bar{\omega}^6\Big\},\end{aligned} \tag{4.6}$$

where the coefficients are explained in Table 4.1. It is clear that there are a multitude of different aberrations with different sensitivity to ω. These can be divided into a few groups, as indicated by the similar lettering of the aberration coefficients. Astigmatism (A_n) describes the deviation from a round lens, so that the lens has different strength in different directions. A lens with spherical aberrations C_n will have different strengths depending on the angle of the rays, as shown in Figure 4.7. Axial Coma (B_n) causes an original spherical object to be imaged as a comet-like shape in the image plane. Star-aberrations make a round object into a star-like shape, while rosette aberrations makes the beam appear as a rosette. More details can be found in e.g. Erni [89].

Chromatic aberrations have not been included in Equation (4.6), as these aberrations are slightly different from the geometrical axial aberrations. These originate from the temporal and spatial incoherence of the electron source. The chromatic aberration effect shown in Figure 4.7 is one of many, and blurs the focal point according to $\delta_C = C_C|\omega|\frac{\Delta E}{E_0}$, where ΔE is the energy spread about the average energy E of the electrons [89]. This aberration effectively changes the envelope of the objective lens transfer function in HRTEM, which will be discussed later, and redistributes intensity to the side-lobes of a STEM probe.

Table 4.1: Overview of the most important geometric lens aberration coefficients in TEM, adapted from [89].

Aberration	Explanation
A_0	Beam shift
C_1	Defocus
A_1	Two-fold astigmatism
B_2	Second-order axial coma
A_2	Threefold astigmatism
C_3	Third-order spherical aberration
S_3	Third-order star-aberration
A_3	Fourfold Astigmatism
B_4	Fourth-order axial coma
D_4	Fouth-order three-lobe aberration
A_4	Five-fold astigmatism
C_5	Fifth-order spherical aberration
S_5	Fifth-order star-aberration
R_5	Fifth-order rosette aberration
A_5	Sixfold astigmatism

4.5 Imaging

4.5.1 Amplitude contrast

There are many imaging techniques available in a TEM, and techniques based on amplitude contrast are usually the most simple and efficient techniques available. These techniques form images where the contrast is mostly determined by either diffraction effects or mass/thickness effects. The most common amplitude contrast imaging techniques are bright field and dark field imaging. In these techniques, the specimen is illuminated by a parallel beam, and an objective aperture is inserted in the back focal plane of the objective lens. In bright field TEM, the objective aperture is centred on the direct beam in the back focal plane to remove most or all of the scattered beams. This causes the contrast in the bright field image to depend on the total intensity scattered out of the direct beam. As an example, the grains of a polycrystal that have few or no intersections with the Ewald sphere will appear bright as they are unable to elastically scatter electrons out of the direct beam. Conversely, grains that are oriented so that the Ewald sphere intersects many reciprocal lattice points will appear dark. However, if the objective aperture is moved so as to only allow specific reflections in the back focal plane through, a dark field image is formed. Such an image will appear bright where grains scatter to the cor-

responding angle, while all other regions become dark. In practise, the objective aperture is not actually moved, but the beam is tilted so that the diffracted beam travels along the optical axis instead of the direct beam. However, this changes the diffraction condition, and the crystal must also be tilted to compensate. Similarly, if a single-crystal bends, it will go in and out of Bragg condition and bending contours appear.

A variant of the dark field technique is the weak-beam dark field technique [12], where the incoming beam is tilted to a two-beam condition with e.g. $3\vec{g}_{hkl}$ while inserting the objective aperture to only let electrons scattered by $\vec{g}_{hkl}$ through. This will result in a very dark image over all, but which will be very sensitive to any bends or distortions of the crystal lattice. Such distortions are made by e.g. dislocations (see Figure 3.3), where the local lattice planes close to the dislocations are slightly bent by the elastic strain field [8], [12]. This will cause the reciprocal lattice point of the (hkl) planes to locally move closer to the Ewald sphere and satisfy the Laue condition, ultimately resulting in bright contrast in the weak-beam dark field image. Because the bend of the planes is related to the Burgers vector, only reflections where $\vec{b} \cdot \vec{g}_{hkl} \neq 0$ will result in contrast. Hence, by acquiring several weak-beam dark field images of the same area using different $\vec{g}_{hkl}$, it is possible to find the specific conditions for the dislocation to give contrast, and hence determine the Burgers vector. By comparing $\vec{b}$ to the image of the dislocation, the nature (e.g. edge or screw) can also be determined. This is shown in Figure 4.8, where possible screw dislocations forming a square grid in a GB PFZ in a peak aged AA6060 alloy after -20% engineering strain are imaged under different diffraction conditions. In this example, the dislocation character could not be determined because the Burgers vectors of the dislocations were parallel to the projected dislocation lines. Because TEM images are 2D projections of 3D objects, determining whether a dislocation has a screw, edge, or a mixed character is challenging. Without knowing the full orientation of the dislocations through the thickness, determining whether the dislocations are mixed or pure screw is not possible. In this respect, weak-beam dark field tomography experiments are particularly powerful, as the full three-dimensional character of a dislocation can be determined [110]. In addition, STEM can also be tuned to be sensitive to dislocations, and offers another technique to obtain similar results [111]. Determining the dislocation line vector relative to the Burgers vector (i.e. the sign of $\vec{b} \times \vec{t}$, also called the dislocation parity) is much more difficult to determine than the Burgers vector and dislocation character, and requires detailed analysis of images acquired under very specific conditions [112].

Another source of amplitude contrast in TEM is thickness contrast. In most cases, a crystal will scatter more the thicker it is. However, when the thickness of the

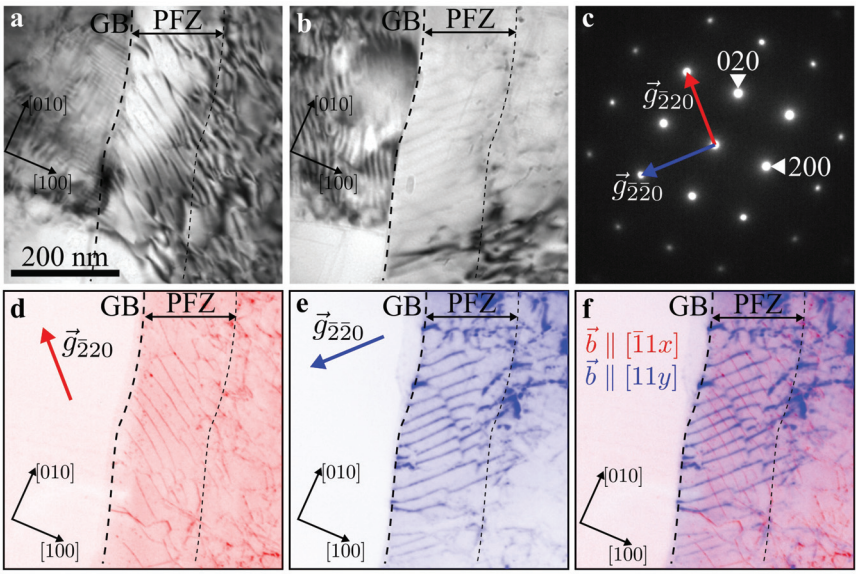

Figure 4.8: Determination of burgers vector of dislocations in a PFZ in peak aged AA6060 after 20% compression. Image **a** and **b** are bright field images of a region acquired when the specimen and beam is tilted to a two-beam condition with $3\vec{g}$ for $\vec{g} = [\bar{2}20]$ and $\vec{g} = [\bar{2}\bar{2}0]$, respectively. Image **d** (red) and **e** (blue) are dark field images formed using the weak $\vec{g} = [\bar{2}20]$ and $\vec{g} = [\bar{2}\bar{2}0]$ reflections in each corresponding case. The two weak-beam dark field images have been overlaid in Image **f**, while image **c** is a zone axis selected area electron diffraction pattern of the region for crystallographic reference. The bright field images contain little useful information, but the weak-beam dark field images show the dislocations much more clearly. There are two perpendicular sets of dislocations that form a square grid. The dislocations in one set is invisible when $\vec{g} = [\bar{2}\bar{2}0]$ (the "red" dislocations) and the other dislocations are invisible when $\vec{g} = [\bar{2}20]$ (the "blue" dislocations). Dislocations are invisible when $\vec{g} \cdot \vec{b} = \vec{0}$, and it is clear that $\vec{b}_{\text{red}} \cdot [110] = 0$, and $\vec{b}_{\text{blue}} \cdot [\bar{1}10]$. Hence, $\vec{b}_{\text{red}} \parallel [1\bar{1}x]$, and $\vec{b}_{\text{blue}} \parallel [11y]$, where x and y must be determined by a third diffraction condition. Given the orientation between these Burgers vectors and the dislocation lines, the dislocations must therefore be either screw (if they lie in the image plane) or mixed (if they are oriented out of the image plane).

crystal equals the extinction distance of some reflections, the intensity of these reflections decrease instead. This gives rise to thickness contours if the specimen thickness varies. In addition, heavier elements will have a similar effect, so that an increase in scattered intensity can be both due to an increase in thickness or average mass. Because the extinction distance varies with both the lattice and the form factors of the atoms, changes in mass can also give rise to contours or other types of contrast.

4.5.2 Phase Contrast

Instead of amplitude contrast, TEM images with phase contrast can be formed by e.g. the HRTEM technique. In HRTEM, the interference between electrons exiting the specimen at different positions are imaged. This requires very high magnifications of about a million times, which will enable imaging of the interference pattern of waves scattered to different angles at different positions by the sample. For this to occur, there must be a correlation between where the electrons exit the specimen, and their phase. The interactions of single electrons as they pass through the specimen are therefore important. These interactions are possible to determine for a crystal that is oriented in a zone axis, because the electrostatic potentials of the atoms will align in columns along the beam direction. These columns will act as a wave-guide for the electrons and confine them, usually referred to as channelling [113]. However, as an electron travels along an atomic column, its phase will vary depending on the extinction distance ξ [6], [113]. This can be thought of as each atom acting as a lens that focus the electron beam, and that the series of lenses formed by a column of atoms thus give rise to a periodic focusing and defocusing of the electrons as they travel along the column. Hence, the electron will be relatively confined to an atomic column and exit the crystal at a given position with a phase that depends on the thickness of the specimen and the periodicity of its focusing and de-focusing. This makes it possible, in principle, to relate the exit wave to the projected crystal potential [114], [115].

Direct interpretation of HRTEM images is difficult due to how aberrations in the objective lens affect different diffracted waves. The aberrations will cause the phases and positions of the different diffracted waves to shift and reduce resolution and especially complicate the interpretation of the images. How a certain diffracted wave is transferred from the specimen to the objective lens image plane is described by the contrast transfer function (CTF) [89]

$$T(\omega) = A\left(\omega\right) E\left(\omega\right) \Im\left\{e^{-\left(\frac{2\pi i}{\lambda}\Re\{\chi(\omega)\}\right\}}\right\}, \tag{4.7}$$

where $A\left(\omega\right)$ and $E\left(\omega\right)$ is the objective lens aperture function (to describe removal of diffracted waves) and the envelope introduced by chromatic aberrations, re-

spectively. In HRTEM, we are most interested in how the phase difference varies between electrons scattered by various atomic planes, as this relates to the crystal lattice and enables imaging. Hence, it is more convenient to describe the CTF in terms of spatial frequencies or wave vector transfers $|\vec{k}| \approx |\omega|/\lambda$. In addition, if the microscope is uncorrected, the main geometrical aberrations are the spherical aberrations C_3 and defocus C_1, so that the aberration function in the HRTEM CTF becomes [6], [89]

$$\chi\left(\vec{k}\right) \approx C_1 \frac{1}{2}\left(|\vec{k}|\lambda\right)^2 + C_3 \frac{1}{4}\left(|\vec{k}|\lambda\right)^4. \tag{4.8}$$

The remaining parts of Equation (4.7), namely the aperture and envelope functions, can be written as [89]

$$A\left(\vec{k}\right) = \left\{ \begin{array}{ll} 1, & |\vec{k}| < |\vec{k}_a| \\ 0, & |\vec{k}| > |\vec{k}_a| \end{array} \right\}, \tag{4.9}$$

and

$$E\left(\vec{k}\right) = E_t\left(\vec{k}\right) E_s\left(\vec{k}\right). \tag{4.10}$$

The cutoff $|\vec{k}_a|$ in Equation (4.9) represents the radius of the aperture inserted in the back focal plane of the objective lens lens, or the maximum collection angle of the lens, while the two functions $E_t\left(\vec{k}\right)$ and $E_s\left(\vec{k}\right)$ in Equation (4.10) are envelope functions due to temporal and spatial incoherence of the electron source, respectively. Both of these envelopes depend on the aberration function χ given by Equation (4.8) as well as various characteristics of the illumination system, and can be written [89]

$$E_t\left(\vec{k}\right) = e^{-2\left(\frac{\pi \Delta C_1}{\lambda}\left(\frac{\partial \chi}{\partial C_1}\right)\right)^2} \approx e^{-\frac{1}{2}\left(\pi \Delta C_1 \lambda |\vec{k}|^2\right)^2}, \tag{4.11}$$

with

$$\Delta C_1 = C_c \sqrt{\left(\frac{\Delta U}{U_0}\right)^2 + 4\left(\frac{\Delta I}{I_0}\right)^2 + \left(\frac{\Delta E_{rms}}{E_0}\right)^2}, \tag{4.12}$$

and

$$E_s\left(\vec{k}\right) = e^{-\left(\frac{\pi}{r_s}[\nabla \chi]\right)^2} \approx e^{-\left(\frac{\pi}{r_s}\right)^2\left(\left(|\vec{k}|\lambda\right)^2 C_1^2 + 2\left(|\vec{k}|\lambda\right)^4 C_1 C_3 + \left(|\vec{k}|\lambda\right)^6 C_3^2\right)}. \tag{4.13}$$

In Equation (4.12), $\Delta U/U_0$, $\Delta I/I_0$, and $\Delta E_{rms}/E_0$, are the instability of the acceleration voltage in the microscope, the instability of the lens current, and the relative energy spread of the electron beam, respectively. As such, the temporal incoherence described by Equation (4.11) is determined by instrument instabilities

that lead to a spread in phase of electrons that interact with the specimen and reduce the contrast available from large wave vector transfers. The spatial incoherence described by Equation (4.13) is related to the electron source size r_s, and how this affects the wave vector transfers as they pass through an aberrated lens.

Figure 4.9 shows the CTF of a microscope in the absence of any corrections except for an optimization of the defocus to cancel spherical aberrations. This defocus value, $C_1 = -\sqrt{\frac{4}{3}\lambda C_3}$, is called the Scherzer defocus, and corresponds to the broadest possible pass band for low spatial frequencies. How the CTF varies with defocus is shown in Figure 4.10, and it is clear that the CTF oscillations become worse for lower $\vec{k}$ with a C_1 not equal to the Scherzer defocus. This is important, because the maximum interpretable resolution of a HRTEM image corresponds to the first contrast reversal, i.e. where the CTF first becomes zero, after which the oscillations make it impossible to interpret objects in the image directly. Of course, the image contains information even if the CTF starts to oscillate, but the envelope functions terminate the information transfer at some point and sets an information limit. For actual experiments, factors such as specimen drift and camera response will also affect the resolution.

4.5.3 Scanning Transmission Electron Microscopy

STEM is a technique where the beam is focused to a spot instead of being made parallel. By scanning the beam across the specimen, and detecting electrons scattered to various angles, an image can be reconstructed. Figure 4.11 illustrates the difference between conventional TEM and STEM. By collecting electrons that have scattered to large angles with an annular detector, a so-called high-angle annular dark field (HAADF) STEM image is acquired. These images are very useful because the intensity in each pixel roughly corresponds to the square of the atomic number Z [6], [89], [91], [116], [117]. Hence, HAADF STEM images are also referred to as Z-contrast images. This is because heavier atoms have a higher probability of scattering an electron to high angles where Bragg scattering is limited, and because integrating the scattering over an annular region in reciprocal space produces incoherent images [116]. However, for high-resolution HAADF STEM images, the intensity will only follow a clear Z dependency for relatively thin specimens where channelling is still strong [117]–[120]. When the electron probe dechannels, the background intensity in the image starts to increase while the Z-contrast scattering roughly stays the same for heavy elements [119]. Strain and thermal diffuse scattering are also important contributors to the STEM image intensities, and caution is important both when forming and interpreting HAADF STEM images [121]. Nevertheless, HAADF STEM images provide an efficient way of observing the crystal structure directly, which is a huge advantage com-

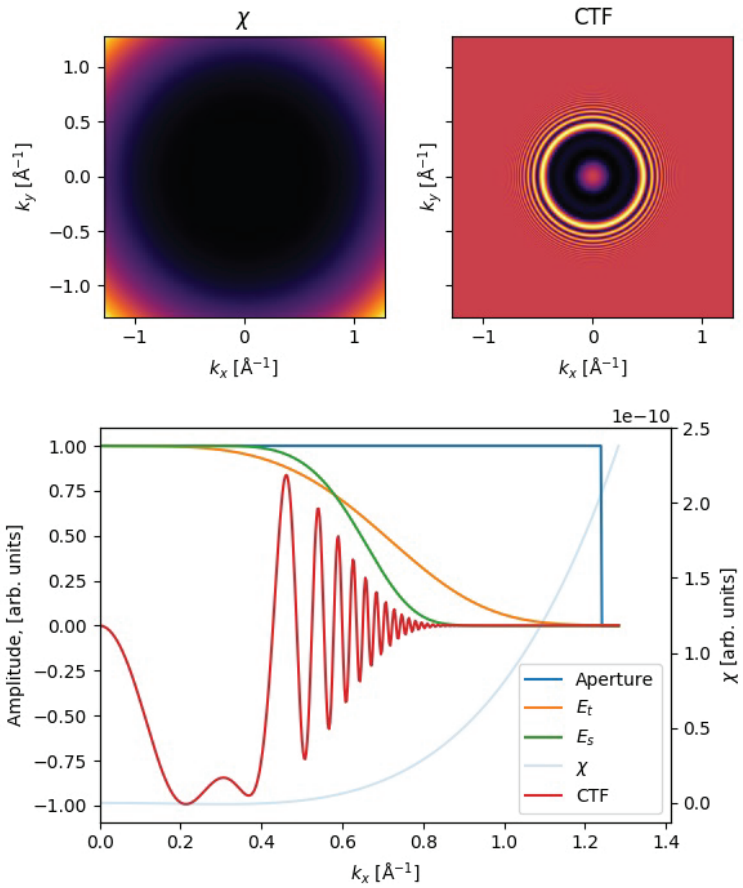

Figure 4.9: The aberration function χ and the CTF of a microscope with $C_3 = 1$ mm, $r_s = 12.5$ nm, $\Delta E_{rms} = 0.6$ eV, and $U = 200$ kV. Instabilities in lens current and high tension has been neglected. A defocus equal of $C_1 = -58$ nm, which is equal to the Scherzer defocus is used. In this case, the point resolution is about 2.3 Å, after which the oscillations in the CTF makes it difficult to extract spatial information. The information limit however, is better, and is about 1.3 Å. After this value, very little spatial information is transferred to the image.

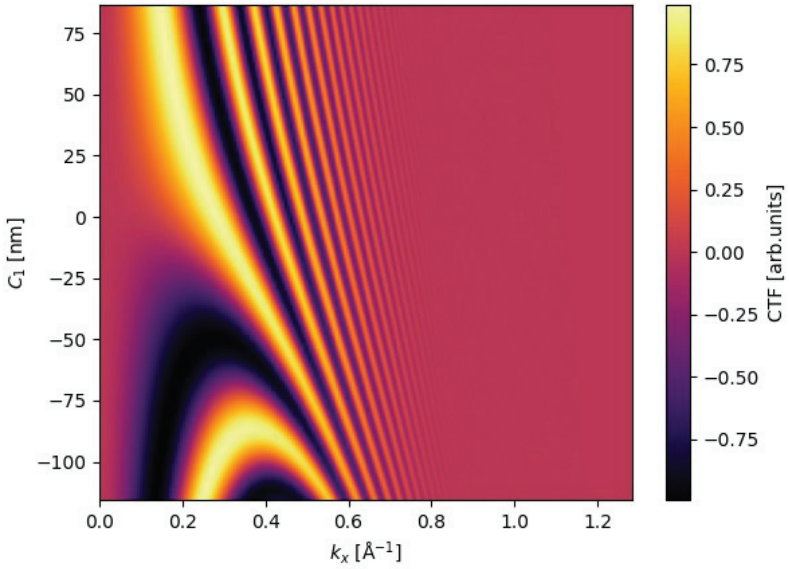

Figure 4.10: Dependency of the CTF on the defocus C_1 for a microscope with the same parameters as in Figure 4.9.

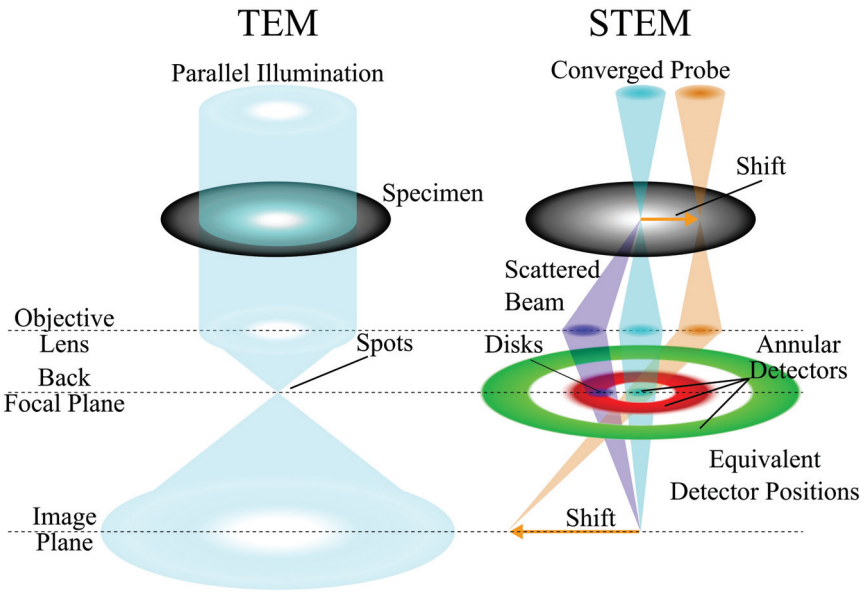

Figure 4.11: Comparison between conventional TEM mode and STEM mode. In TEM, a parallel beam illuminates the specimen and a spot-diffraction pattern appears in the back focal plane of the objective lens, while an image appears in the back image plane. In STEM, the beam is converged to a small probe with convergence angle α by the illumination system, and scanned across the specimen using the deflector coils above the specimen. Because a continuous range of wave vectors, $\vec{k} \in \left[-\vec{k}_\alpha, \vec{k}_\alpha\right]$, are incident on the specimen, discs will appear in the back focal plane of the objective lens with radius $\propto 2\alpha$. In the image plane, the beam forms a sharp spot. The projection system brings the back focal plane to the detection plane, where various detectors can inserted. Usually, annular detectors of a fixed size are inserted, and the projector lenses are adjusted to bring various parts of the back focal plane into the angular range of the detectors. These detectors will have equivalent "virtual" detectors in the back focal plane of the objective lens, as indicated.

pared to the HRTEM technique. In addition, other scattering events ma be recorded than the high-angle events. With decreasing inner-angle, the resulting image will contain more contributions from coherent scattering and phase information. For instance, by acquiring a medium-angle annular dark field or an annular bright-field signal instead of a HAADF signal, strain contrast becomes more important and can be used to observe e.g. dislocations [111].

The resolution in STEM depends on the size of the probe. If the probe can be made smaller than a certain size, then correspondingly sized objects may be resolved. However, to make the beam small, a condenser aperture is used, in addition to demagnifying the electron source by the illumination system. The aperture will

cause the focused beam to become an Airy disk and the size will depend on the Rayleigh criterion from Equation (4.2), which is usually written as [89]

$$\delta_D = 0.61\frac{\lambda}{\alpha}, \tag{4.14}$$

for STEM. It is clear that to resolve small objects, α must be as large as possible. However, as for HRTEM, aberrations will get increasingly worse the larger the collection angle of the lens. In STEM, the probe is formed by the illumination system and the pre-specimen objective pole-piece. Aberrations in this lens will therefore reduce resolution by increasing the size of the electron probe.

4.6 Multislice simulations

TEM image simulations are often useful when interpreting and quantifying TEM experimental results. One of the most popular image simulation techniques is the multislice approach. In these simulations, an atomic model of a specimen is constructed based on initial guesses, and sliced into several stacks. Each of these stacks are thin, containing about only one atom in the thickness-direction, and the quantum mechanical equations of how an electron will interact with the electrostatic potentials can be solved. The resulting electron wave from one slice is then propagated to the next slice and the calculation is repeated. By sequentially solving the propagation problem, the final exit wave and the resulting image can be simulated. For HRTEM, the exit wave is of importance, while for HAADF STEM, the scattering to high angles is computed instead. The greatest benefit of multislice simulations is that images can be simulated very efficiently as a function of thickness. Comparing these images to experimental ones will aid when attempting to discern the atomic structure of a real physical specimen, as in Paper 3 of this thesis [122].

In practise, multislice simulations solve the Schröedinger equation through an iterative scheme that Taylor expands each solution in powers of the slice thickness Δz [92]. The interaction between the electron wave and the specimen potential is done by projecting the electrostatic potential to a single plane within the slice, and letting the electron wave function interact at this plane through the transmission function $t_n(x, y)$. Between each discrete plane, the wave function is propagated by the Fresnel propagator $p_n(x, y, \Delta z)$. The result is that the wave function emitted through slice number $n + 1$ is [92]

$$\Psi_{n+1}(x, y) = p_n(x, y, \Delta z_n) \otimes [t_n(x, y)\, \Psi_n(x, y)] + \mathcal{O}\left(\Delta z^2\right). \tag{4.15}$$

The convolution in Equation (4.15) is computationally ineffective, and the problem is usually solved in Fourier space. This requires that the space (x, y) is both

periodic and is sampled on a grid of size $N_x \times N_y = 2^n \times 2^n$. In addition, to avoid aliasing, a bandwidth of $2/3$ is usually applied as well [92]. The resolution of these simulations is therefore determined by the size of the specimen model. If L_x and L_y are the dimensions in the x and y dimensions, then the minimum reciprocal distance is $\Delta k_x = 1/L_x$, and $\Delta k_y = 1/L_y$. Hence, the maximum reciprocal distance (corresponding to the smallest resolvable distance) is $N_x \Delta k_x$ and $N_y \Delta k_y$. This is important for HAADF STEM simulations, because this will limit the maximum scattering angle that will be possible to simulate. Of course, in the case of HAADF STEM simulations, the probe step size will also influence the resolution of the resulting image. For relatively thick models, simulation times can become considerable, as the full multislice simulation must be performed at each probe position. In addition, because thermal diffuse scattering is important for experimental STEM image contrast [121], several multislice simulations should be averaged, where each is a result of a slightly different atomic configuration of the model. This approach is called the frozen phonon approximation, where one assumes that the speed of the electrons are much higher than the thermal vibration velocity of the vibrating atoms. This makes each electron effectively see a "snapshot" of the crystal with atoms in a frozen configuration. By randomly shifting the atoms by a certain amount (given by the Debye-Waller factors [123]) between each multislice simulation, thermal diffuse scattering can be accounted for in the image simulations [92], [121]. Therefore, multislice simulations greatly benefit from parallel computing and are particularly well-suited for GPU calculations [124]. The MULTEM software developed by Lobato and Dyck [124] has been used in Paper 3 of this thesis to perform multislice TEM image simulations in order to better understand the structure of sheared precipitates in the Al-Mg-Si alloy system [122].

4.7 Data Analysis

Data acquired from TEM experiments vary in complexity and quality, and it is often necessary to analyse the data to extract relevant information. TEM data has traditionally been treated and analysed in proprietary software, which have limited flexibility and access to state-of-the-art data processing algorithms and libraries. Hence, in this work, data analysis has mostly been done using the Python open source HyperSpy package [125]. This package offers an effective as well as intuitive way of inspecting and treating multi-dimensional data. It has its origin from the electron microscopy community, but it is very general, and mechanical test data could, in principle, also be analysed and treated using HyperSpy.

4.7.1 Analysis of SPED data

SPED data, which in its nature is four dimensional (two spatial and two reciprocal dimensions), require advanced analysis to extract relevant information. The most

simple approach to do this is to integrate the intensities in certain regions of each PED pattern in the data cube and form virtual images. For example, by integrating intensities including the direct beam gives a virtual bright field image, while integrating intensities inside virtual apertures that do not contain the direct beam gives virtual dark field images that show which part of the specimen diffracts to a certain angular range. This is useful to get a quick overview of the data, but more detailed analysis involving machine learning can extract variations in the PED patterns that would not be possible to do otherwise. The open source Python package PyXem [126], which is based on HyperSpy [125], has been used to extensively pre-process and post-process SPED data in this work.

SPED data can also be used to create orientation maps of a specimen. Orientation indexing has been done in the *NanoMegas ASTAR Index* software, where each PED pattern in a SPED stack is compared to kinematically simulated diffraction patterns stored in a library. The orientation data from this analysis was then treated using the MTEX MATLAB toolbox [127]. This toolbox is developed for the electron backscatter diffraction community to visualise and analyse orientation data, and offers great flexibility and robustness. In particular, this toolbox enabled Paper 1 by making it possible to inspect and treat the orientation data from different data sets in an identical manner [88]. MTEX was also used to investigate many different analysis methods, such as grain reconstruction, misorientation analysis, Schmid and slip system analysis, and various axis-angle approaches. Eventually, the orientation data for this paper was only treated using a relatively simple misorientation analysis, but the other investigations and analysis helped ensure the validity of the data. For instance, by spending considerable time testing various analysis tools on the data, it was discovered that the orientation data from the *NanoMegas ASTAR Index* did not correlate with the specimen coordinate system, because of software settings and misalignment between the PED patterns and the scan grid. While this is a common problem, and not especially relevant for the paper or indeed this thesis, it shows the benefit of working with an open source software developed by its own users, namely that the flexibility to inspect complex data sets are necessary in order to accurately trust and publish data.

4.7.2 Analysis of STEM data

In the case of atomic resolution STEM images, the quality is usually reduced due to specimen drift and scan noise. These images are usually formed by scanning the region row by row, and the relatively large jump back to the first column after a row is finished will typically cause instabilities in the beam position. To reduce the influence of this scan noise, it is better to acquire several fast exposures rather than one single long one, and align the resulting image stack by post processing. The *SmartAlign* plugin to *Gatan Digital Micrograph* made by Jones *et al.* [128]

offers an integrated way to both acquire and post-process this kind of data in order to correct for both scan distortions and specimen drift. A fast acquisition time is used, and several frames are acquired (like a movie). For each frame, the scan directions are rotated 90 ° to vary the slow and fast scan directions. During post-processing, the image stack is first rigidly aligned, i.e. the images are shifted to optimize their correlation, and then it is non-rigidly aligned [128]. During non-rigid alignment, the images are allowed to stretch slightly in different directions to make the images in the stack fit better to each other. The average through the aligned stack will be an image where scan and specimen distortions are greatly reduced. Of course, since non-rigid alignment may distort the data, it is useful to also acquire a high-signal image with a long acquisition time to compare with the aligned stack.

Part II

Papers

Paper 1

Emil Christiansen, Calin Daniel Marioara, Knut Marthinsen
Odd Sture Hopperstad, Randi Holmestad

Lattice Rotations in precipitate free zones in an Al-Mg-Si alloy

Materials Characterisation **144** (2018) 522-531.
https://doi.org/10.1016/j.matchar.2018.08.002

Materials Characterization 144 (2018) 522–531

Contents lists available at ScienceDirect

Materials Characterization

journal homepage: www.elsevier.com/locate/matchar

Lattice rotations in precipitate free zones in an Al-Mg-Si alloy

Emil Christiansen[a,b,*], Calin Daniel Marioara[a,c], Knut Marthinsen[a,d], Odd Sture Hopperstad[a,e], Randi Holmestad[a,b]

[a] Centre for Advanced Structural Analysis (CASA), NTNU – Norwegian University of Science and Technology, Trondheim N-7491, Norway
[b] Department of Physics, Faculty of Natural Sciences, NTNU – Norwegian University of Science and Technology, Høgskoleringen 5, Trondheim N-7491, Norway
[c] SINTEF Industry, Trondheim N-7465, Norway
[d] Department of Materials Science and Engineering, Faculty of Natural Sciences, NTNU – Norwegian University of Science and Technology, Alfred Getz vei 2, N-7491 Trondheim, Norway
[e] Department of Structural Engineering, Faculty of Engineering, NTNU – Norwegian University of Science and Technology, Richard Birkelands vei 1a, N-7491 Trondheim, Norway

ARTICLE INFO

Keywords:
Aluminium alloy
Deformation
Al-Mg-Si alloy
Transmission electron microscopy
Scanning precession electron diffraction
Precipitate free zones

ABSTRACT

Scanning precession electron diffraction and automated crystal orientation mapping in a transmission electron microscope (TEM) have been applied to quantitatively study the crystal orientation of precipitate free zones (PFZs) of four GB regions in an AA6060 alloy in peak aged condition (temper T6) after uniaxial compression to 20% engineering strain. The PFZ width in the alloy was found to be $w = 170 \pm 40$ nm. The results show that some PFZs develop significant misorientations relative to their parent grain, and represent, to the best knowledge of the authors, the first quantitative evidence of this. This misorientation may either be constant inside a particular PFZ, making it appear like a band or a very elongated subgrain, or be partitioned in discrete regions with a diameter comparable to the PFZ width, making the former PFZ into a collection of small grains. The band-like PFZ observed in this work had a misorientation relative to its parent grain of $\approx 7^{\circ}$, while the grain-like PFZ had grains with misorientations between $\approx 12^{\circ}$ and $\approx 20^{\circ}$ relative to its parent grain. The other PFZs that were observed had only limited misorientations relative to their parent grains, and had either dislocations perpendicular to the GB plane or a dislocation wall at the transition region. A general TEM study of the material at various engineering strains was also conducted and suggests that grain-like PFZs are more frequent for larger strains, indicating that the different PFZ features are likely due to different strain localisation in individual PFZs. This localisation is expected to be influenced by the orientation of the loading axis relative to crystal orientations and GB planes. It is also suggested that the different PFZ features engender different work hardening rates and possibly affect nucleation of intergranular fracture. The results support previous studies on the microstructure evolution of PFZs in age-hardenable aluminium alloys during deformation.

1. Introduction

Precipitate free zones (PFZs) along grain boundaries (GBs) in age-hardenable aluminium alloys and their relation to material properties have been studied for many years [1-5]. The review by Vasudévan and Doherty [5] covers the earlier works on the topic and concludes that, while particles and precipitates on GBs are the most important sites for nucleation and growth of intergranular ductile fracture, PFZs also serve their part by localising strain and accelerating void nucleation and growth at the GB particles. PFZs form due to vacancy and/or solute diffusion to grain boundaries [6], where solute form precipitates and particles, while at the same time the precipitation potential in the PFZ is suppressed. Whereas small metastable precipitates that form homogeneously throughout the grain are beneficial to strength [7], these GB precipitates and particles can be detrimental to ductility [5]. Because the PFZ lacks hardening precipitates, strain may localise in these regions and thus promote intergranular fracture. This is especially true for GBs inclined to the loading direction so that the shear stress along their PFZs becomes large [8]. However, since the PFZs typically retain some solute in solid solution [6], they will be stronger than pure aluminium [9]. It is clear that the material behaviour depends on the width and work hardening of the PFZs, the GB precipitation, and the grain interior strength, which makes it challenging to isolate influences from individual parameters. Because of this complexity, both experiments and simulations are necessary in order to elucidate the impact of each parameter. This work is an experimental study of lattice

* Corresponding author at: Centre for Advanced Structural Analysis (CASA), NTNU, Trondheim N-7491, Norway.
E-mail address: emil.christiansen@ntnu.no (E. Christiansen).

https://doi.org/10.1016/j.matchar.2018.08.002
Received 12 February 2018; Received in revised form 1 July 2018; Accepted 1 August 2018
Available online 03 August 2018
1044-5803/ © 2018 Elsevier Inc. All rights reserved.

orientations inside PFZs of an Al-Mg-Si alloy after deformation. No attempt is made to provide direct information regarding the influences of different parameters, but rather to provide insight into the strain localisation in the PFZs in an age-hardenable aluminium alloy. Such insight should prove relevant for simulations such as the ones by e.g. Pardoen et al. [10,11] that establish continuum models with assumptions based on microstructural knowledge.

A study by Schwellinger [4] showed that PFZs in Al-Mg-Si alloys may develop misorientations of ~20° relative to their parent grains when such alloys were strained close to fracture. He observed walls with large dislocation densities at the PFZ boundaries (i.e., the interface between PFZ and precipitate strengthened grain), and suggested that these may serve as void initiation sites when impinged by slip bands from the grain interiors. This suggestion was motivated by observations of Gardner et al. [12] and Wilsdorf [13] who showed how dislocation structures can serve as nucleation sites for voids in pure metals. More recent studies on pure tantalum crystals support this idea, and attribute such void formation to vacancy condensation at dislocation cell boundary block walls [14]. Although void nucleation and growth in precipitate strengthened alloys will be different from that in pure metals, it seems reasonable that dislocation structures should have some impact on ductile fracture.

In addition to Schwellinger [4] there are several studies that have reported on dislocation structures in PFZs of aluminium alloys [15-18]. Styczyńska and Łojkowski [15] observed by *in situ* TEM straining experiments that dislocation sources at GBs became active before sources inside the grain interiors. This resulted in dislocations bowing out from the GB and becoming pinned at the precipitates at the PFZ boundary, before penetrating into the grain interiors. During cyclic loading, Jain [16] observed dislocation networks within grains that terminated at the outer edges of the PFZs. He also observed dislocation structures inside the PFZs similar to those observed by Schwellinger [4]. Watanabe et al. [17] did not study PFZs specifically, but noted that some PFZs in an Al-Mg-Sc alloy under cyclic loading became misoriented relative to their parent grains. Khadyko et al. [18] observed several different dislocation structures in PFZs and their vicinity in an Al-Mg-Si alloy stretched to fracture in uniaxial tension. In most PFZs, both inside and outside the neck, dislocations spanned the PFZs and appeared almost perpendicular to the GB plane. Inside the neck however, some GB PFZs were misoriented relative to their parent grains, or had dislocation walls along their PFZ boundaries. Khadyko et al. [18] also performed crystal plasticity simulations taking the dislocation storage close to PFZs into account, and observed an increased stress and strain localisation within PFZs compared to a model with no PFZ, as well as a lattice rotation within the PFZs. Such effects were larger for PFZs inclined to the loading axis. Even though misoriented PFZs have been observed in strained aluminium alloys for the last 35 years, and several hypotheses exist regarding their importance, the only work attempting to quantify such misorientations is the one by Schwellinger [4]. With the advent of more advanced techniques, it is now possible to investigate the misorientations in greater detail. Therefore, the aim of the present study is to determine crystal orientations within PFZs along grain boundaries in an age-hardenable aluminium alloy.

Quantification of crystal lattice orientations is possible on the nanoscale by automated crystal orientation mapping [19] of scanning precession electron diffraction (SPED) [20,21] data. This technique is perfect for studying orientations within PFZs because it can be combined with a conventional TEM study of the exact same region. This means that imaging, dislocation analysis, and crystal orientation mapping can be performed from the same GB region and neighbourhood.

The alloy used in this study is the lean Al-Mg-Si alloy AA6060. When this alloy is heat treated, small metastable precipitates form homogeneously inside the grains through vacancy and solute condensation from a super saturated solid solution and subsequent growth [22-24]. The main hardening precipitate phase in this alloy system is the β″ precipitate, which forms as long needles along the ⟨100⟩ directions of the aluminium matrix in the peak aged condition (T6 temper) [25]. This precipitate phase has a monoclinic unit cell with $a = 1.516$ nm, $b = 0.405$ nm, $c = 0.674$ nm, and angle $\beta = 105.3$ [26]. The needles are coherent with the matrix along their length, and strain their local matrix neighbourhood in their lateral dimensions [27]. This alloy has been used in several other studies, including Khadyko et al. [18] and Frodal et al. [28], and serves as a model alloy, which also has extensive industrial applications. We have deformed the alloy in compression in order to examine a wide range of strains, which would not be possible in tension. A general TEM investigation of PFZs of several GBs in specimens compressed to 5%, 10%, 20%, and 50% engineering strains has been conducted to investigate the variety of PFZ microstructures that forms. The study focuses, however, on a detailed SPED and orientation mapping study of crystal orientations inside PFZs of four individual GBs in the specimen compressed to 20%, and how these GB PFZs relate to the general observations.

Table 1
Nominal composition of the AA6060 alloy in wt% and at%.

	Fe	Si	Mg	Mn	Cr	Cu	Zn	Ti	Al
wt%	0.193	0.422	0.468	0.015	0.000	0.002	0.005	0.008	Bal.
at%	0.093	0.406	0.520	0.007	0.000	0.001	0.002	0.005	Bal.

2. Materials

The material used in this work was an extruded profile of the AA6060 aluminium alloy. The composition of the alloy is given in Table 1. Small cylinders measuring 9 mm in diameter and 13 mm in length were machined from the profile with their longitudinal direction along the transverse direction (TD) of the profile, see Fig. 1. The cylinders were subjected to a standard T6 heat treatment as illustrated in Fig. 2. The exact same alloy and heat treatment was studied by Frodal et al. [28], where it was found that the material had an equiaxed and recrystallized grain microstructure. The grain size is approximately 60 μm to 70 μm.

Uniaxial compression tests of the cylinders along their longitudinal axis were done in a universal testing machine with a constant crosshead speed of approximately 0.15 mm/min, corresponding to a strain rate of $2 \times 10^{-4}\,s^{-1}$, to 5%, 10%, 20%, and 50% compressive engineering strain. In order to limit friction between the specimens and compression platens, the contact surfaces were lubricated with *Dow Corning Molykote G-n Metal Assembly Paste*. The degree of barrelling was less than 6% in all tests. Due to the anisotropy of the material, the aspect ratio of the specimens changed during compression, and in the most severe case (i.e., at 50% engineering strain) the aspect ratio between the extrusion direction (ED) and the normal direction (ND) of the cylinders was

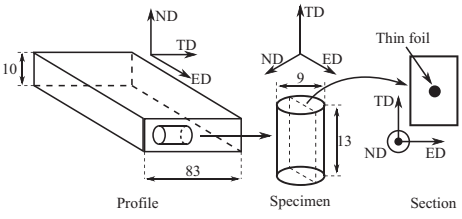

Fig. 1. Sketch of compression specimen geometry. The extruded profile coordinate system is shown: extrusion direction (ED); transverse direction (TD); and the normal direction (ND). Cylindrical specimens were machined from the extruded profile with longitudinal axes along the TD. Sections of the TD-ED plane were cut from the approximate middle of the cylinders after compression, and TEM thin foils were prepared from various locations of the section. Measures are in mm. Not to scale.

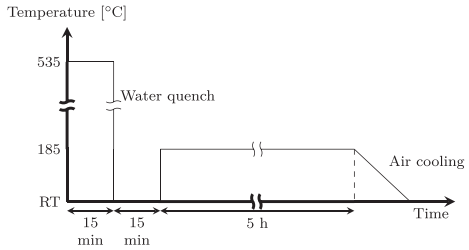

Fig. 2. Sketch of the alloy heat treatment. The specimens were solution heat treated at 535 ° C for 15 min in a salt bath and quenched to room temperature (RT) in water, and then naturally aged for 15 min at RT with subsequent artificial ageing for 5 h at 185 ° C in an oil bath. At the end of artificial ageing, the specimens were cooled to RT in still air.

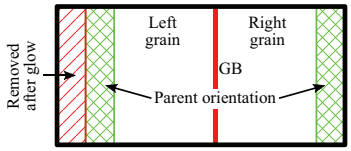

Fig. 3. Illustration of SPED map and regions used for parent grain orientation calculations. The first 20 pixels (64 nm) of each line are removed due to afterglow effects and are shown as the red hashed area. The mean orientation of a region 20 pixels wide on each side (shown as green square-hashed regions) is used as a reference for that particular parent grain when calculating misorientation angles. Size of raw data scan is 1024 × 2048 pixels, and only a part of a full scan is illustrated. Not to scale. (For interpretation of the references to color in this figure legend, the reader is referred to the web version of this article.)

≈ 1.4. Results presented in this work are from undeformed and 20% compressed specimens, but observations from the other compression levels are mentioned and discussed as well. The SPED and orientation mapping results presented here are from a single TEM thin foil to ensure that the macroscopic strain of the GBs studied is roughly the same. In order to compare PFZ microstructures of different GBs, the study is limited to high angle grain boundaries (HAGBs).

Sections containing the TD and extrusion direction (ED), i.e. the TD-ED plane, of the compression specimens were cut close to the specimen centres as indicated in Fig. 1. These sections were mechanically polished down to a thickness of ≈ 200 µm to ≈ 300 µm before 3 mm disks were cut out. The compression axis (CA) of the specimens was marked by cutting notches on opposite sides of each disk using a scalpel, before they were polished further on both faces down to a final thickness of ≈ 50 µm to ≈ 120 µm. Electropolishing was done in a *Struers Tenupol 3* unit operating at 20 V using a mixture of 1/3 HNO_3 (Nitric acid) and 2/3 CH_3OH (Methanol) as electrolyte, which was kept at − 25 ± 5 ° C. The orientation of the CA in TEM images was determined by imaging the thin foils and their CA notches through a visible light microscope after inserting them in the TEM holder, and correcting for image rotations in the TEM. The errors in CA orientation are estimated to be in the order of ± 5°.

TEM investigations were carried out on three different instruments. A double tilt holder and a *Philips CM30* with a LaB_6 filament operating at 150 V equipped with film and a *Gatan PEELS model 601* were used for precipitate statistics using the method in [25,29]. For bright-field (BF) and weak-beam dark-field (WBDF) studies of deformed microstructures, a LaB_6 *JEOL JEM2100* with an accelerating voltage of 200 kV was used with a double tilt holder. Measurement of the PFZ width *w* was conducted on images from this microscope by measuring the shortest distance from the GB to the first intersection with a precipitate at 64 equidistant points along the GB and taking the average. WBDF imaging was performed close to the conventional $\vec{g} - 3\vec{g}$ diffraction condition with the diffracted beam along the optical axis by first tilting the specimen to a two-beam condition for $\vec{g}$ and subsequently tilting the incoming electron beam so that the $\vec{g}$ diffracted beam travelled along the optical axis. The tilt of the electron beam also caused $3\vec{g}$ to excite, leaving $\vec{g}$ weak with a positive excitation error and suitable for WBDF imaging. Finally, an in-plane rotation holder with single tilt and a *JEOL JEM2100F* operating at 200 kV equipped with a *NanoMEGAS DigiSTAR* system were used to perform SPED [20,21] with a spot size of 1.0 nm and a nearly parallel beam. Deflector coils above the specimen were used to precess the beam around the optical axis with an angle of 1.0° and a frequency of 100 Hz. Another set of coils below the specimen counteracts the precession, giving the same result as that of precessing the specimen in a stationary beam. In diffraction, this gives a precession electron diffraction pattern (PED) which can be considered equivalent to an electron diffraction spot pattern that is averaged through several incoming beam directions. Thus, more of the reciprocal space of the crystal is probed, and dynamical diffraction effects are somewhat reduced. This probe was then scanned across the specimen in a 320 × 640 pixel raster with step length 3.2 nm resulting in a rectangular scan region of 1024 × 2048 nm^2. At each probe position, a PED pattern was acquired. Acquisition of the PED patterns was done by illuminating the microscope phosphorous screen (tilted 30°) and acquiring images of this by an external Allied StingRay CCD camera with 144 × 144 pixels and 8-bit depth. The exposure time was 40 ms and synchronized with the scan dwell time. Each grain boundary was aligned along the tilt axis of the rotation holder and oriented edge-on to the optical axis. For each SPED scan, the slow scan direction was aligned along the GB. Due to the slow decay of the phosphorous screen, afterglow caused the spots in the last diffraction patterns of a line to remain significant in the diffraction patterns of the next line. Therefore, the first 20 pixels (64 nm) of each line were removed as indicated in Fig. 3, and are not present in the misorientation maps. Afterglow effects are present in the remaining pixels as well, and will influence the appearance of features in the scan. However, due to the long exposure time and small step size, this afterglow effect is not detrimental to the technique.

Orientation mapping based on the 4D SPED data was performed by matching each PED pattern of the SPED stacks to a bank of simulated Al spot diffraction templates by the commercial *NanoMEGAS ASTAR Index* package. The procedure is explained in detail by Rauch and Véron [19]. The resulting data set consists of crystal Euler angles, the cross-correlation index between each experimental pattern and its matched template, and the reliability of each match. In this work, accepted matches for each PED pattern have at least 15% higher cross-correlation index than the second best match of that particular PED pattern, and a cross-correlation index of at least 15.0. These thresholds have been somewhat arbitrarily chosen, but are motivated by the fact that both of these values should be reasonably high for a good match. SPED frames with matches not fulfilling these criteria are not analysed, and appear white in the misorientation maps. The quality of orientation mapping results was controlled by comparing regions of low cross-correlation index and reliability to the raw data in the SPED stack.

The *MATLAB* open source toolbox *MTEX* [30] was used to analyse the orientation mapping results. For each SPED scan, the orientation of the left-hand side and right-hand side "parent grains" were calculated by averaging the orientations within narrow regions (64 nm wide) along the left-hand side and right-hand side of the scan, respectively. These regions are illustrated in Fig. 3. These parent orientations serve as a reference, and the orientations on either side of the GB are compared to their respective parent grains to calculate misorientation maps. To make comparisons between the misorientation maps easier, the misorientation scalebars for each misorientation map are the same, and the minimum and maximum values correspond to the overall minimum and

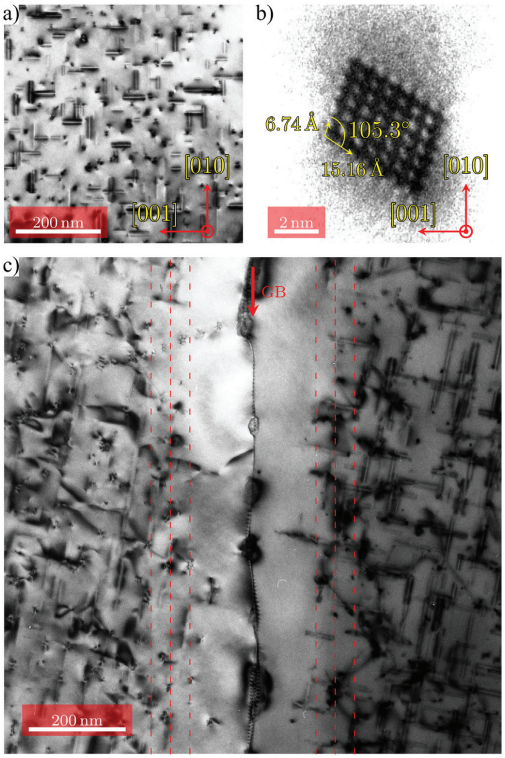

Fig. 4. Microstructure of the undeformed alloy. In a) the BF TEM image shows the precipitates along [001] and [010] in aluminium as sets of two parallel lines of strain contrast and the precipitates along [100] as dots. In b) the HRTEM image of one cross-section is shown, with parameters for the β″ phase overlaid [26]. Both a) and b) were acquired in the [100] zone axis of aluminium. Subfigure c) shows a representative HAGB with PFZs on either side. The GB is marked by a red arrow, and the PFZ width $w = 170$ nm with its standard deviation of 40 nm are marked by dashed lines. (For interpretation of the references to color in this figure legend, the reader is referred to the web version of this article.)

maximum values of measured misorientation angle. Pole figures are in stereographic projection, and all orientations in the corresponding misorientation map are included. Note that the pole figures only show the orientations on either side of the grain boundaries in relation to each other, and should not be correlated to the specimen or scan coordinate axes.

3. Results

TEM studies of the alloy in the undeformed state were performed to establish a reference for the investigation of the deformed states. Fig. 4 presents TEM images of the microstructure of the alloy prior to deformation. The characteristic diffraction contrast of β″ precipitates is clearly seen in the BF image. The precipitates are oriented with their longitudinal axis along ⟨100⟩ directions and appear as needles along [010] and [001], while the ones along [100] are aligned out-of-plane and appear as dots. When imaged in high resolution TEM (HRTEM), these cross sections show the β″ crystal periodicity. All cross-sections observed were consistent with the β″ crystal structure [26]. From several images similar to the ones presented in Fig. 4a and b, as well as thickness measurements using electron energy loss spectroscopy, the average needle length, cross-section area, number density, and volume fraction were estimated to be $\bar{l} = 40 \pm 1$ nm, $\bar{\sigma} = 19.1 \pm 0.8$ nm^2, $\bar{\rho} = 5556 \pm 629$ #/μm^3, and $\overline{V_f} = 0.42 \pm 0.05$%, respectively. The BF TEM image of a HAGB presented in Fig. 4c shows a characteristic GB PFZ in the undeformed state. Measurements of the PFZ widths of three different GBs resulted in a mean PFZ width of $w = 170$ nm with a standard deviation of 40 nm. This standard deviation serves as an estimate of the width of the transition zone between PFZ and the grain interior. PFZ widths of both HAGBs and low angle GBs (LAGBs) were measured, and no large variations in PFZ width were observed.

Based on conventional BF TEM investigations of the deformed states, four main features of the deformed PFZ microstructure were defined. These are “perpendicular dislocations” that span the PFZ, “dislocation walls” in the transition regions, “PFZ misorientation bands”, and “PFZ grains”, from now on referred to as (in italic) *dislocations*, *walls*, *bands*, and *grains*, respectively. Specimens compressed 20% or more contain all four features, while the less deformed specimens only exhibit *dislocations*, *walls*, and *bands*. Results from a detailed investigation using TEM and orientation mapping SPED of four GBs in a thin foil from a 20% compressed specimen are presented in the following and summarized in Table 2.

Fig. 5 presents WBDF, BF, and orientation mapping data from a HAGB (parent-parent misorientation $\varphi = 24^\circ$ and CA-GB angle $\Phi = -66^\circ$) exhibiting PFZs with perpendicular dislocations, i.e. the *dislocations* feature, on both sides. The dislocation density inside the PFZs is much lower than in the grain interiors. As can be seen from the WBDF and BF images, the projected image-plane traces of the few dislocations inside the PFZ have relatively high angles relative to the projected GB trace. Thus, the dislocations appear to be oriented perpendicularly to the GB plane. However, the true three dimensional orientation of the dislocations could not be established. In the WBDF image in Fig. 5a, the dislocations in the left-hand side PFZ are investigated. These dislocations can be divided into two groups, “b1” and “b2”, based on their orientation relative to the GB plane. Other PFZs with the *dislocations* feature show similar tendencies. Different $\vec{g} - 3\vec{g}$ conditions were investigated, and the “b1” dislocations satisfy the invisibility criterion $\vec{g} \cdot \vec{b} = 0$ when $\vec{g} = [0\bar{2}2]$ is imaged, using the indexing of the inset diffraction pattern in Fig. 5a. Similarly, the “b2” dislocations disappear when $\vec{g} = [0\bar{2}\bar{2}]$ is used as imaging condition. Therefore, the dislocations in the “b1” group have $\vec{b} \parallel [x_1 11]$ and the ones in the “b2” group have $\vec{b} \parallel [x_2 \bar{1}1]$, where x_1 and x_2 are unknown Miller indices as only one invisibility condition was found for each set. Thus, the dislocations in “b1” have different Burgers vectors than the ones in the “b2” group. Furthermore, it is likely that all the dislocations in each group have the same Burgers vector. Hence it is clear that the

Table 2
Summary of the SPED orientation mapping results for the four HAGBs presented in Figs. 5 to 8 from a specimen deformed to 20% engineering strain. The CA-GB angle Φ and GB misorientation angle φ for each GB are given, along with the maximum misorientation θ, and observed features for either side of the GBs.

Figure	Φ [°]	φ [°]	Side	θ [°]	Feature
Fig. 5	−66	24	Left	1.3	*Dislocations*
			Right	1.9	*Dislocations*
Fig. 6	64	21	Left	3.8[a]	*Dislocations*
			Right	5.8[a]	*Wall*
Fig. 7	16	28	Left	7.6	*Band*
			Right	3.0	*Wall*
Fig. 8	45	38	Left	20.0	*Grains*
			Right	11.6	*Grains*

[a] The misorientation values inside the relevant PFZ areas are much lower than the maximum value. Relevant values are ~1°, and ~2.5°, for the left-hand and right-hand side respectively.

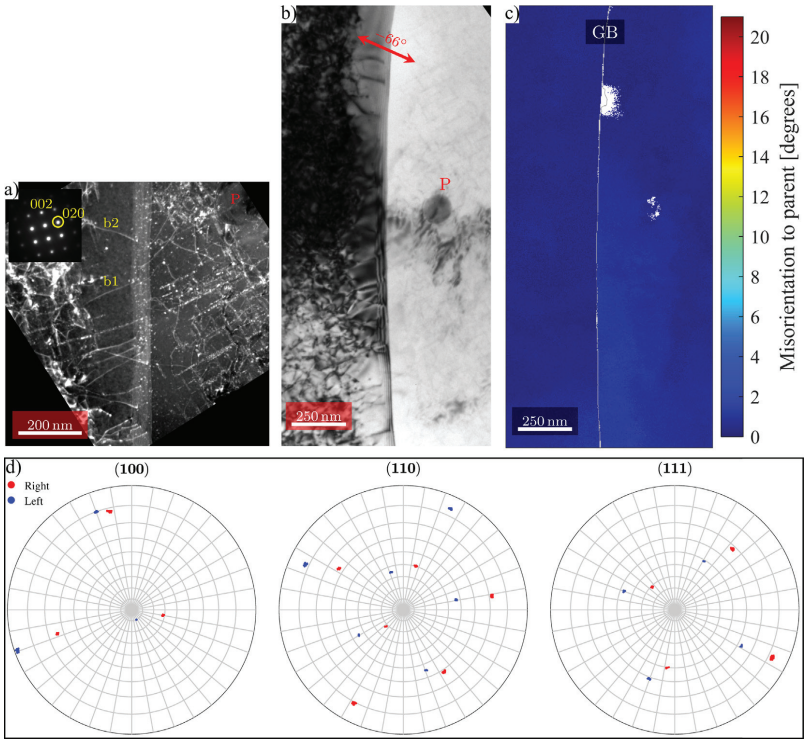

Fig. 5. PFZs exhibiting *dislocations*. The parent-parent misorientation is $\varphi = 24^{\circ}$, and the CA-GB angle is $\Phi = -66^{\circ}$ as indicated by the double arrow in b). Nearly perpendicular dislocations are present in the PFZs of both grains. The WBDF image in a) was acquired under $\vec{g} - 3\vec{g}$ conditions, using the $\vec{g} = [020]$ reflection of the left-hand side grain as indicated by the inset electron diffraction pattern. Note that the inset electron diffraction pattern was acquired in a [100] zone axis, before tilting the specimen and electron beam to $\vec{g} - 3\vec{g}$ conditions required for WBDF imaging as explained in the Materials section. This tilting also caused the GB plane to become inclined to the electron beam. The $\vec{g} \cdot \vec{b} = 0$ condition for dislocations "b1" and "b2" is satisfied for $\vec{g} = [0\bar{2}2]$ and $\vec{g} = [02\bar{2}]$, respectively. The BF TEM image in b) shows a larger view of the GB, with a particle labelled "P" as a reference to the WBDF image. No significant misorientation angles can be seen in the map presented in c). The GB plane is shown as a thin grey line. Note that images b) and c) were acquired with the GB plane edge on to the electron beam. Pole figures of the (100), (110), and (111) poles are given in d), where 86522 and 103809 data points are included for the left-hand and right-hand sides, respectively.

PFZ contains relatively few dislocations, and these dislocations can be separated into sets of different orientation and Burgers vector. Burgers vector analysis was not performed for other PFZs with the *dislocations* feature. Regarding the crystal orientation mapping results, it is clear that misorientation variations between the PFZs and their parent grain interiors are very small. This is also easily seen from the pole figure data, where the orientation measurements for each grain are concentrated to very small areas.

Fig. 6 presents data for a HAGB (parent-parent misorientation $\varphi \approx 21^{\circ}$ and CA-GB angle $\Phi = 64^{\circ}$) where the PFZ on the left-hand side contains *dislocations*, while the PFZ on the right-hand side displays a *wall*. In the BF TEM image, the *wall* is visible as a relatively sharp contrast change from the precipitate hardened grain interior to the PFZ. Correspondingly, there is a sharp misorientation change of $\approx 2^{\circ}$–3° at this boundary in the misorientation angle map. Such an abrupt change in misorientation angle indicates a local concentration of tangled dislocations. The pole figures indicate a slightly larger variation of orientations in the right-hand side grain than in the other grain.

Fig. 7 presents results from a HAGB (parent-parent misorientation $\varphi = 28^{\circ}$ and CA-GB angle $\Phi = 16^{\circ}$) with a *band* on its left-hand side, clearly seen as contrast in the BF image. Indeed, the misorientation map shows that this PFZ has developed a misorientation of 4.5° to 7.0° relative to its parent grain. In the PFZ on the other side of the GB, a *wall* is present (not visible under the particular conditions of the BF image), giving this PFZ a misorientation of ~ 2°. The distinction between a *wall* and a *band* is somewhat diffuse, as both features are very similar. However, a PFZ with a *band* has larger misorientations than a PFZ with a *wall*. While a PFZ with a *wall* feature is misoriented 2° to 3°, a PFZ with a *band* feature is misoriented 4.5° to 7.0°. Additionally, the boundary between the PFZ and the grain interior tends to be sharper for a *band* than a *wall*. The pole figures show the greater variation of orientations in the left-hand side grain compared to the right-hand side grain.

Results from a HAGB (parent-parent misorientation $\varphi = 38^{\circ}$ and CA-GB angle $\Phi = 45^{\circ}$) exhibiting the last feature, PFZ *grains*, are presented in Fig. 8. The GB interface appears jagged and is not as straight as for the other GBs presented previously. It can be seen from the BF TEM image that there are regions of different contrast within the PFZ to either side of the GB. In the misorientation map, these regions show large misorientations relative to their parent grains. For the right-hand side, regions of significant misorientations are present only in the lower part of the PFZ, with misorientations close to 0° at the top, and 3°, 6.5°,

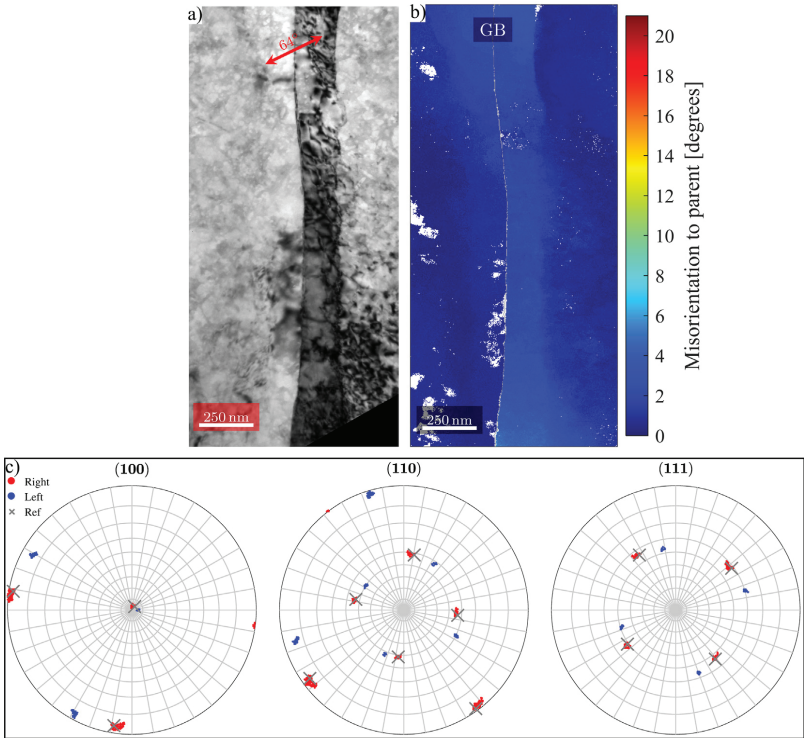

Fig. 6. GB with dislocation *wall* at the PFZ boundary in one of the grains. The parent-parent misorientation is $\varphi = 21^{\circ}$, and the CA-GB angle is $\Phi = 64^{\circ}$ as indicated by the double arrow in a). A dislocation wall, i.e., a *wall* feature, is seen at the boundary of the right-hand side PFZ in the BF TEM image shown in a). In b) the misorientation angles in degrees of each grain are shown, and the *wall* feature of the right-hand side PFZ corresponds to misorientations 2° to 3°. The GB plane is shown as a thin grey line. Pole figures of the (100), (110), and (111) poles are given in c), where 80514 and 107070 data points are included for the left-hand and right-hand sides, respectively. The parent orientation of the right-hand side grain is marked by a cross.

8.5°, and 11°, sequentially down along the PFZ. The PFZ on the other side of the GB contains only regions of high misorientation, with values ranging from 12° to 20°. In addition, there are some regions with 10° misorientation that appear more than 200 nm from the GB, indicating that they have formed just outside the PFZ. Boundaries between regions are very sharp in the left-hand side PFZ, while they are more diffuse in the other. However, in all cases the interface between the PFZ grains and the parent grain is very sharp. The variations in orientations are very clear in the pole figures as well, where the left-hand side has a much larger orientation variation.

4. Discussion

The purpose of this study is to investigate how PFZs in a material behave when the material is deformed, with special emphasis on strain and crystal orientations. Based on the results obtained, it is clear that some PFZs can develop significantly different orientations than their parent grains, while others do not. PFZs may develop *dislocations*, *walls*, *bands*, or *grains*.

Regarding the *grains* that can form in PFZs, it should be noted that the orientation mapping algorithm can be somewhat misleading when it comes to the sizes of the grains. First of all, due to the phosphorescent screen and the resulting afterglow, any given pixel in the SPED data will consist of a mix of the PED pattern in that pixel and the previous pixels. This may cause problems when indexing the orientations, and boundaries between neighbouring grains tend to smear out in the fast scan direction. Secondly, if grains are overlapping, the indexing algorithm will tend to favour one of the orientations. This will occur at GBs inclined to the beam direction and influence the apparent sizes and shapes of the grains. However, when comparing the orientation maps with the TEM images, it becomes clear that the amount of overlap is limited, and the shapes and sizes of the grains in the orientation maps are qualitatively correct.

The features observed here are similar to results published by Jain [16], Styczyńska and Łojkowski [15], Khadyko et al. [18], and Schwellinger [4]. Jain [16] observed PFZ microstructures similar to *dislocations* and *walls* in his overaged Al-Mg-Si alloy subjected to cyclic loading. His results indicate that many more cycles are necessary for the *wall* feature to form than for the *dislocations*. The *in situ* experiments by Styczyńska and Łojkowski [15] show that dislocations start by bowing out from the GB into the PFZ as half-loops at very low strains. These half-loops are pinned by precipitates at the PFZ boundary, and look similar to the *dislocations* feature. The strain that was required for these half-loops to form in the *in situ* study was very low, and only a few PFZs contained them, while other PFZs were unaffected by deformation. Further deformation caused dislocations to gather along the PFZ edge, similar to the *walls* in the present work. The study by Khadyko et al. [18] considered the same alloy and heat treatment as the present study,

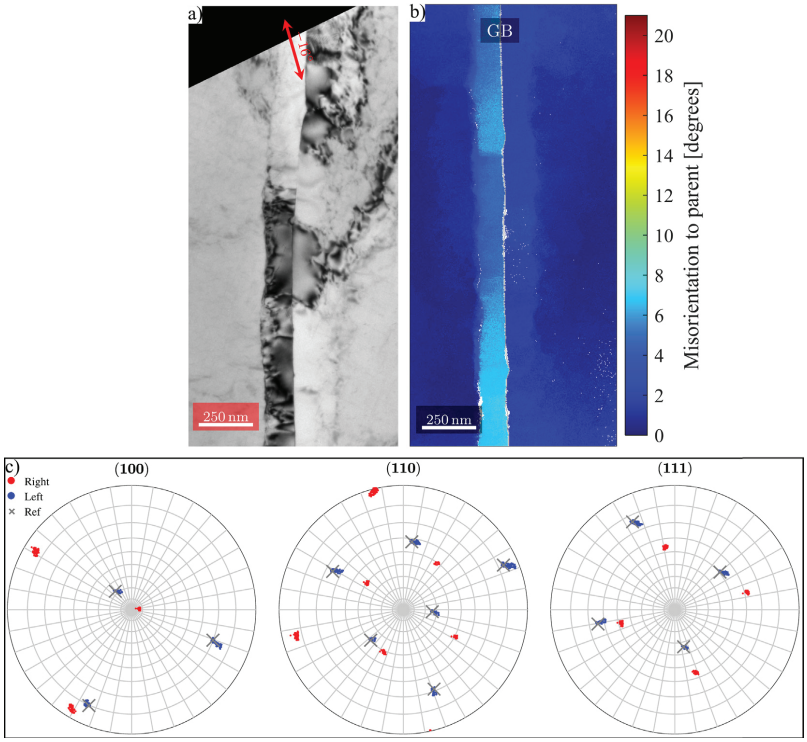

Fig. 7. PFZs exhibiting the *band* and *wall* feature. The parent-parent misorientation is $\varphi = 28^{\circ}$, and the CA-GB angle is $\Phi = 16^{\circ}$ as indicated by the double arrow in a). The BF TEM image in a) shows a band-like contrast in the left-hand side PFZ, while the contrast to the right of the GB is not as regular. In b) the misorientation angles in degrees of each grain are shown, and the band-like contrast of the left-hand side PFZ corresponds to misorientations 4.5° to 7°, which is labelled as a *band* feature. In the right-hand side PFZ, the misorientations indicate that a *wall* is present. The GB plane is shown as a thin grey line. Pole figures of the (100), (110), and (111) poles are given in c), where 86568 and 103610 data points are included for the left-hand and right-hand sides, respectively. The parent orientation of the left-hand grain is marked by a cross.

but under tension rather than compression. *Dislocations* were observed both inside and outside the neck of the specimens, while *walls* were only observed inside the neck. Additionally, *bands* were sometimes also seen inside the neck, but less often than *walls*. These three reports indicate that *walls* and *bands* require higher strains in order to form, compared to *dislocations*. The only previous report of features similar to *grains* known to the authors, is the one by Schwellinger [4]. In the present work, *grains* were only observed in specimens compressed to 20% engineering strain or more, and they seemed more frequent in specimens compressed to 50% engineering strain. We therefore suggest that the density of PFZ *grains* increases with increasing strain.

A full and rigorous discussion on the mechanisms responsible for each feature is out of scope of the current work. However, a brief discussion on the evolution of the features is given. Based on our and previous results it is reasonable to assume that the local strain around GBs determines what PFZ feature is formed at each particular GB. If a GB is subjected to low local strains, *dislocations* are formed, while for larger strains, *walls*, *bands*, or *grains* are formed. Because the local strain required for *walls* is lower than what is required for *bands*, it follows that each feature develops from another. As very low strains are required for *dislocations*, this is the first feature to form in any PFZ. When the global strain increases, so does the local strain, and eventually the *walls* feature may form where the local strains are large enough. Similarly, *bands* will also form once the local strain reaches some critical value. We therefore propose the following: during straining, dislocations are emitted as loops from the GBs and are pinned by precipitates at the outer edges of the PFZ, and all PFZs develop *dislocations* initially. As the deformation continues and GBs experience different stress and strain states, some PFZs develop *walls* due to many dislocations emitting from the GB and forming tangles among the precipitates in the PFZ transition region. This is supported by other studies as well [15,16]. Upon further straining, some of these *walls* progress and develop into *bands*. As strain concentrates yet further at some GBs, the soft PFZ must form small grains in order to maintain compatibility with the harder grain interior and the neighbouring grain. It is clear that significant strains are required to form the large misorientations related to *grains*. Because some GB PFZs develop *dislocations*, while others develop *grains*, there must be large differences in local strains in GB PFZs in peak-aged AA6060.

The angle between the deformation axis and the GB plane is one parameter that has proven to influence the localisation of strain in PFZs [8,18,31], and this angle will then influence which features form at the different PFZs at a given global strain. For example, the only case of PFZ *grains* observed in this study occurred at a GB inclined 45° to the CA, which would result in maximum shear along the GB and large strain localisation in the PFZ. However, during deformation of a polycrystal,

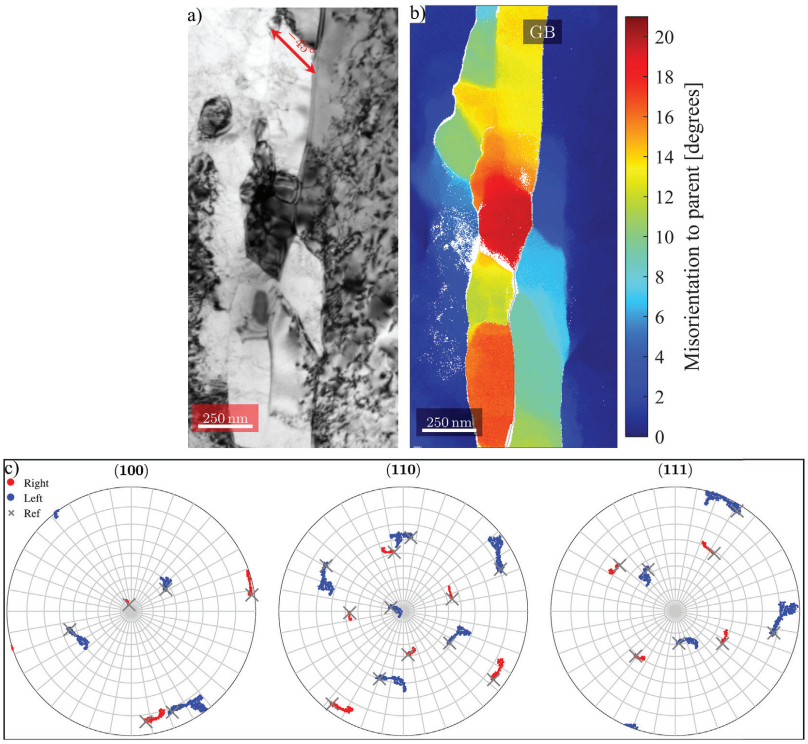

Fig. 8. PFZ with small regions of high misorientations relative to parent grain orientations, i.e. *grains*, observed by BF TEM and SPED orientation mapping. The parent-parent misorientation is $\varphi = 38^{\circ}$, and the CA-GB angle is $\Phi = 45^{\circ}$ as indicated by the double arrow in a). The PFZs to either side of the GB have formed regions of different contrast in the BF TEM image shown in a). In b), the misorientation angles in degrees of each grain are shown. The GB plane is shown as a thin grey line. Pole figures of the (100), (110), and (111) poles are given in c), where 103805 and 82316 data points are included for the left-hand and right-hand sides, respectively. The parent orientation of the two grains are marked by crosses.

the individual grains will change shape and rotate, causing the angle between the CA and the GB planes to change. Therefore, a GB may pass through the 45° orientation and strain may localise before the GB rotates away from this critical orientation. It is therefore difficult to perform systematic studies on the importance of this parameter. The other features seem to form with no clear dependence on the CA orientation.

The effect of the observed PFZ features on material properties is challenging to establish. The work hardening in most PFZs is limited, since most PFZs exhibit the *dislocations* feature which corresponds to low dislocation densities compared to their parent grain. Some models, e.g. the one used by Pardoen and Massart [11], assumes extensive work hardening potential in PFZs. Such models will not be valid for most PFZs in peak-aged AA6060. On the other hand, the other three features will provide additional barriers for dislocation movement, and lead to a modified work hardening behaviour.

Perhaps most interesting, is the effect of *grains* on the PFZ strength. Assuming the PFZ behaves as a polycrystal consisting of grains with diameter $d \approx w$, a Hall-Petch type of approach is reasonable. When a general polycrystal deforms, dislocations slipping on the same slip plane will pile-up against grain boundaries which act as dislocation motion barriers. The shear stress in front of a pile-up increases linearly with the number of dislocations, and the applied shear stress. Once enough dislocations have piled-up to initiate slip in the neighbouring grain, the frontmost dislocation may transmit to the other grain. However, if the grains in the polycrystal are small, there will be a limited number of dislocations that can fit inside each grain. Because of this, a higher stress must be applied in order to transmit dislocations across grain boundaries. This will strengthen the material, and leads to the so-called Hall-Petch grain boundary strengthening mechanism expressed by $\sigma_{HP} = \sigma_0 + k/\sqrt{d}$ [32,33]. In the Hall-Petch relation, σ_0 is the friction stress, k is a constant describing the strength of the boundaries, and d is the grain diameter of the material. An identical relationship is applicable for materials with small cells separated by dislocation walls [9]. For aluminium alloys, k is in the range $\sim 0.01 - 0.3$ MPa$\sqrt{\text{m}}$, depending on the nature of the boundaries and/or cell walls [9,34]. In the case of PFZ *grains*, the number of dislocations that may pile-up inside a single PFZ grain is very limited, and the strength of the PFZ should increase. Assuming that the PFZ is completely drained of solute, the friction stress of the PFZ is equal to the flow stress of high purity aluminium, i.e. $\sigma_0 \approx 11$ MPa [35]. Fig. 9 shows how σ_{HP} changes as a function of d for different values of k. Approximating the PFZ *grains* as spherical grains, the equivalent diameters of the different grains present in the PFZs shown in Fig. 8b were also calculated and are plotted for reference. It is obvious that for weak boundaries, i.e. $k < 0.1$ MPa$\sqrt{\text{m}}$, the strength of the PFZ is much lower than the flow stress of the alloy. However, for $k \geq 0.1$ MPa$\sqrt{\text{m}}$, the strength of the PFZ will be comparable to the grain interior. The important point in this analysis is the

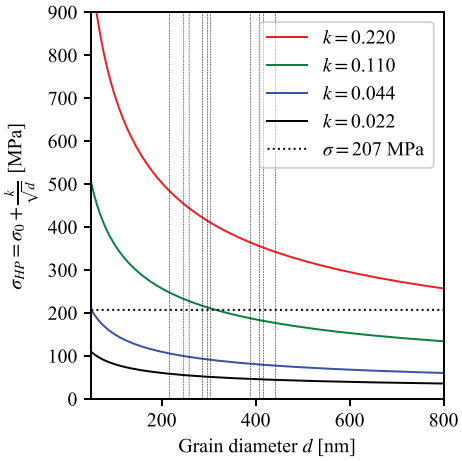

Fig. 9. Plot of Hall-Petch strengthening of polycrystalline aluminium σ_{HP} as a function of grain diameter d for different grain boundary diffusivity parameters k. The unit of k is MPa$\sqrt{\text{m}}$ and has been omitted from the legend for clarity. Vertical dashed lines indicate measured equivalent diameters of grains observed in the PFZs in Fig. 8b, while the horizontal dotted line show the flow stress of the bulk material [28].

fact that PFZs with *grains* may become stronger than the grain interior. This will cause dislocations approaching from the grain interior to pile-up against the PFZ. As a result, PFZ *grains* will screen the GB from pile-ups and will thus inhibit void nucleation at the GB. On the other hand, Schwellinger [4] suggested that large dislocation densities at the PFZ boundaries could provide locations for void nucleation through vacancy condensation, especially when impinged by slip bands from the grain interiors. Recent work on pure tantalum suggests that dislocation structures formed during deformation, rather than pre-existing GBs, are preferred sites for voids as well [14]. It should be noted, however, that very large local stresses would be required for voids to nucleate purely through plasticity and whether or not this may occur at the PFZ boundary will depend on whether the material favours planar slip. Thus, while PFZ *grains* might screen GBs from pile-ups and inhibit void nucleation, dislocation pile-ups at PFZ boundaries might nucleate voids there instead.

The different PFZ features found in the present work should be considered when designing models and simulations. Further work should include experimental investigations of whether the same features appear in alloys with different strengths and PFZ widths, as well as simulations of the impact of these features on material properties.

Finally, it should be noted that the thin foil preparation of the specimens might have influenced the microstructure. Especially dislocations originally present within PFZs might have escaped as a result of the thinning process. Therefore, the dislocation density in PFZs exhibiting *dislocations* may be higher than observed in the present work. However, it is unlikely that the sample preparation has altered the original microstructure of the *grains* feature markedly.

5. Conclusions

A detailed TEM and SPED orientation mapping study of four different HAGBs in the AA6060 aluminium alloy in peak aged condition compressed by 20% engineering strain has been performed along with a more general BF TEM study of specimens compressed to 5%, 10%, 20% and 50% engineering strain. The results show that different PFZs in the same material can develop significantly different crystal orientations than their parent grains. We also show that in regions where such orientation differences do not form, the dislocation density inside the PFZ is much smaller than inside the grains. Four different microstructural features can be used to describe PFZs in the deformed state. These are "perpendicular dislocations" that span the PFZs, dislocation "walls" along the PFZ/bulk transition regions, PFZ "misorientation bands", and PFZ "grains", labelled as *dislocations*, *walls*, *bands*, and *grains*, respectively. A PFZ with *dislocations* tends to contain sets of dislocations parallel to each other, all showing large angles to the GB interface. *Walls* are characterized by relatively small misorientation ($\sim 3°$) between PFZ and parent grain. PFZ *bands* are similar to *walls*, but have a higher misorientation (between 4.5° and 7°) relative to their parent grain. PFZ *grains* are misoriented between 12° and 20° from their parent grain, and are separated from each other by LAGBs. The different features have been observed before, but the misorientations have not been quantitatively studied in detail. Based on the current investigation and reports from the literature, it is suggested that the features develop from each other during deformation. *Dislocations* appear in PFZs at small strains, but at larger strains, *walls* at the transition region between the PFZ and the grain interior may form. Further deformation results in PFZ *bands*. Finally, PFZ *grains* form at large strains. The local environment of the individual PFZ, including the angle between CA and GB, GB misorientation angle, and the orientation of each grain relative to the CA, is assumed to influence the global strain required to form each feature at a particular GB PFZ. GBs oriented close to 45° to the loading axis are suggested to form PFZ *grains* earlier than other GBs. Future works should investigate the impact of these PFZ features on material properties, and whether these features occur in other alloys with different strengths and PFZ widths.

Acknowledgments

This research was conducted at the Centre for Advanced Structural Analysis (CASA), funded by the Research Council of Norway [grant number 237885] and several public and company partners.

The TEM work was carried out using the NORTEM infrastructure funded by the Research Council of Norway [grant number 197405].

Data Availability

The raw data required to reproduce these findings cannot be shared at this time due to legal or ethical reasons. The processed data required to reproduce these findings cannot be shared at this time due to legal or ethical reasons.

References

[1] N. Ryum, The influence of a precipitate-free zone on the mechanical properties of an Al-Mg-Zn alloy, Acta Metall. 16 (3) (1968) 327–332, https://doi.org/10.1016/0001-6160(68)90018-7.
[2] M. Abe, K. Asano, A. Fujiwara, Influence of the precipitate-free zone width on the tensile properties of an Al-6 Wt pct Zn-1.2 Wt pct Mg alloy, Metall. Trans. 4 (6) (1973) 1499–1505, https://doi.org/10.1007/BF02668000.
[3] T. Kawabata, O. Izumi, Ductile fracture in the interior of precipitate free zone in an Al-6.0%Zn-2.6%Mg alloy, Acta Metall. 24 (9) (1976) 817–825, https://doi.org/10.1016/0001-6160(76)90048-1.
[4] P. Schwellinger, Investigation of the mechanisms of ductile intergranular fracture in Al-Mg-Si alloys with special reference to void formation, Z. Met. 71 (8) (1980) 520–524.
[5] A.K. Vasudévan, R.D. Doherty, Grain boundary ductile fracture in precipitation hardened aluminum alloys, Acta Metall. 35 (6) (1987) 1193–1219, https://doi.org/10.1016/0001-6160(87)90001-0.
[6] P.N.T. Unwin, G.W. Lorimer, R.B. Nicholson, The origin of the grain boundary precipitate free zone, Acta Metall. 17 (11) (1969) 1363–1377, https://doi.org/10.1016/0001-6160(69)90154-0.
[7] R.B. Nicholson, G. Thomas, J. Nutting, The interaction of dislocations and precipitates, Acta Metall. 8 (3) (1960) 172–176, https://doi.org/10.1016/0001-6160(60)90125-5.
[8] T.F. Morgeneyer, M.J. Starink, S.C. Wang, I. Sinclair, Quench sensitivity of toughness in an Al alloy: direct observation and analysis of failure initiation at the precipitate-free zone, Acta Mater. 56 (12) (2008) 2872–2884, https://doi.org/10.

1016/j.actamat.2008.02.021.
[9] E. Huskins, B. Cao, K. Ramesh, Strengthening mechanisms in an Al–Mg alloy, Mater. Sci. Eng. A 527 (6) (2010) 1292–1298, https://doi.org/10.1016/j.msea.2009.11.056.
[10] T. Pardoen, D. Dumont, A. Deschamps, Y. Brechet, Grain boundary versus transgranular ductile failure, J. Mech. Phys. Solids 51 (4) (2003) 637–665, https://doi.org/10.1016/S0022-5096(02)00102-3.
[11] T. Pardoen, T.J. Massart, Interface controlled plastic flow modelled by strain gradient plasticity theory, C.R. Mec. 340 (2012) 247–260, https://doi.org/10.1016/j.crme.2012.02.008.
[12] R.N. Gardner, T.C. Pollock, H.G.F. Wilsdorf, Crack initiation at dislocation cell boundaries in the ductile fracture of metals, Mater. Sci. Eng. 29 (2) (1977) 169–174, https://doi.org/10.1016/0025-5416(77)90123-9.
[13] H.G.F. Wilsdorf, The ductile fracture of metals: a microstructural viewpoint, Mater. Sci. Eng. 59 (1) (1983) 1–39, https://doi.org/10.1016/0025-5416(83)90085-X.
[14] P. Noell, J. Carroll, K. Hattar, B. Clark, B. Boyce, Do voids nucleate at grain boundaries during ductile rupture? Acta Mater. 137 (2017) 103–114, https://doi.org/10.1016/j.actamat.2017.07.004.
[15] M. Styczyńska, W. Łojkowski, Grain boundaries as dislocation sources in a material with precipitate-free zones, Scr. Metall. 19 (12) (1985) 1409–1413, https://doi.org/10.1016/0036-9748(85)90141-3.
[16] M. Jain, TEM study of microstructure development during low-cycle fatigue of an overaged Al-Mg-Si alloy, J. Mater. Sci. 27 (2) (1992) 399–407, https://doi.org/10.1007/BF00543929.
[17] C. Watanabe, R. Monzen, K. Tazaki, Effects of Al_3Sc particle size and precipitate-free zones on fatigue behavior and dislocation structure of an aged Al–Mg–Sc alloy, Int. J. Fatigue 30 (2008) 635–641, https://doi.org/10.1016/j.ijfatigue.2007.05.010.
[18] M. Khadyko, C.D. Marioara, I.G. Ringdalen, S. Dumoulin, O.S. Hopperstad, Deformation and strain localization in polycrystals with plastically heterogeneous grains, Int. J. Plast. 86 (2016) 128–150, https://doi.org/10.1016/j.ijplas.2016.08.005.
[19] E.F. Rauch, M. Véron, Automated crystal orientation and phase mapping in TEM, Mater. Charact. 98 (2014) 1–9, https://doi.org/10.1016/j.matchar.2014.08.010.
[20] R. Vincent, P.A. Midgley, Double conical beam-rocking system for measurement of integrated electron diffraction intensities, Ultramicroscopy 53 (3) (1994) 271–282, https://doi.org/10.1016/0304-3991(94)90039-6.
[21] J.S. Barnard, D.N. Johnstone, P.A. Midgley, High-resolution scanning precession electron diffraction: alignment and spatial resolution, Ultramicroscopy 174 (2017) 79–88, https://doi.org/10.1016/j.ultramic.2016.12.018.
[22] I. Kovaćs, J. Lendvai, E. Nagy, The mechanism of clustering in supersaturated solid solutions of A1-Mg_2Si alloys, Acta Metall. 20 (7) (1972) 975–983, https://doi.org/10.1016/0001-6160(72)90092-2.
[23] G.A. Edwards, K. Stiller, G.L. Dunlop, M.J. Couper, The precipitation sequence in Al–Mg–Si alloys, Acta Mater. 46 (11) (1998) 3893–3904, https://doi.org/10.1016/S1359-6454(98)00059-7.
[24] K. Matsuda, Y. Sakaguchi, Y. Miyata, Y. Uetani, T. Sato, A. Kamio, S. Ikeno, Precipitation sequence of various kinds of metastable phases in Al-1.0mass% Mg_2Si-0.4mass% Si alloy, J. Mater. Sci. 35 (1) (2000) 179–189, https://doi.org/10.1023/A:1004769305736.
[25] C.D. Marioara, S.J. Andersen, H.W. Zandbergen, R. Holmestad, The influence of alloy composition on precipitates of the Al-Mg-Si system, Metall. Mater. Trans. A 36 (13) (2005) 691–702, https://doi.org/10.1007/s11661-005-1001-7.
[26] S.J. Andersen, H.W. Zandbergen, J. Jansen, C. Træholt, U. Tundal, O. Reiso, The crystal structure of the β" phase in Al-Mg-Si alloys, Acta Mater. 46 (9) (1998) 3283–3298, https://doi.org/10.1016/S1359-6454(97)00493-X.
[27] S. Wenner, R. Holmestad, Accurately measured precipitate-matrix misfit in an Al-Mg-Si alloy by electron microscopy, Scr. Mater. 118 (2016) 5–8, https://doi.org/10.1016/j.scriptamat.2016.02.031.
[28] B.H. Frodal, K.O. Pedersen, T. Børvik, O.S. Hopperstad, Influence of pre-compression on the ductility of AA6xxx aluminium alloys, Int. J. Fract. 206 (2) (2017) 131–149, https://doi.org/10.1007/s10704-017-0204-4.
[29] S.J. Andersen, Quantification of the Mg_2Si β" and β' phases in AlMgSi alloys by transmission electron microscopy, Metall. Mater. Trans. A 26 (8) (1995) 1931–1937, https://doi.org/10.1007/BF02670664.
[30] F. Bachmann, R. Hielscher, H. Schaeben, Grain detection from 2d and 3d EBSD data–Specification of the MTEX algorithm, Ultramicroscopy 111 (12) (2011) 1720–1733, https://doi.org/10.1016/j.ultramic.2011.08.002.
[31] G. Lütjering, J. Albrecht, C. Sauer, T. Krull, The influence of soft, precipitate-free zones at grain boundaries in Ti and Al alloys on their fatigue and fracture behavior, Mater. Sci. Eng. A 468-470 (2007) 201–209, https://doi.org/10.1016/j.msea.2006.07.168.
[32] E.O. Hall, The deformation and ageing of mild steel: III discussion of results, Proc. Phys. Soc. Sect. B 64 (9) (1951) 747–753, https://doi.org/10.1088/0370-1301/64/9/303.
[33] R. Armstrong, I. Codd, R.M. Douthwaite, N.J. Petch, The plastic deformation of polycrystalline aggregates, Philos. Mag. 7 (73) (1962) 45–58, https://doi.org/10.1080/14786436208201857.
[34] A. Loucif, R.B. Figueiredo, T. Baudin, F. Brisset, R. Chemam, T.G. Langdon, Ultrafine grains and the Hall-Petch relationship in an Al–Mg–Si alloy processed by high-pressure torsion, Mater. Sci. Eng. A 532 (2012) 139–145, https://doi.org/10.1016/J.MSEA.2011.10.074.
[35] I. Polmear, Light Alloys, Butterworth-Heinemann, Oxford, 2005, p. 29, https://doi.org/10.1016/B978-075066371-7/50006-2.

Paper 2

Emil Christiansen, Calin Daniel Marioara, B. Holmedal
Odd Sture Hopperstad, Randi Holmestad

Nano-scale characterisation of sheared β” precipitates in a deformed aluminium alloy

Submitted to *Scientific Reports*.

Nano-scale characterisation of sheared β" precipitates in a deformed Al-Mg-Si alloy

Emil Christiansen[1,2,*], **Calin Daniel Marioara**[1,3], **Bjørn Holmedal**[1,4], **Odd Sture Hopperstad**[1,5], **and Randi Holmestad**[1,2]

[1]Centre for Advanced Structural Analysis (CASA), NTNU - Norwegian University of Science and Technology, Trondheim, N-7491, Norway

[2]Department of Physics, Faculty of Natural Sciences, NTNU, Trondheim, N-7491, Norway

[3]Materials and Nanotechnology, SINTEF Industry, Trondheim, N-7465, Norway

[4]Department of Materials Science and Engineering, Faculty of Natural Sciences, NTNU, Trondheim, N-7491, Norway

[5]Department of Structural Engineering, Faculty of Engineering, NTNU, Trondheim, N-7491, Norway

[*]emil.christiansen@ntnu.no

ABSTRACT

This paper compares the nano-scale structure of β" precipitates in a peak-aged Al-Mg-Si alloy before and after deformation. Three complementary advanced transmission electron microscopy techniques are used to reveal the structures and elucidate the interaction between dislocations and β" precipitates. We show that the needle-like and semi-coherent β" precipitates are sheared several times on different planes by dislocations during deformation, with no indications that they are bypassed or looped. Our results suggest that dislocations cut through precipitates and leave behind planar defects lying on planes inclined to $\langle 100 \rangle$ directions inside the precipitates. Single precipitates are sheared on more than one intersection, and we propose that the planar defects introduced by the shearing increase the local precipitate strength.

Introduction

Age-hardenable aluminium alloys, such as the Al-Mg-Si alloys, have a high strength to weight ratio and offer valuable alternatives to e.g. steels in a number of industrial applications. However, the mechanical

properties of these alloys can be challenging to predict, as they depend on numerous parameters. Therefore, numerical models are valuable tools for both alloy development and product design in for example metallurgical, automotive, and aerospace industries[1–4]. In this respect, knowledge and understanding of the underlying physical processes responsible for the mechanical properties are essential. One of the most important physical processes is the interaction between gliding dislocations and nanoscale metastable precipitates in the material, as this interaction has a large impact on strength, work hardening, and fracture[5,6]. Because the dislocation-precipitate interactions occur on the nanoscale and at very short time intervals, they are not easily accessible for direct study, but can be indirectly studied by comparing the atomic structure of precipitates before and after deformation.

Precipitates in age-hardenable aluminium alloys are formed toward the end of the heat-treatment process and serve as obstacles to moving dislocations. They usually start out as small and coherent phases embedded in the aluminium matrix early in the ageing procedure. With increasing ageing time, they grow and change both in structure, composition, and shape. To predict the strength and work hardening of age-hardenable aluminium alloys, it is necessary to know both the phase, size, shape, and number density of precipitates as well as the individual dislocation-precipitate interactions for the various precipitate phases. There are two main types of precipitate-dislocation interactions: bypassing and shearing. Whether a particular precipitate is bypassed or sheared depends on the phase, size, and shape of the precipitate.

Dislocations bypass non-shearable precipitates during deformation by looping mechanisms, which result in various dislocation structures around the precipitate[7]. For example, the Orowan mechanism leaves precipitates encircled by dislocation loops that increase the dislocation density and contribute to the initial work hardening of the material.

When shearable precipitates are cut by dislocations, steps will form on the precipitate-matrix interface and various defects inside the precipitate structure can form[8]. The shearing mechanism is directly linked to the structure of the precipitate, and different precipitate phases will behave differently during deformation. For instance, Deschamps *et. al.*[9] observed that both of the lath-like δ' and T_1 precipitates in an Al-Cu-Li alloy were shearable, but the T_1 precipitates were sheared in single steps only. Slip was localised in the δ' strengthened alloy, but not in the T_1 strengthened alloy. Hence, even though precipitates in both cases were shearable, the mechanism for shearing was different and this affected the mechanical properties. In

other words, complex shearing mechanisms must be understood for each precipitate phase present in an alloy.

The precipitates in peak-aged Al-Mg-Si alloys are usually of the β" phase, which is semi-coherent with the matrix and appear as needles oriented along $\langle 001 \rangle_{\mathrm{Al}}$[10,11]. *In situ* investigations performed on an Al-Mg-Si-Cu alloy, containing both needle-like β" precipitates and lath-like L precipitates, suggest that both shearing and bypassing of precipitates occur at room temperature, and that increasing temperature facilitates cross-slip and bypassing[12,13]. However, whether the lath-like or needle-like precipitates are sheared was not determined. Donnadieu *et. al.*[14] measured the strain fields around the precipitates and performed simulations of the dislocation-precipitate interactions. Their results suggest that the lath-like precipitates were sheared, and the rod-like precipitates were looped. However, the *in situ* study by Misumi *et. al*[15] shows that β" precipitates are shearable, indicating that the strain field simulations by Donnadieu *et. al.* might have some shortcomings. Ryen *et. al.*[16] showed that after large deformations, the needle-axis of β" precipitates changed, indicating that they were uniformly sheared by dislocations. Furthermore, Poole *et. al.*[17] showed indirectly that β" precipitates are sheared as well, through slip-line and work hardening investigations. Hence, there is strong evidence that β" precipitates are shearable. However, despite these studies, the internal structure of β" precipitates after deformation is still unknown. Studies of the internal structure of precipitates in plastically deformed materials could provide detailed information on the interaction between dislocations and precipitates that would be useful for models of strength, work hardening and fracture of these industrially important alloys.

The atomic structure of β" precipitates is characterised by stackings of a specific basic unit usually referred to as a β" "eye"[18]. The most common arrangement of eyes produces a monoclinic unit cell (space group C2/m) with $a = 1.516$ nm, $b = 0.405$ nm, $c = 0.674$ nm, and $\beta = 105.3°$, and composition $Mg_5Si_4Al_2$, but less common stacking variations produce other unit cells[10,18,19]. The orientation relationship between the unit cell of the most common β" and the matrix is $(001)_{\mathrm{Al}} \parallel (010)_{\beta"}$, $[\bar{3}10]_{\mathrm{Al}} \parallel [001]_{\beta"}$, and $[230]_{\mathrm{Al}} \parallel [100]_{\beta"}$[10,19].

Shearing of β" precipitates by dislocations is a complex problem. Because the internal structure of this phase is not compatible with the matrix, the slip systems of the two phases do not match. Hence, β" eyes cannot be shifted by a matrix Burgers vector and remain well-ordered with respect to unit cells

above and below the shearing plane. There are therefore two options. Either the atoms in the shearing plane must reorganise and form a planar defect (referred to as incompatible shearing), or the eyes must shift by a compatible shift (referred to as compatible shearing). The planar defect in the former case disrupts the crystal structure of the precipitate close to the shearing plane, while the precipitate shearing and matrix deformation in the latter case will be incompatible. This incompatibility, in turn, must be accommodated by elastic strain fields in the matrix or defects at the interface between the precipitate and the matrix. The main difference between the compatible and incompatible shearing processes is that the latter disrupts the internal structure of the precipitate, while the former disrupts the surroundings of the precipitate instead. Based on investigations of the structure after shearing, it is thus possible to say which process has occurred, and possibly what plane the precipitate was sheared on. This will be important information, especially when considering multiple shearing events and the evolution of the precipitate strength during deformation.

Ardell[8] describes five different strengthening contributions for shearable precipitates: *chemical strengthening* due to steps on the precipitate-matrix interface; *stacking fault strengthening* due to difference in stacking fault energies in the two phases; *modulus hardening* due to difference in elastic modulus of the two phases; *coherency strengthening* from the strain field surrounding the precipitates; and *order strengthening* due to formation of anti-phase boundaries on the shear plane within the precipitate. In the case of β" precipitates, it seems reasonable that the local order strengthening contribution in the shearing plane will be the one most affected by shearing if β" precipitates deform by incompatible shearing. Conversely, if β" precipitates deform by compatible shearing instead, coherency and elastic modulus strengthening will likely be the ones most affected. Hence, determining if planar defects form in β" precipitates after deformation will provide valuable information regarding the strength evolution of these precipitates during deformation. In addition, because dislocations in Al-Mg-Si alloys may cross-slip and change their glide plane to $\{001\}_{\mathrm{Al}}$ at room temperature[20], it will also be important to determine which planes the possible planar defects lie on. With this in mind, there are two important questions that should be addressed: on which planes are β" precipitates sheared by dislocations, and will this shearing of the precipitates introduce interfacial or planar defects?

To address these questions, we have studied a lean Al-Mg-Si alloy (Mg + Si less than 1 at.%) in peak

hardness condition by several advanced transmission electron microscopy (TEM) techniques before and after plastic deformation in compression to 5%, 10%, and 20% engineering strain. Firstly, precipitates with their longitudinal axis aligned with the electron beam (i.e. oriented out-of-plane) have been studied in high-resolution TEM (HRTEM) and high-angle annular dark field (HAADF) scanning TEM (STEM). Secondly, precipitates with their longitudinal axis aligned perpendicular to the electron beam (i.e. oriented in-plane) were investigated by scanning precession electron diffraction (SPED) and non-negative matrix factorisation (NMF) machine learning[21–24]. These advanced techniques depend on complex electron interactions within the material and are succinctly described in the following.

HRTEM is a technique where the projected crystal structure is imaged through complex electron interference processes[25]. The resulting exit wave will be thickness dependent and advanced techniques are needed to directly infer the projected electrostatic potential[26]. Nevertheless, the interference between electrons will depend on the crystal periodicity, as this reflects the periodicity of the electrostatic potential in the specimen. Hence, HRTEM images will exhibit the same periodicity as that of the projected crystal lattice even for a relatively thick crystal. In the present work, HRTEM is used to study the periodicity of the projected crystal structure of precipitates and especially how the periodicity change after deformation. If precipitates contain planar defects (incompatible shearing), the projected lattice should become blurred. If the shearing is compatible with the precipitate structure, the projected crystal lattice should be preserved after deformation.

In atomically resolved HAADF STEM, a small and converged electron probe is scanned across a specimen oriented in a zone axis, and a Z-contrast image is formed by collecting electrons scattered to high angles[27,28]. The electron beam channels along the atomic columns and scatters to high angles with a probability that increases with the mass of the scattering atoms. Hence, intensities in each pixel in the resulting image scale with the average Z-number. HAADF STEM images are formed "sequentially" as the beam propagates through the specimen, and this leads to challenges when interpreting images of thick specimens, especially if there are structural variations along the beam direction. For thick specimens, the channelling process can become quite complex and prevent direct quantitative interpretation of the image[28]. Still, HAADF STEM is most sensitive to the structure of the specimen close to the entrance surface and less sensitive to the structure close to the exit surface. Defects close to the entrance surface

will therefore influence the images more than defects close to the exit surface of the specimen. However, exactly how different defects and interfaces affect the channelling is difficult to predict without also performing STEM simulations. The main application of the HAADF STEM technique in the current paper is to verify the atomic structure of the precipitates after deformation. In addition, this technique will also provide valuable information for future modelling studies. As a final point, it should be mentioned that the scanning of the electron probe introduces noise that complicates the interpretation of the data. The noise can be reduced by acquiring stacks of several short-exposure images of the same area and then applying various rigid and non-rigid image registration algorithms to the data. *Smart Align* is a tool for performing such registrations, and all STEM images shown in this work have been smart-aligned[29]. However, conventional STEM images have also been acquired and used to validate the smart-aligned images.

SPED is another scanning diffraction technique, but in this case, the electron beam is precessed about the optical axis to average out dynamical diffraction effects, although some of these effects will still be present[22,24]. Unlike HAADF STEM, where all the electrons scattered to higher angles are collected for each pixel, SPED collects a complete 2D precession electron diffraction pattern for each scan pixel. The resulting dataset therefore has four dimensions: two spatial dimensions (x, y, image), and two reciprocal space dimensions (k_x, k_y, diffraction pattern) that contain crystallographic information. The dataset can be reduced by post-processing by creating virtual images. These images are 2D spatial maps of the intensity of certain regions in the diffraction patterns. In the case of a virtual bright field (VBF) image, the intensity within a region containing the direct beam is integrated for each diffraction pattern, and assigned to corresponding scan pixels. A VBF image is therefore comparable to a conventional TEM bright field image, but with reduced dynamical effects. Intensities within annular regions can be chosen to create virtual annular dark field (VADF) images. These virtual images provide a compact way of visualising the spatial variation of certain diffraction conditions, without the complexity introduced by dynamical effects as in conventional TEM imaging.

An alternative to creating virtual images is to apply machine learning algorithms. In this work, the NMF algorithm is used to learn the individual parts that make up different diffraction patterns[21]. NMF factorises each SPED dataset into a set of factors or basis images. These factors are statistical representations of

contributions to the different diffraction patterns, and the corresponding loading maps are arrays that determine how these representations are mixed. NMF is therefore able to extract signals that are very weak in individual diffraction patterns, but are statistically significant in the dataset. In this work, NMF factors corresponding to in-plane precipitates have been manually identified, and their loading maps are used to highlight in-plane precipitates in VBF images. In addition, VADF images sensitive to precipitate cross-section scattering are also formed in order to separate these cross-sections from other features in both the VBF images and the NMF loading maps. This is necessary because the NMF is not completely capable of separating the relatively sparse scattering of in-plane needles from the dense scattering of precipitate cross-sections. Hence, while the HRTEM and HAADF STEM techniques provide information about the precipitate structures in cross-section, SPED can be used to investigate the precipitate structure along the length of the needle-shaped precipitate.

Results

Initial study

An initial conventional TEM bright field study established the need for more advanced characterisation techniques. As Fig. 1 shows, the bright field contrast in deformed alloys is dominated by dislocations, making it nearly impossible to study the precipitates. Nevertheless, it is clear that the strain fields around precipitates, seen as dark regions along the needle lengths in Figure 1a, seem to be suppressed or to disappear completely in deformed specimens. This suppression can either be due to a cancellation between the strain fields of precipitates and dislocations or because the coherency of the precipitates is lost. The latter indicates the presence of interfacial defects or internal changes inside the precipitate structure. In some cases, small disturbances in contrast (see Fig. 1b) or slight bends (see Fig. 1d) can be discerned as well.

Study of precipitate cross-sections

Figure 2 presents HRTEM images of precipitate cross-sections reflecting the variation in sharpness of the precipitate projected crystal lattice in each condition. Precipitates in the undeformed state usually produce HRTEM images where the crystal lattice of the β” precipitate is visible, but a few precipitates

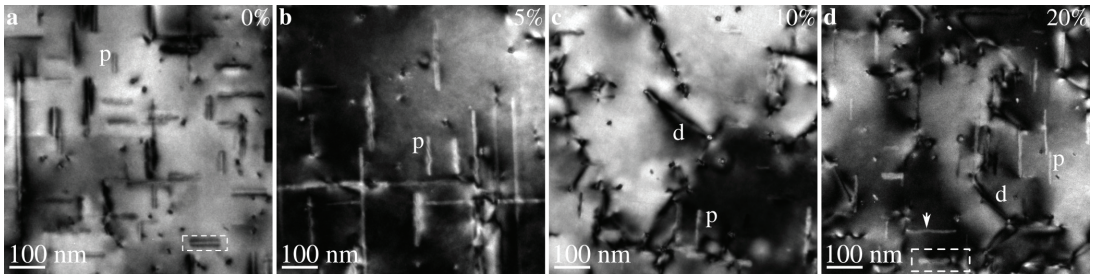

Figure 1. TEM $[001]_{Al}$ zone axis bright field images of the alloy in (**a**) the undeformed condition and after (**b**) 5%, (**c**) 10%, and (**d**) 20% compressive engineering strain. Some precipitates labelled "p" have been marked, as well as dislocations "d" in some cases. The arrow in (**d**) shows a bend in one of the precipitates. Imaged areas are approximately the same as those studied using SPED. The precipitates in (**a**) and (**d**) marked by dashed boxes are studied in greater detail in Figure 5.

appear blurred or with reduced resolution or contrast. This variation is natural, as some precipitates do not pass through the entire thin foil and overlap with the matrix, destroying the coherency of the exit wave. With increasing deformation, precipitate cross-sections appear more and more blurred. This indicates that the projected crystal lattice of precipitates after deformation is disturbed. After 20% compression, all precipitate cross-sections appear blurred. In addition, the blurring is not uniform, and the periodicity of the crystal lattice of the β" precipitate along one $\langle 110 \rangle_{Al}$ is usually preserved. This is most clearly seen by the inset power spectrum in Fig. 2h. Hence, deformation appears to smear out the projected crystal lattice of the precipitates, except in one particular direction. It should be mentioned that the projected crystal lattice of precipitates in the compressed specimens is often too severely blurred to identify the crystal structure, and some of the imaged precipitates may not be β" precipitates but have other structures. However, most of the imaged precipitates should be β" precipitates, as this is the predominant phase in the bulk microstructure as confirmed by the HRTEM images in the undeformed condition. The blurring gives precipitate cross-sections in the deformed specimens a more roundish shape and slightly increased cross-sectional area. Measurements indicate that the mean cross-sectional areas of precipitates are 19 nm^2 and 24 nm^2 in undeformed and 20% compressed specimens, respectively (see Supplementary Fig. S1 online for histograms).

Figure 3 presents filtered averages of smart-aligned[29] HAADF STEM image stacks of precipitate cross-sections in specimens from different compression levels. The atomic columns of precipitates are

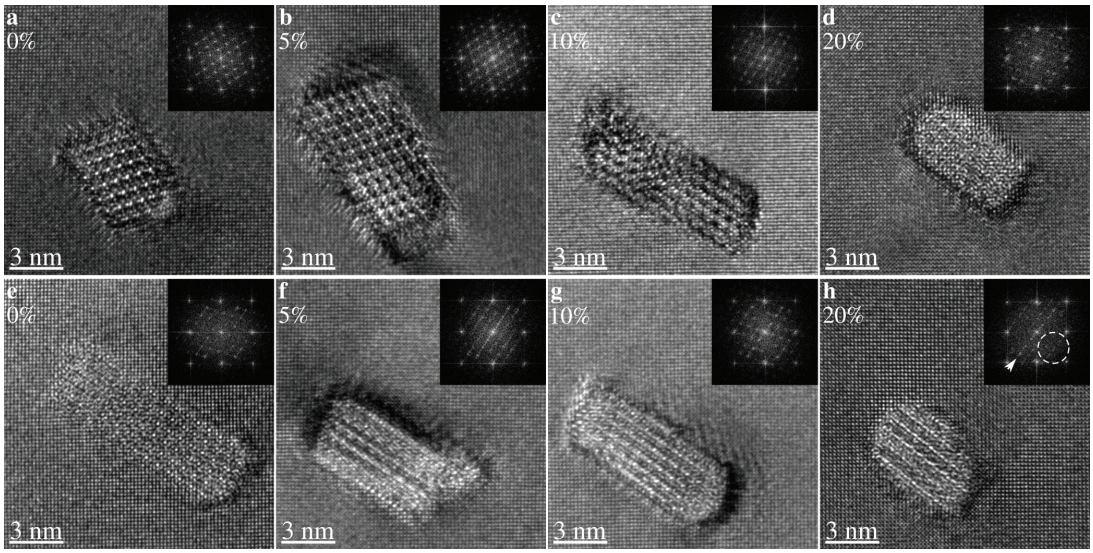

Figure 2. Representative $[001]_{Al}$ zone axis HRTEM images of precipitate cross-sections in undeformed condition (**a**,**e**), and after 5% (**b**,**f**), 10% (**c**,**g**), and 20% (**d**,**h**) compressive engineering strain. The global compression axis lies in-plane. Power spectra of fast Fourier transforms of each image are inset in top-right corners. The top row (**a**-**d**) is representative of precipitates with the sharpest outline and sharpest lattice, while the bottom row (**e**-**h**) is representative of precipitates with the most blurred lattices. In (**h**), the missing precipitate frequencies are marked in the fast Fourier transform spectrum by a dashed circle, and the remaining frequencies are marked by an arrow.

resolved in both undeformed and deformed specimens, and the β" eyes can be easily identified. This means that the precipitates do not change their overall structure after deformation. However, precipitates in deformed specimens usually exhibit blurred regions close to some of its edges where the β" eyes cannot be identified. The appearance of these regions varies from precipitate to precipitate, and also with the focus of the electron probe.

Study of the longitudinal precipitate structure

Figure 4 presents results from SPED experiments on specimens in undeformed and 20% compressed conditions. Precipitates in 5% and 10% compressed specimens show results similar to the 20% compressed specimens, and have been omitted for brevity (see the Supplementary Fig. S2, S3, S4, and S5 online for more detailed presentation of individual NMF factors and loadings for undeformed, 5%, 10%, and 20% compressed conditions, respectively). VBF and VADF images of the two conditions are shown, along with

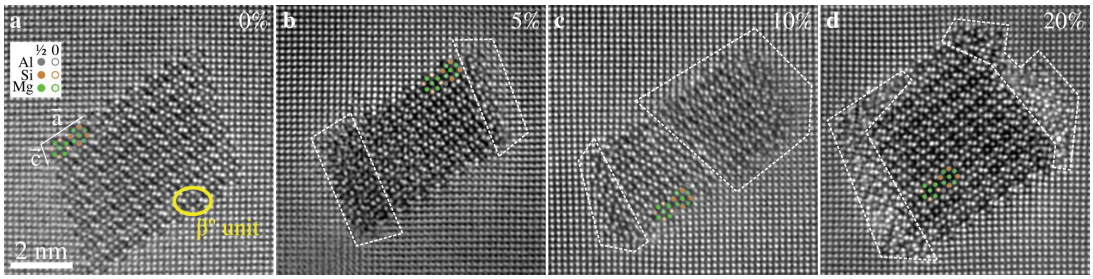

Figure 3. Smart-aligned and filtered $[001]_{Al}$ zone axis HAADF STEM images of precipitates in (**a**) undeformed, and after (**b**) 5%, (**c**) 10%, and (**d**) 20% compressive engineering strain. An overlay of the β" precipitate structure is also included, based on Wenner *et al.*[30]. The relative position of the overlaid atoms in the out-of-plane direction is indicated by full and empty circles, referring to $1/2 \cdot b_{\beta"}$ and $0 \cdot b_{\beta"}$, respectively. A β" unit referred to as a β" "eye" is circled in yellow in (**a**). Precipitates in deformed specimens typically have regions (dashed) with reduced contrast/resolution along some of the edges.

selected precession electron diffraction patterns and NMF results. There are two distinct orientations for each set of in-plane needle axis orientations. Green pixels show precipitates with their longitudinal axis aligned vertically ($[010]_{\beta"} \parallel [010]_{Al}$), while red pixels show precipitates aligned horizontally ($[010]_{\beta"} \parallel [100]_{Al}$). NMF separates both variants for each orientation of the longitudinal axis. In undeformed specimens, the SPED results are as expected. Precipitates are surrounded by strain fields and appear straight with an even distribution of NMF loading intensity. The selected precession electron diffraction pattern of a precipitate cross-section shows that out-of-plane needles are in a $[010]_{\beta"}$ zone axis (compare with the fast Fourier transform spectra insets in Fig. 2). After 20% compression, however, the precipitates scatter differently. Firstly, no strain field contrast is observed around in-plane precipitates. Secondly, the selected precession electron diffraction pattern indicates that scattering from precipitate cross-sections is suppressed, especially for some of the small scattering angles. Finally, the NMF loading intensities vary along the needles. This is clear from the loading maps, where the colouring appears segmented and irregular. Sometimes, this segmentation appears like a series of spots, and the VADF images must be used to establish whether a spot is due to a cross-section, or is indeed due to an in-plane needle.

Figure 5 shows a close-up comparison between a needle in undeformed and in 20% compressed condition. The needles have the same orientation and therefore their most significant NMF loading is also similar. While the needle in the undeformed specimen shows a clear strain field in VBF, the needle in the 20% compressed specimen does not. Instead, this needle shows a dark contrast at one end, which is

due to a dislocation that is pinned by the precipitate, as seen in Figures 1d and 4g. The NMF loading intensities of the two needles are also different, being relatively constant in the undeformed specimen, whereas it varies along the needle in the 20% compressed specimen. There are three plateaus visible in the NMF loading profile of the needle in the deformed specimen, and these correspond to three regions with different intensity in the loading map. This indicates that the different parts of the same precipitate scatter electrons differently. The interfaces between these parts are also important. They are slanted with respect to the longitudinal direction of the needle and of significant width. The width of these interface regions indicates that the interface plane is inclined to the electron beam which travels along $[001]_{\mathrm{Al}}$. Hence, the interface between the different regions cannot be any of the $\{001\}_{\mathrm{Al}}$ planes. Instead, the $\left(1\bar{1}1\right)_{\mathrm{Al}}$ plane is more likely, as this will both have a trace along $[110]_{\mathrm{Al}}$ in the $(001)_{\mathrm{Al}}$ plane, and be inclined to the electron beam. Because this is one of the primary glide planes for dislocations in the matrix, it is likely that the regions visible in the NMF loading maps are related to shearing of the precipitate by dislocations gliding on these planes.

Finally, it should be mentioned that the variation of in-plane needle NMF loadings only means that the different regions scatter in different ways. Thus, the actual scattering may vary within the dark segments as well, as the NMF loadings only show that the scattering in these regions is different compared to the bright regions. This means that different parts of dark regions may, in principle, also scatter differently from each other. The intensity of the reflections in the precession electron diffraction patterns corresponding to in-plane needles is often too weak to be seen in the raw data, and it is therefore not possible to say anything about the actual differences between the dark and bright regions in the NMF loadings. It might therefore be that the total scattering in the dark regions is weaker, or that the dark regions scatter to other angles.

Discussion

The HRTEM results show that the internal precipitate structure is affected by deformation. Because HAADF STEM images show that the precipitate interiors have the expected β" structure, the blurry HRTEM images cannot be due to an overall structural change. This suggests that when β" precipitates are sheared, the internal structure must change locally. Such local changes must be planar defects. Furthermore,

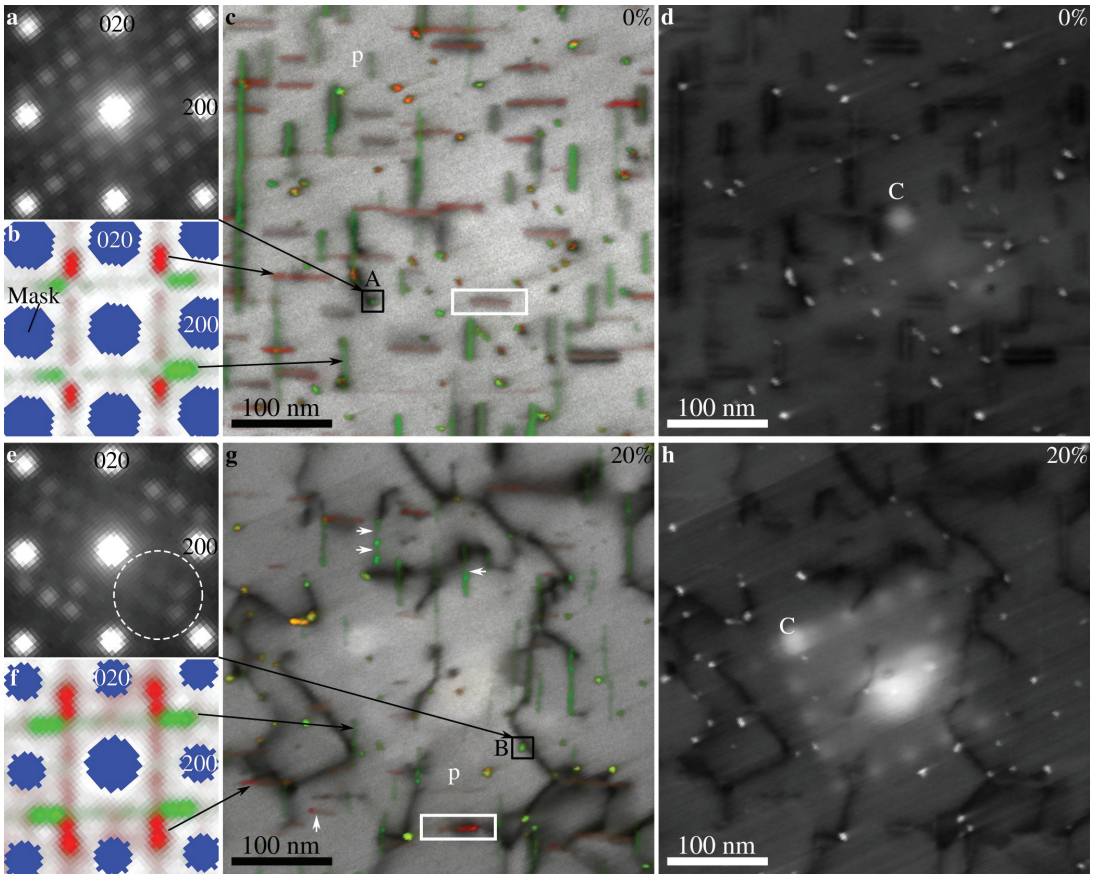

Figure 4. $[001]_{Al}$ zone axis SPED results from undeformed (**a**-**d**) and 20% compressed (**e**-**h**) specimens. Single-pixel precession electron diffraction patterns of precipitate cross-sections marked "A" and "B" are shown in (**a**) and (**e**), normalised NMF factors from in-plane precipitates are shown in (**b**) and (**f**), VBF with overlaid normalised NMF loadings are shown in (**c**) and (**g**), while precipitate cross-section sensitive VADF images are shown in (**d**) and (**h**). NMF loadings also highlight some precipitate cross-sections and the VADF images should be used to separate precipitate segments and cross-sections. Green pixels in the factors and loadings are due to precipitates with $[010]_{\beta''} \parallel [010]_{Al}$ (vertical orientations), while red pixels are due to precipitates with $[010]_{\beta''} \parallel [100]_{Al}$ (horizontal orientations). Precipitates in the deformed specimen appear segmented, some are marked by white arrows. Blue areas in the NMF factors correspond to reflections from the aluminium matrix that were masked out during the decomposition. The dashed circle in (**e**) marks weak precipitate reflections. The framed precipitates in (**c**) and (**g**) are studied in greater detail in Fig. 5. "C" marks amorphous contamination features formed during SPED alignment and preliminary SPED scans.

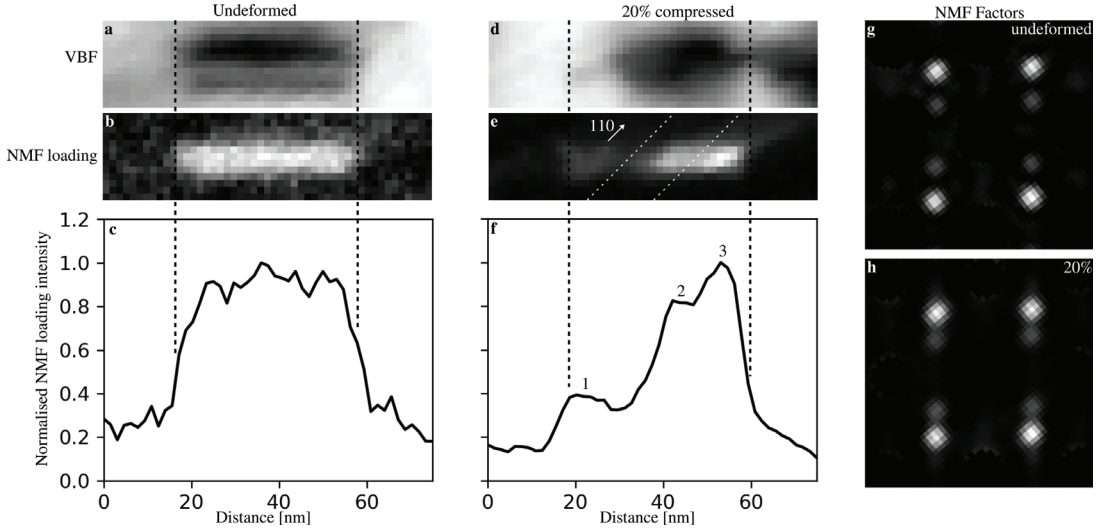

Figure 5. Close-up comparison between in-plane needles (marked by boxes in Figures 1 and 4) in SPED scans of undeformed (**a**-**c** and **g**) and 20% compressed specimens (**d**-**f** and **h**). VBF images are shown in (**a**) and (**d**), while NMF loadings corresponding to the factors shown in (**g**) and (**h**) are shown in (**b**) and (**e**). Vertical sums (profiles) of the NMF loadings are shown in (**c**) and (**f**). Three plateaus are identified in the profile of the needle in the 20% compressed specimen, labelled 1, 2, and 3. The interfaces between the regions in (**e**) that correspond to these plateaus are shown as dashed lines and are approximately along $[110]_{\mathrm{Al}}$. The NMF factors of the loadings are shown in (**g**) and (**h**).

this means that the shearing is incompatible with the precipitate structure, i.e. that the precipitates are sheared by matrix Burgers vectors. In addition, the shearing introduces steps at the precipitate-matrix interface, which increase the projected cross-sectional area of the precipitates and further blur the edges of precipitates in HRTEM. Whether the shearing is achieved by a gliding dislocation through the precipitate or by a collective shift of the precipitate structure is not known however.

Figure 6 summarises our interpretations of the results. This figure illustrates that the steps and planar defects induced by the shearing may overlap when projected along the needle longitudinal axis. When a sheared precipitate is observed along the needle lengths using HRTEM or HAADF STEM, the images will contain regions that are a mix of β" and matrix structures (from the steps) and disrupted structures (from the planar defects). The figure also shows schematically how the defects overlap when projected perpendicularly to the needle longitudinal direction, as is the case in SPED (see Figure 4 and 5). The NMF results from SPED show that in-plane needles have small regions that scatter as expected, and other regions that scatter differently. Our hypothesis is that the planar defects disrupt scattering enough to make the loadings of the NMF factors of the in-plane needles considerably weaker. This is based on the fact that the atomic disruptions introduced by a planar defect likely will affect one or two β" eyes above and below it, and that this region makes out a significant part of the precipitate as the beam travels through its transverse direction. In addition, the signal from in-plane needles is originally very weak in undeformed specimens, and any reduction in this signal will influence the NMF loadings. Hence, wherever the beam intersects one of these planar defects, the resulting precession electron diffraction pattern will contain less intensity in corresponding diffraction spots. The width of the interface between the NMF loading plateaus in the needle in Fig. 5 indicates that the planar defects are observed at an angle, and that they must lie on any other plane than $\{001\}_{\mathrm{Al}}$. This is consistent with shearing on $\{111\}_{\mathrm{Al}}$ matrix glide planes, and we therefore propose that shearing of β" precipitates does not require cross-slip to e.g. the $\{001\}_{\mathrm{Al}}$ planes. In addition, due to the interfaces and the large and continuous dark regions (the plateaus in Figure 5), we suggest that several closely spaced planar defects overlap when needles are observed along $\langle 100\rangle_{\mathrm{Al}}$ and perpendicular to their longitudinal axis, as illustrated in Fig. 6. Repeated shearing events in the same plane seem unlikely, as this would lead to relatively narrow dark regions in the NMF loading maps and bigger steps on the needle interfaces. However, this has not been possible to confirm

directly. If this interpretation is correct, it will mean that the loss of precipitate strength due to a reduction in cross-sectional area in the shearing plane is compensated by a local increase in e.g. order hardening in this plane. This local hardening would then cause dislocations gliding in the same plane to e.g. cross-slip to nearby planes before shearing the precipitate and introduce new planar defects. As more and more planes become sheared, dislocations must cross-slip further and further in order to find an undisturbed part of the precipitate to shear through. This is in agreement with observations made by Poole *et al.*[17] on an Al-Mg-Si-Cu alloy and similar to processes proposed for the Al-Cu-Li alloy studied by Deschamps *et al.*[9].

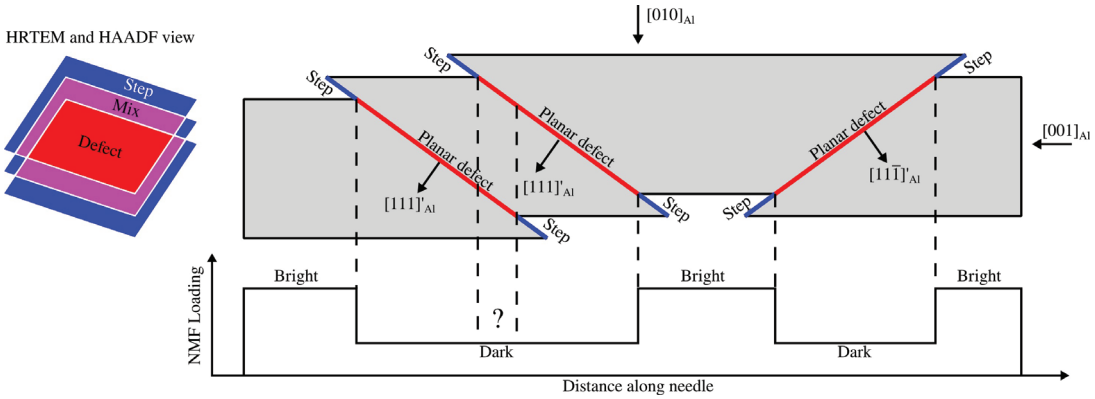

Figure 6. Schematic illustration of a $[100]_{Al}$ section of a sheared β" precipitate and how deformation induced defects will appear in HRTEM, HAADF STEM and SPED. The precipitates are sheared on $\{111\}_{Al}$ planes (marked by the projection of their $\langle 111\rangle'_{Al}$ plane normals), and the shearing planes become planar defects because these are not slip planes in the β" phase. Each shearing event also creates steps on the precipitate-matrix interface. Traces of the planar defects and steps are shown in red and blue, respectively. The cross-sectional view to the left is a projection of the needle along $[001]_{Al}$, and shows the defects and steps in projection, with overlap between planar defects and steps shown as magenta regions. The SPED NMF loading intensity variation of in-plane needles is shown schematically as well and is explained as the projection of the planar defects along $[010]_{Al}$. Whether the projection of the steps influence scattering is not known.

HAADF STEM shows that the atomic structure of the precipitate interiors is unchanged by deformation. How the blurred regions observed in the HAADF STEM results fit together with the planar defects and steps revealed by HRTEM and SPED is challenging to explain. First of all, a sheared precipitate should contain three different regions when observed along its longitudinal axis; an interface step on one side where the beam first travels through the matrix and then through the precipitate, an internal region where the beam travels across the planar defect, and finally a second interface step on the other side where the

beam first travels through the precipitate and then through the matrix. These three regions are observed in the HAADF STEM images in Fig. 3, where an internal well-resolved region lies between two blurry edges and are schematically illustrated in Figure 6. It therefore seems likely that the blurry regions in the STEM images are due to the steps, and the well-resolved region corresponds to the area with overlapping β" structures and a planar defect somewhere in the thickness direction. However, this raises the question: why does the internal structure of sheared precipitates appear blurry in HRTEM, but well-resolved in STEM? If the atomic columns of the precipitate are well-aligned above and below the shearing plane, the STEM images should show well-resolved β" eyes. However, this would mean that the precipitates are sheared in a manner compatible with their structure. This is at odds with both the SPED and the HRTEM results, however, and therefore does not offer a satisfactory explanation. Hence, it is more likely that the difference between the HRTEM and HAADF STEM results originates from the image forming mechanisms. A possible explanation in this regard is that only parts of the precipitate contribute to the STEM image, as STEM is most sensitive to the specimen closest to the entrance surface. However, if this was the case, the steps should not be blurry either. The fact that the steps remain blurry and detectable indicates that the shearing plane lies close enough to the entrance surface to contribute significantly to the image. The contrast in the STEM images therefore cannot be explained solely by the sequential nature of the STEM image forming mechanisms. Another explanation is that the beam channelling conditions might be very different in the different regions. However, to address this issue, detailed STEM image simulations coupled with accurate structural models of sheared precipitates are necessary, but out of scope of the current study.

Our results support observations and experiments done by Poole *et al.*[17] and Ryen *et al.*[16]. Poole *et al.* observed macroscopically that β" precipitates must be sheared, but could not observe this directly. This is not surprising, given the detailed study required for such observations. Meanwhile, the rotations of the precipitates longitudinal axis observed by Ryen *et al.* can be explained by several shearing events of the needles in a preferred direction. In addition, the planar defects observed in the present work provide information of the shearing process on the sub-nanometre level, which may be used to refine simulations that previously only accounted for the precipitates elastic strain fields[14]. However, some important details are still missing, but further studies based on atomistic simulations of sheared structures coupled with

TEM image simulations may provide more detailed insight in the future.

Conclusion

We conclude that β" precipitates in peak hardness Al-Mg-Si alloys are sheared several times by matrix dislocations gliding on $\{111\}_{\mathrm{Al}}$. This introduces planar defects within the precipitates, as the shear is not compatible with the precipitate structure. The planar defects are not anti-phase boundaries, but their exact atomic structure is unknown. They are inclined to $\langle 001\rangle_{\mathrm{Al}}$ directions and appear to be closely spaced, but not co-planar, suggesting that dislocations avoid shearing a precipitate in the same plane. These conclusions are important for further development of models of strength, work hardening, and fracture of alloys containing these precipitates.

Methods and Materials

Material

The AA6060 aluminium alloy used in this study has been investigated in several other studies, and the reader is referred to these previous works for details, while a short summary is presented here[31–33]. The alloy contained 0.422 wt% Si and 0.468 wt% Mg, and was extruded as a 10 mm thick profile measuring 83 mm in width. Cylindrical compression specimens (13 mm in length and 9 mm in diameter) were machined with their longitudinal direction along the transverse direction (TD) of the profile. These compression specimens were then solution heat-treated at 540 °C for 15 min before being quenched in water. They were subsequently naturally aged for 15 min at room temperature, and finally artificially aged to peak hardness at 185 °C for 5 hours. After heat-treatment, the average precipitate length, cross-section, number density, and volume fraction measured by TEM were $\bar{l} = 40 \pm 1$ nm, $\bar{\sigma} = 19.1 \pm 0.8$ nm^2, $\bar{\rho} = 5556 \pm 629$ #/μm^3, and $\bar{V_f} = 0.42 \pm 0.05\%$, respectively[33]. All of the observed precipitates were consistent with the β" phase, except for relatively few inhomogeneously nucleated precipitates that were of an over-aged character. The material has an equiaxed grain structure with a strong cube texture and minor Goss components[31,32].

Compression tests

Three heat-treated compression specimens were subjected to uniaxial compression at a strain rate of 2×10^{-4} s^{-1} in a universal testing machine to a final engineering strain of 5%, 10% and 20%, respectively. *Dow Corning Molykote G-n Metal Assembly Paste* was used to reduce the friction at the contact surfaces between the specimen and the platens, resulting in barrelling less than 6%.

Thin foil preparation

TEM thin foils were made by sectioning the compression specimens along the extrusion plane so that the global compression axis lies in the thin foil plane. Sections close to the specimen centres were mechanically polished down to ≈ 300 μm before standard 3 mm disks were punched out. The disks were further polished down to ≈ 100 μm before they were electropolished with a standard electrolyte (a mixture of $1/3$ HNO_3 and $2/3$ CH_3OH) in a *Struers TenuPol 5* twin-jet electropolisher. The electrolyte was kept at -25 ± 5 °C, and a voltage of 20 V was applied. The thin foils were plasma cleaned in a *Fischinone 1020 Plasma Cleaner* for 5 min before the TEM investigations. It should be noted that the preparation of TEM thin foils and the investigation itself were conducted three years after the completion of the compression tests. In the meantime, the specimens were stored at room temperature.

Microscopy

A *JEOL JEM2100F* operating at 200 kV was used to perform HRTEM and SPED. A *Gatan 2k UltraScan CCD* was used for the HRTEM studies. More than 50 precipitates for each condition were imaged in HRTEM, and representative images reflecting this variation were chosen for this paper. SPED was done by the *NanoMEGAS DigiSTAR* system, with a precession angle of 1° and precession frequency of 100 Hz[22,24]. The nominal probe size was 1 nm, and a step size of 1.52 nm was used to scan the specimen. Typical scan sizes were 400×400 pixels (608×608 nm2). An external *Allied StingRay* CCD camera binned to 144×144 pixels with 8-bit depth was used to acquire images of the phosphorous screen (showing the precession electron diffraction patterns) with an exposure time of 40 ms. The exposure time and typical scan size resulted in acquisition times of approximately two hours.

A double-corrected cold-FEG *JEOL ARM200F* operating at 200 kV was used to perform HAADF STEM imaging of precipitate cross-sections to complement the HRTEM studies. The images were acquired

using the *Smart Align* plugin to *Gatan Digital Micrograph*, and both rigid and non-rigid registration were used to produce aligned stacks of images formed with a collection angle of 48 – 206 mrad[29]. HAADF images presented in this work are averages through these aligned stacks. The scans were conducted with a pixel dwell time of 2 µs and with pixel sizes < 8 pm. Typically, 10 or 12 frames were acquired for each image stack. Conventional HAADF STEM images of each area were also acquired to validate the smart aligned images.

Analysis

ImageJ was used to measure the cross-sectional area of precipitates from HRTEM images. Only precipitates in undeformed and 20% compressed specimens were measured. There are significant uncertainties and error sources connected to these measurements, the largest being difficulties in determining the edges of precipitate cross-sections in deformed specimens. The relative error in cross-sectional area measurements for precipitates in the deformed state is estimated to be approximately 10%. Only precipitates in a single grain were measured. The average cross-sectional area measured in undeformed alloys matches perfectly that of a previous study, which suggests that the variation in precipitation in different grains is limited in this material[33].

HAADF STEM images were filtered in Fourier space by applying a mask with radius 8.38 1/nm $\approx 1.2 \cdot d_{220}$, where d_{220} is the reciprocal spacing of the aluminium $(220)_{\mathrm{Al}}$ planes. The edge of the mask had a Gaussian shape with a half-width of 10% of the mask radius. Intensities of all TEM, HRTEM, HAADF STEM, and virtual SPED images in this paper have been limited to the 0.01 and 0.99 percentiles of the data to enhance contrast.

The open-source Python packages *HyperSpy* and *PyXem* were used to create VBF and VADF images of the SPED data[34,35]. These virtual images were made by assigning pixel intensities based on the integrated intensity within certain regions of the corresponding precession electron diffraction patterns. For VBF images, this region was $0 – 4.91 \cdot 10^{-4}$ mrad (slightly larger than the size of the direct beam), while for VADF images, intensities within the virtual annulus of $4.83 \cdot 10^{-4} – 1.29 \cdot 10^{-2}$ mrad (from the edge of the direct beam and up to the edge of the $\{002\}_{\mathrm{Al}}$ reflections) were used.

The same python packages were used to perform unsupervised NMF machine learning of the SPED

data[21]. In the current work, the NMF algorithm was used to separate the data into 100 linearly independent factors and corresponding loadings. The factors and loadings corresponding to in-plane needles are of special interest and were extracted from the NMF results by manual examination. This was done by comparing the factors to simulated kinematic selected area electron diffraction patterns of in-plane needles of the β" phase, and by considering the corresponding loadings. Electrons propagating perpendicularly to the needle longitudinal directions may scatter from planes with a relatively large excitation error because of the thin needle dimensions. Hence, needles of different phases can scatter quite similarly when observed edge-on. Therefore, several different phases contribute to the in-plane needle NMF factors and loadings. Similarly, these factors will also contain some signals that overlap with the signal from precipitate cross-sections, and the loading maps will therefore also show precipitate cross-sections. VADF images can be used to identify the cross-sections, and the NMF loading maps should be considered in parallel with these.

Distortions in SPED

Because the acquisition time of SPED scans can be quite long (∼hours), specimen drift will distort the scans and cause a square scan grid to become non-square on the specimen. This distortion is important to have in mind when considering the SPED results, as it affects angles between objects in virtual images. Specimen drift is unavoidable but can vary in severity. Therefore, conventional TEM images have been used to validate the SPED scans and to make sure that the scan distortions are not too severe. In principle, the SPED scans can be made to fit the TEM images using affine transformations, but such processing has not been done in the current work. In addition, the precession electron diffraction pattern is formed on a tilted screen, and the external camera is also tilted relative to the screen. Hence, the resulting precession electron diffraction patterns are also distorted. However, this distortion is of little consequence to the present study, as the interest is in relative orientations and qualitative considerations.

Data availability

The datasets generated during and/or analysed during the current study are available in the Zenodo repository, https://doi.10.5281/zenodo.2652906[36]. This repository contains many more TEM, HRTEM, and STEM images than shown here, in addition to the smart-align image stacks.

References

1. Deschamps, A. & Brechet, Y. Influence of predeformation and ageing of an Al–Zn–Mg alloy—II. Modeling of precipitation kinetics and yield stress. *Acta Materialia* **47**, 293–305, DOI: 10.1016/S1359-6454(98)00296-1 (1998).

2. Esmaeili, S., Wang, X., Lloyd, D. J. & Poole, W. J. On the precipitation-hardening behavior of the Al-Mg-Si-Cu alloy AA6111. *Metall. Mater. Transactions A: Phys. Metall. Mater. Sci.* **34**, 751–763, DOI: 10.1007/s11661-003-1003-2 (2003).

3. Song, M. Modeling the hardness and yield strength evolutions of aluminum alloy with rod/needle-shaped precipitates. *Mater. Sci. Eng. A* **443**, 172–177, DOI: 10.1016/j.msea.2006.08.025 (2007).

4. Granum, H., Myhr, O. R., Børvik, T. & Hopperstad, O. S. Nanostructure-based finite element analyses of aluminium profiles subjected to quasi-static axial crushing. *Thin-Walled Struct.* **131**, 769–781, DOI: 10.1016/J.TWS.2018.07.034 (2018).

5. Nicholson, R. B., Thomas, G. & Nutting, J. The interaction of dislocations and precipitates. *Acta Metall.* **8**, 172–176 (1960).

6. Blankenship Jr., C. P., Hornbogen, E. & Starke Jr., E. A. Predicting slip behavior in alloys containing shearable and strong particles. *Mater. Sci. Eng. A* **169**, 33–41, DOI: 10.1016/0921-5093(93)90596-7 (1993).

7. Stewart, A. T. & Martin, J. W. Dislocation-particle interactions in plastically deformed two-phase aluminium crystals. *Acta Metall.* **23**, 1–7, DOI: 10.1016/0001-6160(75)90062-0 (1975).

8. Ardell, A. J. Precipitation hardening. *Metall. Transactions A* **16**, 2131–2165, DOI: 10.1007/BF02670416 (1985).

9. Deschamps, A., Decreus, B., De Geuser, F., Dorin, T. & Weyland, M. The influence of precipitation on plastic deformation of Al–Cu–Li alloys. *Acta Materialia* **61**, 4010–4021, DOI: 10.1016/J.ACTAMAT.2013.03.015 (2013).

10. Andersen, S. J. *et al.* The crystal structure of the β” phase in Al–Mg–Si alloys. *Acta Materialia* **46**, 3283–3298, DOI: 10.1016/S1359-6454(97)00493-X (1998).

11. Matsuda, K. *et al.* Precipitation sequence of various kinds of metastable phases in Al-1.0mass% Mg2Si-0.4mass% Si alloy. *J. Mater. Sci.* **35**, 179–189, DOI: 10.1023/A:1004769305736 (2000).

12. Vivas, M. *et al.* Determination of precipitate strength in aluminium alloy 6056-T6 from transmission electron microscopy in situ straining data. *Philos. Mag. A: Phys. Condens. Matter, Struct. Defects Mech. Prop.* **76**, 921–931, DOI: 10.1080/01418619708200007 (1997).

13. Delmas, F. *et al.* Straining mechanisms in aluminium alloy 6056. In-situ investigation by transmission electron microscopy. *Mater. Sci. Eng. A* **340**, 286–291, DOI: 10.1016/S0921-5093(02)00184-3 (2003).

14. Donnadieu, P., Dirras, G. F. & Douin, J. *An approach of precipitate/dislocation interaction in age-hardened Al-Mg-Si alloys: Measurement of the strain field around precipitates and related simulation of the dislocation propagation*, vol. 396-402 (Trans Tech Publications, 2002).

15. Misumi, K. *et al.* Three-dimensional characterization of interaction between β" precipitate and dislocation in Al–Mg–Si alloy. *J. Alloy. Compd.* **600**, 29–33, DOI: 10.1016/J.JALLCOM.2014.02.059 (2014).

16. Ryen, Ø., Holmedal, B., Marthinsen, K. & Furu, T. Precipitation, strength and work hardening of age hardened aluminium alloys. In *IOP Conf. Ser.: Mater. Sci. Eng.*, vol. 89, DOI: 10.1088/1757-899X/89/1/012013 (2015).

17. Poole, W. J., Wang, X., Lloyd, D. J. & Embury, J. D. The shearable-non-shearable transition in Al-Mg-Si-Cu precipitation hardening alloys: Implications on the distribution of slip, work hardening and fracture. *Philos. Mag.* **85**, 3113–3135, DOI: 10.1080/14786430500154935 (2005).

18. Saito, T. *et al.* Atomic Structures of Precipitates in Al-Mg-Si Alloys with Small Additions of Other Elements. *Adv. Eng. Mater.* **20**, 1800125, DOI: 10.1002/adem.201800125 (2018).

19. Edwards, G. A., Dunlop, G. L. & Couper, M. J. Fine-scale precipitation in Al Alloy 6061. In *The 4th international conference on aluminum alloys*, 620–627 (Georgia Institute of Technology, Atlanta, Georgia, 1994).

20. Delmas, F. *et al.* Cross-slip and glide in {001} planes of Al-Mg-Si alloy 6056. *Philos. Mag. Lett.* **83**, 289–296, DOI: 10.1080/095008303100 (2003).

21. Lee, D. D. & Seung, H. S. Learning the parts of objects by non-negative matrix factorization. *Nature* **401**, 788–791, DOI: 10.1038/44565 (1999).

22. Vincent, R. & Midgley, P. A. Double conical beam-rocking system for measurement of integrated electron diffraction intensities. *Ultramicroscopy* **53**, 271–282, DOI: 10.1016/0304-3991(94)90039-6 (1994).

23. Eggeman, A. S., Krakow, R. & Midgley, P. A. Scanning precession electron tomography for three-dimensional nanoscale orientation imaging and crystallographic analysis. *Nat. Commun.* **6**, 7267, DOI: 10.1038/ncomms8267 (2015).

24. Barnard, J. S., Johnstone, D. N. & Midgley, P. A. High-resolution scanning precession electron diffraction: Alignment and spatial resolution. *Ultramicroscopy* **174**, 79–88, DOI: 10.1016/j.ultramic.2016.12.018 (2017).

25. Cowley, J. M. & Moodie, A. F. The scattering of electrons by atoms and crystals. I. A new theoretical approach. *Acta Crystallogr.* **10**, 609–619, DOI: 10.1107/S0365110X57002194 (1957).

26. Xu, Q., Van Dyck, D. & Zandbergen, H. W. From thickness dependent exit waves to projected potential: Thickness derivative approach. *Ultramicroscopy* **110**, 535–542, DOI: 10.1016/J.ULTRAMIC.2009.10.008 (2010).

27. Pennycook, S. J. & Jesson, D. E. High-resolution Z-contrast imaging of crystals. *Ultramicroscopy* **37**, 14–38, DOI: 10.1016/0304-3991(91)90004-P (1991).

28. Klenov, D. O. & Stemmer, S. Contributions to the contrast in experimental high-angle annular dark-field images. *Ultramicroscopy* **106**, 889–901, DOI: 10.1016/j.ultramic.2006.03.007 (2006).

29. Jones, L. *et al.* Smart Align—a new tool for robust non-rigid registration of scanning microscope data. *Adv. Struct. Chem. Imaging* **1**, 8, DOI: 10.1186/s40679-015-0008-4 (2015).

30. Wenner, S., Jones, L., Marioara, C. D. & Holmestad, R. Atomic-resolution chemical mapping of ordered precipitates in Al alloys using energy-dispersive X-ray spectroscopy. *Micron* **96**, 103–111, DOI: 10.1016/J.MICRON.2017.02.007 (2017).

31. Khadyko, M., Marioara, C. D., Ringdalen, I. G., Dumoulin, S. & Hopperstad, O. S. Deformation and strain localization in polycrystals with plastically heterogeneous grains. *Int. J. Plast.* **86**, 128–150, DOI: 10.1016/j.ijplas.2016.08.005 (2016).

32. Frodal, B. H., Pedersen, K. O., Børvik, T. & Hopperstad, O. S. Influence of pre-compression on the ductility of AA6xxx aluminium alloys. *Int. J. Fract.* **206**, 131–149, DOI: 10.1007/s10704-017-0204-4 (2017).

33. Christiansen, E., Marioara, C. D., Marthinsen, K., Hopperstad, O. S. & Holmestad, R. Lattice rotations in precipitate free zones in an Al-Mg-Si alloy. *Mater. Charact.* **144**, 522–531, DOI: 10.1016/J.MATCHAR.2018.08.002 (2018).

34. Peña, F. d. l. *et al.* HyperSpy – 1.4.1, DOI: 10.5281/ZENODO.1469364 (2018).

35. Johnstone, D. N. *et al.* pyXem – 0.7.1, DOI: 10.5281/ZENODO.2650296 (2019).

36. Christiansen, E., Marioara, C. D., Holmedal, B., Hopperstad, O. S. & Holmestad, R. Data for "Nano-scale characterisation of sheared β" precipitates in a deformed Al-Mg-Si alloy". Zenodo, V1, DOI: 10.5281/zenodo.2652906 (2019).

Acknowledgements

The authors acknowledge the Centre for Advanced Structural Analysis (CASA), funded by the Research Council of Norway [grant number: 237885] and its industrial partners. In addition, the authors acknowledge the TEM Gemini Centre at NTNU and the NORTEM infrastructure, also funded by the Research Council of Norway [grant number: 197405].

Author contributions statement

E.C, C.D.M, O.S.H, and R.H conceived the experiments, E.C and C.D.M conducted the HRTEM and HAADF STEM experiments, E.C. conducted the SPED experiments and analysed all results. All authors

reviewed the manuscript.

Additional information

Competing interests: The authors declare no competing interests.

Paper 3

Emil Christiansen, Inga Gudem Ringdalen, Ruben Bjørge,
Calin Daniel Marioara, Randi Holmestad

Multislice image simulations of sheared needle-like precipitates in an Al-Mg-Si alloy

Presented at EMAG, Manchester, UK 2019, and to be submitted for publication in *Journal of Microscopy*, EMAG and MMC special issue.

MANUSCRIPT DRAFT
EMAG Special Issue

Multislice image simulations of sheared needle-like precipitates in an Al-Mg-Si alloy

Emil Christiansen[1,2] | **Inga Gudem Ringdalen**[3] | **Ruben Bjørge**[3] | **Calin Daniel Marioara**[1,3] | **Randi Holmestad**[1,2]

[1]Centre For Advanced Structural Analysis (CASA)

[2]NTNU – Norwegian University of Science and Technology

[3]Materials and Nanotechnology, SINTEF Industry

Correspondence
Emil Christiansen, Department of Physics, NTNU – Norwegian University of Science and Technology, Trondheim, Trøndelag, 7194, Norway
Email: emil.christiansen@ntnu.no

Present address
Department of Physics, NTNU – Norwegian University of Science and Technology, Trondheim, Trøndelag, 7194, Norway

Funding information
The Research council of Norway, Grant Numbers: 237885, 231762, 1974905, NN9158K.

Multislice transmission electron microscopy image simulations using the frozen phonon approximation are performed to investigate the image contrast of sheared needle-like β" precipitates in the Al-Mg-Si alloy system. Both high resolution and annular dark field scanning transmission electron microscopy images are simulated based on models of sheared precipitates. The shearing is represented as a rigid translation of the precipitate on matrix slip systems, and the influence of the distribution of translations on the resulting images is investigated. It is found that shearing events mus be spaced a few nano metres apart, and that several segments must overlap through the thickness, in order to reproduce the experimental results.

Keywords — Transmission Electron Microscopy, Multislice simulations, High resolution transmission electron microscopy, Scanning transmission electron microscopy, Aluminium Alloys, Deformation

Abbreviations: TEM, Transmission Electron Microscopy; HRTEM, High-Resolution TEM; STEM, Scanning TEM; BF, Bright Field; ADF, Annular Dark Field; HAADF, High-Angle ADF; MD, Molecular Dynamics.

Introduction

In a recent study, both high resolution TEM (HRTEM) and annular dark field (ADF) scanning TEM (STEM) techniques were applied to study the shearimg mechanism of β" precipitates in the age-hardenable Al-Mg-Si alloy system (Christiansen et al., 2019). The study concluded that these precipitates, which are coherent with the aluminium matrix and appear as needles ($\sim$ 40 nm long in the present case) along $\langle 100 \rangle$ aluminium directions, were sheared by dislocations and supports previous studies (Poole et al., 2005; Misumi et al., 2014). The β" precipitate crystal phase usually has a monoclinic unit cell (a = 15.16 Å, b = 4.05 Å, c = 0.674 Å, and β = 105.3°) with composition $Mg_5Si_4Al_2$, and the following orientation relationship to the matrix: $(001)_{Al} \parallel (010)_{b''}$, $[310]_{Al} \parallel [001]_{b''}$, and $\left[\bar{2}30\right]_{Al} \parallel [100]_{b''}$ (Edwards et al., 1998; Andersen et al., 1998; Saito et al., 2018). Because of this structure, the fcc slip systems of the matrix are not valid for the precipitate phase, and one of the goals of the study was to investigate whether the precipitates were sheared on the matrix slip systems, or by some other mechanism. While providing evidence that the precipitates are sheared on matrix slip systems, it was not possible to provide definite answers regarding the distribution of shearing events along their lengths. In addition, it was not determined how the shear induced steps on the precipitate-matrix interface affected the HRTEM and ADF STEM images of β" precipitates in deformed specimens. Figure 1 shows some experimental HRTEM and ADF STEM images. In specimens compressed by 20% engineering strain, the HRTEM images of precipitates observed edge-on in a [001] matrix zone axis become blurred. In FFT power spectra of these images, Fourier components along bands parallel to $\sim \langle 110 \rangle$ matrix directions are weakened. In ADF STEM images however, some precipitates are blurred, while others remain similar to precipitates in undeformed specimens. Additionally, many precipitates appear with some atomic resolution, but with dark shadow-like regions surrounding them on one end. While producing atomic resolution STEM images, the contrast in these images is disturbed compared to the undeformed case. Features such as blurred wavy lines, or dumbbell-like shapes similar to two merged β" units can be seen in some cases. Given the many possible variations in both shearing plane, direction and combination between several shearing events, interpretations of these experimental results are challenging. The thickness of the specimens was $\sim$ 60 nm, so that the HRTEM images can not be regarded as a direct projection of the crystal electrostatic potential (Xu et al., 2010), and the Z sensitivity of the STEM experiments is reduced (Hillyard and Silcox, 1993; Hillyard et al., 1993; Klenov and Stemmer, 2006; Martinez et al., 2018). At the same time, due to both the sequential image forming mechanisms of ADF STEM, and to the channelling of the convergent beam, the ADF STEM images are believed to depend greatly on the position(s) of the shearing plane(s). The present study applies multislice TEM image simulations of rigidly sheared precipitate models in order to better understand the experimental findings, and to elucidate more details regarding the shearing of β" precipitates. In particular, it is of interest to determine the number of shearing events required to produce the blurry HRTEM images, while at the same time preserving the ADF STEM image contrast. Another task is to investigate the role of how shearing events are distributed along the needles, and how different distributions of shearing events influence the final images.

Methods

The models used in the multislice simulations consist of rigidly displaced β" segments in a matrix of aluminium. To get an accurate model, the precipitate structure and size is set up using values for bulk β" calculated from density functional theory (Ninive et al., 2014). The surrounding aluminium matrix is relaxed, after shearing the precipitates, using molecular statics simulations with LAMMPS (Plimpton, 1995) and the Al-Mg potential by Liu and Adams (1998), while the precipitate is fixed. Precipitates are sheared n times on a given matrix slip system in different configurations. The shears are either distributed along the needle lengths, producing $n + 1$ segments, or they are localised within

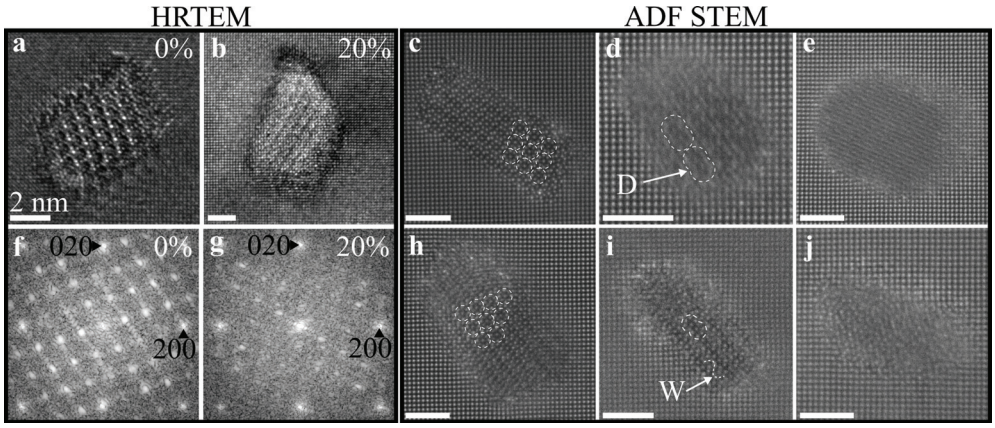

FIGURE 1 Experimental TEM images of β" precipitates, acquired in a [001] zone axis of aluminium. HRTEM images of precipitates in undeformed and after 20% global compression are shown in **a** and **b**, respectively. Corresponding FFT power spectra of Hann-windowed parts of the images (larger than shown here) are presented below their respective HRTEM image, in **f** and **g**, where Fourier components corresponding to (200) and (020) aluminium periodicities are indicated. ADF STEM images of precipitates in the deformed state are shown in the remaining sub-figures. In some STEM images (**c**, **h**), the β" unit can be distinguished (dashed circles) and the precipitates appear similar to the ones in the undeformed condition (not shown). In other images (**d**, **i**), a dumbbell-like shape (marked by "D") reminiscent of two β" units merged together can be seen, while wavy lines (marked "W") are also present in some cases. Additionally, some precipitates appear as a general blurry contrast (**e** and **j**). All scale bars are 2 nm. HRTEM images were acquired on a *JEOL 2100F* operating at 200 kV. STEM images were acquired using a double-corrected *JEOL ARM200-F* operating at 200 kV, a collection angle of 48.21 – 206.4 mrad and a convergence angle of 27.42 mrad. The STEM images presented here are averages of non-rigidly registered STEM stacks produced by SmartAlign (Jones et al., 2015).

either a single plane (producing two segments translated by $n\vec{b}$) or a narrow region (producing two large segments and several closely spaced smaller segments). Figure 2 shows one of the distributed shear models. In the case of HRTEM simulations, the complete model is imaged, while the STEM images are simulated for only a small part of the model in order to reduce calculation time.

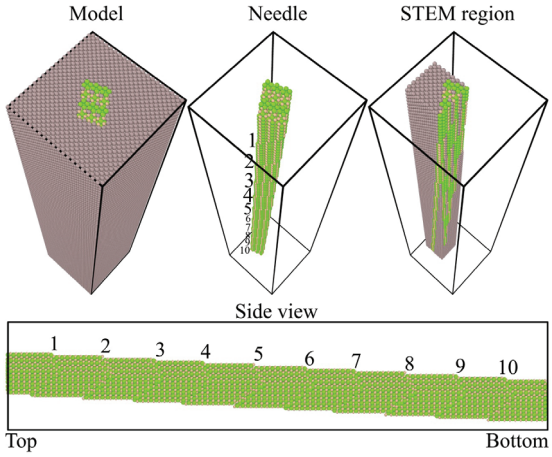

FIGURE 2 One of the models used in the study. The β" precipitate embedded in an aluminium matrix has been sheared n times on a certain slip system at regular intervals (in this case, $n = 10$ and the slip system is $\frac{a}{2}\left[\bar{1}01\right](111)$, but other slip systems are also used in the investigations). For STEM simulations, only a section containing half of the top precipitate cross-section is used, while the whole model is simulated in the HRTEM simulations. The open visualisation tool OVITO was used to visualise the models (Stukowski, 2010).

Multislice simulations were carried out using the MULTEM software by Lobato and Dyck (2015); Lobato et al. (2016), using scattering potentials from Lobato and Dyck (2014). Due to the nature of the problem, relatively large models are required, which calls for fast and efficient computing. Simulations were therefore performed on a cluster using *NVIDIA TESLA P-100* GPUs. An acceleration voltage of 200 kV, a STEM convergence angle of 27.42 mrad, and slice thickness of $\frac{a_{\mathrm{Al}}}{2} = 2.025$ Å was used. The model measured 81.0, 81.0, and 405.0 Å in the x, y, and z directions, respectively. The atomic potentials were resolved with a sampling size of 2048×2048 pixels in the x and y directions, resulting in a real space resolution of 0.012 Å and a maximum scattering angle of 214 mrad. A total of 20 random phonon configurations were averaged for both STEM and HRTEM simulations, using root-mean-square displacements of Al, Mg, and Si atom species of 0.1006 Å, 0.1533 Å, and 0.0793 Å, respectively. These values correspond to the Debye-Waller factors of crystals of the pure elements at 300 K (Peng et al., 1996). For STEM simulations, the probe was scanned using a step size of 0.162 Å. Because the STEM experiments were conducted on an aberration corrected microscope, a low spherical aberration coefficient of $C_3 = -0.3$ µm was used in the STEM image simulations. The HRTEM images, on the other hand, were acquired on an uncorrected microscope, and a relatively large spherical aberration coefficient of $C_3 = 40$ µm was used for HRTEM simulations. STEM images were formed from three angular intervals: 0.0–40.0 mrad, 48.21–206.4 mrad, and 100.0–206.4 mrad, representing bright field, ADF, and high-angle annular dark field images, respectively. The ADF angular interval is based on the collection angle used in the actual STEM experiments, and only results from this angular interval will be presented. The other collection angles used in the simulations were used for verification. In particular, the simulated ADF images appeared qualitatively similar to the simulated high-angle annular dark field images, indicating that the ADF collection interval produces images

with sufficiently incoherent contrast. The present study is limited to a qualitative comparison between experimental and simulated images, as quantitative comparisons are considered challenging due to the large number of possible permutations of shear configurations.

Results and Discussion

Figure 3 presents multislice image simulations of β" precipitate models after varying degree of total shear, when the shearing events are distributed along the needle lengths. In the ADF STEM simulation results, the β" unit corresponding to the initial precipitate segment becomes increasingly diffuse with increasing number of shearing events and decreasing segment thickness. The lower segments are not resolved by ADF STEM, instead these segments reduce the contrast of the final image and lead to a dark region adjacent to the position of the initial segment. After 5 shearing events, the β" unit of the initial segment can barely be distinguished. After 10 shearing events, the contrast from the initial segment vanishes, and the complete precipitate cross section appears like disturbed part of the matrix, with low contrast. It is therefore clear, that if the precipitates are sheared more than 5 times, they may not be resolved by ADF STEM, if these shearing events are distributed along the precipitate lengths. In the HRTEM simulations, dynamical scattering cause the Mg columns of the undeformed β" precipitate structure to become dark, while the Si and Al positions remain visible. With increasing shear, the precipitate outline becomes blurred, and the internal contrast becomes difficult to interpret. In the corresponding FFT power spectra however, the β" periodicities can still be seen. After 5 shearing events however, bands of β" spatial frequencies become slightly weaker, and after 10 shearing events the weakening in these bands is more prominent. The bands are oriented perpendicular to the projection of the shear direction in the image plane, and pass through the spatial frequency corresponding to the shear direction. By inspecting the HRTEM images as they evolve through the thickness (not shown) it is clear that the weakening of the HRTEM Fourier components appear after passing through only three segments, in both the 5 and 10 shearing cases. It is therefore clear that the spacing between the shearing events is the important factor, and not the total number of shearing events. As the weakening of Fourier components does not appear in the 3 shearing case, but does appear in the 5 shearing case, the maximum spacing between shearing events required to weaken the Fourier components is $\approx 18 - 10$ nm (the segment thickness in the 3 and 5 shearing cases, respectively). This means that a certain phase shift must be produced in the beam, and some degree of through-thickness overlap between β" precipitate segments and/or the matrix is required, in order to produce simulation results similar to the experimentally obtained images.

Because of the orientation relationship between the β" phase and the matrix, different matrix slip systems will produce different effects for a given precipitate orientation. Figure 4 presents multislice image simulations of β" precipitate models sheared 5 times distributed along their lengths, and the effect of different slip systems. Four slip systems are studied: $\left[\bar{1}\bar{1}0\right]/(001)$, $\left[1\bar{1}0\right]/(001)$, $\left[\bar{1}01\right]/(111)$, and $\left[1\bar{1}0\right]/(111)$, labelled "S1", "S2", "S3", and "S4", respectively. Slip systems S1 and S2 will require dislocations gliding on $\{001\}$ matrix planes rather than the close-packed $\{111\}$ planes. While these glide planes are less likely, they can occur at room temperature and will become increasingly common with increasing temperature (Delmas et al., 2003). Slip system S3 is the same as was studied in Figure 3. It is clear that different shear directions are more important than the shear plane, at least for the image forming mechanisms. The precipitate atoms in the current models are not relaxed after shearing, and will hence not reflect the actual physical interface between two neighbouring segments. Therefore, while the energy required to shear on $\{111\}$ and $\{001\}$ planes may be very different, the image simulations do not capture eventual perturbations these energies may introduce in atomic positions close to the interface planes. However, the shear directions are important, as these influence the alignment of atomic columns through the thickness. Shearing on the S1 system (i.e. almost parallel to $[001]_{\beta''}$) produces ADF STEM images where no β" units can be distinguished. However, as discussed

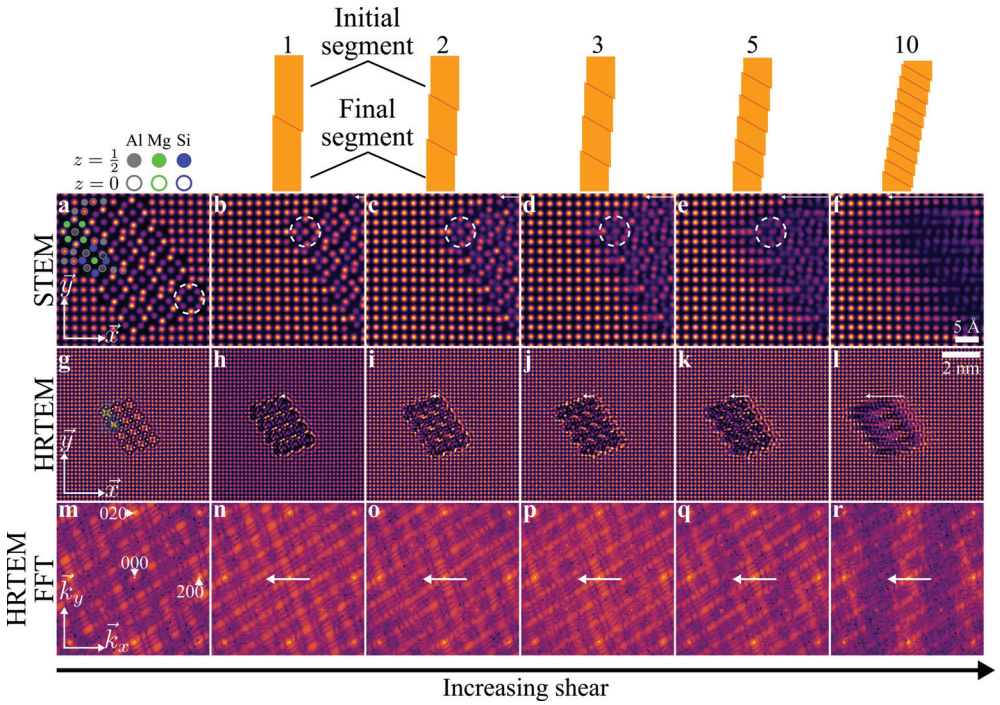

FIGURE 3 Multislice image simulation results of β" precipitates after different degree of total shear distributed along their lengths. The precipitate models have been sheared on the $\left[\bar{1}01\right]/(111)$ matrix slip systems in single steps of $\vec{b} = \frac{a_{\mathrm{Al}}}{2}\left[\bar{1}01\right]$ spaced evenly along the length of the needles by a total of 1 (**b**, **h**, **n**), 2 (**c**, **i**, **o**), 3 (**d**, **j**, **p**), 5 (**e**, **k**, **p**), and 10 (**f**, **l**, **r**) times. Simulation results of an unsheared β" precipitate is shown in **a**, **g**, and **m**. The top row (**a**–**f**) shows ADF STEM simulation results, the middle row (**g**–**l**) shows HRTEM simulation results, while the last row (**m**– **r**) shows FFT power spectra of the HRTEM results. Dashed circles in **a**–**e** indicate the β" unit. The general morphology of the precipitate model is indicated by schematic representations above each corresponding column. Total length of precipitate is 401 Å. Arrows indicate shear direction and magnitude (only direction is indicated for the FFT power spectra). Fourier components corresponding to (200) and (020) aluminium periodicities are indicated in **i**.

previously, the β" unit can barely be distinguished when the model is sheared on the S3 system. Shearing on the S2 and S4 systems (i.e. almost parallel to $[100]_{\beta''}$ on (001) and (111) planes) produces images where distinct dumbbell shapes are visible. These dumbbell shapes appear as two overlapping β" units, similar to the ones observed in experimental ADF STEM images (see Figure 1 **d** and **i**). In the HRTEM images, no clear distinction between the slip systems can be seen, except from the general morphology and shape changes of the precipitates. The FFT power spectra of the simulated HRTEM images still show the characteristic suppression of Fourier components, where the bands remain perpendicular to the shear directions. It is therefore clear that the blurring of HRTEM images depends mostly on the total shear, while the appearance of ADF STEM images depends on both the total shear and the shear direction.

In order to investigate the role of through-thickness overlap between the precipitate phase and the matrix, two other sets of models were prepared, labelled "B" and "C". The "B" models are sheared on a single plane 81 Å below the entrance surface, while the "C" models are sheared on parallel planes distributed within 95 – 142 Å. Figure 5 presents multislice image simulations of these models, where each model has been sheared a total of 10 times. For the "B" type models, it is clear that an initial segment of 81 Å contributes significantly to the final ADF STEM image, even if

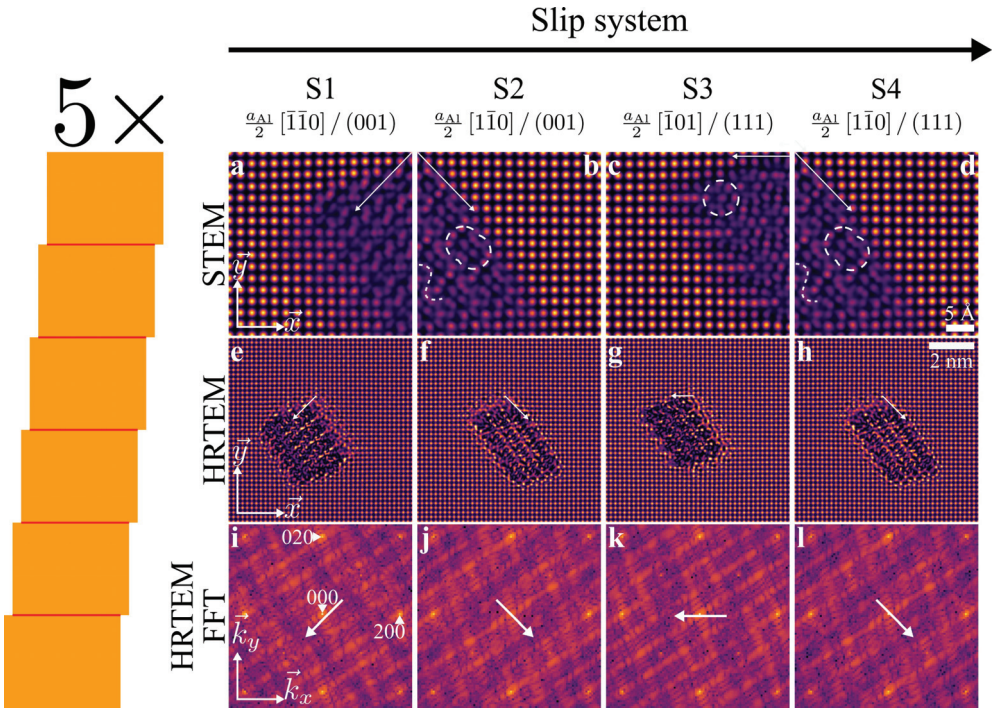

FIGURE 4 Multislice simulation results of β" precipitates after 5 rigid translations distributed through the thickness on different slip systems. Figures **a** – **d** show ADF images, figures **e**–**h** show HRTEM images, while **i**–**l** show FFT power spectra of corresponding HRTEM images. In the STEM simulations, the scanned region contains the complete precipitate cross-section in the "undeformed" case, while only half of the initial precipitate segment is simulated for the sheared precipitates. Dashed circles indicate the β" unit, and "dumbbell" and "wave" features in **b** and **d** are are also indicated. Total length of precipitate is 401 Å. Arrows indicate shear direction and magnitude (only direction is indicated for the FFT power spectra). Fourier components corresponding to (200) and (020) aluminium periodicities are indicated in **i**.

the beam travels through 320 Å of the matrix phase below it. The matrix below this initial segment contributes to the image by smearing most of the atomic columns. The central atomic columns in the β" units align more or less perfectly with the matrix columns below, and hence appear bright and sharp. The surrounding Mg and Si columns however, appear smeared because of their relative shift compared to the matrix columns below. For the lower segment, which lies below 81 Å of aluminium matrix, the precipitate atomic columns can not be distinguished, but reduce the contrast of some of the atomic columns while preserving the contrast of others. In the case where the precipitate is sheared on the S1 slip system, the upper and lower segments are shifted quite far away from each other. The region separating the two segments in the image plane appears dark in STEM. This is because the strain fields of the two segments shift the aluminium matrix atoms slightly differently above and below the shear plane. Hence, resolution and contrast is lost in this region. When the precipitate is sheared on the S2 slip system instead, the two segments barely touch at one end, and no matrix-region is separating them in the image plane. Instead, the strain field of the lower segment causes a disturbance of the aluminium matrix below the initial segment, and the contrast in this part of the STEM image is modified compared to when the precipitate was sheared on the S1 slip system. This modification appears as a wavy line along the shear direction. In the HRTEM images, not much difference between the two slip systems is

visible, and the FFT power spectra resemble those of unsheared precipitates. Distributing the shear across a narrow region does not change the images dramatically, as seen in the results from the "C" type models. The sheared region is not visible in any of the images, and its main effect is to change the relative thickness of the two segments. The initial segment has a thickness comparable to the "B" models, while the lowest segment is shorter than the lowest segment in the "B" models. Hence, only slight contrast perturbations is seen in the ADF STEM images where the beam has scanned across the lowest segment. Where the beam has scanned the initial segments instead, the contrast is similar to the "B" models, but the contrast is lower. This is because of the through-thickness overlap between the initial segment and the thin segments within the sheared region.

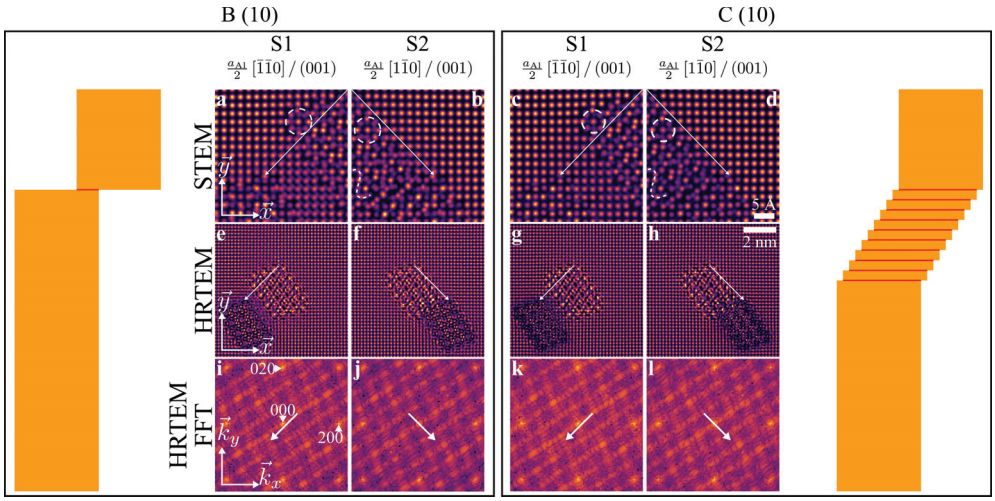

FIGURE 5 Multislice simulation results of β" precipitates after 10 rigid translations concentrated (left) or distributed within a narrow region (right). Figures **a** – **d** show ADF images, figures **e**–**h** show HRTEM images, while **i**–**l** show FFT power spectra of corresponding HRTEM images. Only a region containing half of the upper precipitate segment and most of the lowest segment is simulated. Dashed circles indicate the β" unit, and the dashed wavy lines in **b** and **d** indicate a modulated contrast induced by the overlap with the strained matrix below. Total length of precipitate is 401 Å. Arrows indicate shear direction and magnitude (only direction is indicated for the FFT power spectra). Fourier components corresponding to (200) and (020) aluminium periodicities are indicated in **i**.

The number of experimental HRTEM images showing a decrease in Fourier components along narrow bands was much higher in the deformed case than in the undeformed case, indicating that the decrease of these components are due to precipitate shearing. The simulated HRTEM images only show a similar decrease in Fourier components if the precipitate model is sheared with a spacing of $\sim$ 10 nm, or a frequency of $f \sim \frac{1}{10}$ nm^{-1}. This frequency corresponds to 5 times or more for precipitates of length $\sim$ 40 nm. The local frequency of shearing events can not be too high either, as the thin segments in the "C" models are incapable of weakening the Fourier components. Additionally, the segments must overlap through the thickness, indicating that they can not be shifted too much relative to each other. The multislice simulations therefore indicate that the β" precipitates must be sheared several times, and that these shearing events must be distributed along the precipitate lengths in some fashion. Of course, during deformation, precipitates may be sheared back and forth and on different slip systems. It is therefore not possible to say for certain that each shearing event introduces a single Burgers vector step at the precipitate-matrix interface. However, for a given strain, only a certain number of dislocations will have sheared a precipitate. If many dislocations localise in

planes, then the total number of segments is reduced and their spacing is increased (if the localised planes are randomly distributed along their lengths). Given a shearing event frequency f, and a number of dislocations involved in each shearing event N, the local strain will be $fN|\vec{b}|$. For $f \sim 10$ nm^{-1}, local strain will be large for relatively low values of N. For $N = 2$ and $N = 3$, the local strains will be $\gamma = 0.06$ and $\gamma = 0.09$, respectively. The local strain required to shear precipitates so that the FFT power spectra of their HRTEM images exhibit the characteristic band-like suppression of Fourier components will therefore be very high, if dislocations glide collectively on each glide plane. Distributing the dislocations along the precipitate length instead of localising them will cause precipitates to form HRTEM images with the band-like suppression of Fourier components at lower local strains. The experimental images presented in Figure 1 are from specimens compressed by an engineering strain of 0.2, but similar results were observed for specimens compressed by engineering strains of 0.1 and 0.05, although the more compressed specimens showed cleared signs of e.g. weaker HRTEM Fourier components. It is therefore plausible that dislocations shear precipitates in single steps, but it can not be said for certain. The ADF STEM simulation results (see **b** and **d** in both Figure 4 and Figure 5) also indicate that the first shearing event of precipitates where ADF reveals atomic resolution with "dumbbell" and "wave" features lies ~ 10 nm below the entrance surface. This agrees with the shear event frequency of $1/10$ nm necessary to produce HRTEM images that fit experimental results. Hence, both experimental HRTEM and ADF STEM images indicate that β” precipitates are sheared along their lengths with this frequency.

As a final note, the steps introduced by the shearing events are also of interest. It seems, from the "B" models, that the coherency between β” and the matrix enables precipitate atomic columns to be resolved by ADF STEM, even if they do not pass through the complete specimen thickness, as long as the initial segment thickness is above a threshold. The dark shadow-like regions surrounding the precipitates are due to several lower segments on one side of the precipitates. Hence, steps on one side of the precipitate will appear dark in ADF STEM (where the segments overlap through the thickness), while the steps on the other side will appear like a more blurred part of the precipitate cross-section (where the initial segment overlaps with the matrix below).

Conclusions

Simulated HRTEM and ADF STEM images match experimentally obtained images if the atomic models are sheared with a frequency $\approx 1/10$ nm^{-1}. If the shearing frequency is too high, the phase shift induced in each segment is not enough to be captured and will not lead to a blurring in the HRTEM images. Furthermore, a too high shear frequency will cause the first shearing events to lie too close to the entrance surface and render atomically resolved ADF STEM impossible. Conclusions regarding the magnitude of each shearing event is not possible based on the simulation results alone. However, given the shearing frequency, the local strain required to produce the observed images must be very large if several dislocations are involved with each shearing event. Hence, it is unlikely that many dislocations shear the precipitates on each shear plane. As a final note, shearing events on $\{001\}$ or $\{111\}$ planes cannot be distinguished by observing precipitates edge-on using HRTEM and ADF STEM.

Acknowledgements

The authors gratefully acknowledge the Research Council of Norway for funding through the SFI CASA project (grant number 237885), the NORTEM infrastructure project (grant number 197405), the research project Mind The Gap (grant number 231762), and the Sigma2 high performance computing clusters (grant numbers 269905/NN9158K). The IDUN cluster at NTNU HPC Group is also gratefully acknowledged for the use of computing capabilities.

Conflict of Interest

The authors declare no conflict of interest.

References

S. J. Andersen, H. W. Zandbergen, J. Jansen, C. Træholt, U. Tundal, and O. Reiso. The crystal structure of the β" phase in Al–Mg–Si alloys. *Acta Materialia*, 46(9):3283–3298, 1998. doi: 10.1016/S1359-6454(97)00493-X.

E. Christiansen, C. D. Marioara, B. Holmedal, O. S. Hopperstad, and R. Holmestad. Nano-scale characterisation of sheared β" precipitates in a deformed al-mg-si alloy. *To be published*, 2019.

F. Delmas, J. Majimel, M. Vivas, G. Molenat, A. Couret, and A. Coujou. Cross-slip and glide in {001} planes of Al-Mg-Si alloy 6056. *Philosophical Magazine Letters*, 83(5):289–296, 2003. doi: 10.1080/095008303100.

G. A. Edwards, K. Stiller, G. L. Dunlop, and M. J. Couper. The precipitation sequence in Al–Mg–Si alloys. *Acta Materialia*, 46 (11):3893–3904, 1998. doi: 10.1016/S1359-6454(98)00059-7.

S. Hillyard and J. Silcox. Thickness effects in ADF STEM zone axis images. *Ultramicroscopy*, 52(3–4):325–334, 1993. doi: 10.1016/0304-3991(93)90043-W.

S. Hillyard, R. F. Loane, and J. Silcox. Annular dark-field imaging: Resolution and thickness effects. *Ultramicroscopy*, 49(1–4): 14–25, 1993. doi: 10.1016/0304-3991(93)90209-G.

L. Jones, H. Yang, T. J. Pennycook, M. S. J. Marshall, S. Van Aert, N. D. Browning, M. R. Castell, and P. D. Nellist. Smart Align—a new tool for robust non-rigid registration of scanning microscope data. *Advanced Structural and Chemical Imaging*, 1(1):8, 2015. doi: 10.1186/s40679-015-0008-4.

D. O. Klenov and S. Stemmer. Contributions to the contrast in experimental high-angle annular dark-field images. *Ultramicroscopy*, 106(10):889–901, 2006. doi: 10.1016/j.ultramic.2006.03.007.

X.-Y. Liu and J.B. Adams. Grain-boundary segregation in Al–10%Mg alloys at hot working temperatures. *Acta Materialia*, 46 (10):3467–3476, 1998. doi: 10.1016/S1359-6454(98)00038-X.

I. Lobato and D. Van Dyck. An accurate parameterization for the scattering factors, electron densities and electrostatic potentials for neutral atoms that obey all physical constraints. *Acta Crystallographica Section A*, 70:636–649, 2014.

I. Lobato and D. Van Dyck. MULTEM: A new multislice program to perform accurate and fast electron diffraction and imaging simulations using Graphics Processing Units with CUDA. *Ultramicroscopy*, 156:9–17, 2015. doi: 10.1016/j.ultramic.2015.04.016.

I. Lobato, S. Van Aert, and J. Verbeeck. Progress and new advances in simulating electron microscopy datasets using multem. *Ultramicroscopy*, 168:17–27, 2016.

G. T. Martinez, K. H. W. van den Bos, M. Alania, P. D. Nellist, and S. Van Aert. Thickness dependence of scattering cross-sections in quantitative scanning transmission electron microscopy. *Ultramicroscopy*, 187:84–92, 2018. doi: 10.1016/j.ultramic.2018.01.005.

K. Misumi, K. Kaneko, T. Nishiyama, T. Maeda, K. Yamada, K. Ikeda, M. Kikuchi, K. Takata, M. Saga, and K. Ushioda. Three-dimensional characterization of interaction between β" precipitate and dislocation in Al–Mg–Si alloy. *Journal of Alloys and Compounds*, 600:29–33, 2014. doi: 10.1016/J.JALLCOM.2014.02.059.

P. H. Ninive, A. Strandlie, S. Gulbrandsen-Dahl, W. Lefebvre, C. D. Marioara, S. J. Andersen, J. Friis, R. Holmestad, and O. M. Løvvik. Detailed atomistic insight into the β" phase in Al–Mg–Si alloys. *Acta Materialia*, 69:126–134, 2014. doi: 10.1016/j.actamat.2014.01.052.

L.-M. Peng, G. Ren, S. L. Dudarev, and M. J. Whelan. Debye–Waller Factors and Absorptive Scattering Factors of Elemental Crystals. *Acta Crystallographica Section A*, 52(3):456–470, 1996. doi: 10.1107/S010876739600089X.

S. Plimpton. Fast Parallel Algorithms for Short-Range Molecular Dynamics. *Journal of Computational Physics*, 117(1):1–19, 1995. doi: 10.1006/JCPH.1995.1039.

W. J. Poole, X. Wang, D. J. Lloyd, and J. D. Embury. The shearable-non-shearable transition in Al-Mg-Si-Cu precipitation hardening alloys: Implications on the distribution of slip, work hardening and fracture. *Philosophical Magazine*, 85(26–27): 3113–3135, 2005. doi: 10.1080/14786430500154935.

T. Saito, E. A. Mørtsell, S. Wenner, C. D. Marioara, S. J. Andersen, J. Friis, K. Matsuda, and R. Holmestad. Atomic Structures of Precipitates in Al-Mg-Si Alloys with Small Additions of Other Elements. *Advanced Engineering Materials*, 20(7):1800125, 2018. doi: 10.1002/adem.201800125.

A. Stukowski. Visualization and analysis of atomistic simulation data with OVITO–the Open Visualization Tool. *Modelling and Simulation in Materials Science and Engineering*, 18(1):015012, 2010. doi: 10.1088/0965-0393/18/1/015012.

Q. Xu, D.. Van Dyck, and H. W. Zandbergen. From thickness dependent exit waves to projected potential: Thickness derivative approach. *Ultramicroscopy*, 110(5):535–542, 2010. doi: 10.1016/J.ULTRAMIC.2009.10.008.

Paper 4

Bjørn Håkon Frodal, Emil Christiansen, Ole Runar Myhr,
Odd Sture Hopperstad

The role of quench rate on the plastic flow and fracture of three aluminium alloys with different grain structure and texture

To be submitted for journal publication.

The role of quench rate on the plastic flow and fracture of three aluminium alloys with different grain structure and texture

Bjørn Håkon Frodal[a,b,*], Emil Christiansen[b,c], Ole Runar Myhr[a,b,d], Odd Sture Hopperstad[a,b]

[a] *Structural Impact Laboratory (SIMLab), Department of Structural Engineering, Norwegian University of Science and Technology (NTNU), NO-7491, Trondheim, Norway*
[b] *Centre for Advanced Structural Analysis (CASA), NTNU, NO-7491, Trondheim, Norway*
[c] *Department of Physics, Norwegian University of Science and Technology (NTNU), NO-7491, Trondheim, Norway*
[d] *Hydro Aluminium, Research and Technology Development (RTD), NO-6601 Sunndalsøra, Norway*

Abstract

The yielding, plastic flow and fracture of age hardenable aluminium alloys depend on the quench rate to room temperature after the solution heat-treatment at elevated temperature and before the artificial ageing. We investigate three AlMgSi alloys with different grain structure and crystallographic texture experimentally to determine the effects of quench rate (either water-quenching or air-cooling) on the precipitate microstructure and the mechanical properties, i.e., yield stress, work hardening and ductility. Tensile tests on smooth and V-notch specimens and Kahn tear tests are performed to study the influence of stress state on plastic flow and fracture. In addition, finite element simulations of the mechanical tests are performed for one of the alloys to investigate the validity of an extension of the Gurson model to high-exponent anisotropic plasticity. Transmission electron microscopy investigations show that the alloys and their precipitation microstructure are differently affected by the quench rate. Common for the three alloys is that the precipitate free zones around dispersoids and grain boundaries become larger, and the yield strength of the alloys becomes lower, after air-cooling than after water-quenching. Due to the lower yield strength and a higher work-hardening rate after air-cooling, the failure strain is increased for the smooth and V-notch tensile tests. The crack propagation energy, calculated from the Kahn tear tests, is markedly affected by the quench rate and the effect is different depending on the grain structure and plastic anisotropy, caused by the crystallographic texture. The anisotropic porous plasticity model used in the finite element simulations is able to precisely capture the fracture initiation in all the specimen geometries of the considered alloy, whereas the crack propagation energies of the Kahn tear tests are slightly overestimated.

Keywords: Quench sensitivity, Ductile fracture, Precipitate free zones, Finite element simulations, Anisotropic porous plasticity

1. Introduction

Age hardenable aluminium alloys are widely used, such as in car body panels, aeroplane fuselages, and in load-bearing components for structural applications. High strength and ductility are typically desired for practical applications, and aluminium alloys are attractive due to their high load-bearing capacity and low weight. In addition, properties such as good formability and corrosion resistance, combined with a great potential for recycling, make them appealing to, e.g., the automotive and offshore industry. The thermo-mechanical processing of age hardenable aluminium alloys influences microstructural characteristics such as the grain structure, crystallographic texture and precipitate structure. Thus, by changing the chemical composition, heat treatment and mechanical processing, one can control the yield stress, work hardening and

*Corresponding author
Email address: bjorn.h.frodal@ntnu.no (Bjørn Håkon Frodal)

plastic anisotropy of the alloy. While this flexibility is desired, it can also give rise to processing related issues such as quench sensitivity. The quench rate after homogenization or the solution heat-treatment can affect the age hardening capability of these alloys and slower cooling rates can lead to a lower strength [1]. Albeit high quench rates are favourable to attain preferred mechanical properties, it is not always achievable in practical applications, and in industry it is a common practice to limit the quench rate to prevent distortion [2].

Quench sensitivity is primarily caused by the precipitation of non-strengthening phases on dispersoids and at grain boundaries during cooling, and the number density of the dispersoids is known to increase quench sensitivity [1, 2, 3, 4, 5, 6, 7]. Thus, the age hardenable aluminium alloys experience a solute loss due to this precipitation, and the formation of the strengthening precipitates during the subsequent artificial ageing is reduced. High strength alloys tend to be more quench sensitive, as the alloying elements provide a greater driving force for nucleation of non-strengthening precipitates during quenching [3]. While the dispersoids contribute significantly to the quench sensitivity of the alloys, they are wanted due to their ability to delay and hinder recrystallization during the thermo-mechanical processing, which is beneficial for the mechanical properties of the alloy [8].

Whereas high strength alloys tend to be more quench sensitive, also lean alloys with few dispersoids have been observed to exhibit substantial quench sensitivity [2, 3, 9]. Here the quench sensitivity has been linked to the supersaturation of vacancies, as the high number of vacancies after fast quenching leads to a possible increased rate of precipitate formation during artificial ageing [4, 7, 10, 11, 12, 13]. This mechanism has also been found to affect quench sensitivity in alloys with a high content of dispersoids [4].

Due to vacancy and/or solute diffusion, precipitate free zones (PFZs) form around dispersoids and grain boundaries in age hardenable aluminium alloys [2, 4, 14]. Since the PFZs lack strengthening precipitates, these zones are softer than the rest of the grain, but are typically stronger than pure aluminium as the PFZs retain some solute in solid solution [14]. The PFZs located adjacent to grain boundaries are the location and probably the cause of intercrystalline fracture [15]. Plastic deformation will localize in these weaker zones and crack initiation and growth can occur more easily in the PFZs [16, 17, 18, 19]. Due to this localization of deformation, the PFZs can develop significant misorientations relative to their parent grains, which in turn could contribute to the strengthening of the PFZs [20] and thus delay fracture initiation.

In general, a competition between intercrystalline and transcrystalline fracture is observed in age hardenable aluminium alloys. It has been reported that the fracture mode may change from transcrystalline to intercrystalline fracture due to the precipitation of coarse phases on grain boundaries and the formation of PFZs, which decrease the fracture toughness of the alloy [17, 21, 22, 23, 24]. As a result, fracture toughness may be significantly more sensitive to the quench rate than the strength of the alloy [25]. Dumont et al. [21, 22, 23] studied two 7000 series aluminium alloys using Kahn tear tests and found that a lower quench rate resulted in a lower fracture toughness, which was a result of the increased intercrystalline fracture caused by grain boundary precipitation and variations in the work-hardening rate. Morgeneyer et al. [17] used synchrotron radiation computed tomography to study the failure mechanism ahead of the crack tip in Kahn tear tests for a 6000 series aluminium alloy. They found after a slow quench that fracture was mainly intercrystalline and that there was relatively little damage evolution prior to crack initiation.

In metallic materials, the mechanism for damage evolution and ductile fracture is nucleation, growth and coalescence of microscopic voids [26]. Voids may nucleate at constituent particles or inclusions either by decohesion or by particle cracking [27], or voids may pre-exist in the material [28]. Based on unit cell calculations using the finite element method (FEM), it has been found that damage evolution and ductile failure depend on a number of factors including the volume fraction of voids and particles, their distribution and shape, the plastic anisotropy, strength and work hardening of the matrix material, and on the local stress state [26]. Modelling of ductile materials is often done using micromechanically motivated homogenized material models such as porous plasticity models. In these models, the evolution of microstructural variables is included to describe effects such as material softening. These variables typically account for physical phenomena occurring at the lower scales of ductile failure. The most renowned model based on this micromechanical framework, is the model proposed by Gurson [29]. This model is attractive due to its simple formulation, incorporating only a single microstructural parameter through the volume fraction of microscopic voids. The Gurson model has later been enhanced to give better agreement with unit cell

calculations [30] and extended to include effects such as void nucleation and coalescence [31]. Versions of the model which take the plastic anisotropy of the matrix material into account have also been proposed [32, 33].

In this study, the effect of quench rate on the plastic flow and fracture of age hardenable aluminium alloys is investigated. Using tensile tests on smooth and V-notch axisymmetric specimens, in addition to Kahn tear tests, the influence of stress state on the fracture of three AlMgSi alloys with different grain structure and crystallographic texture is determined. The alloys were solution heat-treated, cooled either in water or air to achieve different quench rates and artificially aged. It is found that the quench rate affects the precipitate structure of the alloys differently, and the slower cooling rate typically leads to wider PFZs around dispersoids and grain boundaries. In addition, finite element simulations of the mechanical tests are performed for one of the alloys, using the Gurson [29] model extended by Dæhli et al. [33] to account for plastic anisotropy. Failure initiation is accurately captured in the finite element simulations, whereas the crack propagation energy in the simulations of the Kahn tear tests is somewhat overestimated.

2. Materials

Three aluminium alloys, namely 6060, 6082.25 and 6082.50, are studied experimentally. The chemical composition of the alloys is given in Table 1. The alloys were provided by Hydro Aluminium as extruded rectangular profiles with a thickness of 10 mm and a width of 83 mm. Three types of specimens were machined from the extruded profiles for mechanical testing, see Section 3.1.

Table 1: Chemical compositions of the aluminium alloys in wt%.

Alloy	Fe	Si	Mg	Mn	Cr	Cu	Zn	Ti	Al
6060	0.193	0.422	0.468	0.015	0.000	0.002	0.005	0.008	Bal.
6082.25	0.180	0.880	0.600	0.530	0.150	0.020	0.005	0.011	Bal.
6082.50	0.200	1.020	0.670	0.540	0.001	0.003	0.005	0.010	Bal.

All specimens were solution heat-treated and artificially aged to temper T6 (peak strength). After the solution heat-treatment, the specimens were cooled to room temperature using either air-cooling (AC) or water-quenching (WQ) to attain two different microstructures for each alloy, giving a total of six distinct materials. The solution heat-treatment consisted of keeping the specimens in a salt bath at 540 °C for 15 min, followed by either water-quenching to room temperature or air-cooling to 50 °C followed by water-quenching to room temperature. In the latter case, the temperature reached 50 °C after approximately 20 min with air-cooling. Subsequently, the specimens were stored at room temperature for 15 min before the artificial ageing to temper T6. To obtain the peak hardness condition, the specimens were kept in an oil bath at 185 °C for five hours and then air-cooled to room temperature. Figure 1 illustrates the temperature history of the specimens during the artificial ageing with either air-cooling or water-quenching after the solution heat-treatment. For each combination of specimen type and heat-treatment procedure, the temperature of one of the specimens was logged by a drilled-in thermo-couple.

The three aluminium alloys have different grain structure and crystallographic texture. The grain structure of the three alloys is shown in Figure 2. The 6060 alloy has a recrystallized grain structure comprised of equiaxed grains of 60-70 µm and exhibits a cube texture with a minor Goss component. A typical fibrous, non-recrystallized grain structure is observed for the 6082.25 alloy, which has a cube texture with orientations along the β-fibre. These grains are several millimetres long in ED, approximately 150 µm in TD and 10 µm in the ND. In addition, the fibrous grain structure comprises sub-grains approximately 2-10 µm in diameter. The large elongated, recrystallized grains of the 6082.50 alloy exhibit a rotated cube texture, and are several millimetres long in ED, about 1-2 mm in TD and 300-400 µm in the ND [34].

For further details about the alloys, the reader is referred to Christiansen et al. [20], Frodal et al. [34] and Khadyko et al. [35].

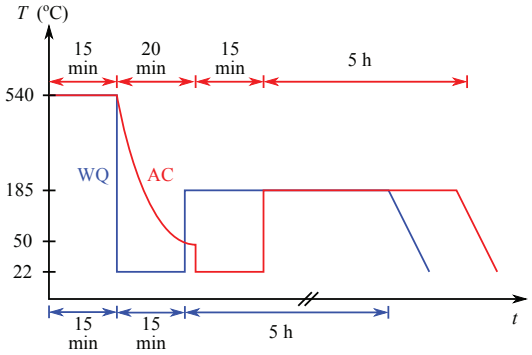

Figure 1: Heat-treatment of the alloys to temper T6, with either air-cooling (AC) or water-quenching (WQ) after the solution heat-treatment.

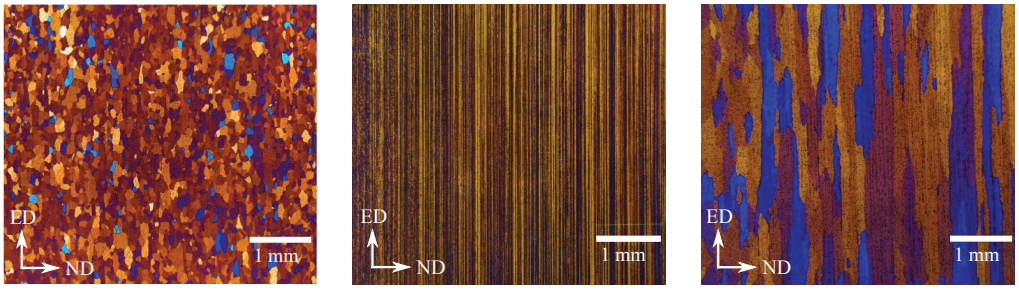

(a) (b) (c)

Figure 2: Grain structure of the three alloys: (a) 6060, (b) 6082.25, and (c) 6082.50. Reprinted by permission from Springer Nature [34].

3. Experimental procedures

3.1. Mechanical testing

In order to study the deformation and fracture mechanisms of these materials, different types of specimens were tested under quasi-static loading conditions, including cylindrical smooth and V-notch tensile specimens and Kahn tear test specimens. Figure 3 shows the geometry of the three types of test specimens. The specimens were machined from the centre of the extruded profile. The tensile axis of the smooth and V-notch tensile specimens was oriented along the transverse direction (TD) of the profile. The Kahn tear test specimens were machined either with the tensile axis along the extrusion direction (ED) or along TD, and always perpendicular to the thickness direction (ND).

A displacement-controlled testing machine was used to perform the experiments, and a constant cross-head velocity of 1.00 mm/min, 0.12 mm/min and 1.00 mm/min were used for the tests on the smooth tensile specimens, the V-notch tensile specimens and the Kahn tear test specimens, respectively.

An in-house measuring system [34] was used to measure the minimum diameters along ED and ND of the smooth and V-notch tensile specimens. The force and minimum diameters of the tensile specimen were continuously measured during the test until fracture. The current area of the minimum cross-section of the axisymmetric tensile specimen can be estimated by an elliptical area as

$$A = \frac{\pi}{4} D_1 D_3 \tag{1}$$

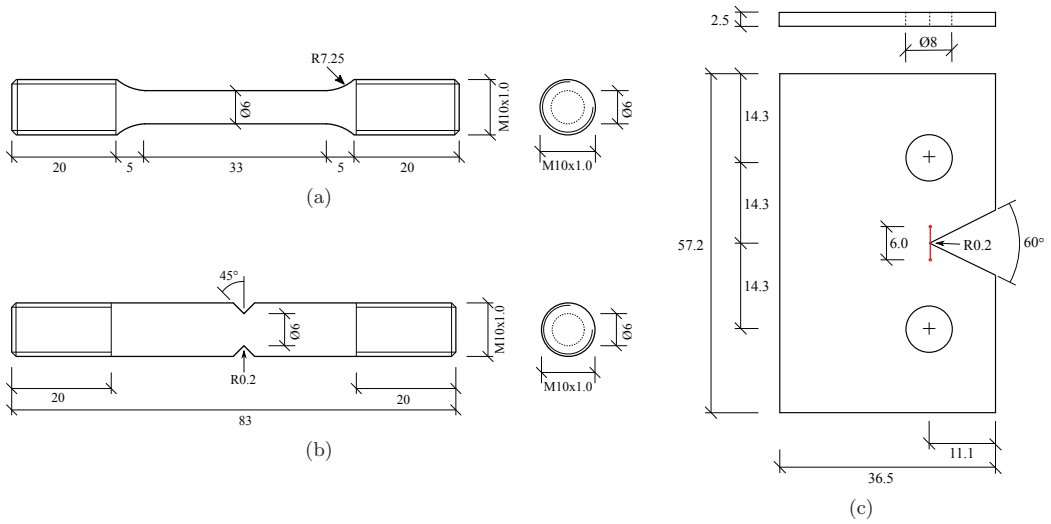

Figure 3: Geometry of the test specimens: (a) Smooth tensile specimen, (b) V-notch tensile specimen, and (c) Kahn tear test specimen with a red line indicating the virtual extensometer used. Dimensions in mm.

where D_1 and D_3 are the measured diameters in ED and ND, respectively. The true stress over the minimum cross-section area is then

$$\sigma_t = \frac{F}{A} \tag{2}$$

where F is the measured force. Assuming plastic incompressibility and negligible elastic strains, the logarithmic strain is given by

$$\varepsilon_l = \ln\left(\frac{A_0}{A}\right) \tag{3}$$

where A_0 is the initial cross-section area of the specimen. It is important to note that σ_t and ε_l represent average values over the minimum cross-section area of the tensile specimen.

In the Kahn tear tests, the force F and the cross-head displacement u were tracked continuously during testing. In addition, the displacement field on the surface of the specimen was obtained by digital image correlation (DIC). The displacement v across the crack tip of the Kahn test specimen was extracted using a virtual extensometer (Figure 3c). In order to quantify the energy required to initiate and propagate a crack across the Kahn test specimen, the unit initiation energy (UIE) and unit propagation energy (UPE) were determined for each test. The UIE is calculated by

$$\text{UIE} = \frac{1}{bw}\int_0^{u_p} F\,du \tag{4}$$

where u_p is the displacement at peak force, b is the initial thickness, and w is the initial minimum width of the specimen. Similarly, the UPE is calculated by

$$\text{UPE} = \frac{1}{bw}\int_{u_p}^{u_f} F\,du \tag{5}$$

where u_f is the displacement where the force has dropped to 1% of the maximum force [36]. These energy measures can provide useful insight when investigating a material's resistance to crack growth, as both strength and ductility are considered.

Three tests were conducted for each combination of specimen type, tensile direction and material, i.e., alloy and cooling rate (air-cooling or water-quenching) after the solution heat-treatment. Hence, a total of 18 tensile tests on smooth specimens, 18 tensile tests on V-notch specimens, and 36 Kahn tear tests were conducted.

3.2. Microstructure characterization

Undeformed samples were anodized at room temperature for 2 min using HBF_4 to reveal the grain structure under polarized light in the optical microscope. Fracture surfaces of the failed V-notch and Kahn tear test specimens were investigated in a Zeiss Gemini Supra 55VP FESEM operated at 20kV.

Precipitation in the different alloys was characterized using transmission electron microscopy (TEM). Thin foils of the materials were prepared using conventional thin foil preparation procedures. Sections from the undeformed regions of the Kahn tear test specimens were cut using an automated high-speed saw. These sections were then polished down to ≈ 300 µm before 3 mm diameter disks were punched out and further polished down to ≈ 100 µm thickness with a mirror-like finish. A twin-jet Struers TenuPol 3 electropolishing system operated at 20 V was used to electropolish the disks and provide electron transparent regions for TEM investigations. The electrolyte consisted of 1/3 HNO_3 (nitric acid) and 2/3 CH_3OH (methanol), and was kept at $\approx -25 \pm 5$ °C during the process. Reliable TEM investigations of precipitation require the thin foil surface normal to be close to a $\langle 001 \rangle$ direction, i.e., a [001] zone axis is desired at relatively low specimen tilt. Because the thin foil preparation technique produces specimens with an inherent variation in quality and the thin areas of the final foils might not contain any grains with a [001] zone axis, several thin foils from each specimen were prepared. In the 6082.50 alloy, this was especially challenging due to the abnormally large grains, and electron backscattering in the scanning electron microscope (SEM) was used to select sections from the Kahn test specimens. Before TEM investigations, the finished thin foils were cleaned for ≈ 3 min in a Fischione 1020 Plasma Cleaner.

TEM investigations were carried out on two different instruments. The water-quenched 6060 alloy was characterized on a Philips CM30 with a LaB_6 filament operated at 150 kV in a previous study [20]. The remaining materials were characterized on a JEOL JEM2100 with a LaB_6 operated at 200 kV. The thickness of the imaged areas in the thin foils was measured by electron energy loss spectroscopy (EELS), using a Gatan PEELS model 601 on the CM30 microscope and a Gatan Imaging Filter system on the JEM2100 microscope. Precipitation in the different materials was evaluated by measuring the average needle length, cross-sectional area, number density, and volume fraction, following the procedure of Andersen [37] and Marioara et al. [38].

4. Experimental results

4.1. Initial microstructure

Figure 4 shows TEM bright field images of the undeformed materials. Air-cooling has an adverse effect on precipitation in all alloys, but the precipitate microstructure of the alloys is differently affected. In the case of the 6060 alloy, the number density of precipitates is reduced in the air-cooled alloy compared to the water-quenched alloy. In the 6082.25 alloy, precipitation becomes very inhomogeneous and is limited to small regions that contain slightly larger precipitates compared to the water-quenched condition. The 6082.50 alloy also exhibits inhomogeneous precipitation after air-cooling, but not to the same degree as the 6082.25 alloy. Where precipitates have formed in the air-cooled 6082.50 alloy, the local number density is greater and the precipitates are smaller, compared to the water-quenched condition. Figure 5 presents TEM images of the dispersoids responsible for the inhomogeneous precipitation in the two 6082 alloys. Air-cooling causes dispersoids to nucleate large precipitates and drain their neighbouring region of solute, suppressing precipitation of strengthening precipitates. Because the number density of dispersoids in the 6082.25 alloy is greater than in the 6082.50 alloy, the PFZs around dispersoids and grain boundaries (GBs) overlap, resulting in PFZs that span entire grains and leave only a few regions of sparse precipitation. Dislocations observed in the PFZs of this alloy are probably generated due to the constraint that are introduced by the growth of large precipitates nucleated on dispersoids. In the 6082.50 alloy, the dispersoid density is substantially lower, so

that strengthening precipitates may form in regions situated a certain distance from each dispersoid. Grain boundary PFZs are also changed by the cooling rate. Figure 6 presents representative TEM bright field images of grain boundary regions and surrounding PFZs. The observed trend is that the slow cooling rate leads to wider PFZs around grain boundaries, similar to the trend of PFZs around dispersoids. Table 2 summarises the TEM observations, where average numbers for needle length, cross-sectional area, number density, and volume fractions are presented, along with approximate PFZ widths. Precipitate statistics were not performed for the air-cooled 6082.25 alloy, due to its severe inhomogeneous precipitate microstructure. Note that the number density estimate for the air-cooled 6082.50 alloy is an overestimate of the average number density, as it is estimated based on the dense precipitation regions. The PFZs around GBs and dispersoids will reduce the actual number density of precipitates in this alloy after air-cooling.

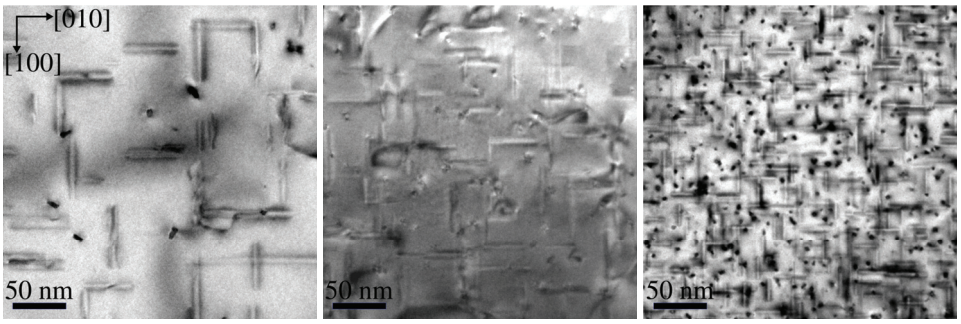

(a) 6060-AC (b) 6082.25-AC (c) 6082.50-AC

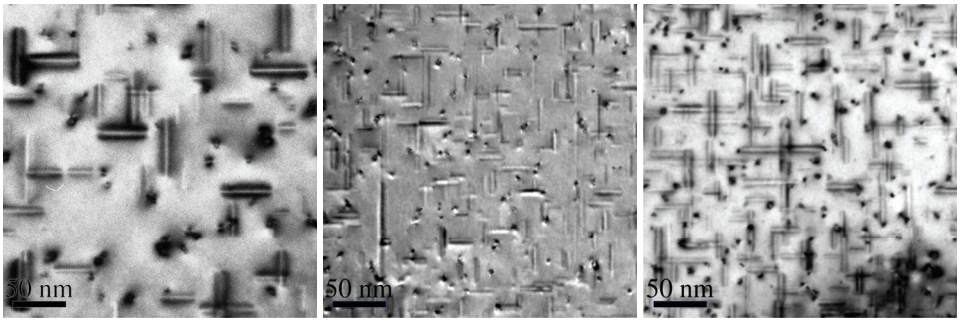

(d) 6060-WQ (e) 6082.25-WQ (f) 6082.50-WQ

Figure 4: TEM [001] zone axis bright field images of precipitation in (a-c) air-cooled and (d-f) water-quenched undeformed materials. The imaged areas are of comparable thickness and identical scale. Precipitates oriented along [100] and [010] matrix crystallographic directions, i.e., lying in the paper plane, are visible through the dark strain field in the surrounding matrix. Precipitates oriented along [001], i.e., out of the paper plane, appear as black dots. Differences in contrast and precipitate appearance are largely due to different specimen tilt and diffraction conditions.

The main result from the TEM study is that air-cooling reduces the total number density of strengthening precipitates in all the studied alloys. Preciptiation is less affected by the cooling rate in the 6060 alloy, and most affected in the 6082.25 alloy where it is almost entirely suppressed. In the 6082.50 alloy, air-cooling results in very dense precipitation with large PFZs around dispersoids scattered throughout the grains. This means that the precipitation microstructure of the 6082.50 alloy becomes inhomogeneous, with soft regions (dispersoids with PFZs) dispersed in a strong matrix (preciptiate strengthened regions), where the strong matrix has a strength comparable to the water-quenched state.

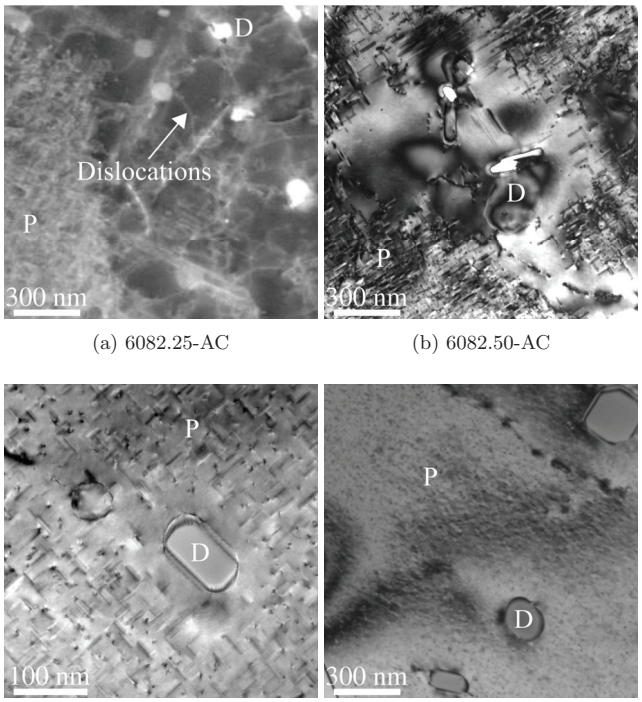

(a) 6082.25-AC (b) 6082.50-AC

(c) 6082.25-WQ (d) 6082.50-WQ

Figure 5: TEM images of precipitation (marked "P") around dispersoids (marked "D") in the dense 6082 alloys after air-cooling (a,b), and after water-quench (c,d). The image in subfigure (a) is a medium-angle annular dark field scanning TEM (STEM) image, while the other images are TEM bright field images. The reason for applying STEM is that the air-cooled condition of 6082.25 contains many dislocations, as indicated, and their strain fields dominate the bright field contrast. Note the difference in scale between subfigure (c) and the other images.

Table 2: Average estimates of precipitation in the alloys. Precipitation in the air-cooled 6082.25 alloy is inhomogeneous, and no statistics are available.

Material	Needle length (nm)	Needle cross-section (nm^2)	Number density ($\#/\mu m^3$)	Volume fraction (%)	PFZ width (nm)
6060-AC	41.8 ± 2.4	23.4 ± 4.2	2839 ± 272	0.27 ± 0.02	478 ± 114
6060-WQ	40.0 ± 1.0	19.1 ± 0.8	5556 ± 629	0.42 ± 0.05	146 ± 41
6082.25-AC	-	-	-	-	$334 \pm 138^{\dagger}$
6082.25-WQ	22.9 ± 0.6	7.0 ± 0.3	40232 ± 3563	0.64 ± 0.05	61 ± 16
6082.50-AC	26.5 ± 0.5	8.3 ± 0.3	$53870 \pm 3826^{*}$	1.18 ± 0.08	211 ± 33
6082.50-WQ	32.1 ± 2.3	10.2 ± 0.5	42183 ± 7534	1.26 ± 0.14	59 ± 11

* The precipitation statistics for the air-cooled 6082.50 alloy is from dense precipitate regions, and the number density do not reflect the inhomogeneous precipitate microstructure.

† PFZs usually span entire grains.

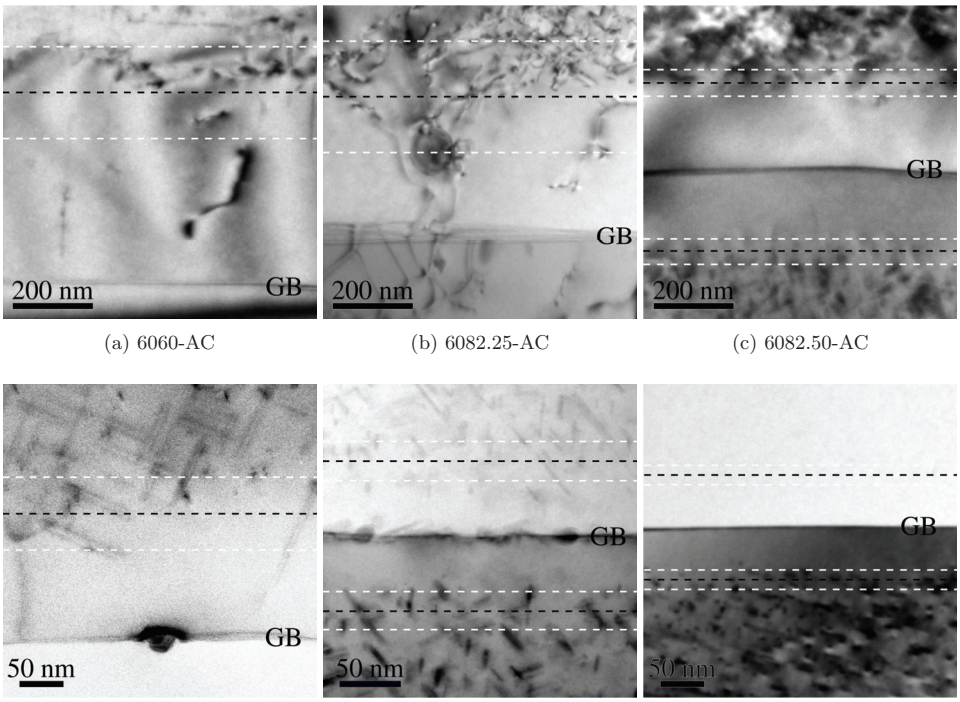

(a) 6060-AC (b) 6082.25-AC (c) 6082.50-AC

(d) 6060-WQ (e) 6082.25-WQ (f) 6082.50-WQ

Figure 6: TEM bright field images of grain boundaries (marked by "GB") and surrounding PFZs in (a-c) air-cooled and (d-f) water-quenched materials. Black dashed lines mark the PFZ width, while the white dashed lines mark the estimated error of the PFZ width. The scale in subfigures (a-c) is the same, but for subfigures (d-f) the scale is larger for subfigure (e) than for subfigures (d) and (f).

4.2. Mechanical response

4.2.1. Tensile tests on smooth and V-notch specimens

Figure 7 presents the true stress-strain curves from the tensile tests on smooth specimens plotted up to failure. Three parallel tests were performed for each material. Only two repeat tests were successful for the water-quenched and air-cooled 6082.50 alloy, as the other specimens failed close to the grip section. Comparing the two heat-treatments, it is obvious that the strength is lower with air-cooling than with water-quenching for all the alloys. The strain to failure is greater with air-cooling than with water-quenching for the 6060 and 6082.25 alloys. For the 6082.50 alloy, a large scatter is observed in the failure strain for the water-quenched material, and the failure strain for the air-cooled material is within this range. The scatter is caused by the large grains of this alloy, as the number of grains across the specimen diameter is small. Relatively little scatter is observed for the other materials. For the water-quenched materials, the initial yield stress is the lowest for the 6060 alloy, while the two 6082 alloys have a higher and similar initial yield stress, with the 6082.25 alloy a little higher than the 6082.50 alloy. With air-cooling, the initial yield stress of the 6082.25 alloy is the lowest, and the initial yield stress of the 6060 alloy is between the two 6082 alloys. Thus, the largest difference in strength due to the heat-treatment is observed for the 6082.25 alloy, see Table 3.

The stress-strain curves up to failure from the tensile tests on V-notch specimens are presented in Figure 8. Three repeat tests are shown for each material and the scatter is small. It is evident that the stress level is

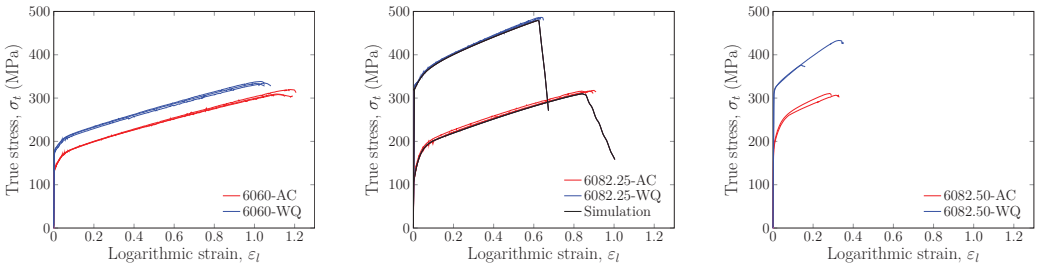

Figure 7: Stress-strain curves from the tensile tests on smooth specimens: (a) 6060, (b) 6082.25, and (c) 6082.50. Simulation results are shown for the 6082.25 alloy.

Table 3: Initial yield stress at 0.2% plastic strain, $\sigma_{0.2}$, from the smooth tensile tests, with standard deviations.

Material	$\sigma_{0.2}$ (MPa)
6060-AC	132.6 ± 0.5
6060-WQ	176.4 ± 2.7
6082.25-AC	113.4 ± 3.0
6082.25-WQ	327.7 ± 0.5
6082.50-AC	179.5 ± 6.4
6082.50-WQ	315.0 ± 1.3

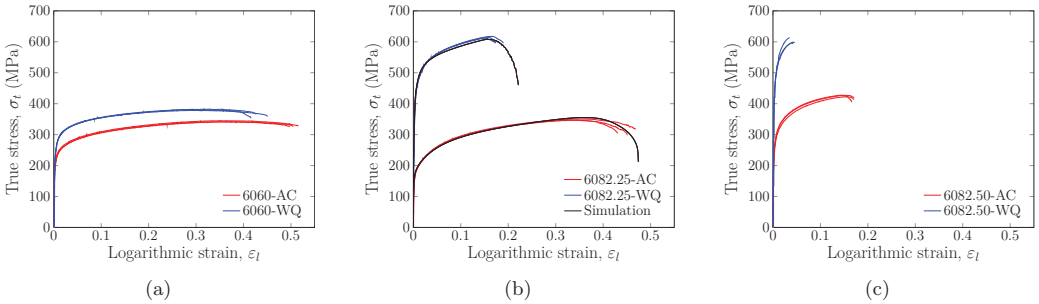

Figure 8: Stress-strain curves from the tensile tests on V-notch specimens: (a) 6060, (b) 6082.25, and (c) 6082.50. Simulation results are shown for the 6082.25 alloy.

elevated in the V-notch specimens compared to the smooth specimens due to the notch strengthening effect, which is caused by the triaxial stress field in the notch. Similar trends are observed here as in Figure 7, but the failure strain is clearly lower with water-quenching than with air-cooling in the tensile tests on the V-notch specimens—and this holds for the 6082.50 alloy as well. By comparison of Figure 7 and Figure 8, it is found that the failure strain is substantially lower in the tensile tests on V-notch specimens, due to the increased stress triaxiality induced by the sharp notch.

Lankford coefficients measured in the tensile tests on smooth and V-notch specimens are given in Table 4. These coefficients give the ratio between the incremental strains in ED and ND, and thus represent the evolution of the cross-section of the specimen with plastic deformation. Small variations in the Lankford coefficients are observed between the materials with the different cooling rates. For the 6060 and 6082.50 alloys, the air-cooled materials appear to be slightly less anisotropic than the water-quenched materials, in

Table 4: Measured Lankford coefficients from the smooth and V-notch tensile tests, with standard deviations.

Material	Smooth	V-notch
6060-AC	3.67 ± 0.07	1.94 ± 0.15
6060-WQ	3.95 ± 0.11	2.04 ± 0.25
6082.25-AC	0.84 ± 0.00	0.81 ± 0.01
6082.25-WQ	1.10 ± 0.01	0.94 ± 0.01
6082.50-AC	0.32 ± 0.09	0.35 ± 0.04
6082.50-WQ	0.19 ± 0.05	0.22 ± 0.06

the sense that the Lankford coefficient is closer to unity, whereas the opposite trend is found for the 6082.25 alloy. The Lankford coefficients obtained from the tensile tests on the smooth and V-notch specimens are similar for the two 6082 alloys, while the coefficients for the 6060 alloy are markedly lower in the V-notch specimens. The latter observation indicates that the plastic flow is strongly influenced by the triaxial stress field imposed by the sharp notch.

4.2.2. Kahn tear tests

Figure 9 displays the force-displacement curves from the Kahn tear tests. The virtual extensometer situated across the notch tip, depicted in Figure 3c, is used to obtain a measure of the notch tip opening displacement. The differences in strength of the air-cooled and water-quenched materials observed in the tensile tests on smooth and V-notch specimens are also seen here. The peak force is consistently lower for the air-cooled than for the water-quenched materials, and thus crack initiation always occurs at a lower force for the former materials. Variations between the two loading directions are also observed. For the 6060 alloy, the test in the transverse direction (TD) has the highest peak force, whereas the test in the extrusion direction (ED) has the highest peak force for the two 6082 alloys. For the 6082.50 alloy, tests along ED give markedly higher ductility than tests along TD, while the difference for the 6082.25 alloy is small. This large difference in ductility with loading direction is attributed to the grain structure of the 6082.50 alloy. The large elongated grains of this alloy, which are several millimetres along ED [34], make the material more susceptible to intercrystalline fracture when loaded along TD, see Section 4.3.

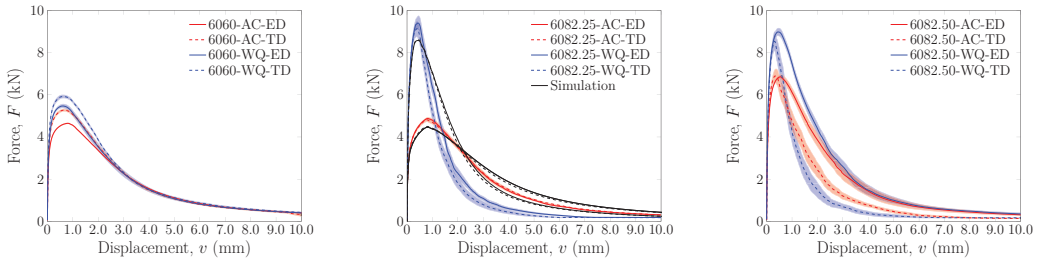

Figure 9: Force-displacement curves from the Kahn tear tests showing the mean curve with the scatter in shaded colour: (a) 6060, (b) 6082.25, and (c) 6082.50. Simulation results are shown for the 6082.25 alloy.

Table 5 presents the unit initiation energies (UIEs) and unit propagation energies (UPEs) calculated based on the Kahn tear tests, see Equation (4) and (5). Here, the cross-head displacement has been used to calculate these energies in accord with ASTM [36]. The UIE and UPE are the energies per unit area required to initiate crack growth and propagate a crack through the material, respectively. Similar values of the UIE are found for the same alloy and loading direction. Albeit the force level is significantly lower for the air-cooled materials than the water-quenched materials, the UIEs are similar, indicating that the

displacement to crack initiation is larger for the air-cooled materials.

Table 5: Unit initiation energy (UIE) and unit propagation energy (UPE) from the Kahn tear tests, with standard deviations.

Material	UIE (kJ/m^2)		UPE (kJ/m^2)	
	ED	TD	ED	TD
6060-AC	94.0 ± 0.7	102.5 ± 4.0	231.0 ± 2.0	250.0 ± 7.1
6060-WQ	87.8 ± 7.7	109.2 ± 1.8	249.2 ± 8.1	267.2 ± 0.9
6082.25-AC	144.7 ± 2.7	132.5 ± 5.8	213.1 ± 1.1	218.0 ± 3.2
6082.25-WQ	147.6 ± 9.9	135.5 ± 9.5	145.1 ± 9.1	118.2 ± 16.0
6082.50-AC	115.9 ± 3.5	81.6 ± 3.9	244.8 ± 24.6	153.6 ± 16.7
6082.50-WQ	128.3 ± 5.1	98.9 ± 5.1	276.2 ± 18.5	101.5 ± 3.7

The UPE is greater for the water-quenched material than for the air-cooled material in both loading directions for the 6060 alloy, suggesting that the water-quenched material has a higher resistance to crack propagation. This trend is reversed for the 6082.25 alloy, and the air-cooled material has the greatest propagation energy in both loading directions. For the 6082.50 alloy, the loading direction has a substantial effect on the UPE, and this effect is greater for the water-quenched material than for the air-cooled material. The result is that for the 6082.50 alloy, the water-quenched material has the highest UPE in ED, whereas the air-cooled material has the highest UPE in TD.

4.3. Fractography

To get a deeper understanding of the mechanisms involved in the fracture process, a fractographic analysis of the tested specimens is performed in the SEM. Figure 10 presents the fracture surfaces of the V-notch tensile specimens for the three alloys with air-cooling and water-quenching. Three distinct fracture surface shapes are observed, where each alloy exhibits a distinct shape. The 6060 alloy displays a flat diamond-shaped fracture surface. A flat circular cross-section is recognized for the 6082.25 alloy, whereas the 6082.50 alloy demonstrates a slant circular fracture surface which is a result of the large grains. The diamond-shaped fracture surface found for the 6060 alloy is caused by the strong cube texture in combination with the superimposed triaxial stress field of the V-notch specimen [39]. This diamond-shaped cross-section will yield inaccuracies in the logarithmic strain measure, defined by Equation (3), for large deformations, as the area calculation used in the strain measure is based on an assumption of an elliptical minimum area, see Equation (1).

Fracture is mainly transcrystalline for the 6060 and 6082.25 alloys, with some areas of intercrystalline fracture. In contrast, the 6082.50 alloy has substantial amounts of intercrystalline fracture, see also Figures 11, 12, and 13. In general, the same fracture surface shapes and fracture modes are observed for the air-cooled and water-quenched materials in Figure 10. The air-cooled materials have smaller fracture areas than the water-quenched materials, in agreement with larger fracture strains, see Section 4.2.1. For the 6060 and 6082.25 alloys, the fracture is mainly transcrystalline for both the air-cooled and the water-quenched materials, whereas the amount of intercrystalline fracture is greater for the water-quenched material than for the air-cooled material for the 6082.50 alloy.

Figure 11 shows the fracture surfaces of the Kahn tear test specimens for the 6060 alloy, including the two loading directions and the air-cooled and water-quenched materials. The fracture surfaces are clearly distinct and variations are seen between the two loading directions and the two cooling rates. For the materials loaded along ED, transcrystalline fracture is dominant. In contrast, along TD a considerable amount of the fracture surface is covered with areas of intercrystalline fracture. As this alloy has equiaxed grains, the more probable cause of this difference is the crystallographic texture. The Goss texture component is likely to cause greater imbalance and stress concentrations between grains when loaded along TD, leading to highly localized deformation in the PFZs and along grain boundaries. This will in turn lead to different behaviours along different material orientations as observed for loading along ED and TD. Comparing the different cooling rates it is evident that the width of the fracture area for the water-quenched material is smaller than that for

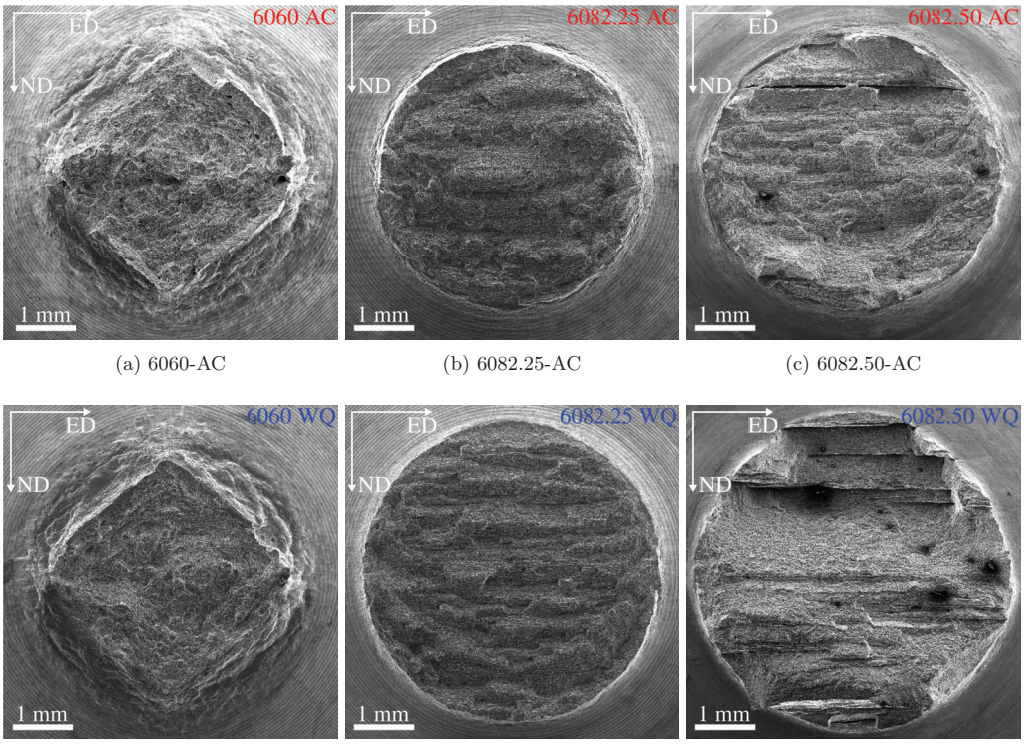

(a) 6060-AC (b) 6082.25-AC (c) 6082.50-AC

(d) 6060-WQ (e) 6082.25-WQ (f) 6082.50-WQ

Figure 10: Fracture surfaces of the V-notch tensile specimens for the three alloys with air-cooling, AC (top) and water-quenching, WQ (bottom).

the air-cooled material loaded along ED, suggesting that the water-quenched material has a greater ductility. For the specimens loaded along ED, the fracture surfaces of the air-cooled and water-quenched materials are similar, displaying similar dimple structures. A greater difference is observed between the two cooling rates for the specimens loaded along TD. The air-cooled material has a larger amount of intercrystalline fracture than the water-quenched material, again suggesting that the water-quenched material has a greater ductility.

Figure 12 depicts the fracture surfaces of the Kahn specimens for the 6082.25 alloy, including the two cooling rates and the two loading directions. The fracture surfaces are similar in all these cases. Transcrystalline fracture is dominant with only minor intercrystalline fracture, i.e., some areas of intercrystalline fracture can be seen between the large areas filled with dimples formed in the grain interior.

The fracture surfaces of the Kahn specimens for the 6082.50 alloy, including the two cooling rates and the two loading directions, are shown in Figure 13. In contrast to the 6082.25 alloy, the 6082.50 alloy clearly shows distinct fracture surfaces for the different cases. For the tests loaded along ED, only transcrystalline fracture is seen for the water-quenched material. In contrast, large areas of intercrystalline fracture are observed for the air-cooled material, indicating a failure mode with lower ductility than for the water-quenched material. Larger amounts of intercrystalline fracture are observed for the Kahn specimens loaded along TD due to the grain structure of this alloy. The large elongated grains, see Figure 2, make the material less susceptible to intercrystalline fracture in ED as the fracture path is forced through the grains by the notch of the Kahn specimen. The ratio of intercrystalline to transcrystalline fracture for the specimens

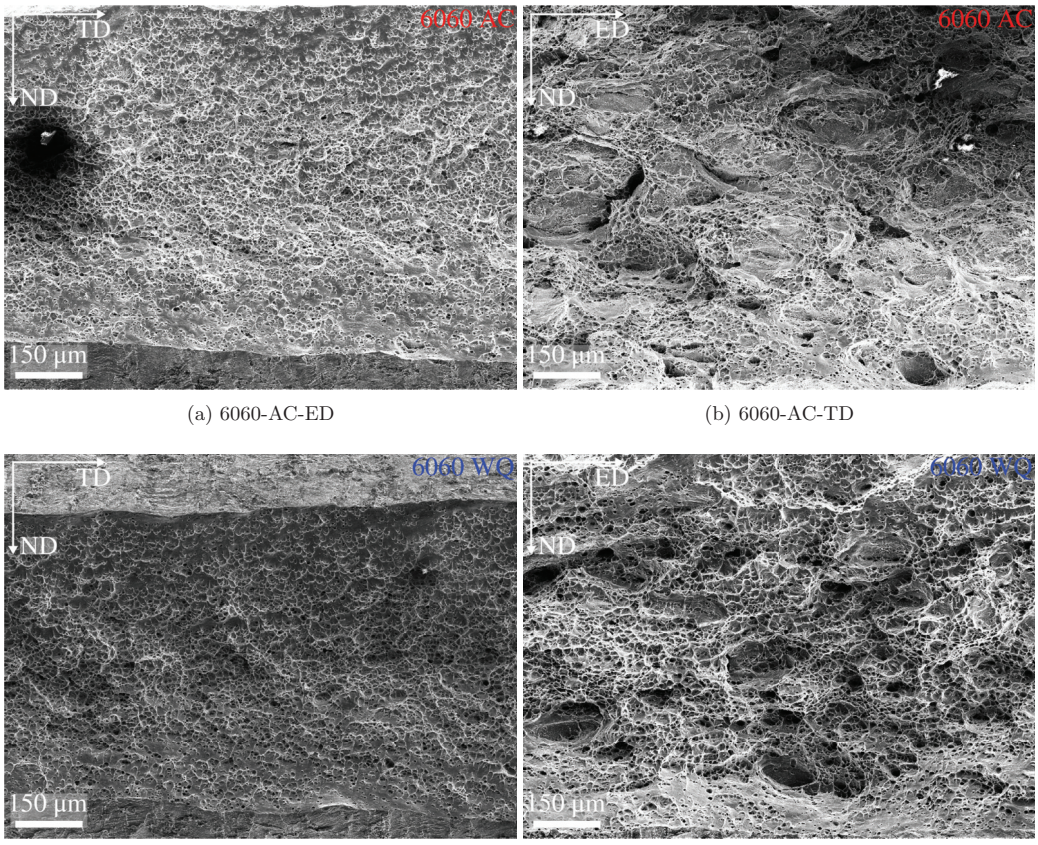

(a) 6060-AC-ED (b) 6060-AC-TD

(c) 6060-WQ-ED (d) 6060-WQ-TD

Figure 11: Fracture surfaces of the Kahn tear test specimens for the 6060 alloy.

loaded along TD appears to be larger for the water-quenched material than for the air-cooled material. Thus, different trends of intercrystalline fracture are seen for the two loading directions. This indicates that for loading along ED, the water-quenched material is the most ductile, whereas it is the air-cooled material that is the most ductile when loaded along TD.

Constituent particles can be seen at the bottom of many of the dimples for all materials, indicating ductile fracture involving nucleation, growth and coalescence of voids. Voids may be nucleated from constituent particles either by decohesion or by particle cracking [27], or may pre-exist in the materials [28]. The 6060 alloy contains constituent particles of type AlFeSi, while the two 6082 alloys contain constituent particles of type AlFeSiMn, and the particles are larger in the two 6082 alloys than in the 6060 alloy [34]. Cracked particles can be found at the bottom of some dimples. These particles cracked during the extrusion process, and fully or partially cracked particles can be found in undeformed samples [34]. In some areas, intercrystalline fracture with a high density of smaller dimples is revealed, it is reasonable to assume that these dimples are caused by void growth within the PFZ, possibly nucleated at grain boundary precipitates [19].

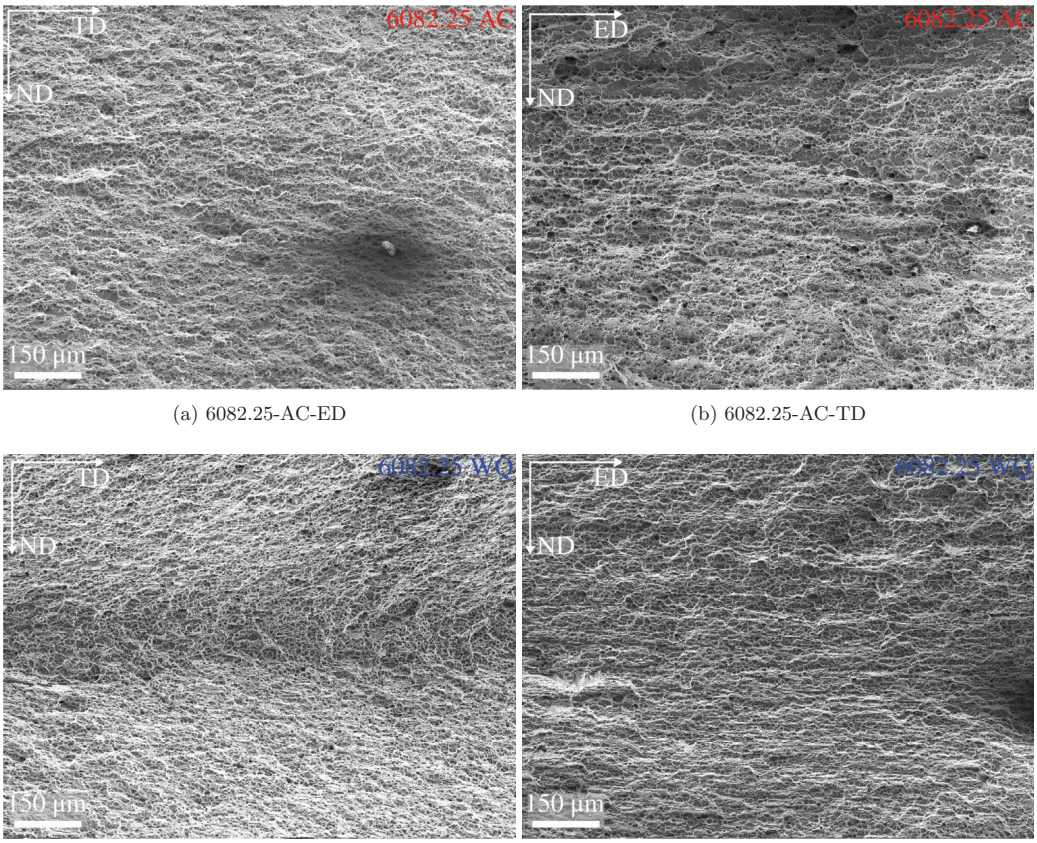

(a) 6082.25-AC-ED (b) 6082.25-AC-TD

(c) 6082.25-WQ-ED (d) 6082.25-WQ-TD

Figure 12: Fracture surfaces of the Kahn tear test specimens for the 6082.25 alloy.

5. Numerical study

5.1. Constitutive model

In this section, the constitutive relations of the porous plasticity model, which is used in the subsequent finite element simulations of some of the tests, are outlined. It is assumed that that elastic deformations are infinitesimal, while plastic deformations and rotations may be finite. A corotational formulation of the anisotropic porous plasticity model is used, and the components of the Cauchy stress tensor and the rate of deformation tensor are expressed in a co-rotated coordinate system by

$$\hat{\sigma}_{ij} = R_{ki}\sigma_{kl}R_{lj} \quad \wedge \quad \hat{D}_{ij} = R_{ki}D_{kl}R_{lj} \tag{6}$$

where $\mathbf{R}$ is the rotation tensor from the polar decomposition of the deformation gradient $\mathbf{F}$. The rate of deformation tensor $\mathbf{D}$ is additively decomposed into elastic and plastic parts

$$\hat{D}_{ij} = \hat{D}^e_{ij} + \hat{D}^p_{ij} \tag{7}$$

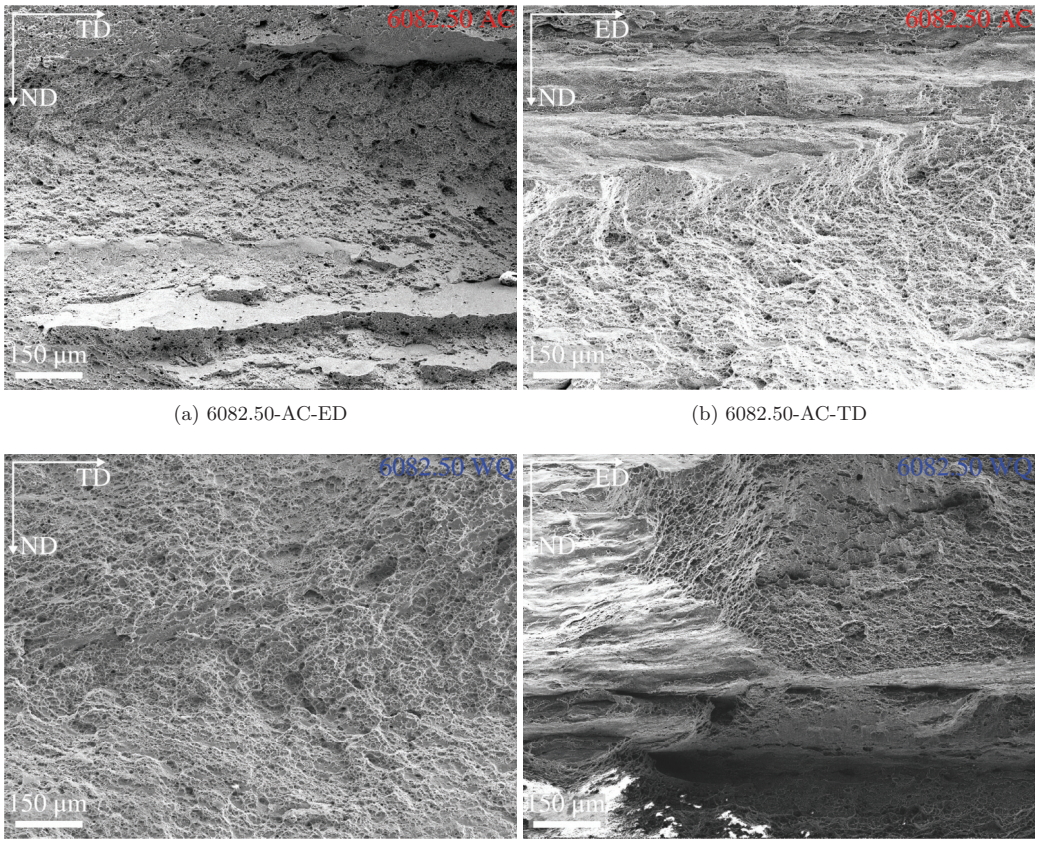

(a) 6082.50-AC-ED (b) 6082.50-AC-TD

(c) 6082.50-WQ-ED (d) 6082.50-WQ-TD

Figure 13: Fracture surfaces of the Kahn tear test specimens for the 6082.50 alloy.

where $\mathbf{D}^e$ and $\mathbf{D}^p$ are the elastic and plastic rate of deformation tensors, respectively. In the co-rotated coordinate system, the rate form of the generalized Hooke's law can be expressed as

$$\dot{\hat{\sigma}}_{ij} = \frac{E}{1+\nu}\hat{D}'^{e}_{ij} + \frac{E}{3\left(1-2\nu\right)}\hat{D}_{kk}\delta_{ij} \tag{8}$$

where $\mathbf{D}'^e$ is the deviatoric part of the elastic rate of deformation tensor, δ_{ij} is the Kronecker delta, and E and ν are Young's modulus and Poisson's ratio, respectively.

Plastic yielding is governed by the heuristic extension of the Gurson-Tvergaard-Needleman model [29, 30, 31] proposed by Dæhli et al. [33], and the yield function takes the form

$$\Phi\left(\boldsymbol{\sigma}, p, f\right) = \left(\frac{\varphi\left(\boldsymbol{\sigma}\right)}{\sigma_y}\right)^2 + 2q_1 f^* \cosh\left(\frac{q_2\hat{\sigma}_{kk}}{2\sigma_y}\right) - 1 - \left(q_1 f^*\right)^2 \leq 0 \tag{9}$$

where σ_y is the matrix flow stress, f^* is the effective void volume fraction introduced by Tvergaard and Needleman [31], and q_i are the model parameters suggested by Tvergaard [30]. The equivalent stress φ is now defined by the Yld2004-18p model proposed by Barlat et al. [40], which accounts for the plastic

anisotropy of the matrix material, as

$$\varphi\left(\boldsymbol{\sigma}\right) = \left(\frac{1}{4}\sum_{k=1}^{3}\sum_{l=1}^{3}\left|S_k^{(1)} - S_l^{(2)}\right|^a\right)^{\frac{1}{a}} \tag{10}$$

where a is an exponent determining the the curvature of the yield surface, and $S_k^{(1)}$ and $S_l^{(2)}$ are the principal values of the tensors $\boldsymbol{s}^{(1)}$ and $\boldsymbol{s}^{(2)}$, respectively. The tensors $\boldsymbol{s}^{(1)}$ and $\boldsymbol{s}^{(2)}$ are determined by the linear transformations

$$\hat{s}_{ij}^{(1)} = \hat{A}_{ijkl}^{(1)}\hat{\sigma}'_{kl} \quad \wedge \quad \hat{s}_{ij}^{(2)} = \hat{A}_{ijkl}^{(2)}\hat{\sigma}'_{kl} \tag{11}$$

where the fourth-order tensors $\boldsymbol{A}^{(1)}$ and $\boldsymbol{A}^{(2)}$ contain coefficients describing the plastic anisotropy [33, 40], and $\boldsymbol{\sigma}'$ is the deviatoric part of the Cauchy stress tensor. The associated flow rule is used, and the plastic rate of deformation tensor reads

$$\hat{D}_{ij}^p = \dot{\lambda}\frac{\partial\Phi}{\partial\hat{\sigma}_{ij}} \tag{12}$$

where $\dot{\lambda} \geq 0$ is the plastic multiplier. The matrix equivalent plastic strain is then related to the plastic power through

$$p = \int_0^t \dot{p}\,dt = \int_0^t \frac{\hat{\sigma}_{ij}\hat{D}_{ij}^p}{\left(1-f\right)\sigma_y}\,dt \tag{13}$$

where f is the void volume fraction.

The flow stress of the matrix material is described by an extended Voce hardening rule

$$\sigma_y = \sigma_0 + \sum_{i=1}^{3} Q_i\left(1 - \exp\left(-\frac{\theta_i}{Q_i}p\right)\right) \tag{14}$$

where σ_0 is the initial yield stress, and Q_i and θ_i are parameters controlling the work hardening. Plastic incompressibility of the matrix material gives the evolution of the void volume fraction as

$$\dot{f} = \left(1-f\right)\hat{D}_{kk}^p \tag{15}$$

The effective void volume fraction is given by [31]

$$f^*(f) = \begin{cases} f & \text{if } f \leq f_c \\ f_c + \frac{f_U^* - f_c}{f_F - f_c}\left(f - f_c\right) & \text{if } f > f_c \end{cases} \tag{16}$$

where f_c is the critical void volume fraction where an accelerated void growth is initiated, $f_U^* = 1/q_1$ is the ultimate value, and f_F is the void volume fraction where the material has completely lost its load-carrying capacity. In the subsequent finite element simulations, element deletion is used to describe crack propagation, and the element is deleted when $f = f_F$ in all integration points.

Finally, the loading/unloading conditions of plasticity are given in Kuhn-Tucker form as

$$\Phi \leq 0, \quad \dot{\lambda} \geq 0, \quad \dot{\lambda}\Phi = 0 \tag{17}$$

whereas the consistency condition, used to determine the plastic multiplier $\dot{\lambda}$ in the plastic domain, is expressed by

$$\dot{\lambda}\dot{\Phi} = 0 \tag{18}$$

The porous plasticity model has been implemented into a user material subroutine (VUMAT) for Abaqus/Explicit [41]. To ensure sufficient accuracy of the integration point values, sub-stepping is employed [33].

5.2. Finite element modelling and simulations

In the following, finite element simulations of the tensile tests and the Kahn tear tests for the 6082.25 alloy are presented, which are based on the porous plasticity model described in Section 5.1. The other two alloys demonstrate effects and properties that the porous plasticity model is unable to capture. The 6060 alloy develops a diamond-shaped minimum cross-section in the V-notch tensile tests, see Section 4.3, which can only be replicated by crystal plasticity finite element analyses, see Khadyko et al. [39]. Failing to simulate the correct deformation mode will yield uncertainties in the strain measure and thus on the calculated failure strain. For the 6082.50 alloy, the less ductile fracture mode observed especially for loading along TD, see Section 4.3, is poorly described by the porous plasticity model. This model considers growth and coalescence of voids in a homogeneous solid which is unable to capture the highly localized damage evolution and failure mode of intercrystalline fracture.

Isotropic elasticity is assumed in the simulation with a Young's modulus of $E = 70000$ MPa and a Poisson's ratio of $\nu = 0.3$, which are typical values for aluminium. The standard Tvergaard [30] parameters $q_1 = 1.5$, $q_2 = 1$ are used to define the pressure sensitivity of the yield surface. As an alternative, these parameters could have been determined from unit cell computations (see, e.g., [33]) and may depend on, e.g., the work-hardening behaviour and plastic anisotropy of the material. Thus, the remaining model parameters to identify are the anisotropy parameters controlling the shape of the yield surface (Equation (10) and (11)), the work-hardening parameters (Equation (14)), and the porous plasticity damage parameters (Equation (16)).

The anisotropy parameters controlling the shape of the yield surface concerning deviatoric stress states can be identified either from a large number of experimental tests [42] or from micro-mechanical simulations [43] by combining crystal plasticity with the finite element method (CP-FEM). The anisotropic yield surfaces of these alloys have previously been calibrated by Frodal et al. [43] utilising CP-FEM. Figure 14 depicts the initial yield surface of the 6082.25 alloy for porosity $f = 0$, together with the normalized initial yield stress in uniaxial tension, and Lankford coefficients versus tensile direction in the ED-TD plane.

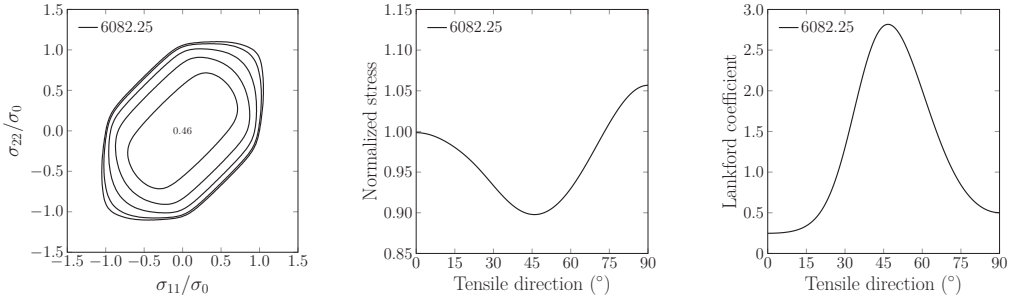

Figure 14: (a) Initial yield surface of the 6082.25 alloy depicted in the ED-TD plane with contours of normalized shear stress plotted in 0.1 increments, with the maximum value in the centre, and (b) normalized yield stress and (c) Lankford coefficient versus tensile direction for uniaxial tension in the ED-TD plane.

The finite element meshes of the smooth and V-notch tensile specimens and Kahn tear test specimen are shown in Figure 15. Due to the orthotropic material symmetry, only one-eighth of the smooth and V-notch tensile specimens and one-quarter of the Kahn tear test specimen are modelled to reduce the computational time. Linear eight-node solid elements with reduced integration (C3D8R) are used. The dimensions of the elements located in the centre of the specimens are $30 \times 40 \times 40$ µm^3, with the shortest element length along the tensile direction. Mass scaling is used to reduce the computational time, and it is ensured that the response is quasi-static, i.e., that the kinetic energy is negligible compared with the internal energy. The appropriate symmetry boundary conditions are enforced and loading is applied to the end of the smooth and V-notch tensile specimens. An analytic rigid pin is used to apply the load onto the Kahn tear test

specimen, where a friction-less surface-to-surface contact formulation is used between the specimen and the rigid pin.

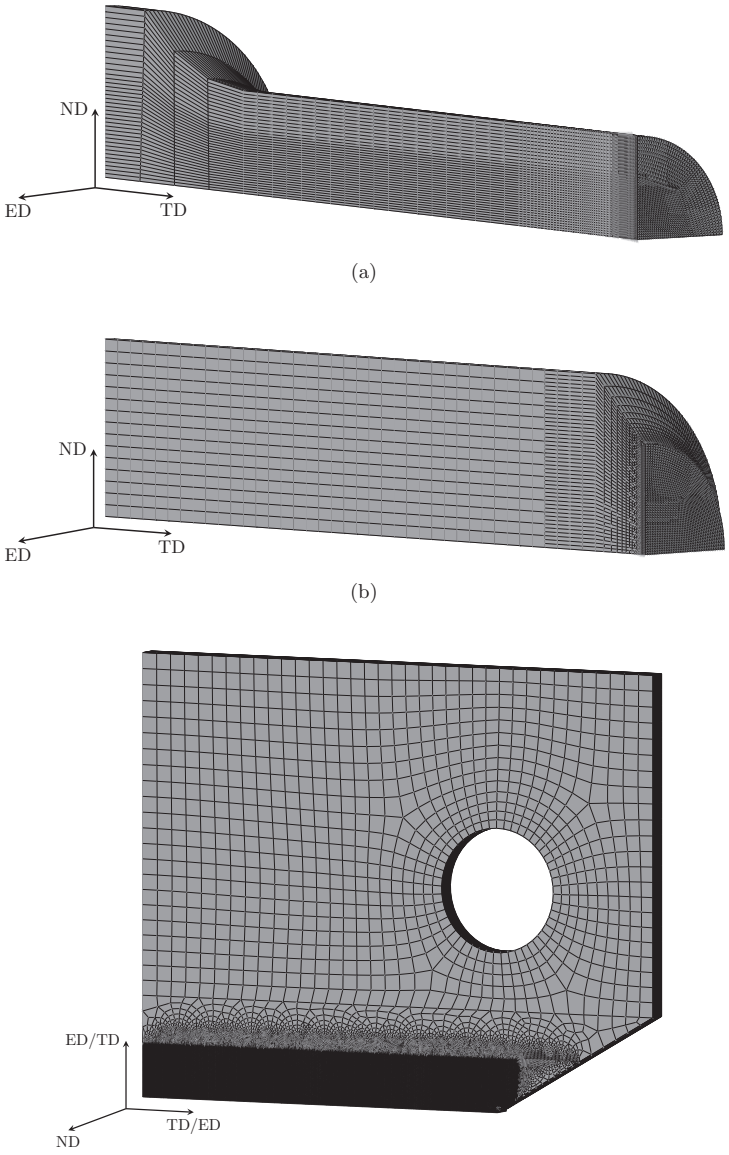

Figure 15: Finite element meshes of (a) the smooth tensile specimen, (b) the V-notch tensile specimen, and (c) the Kahn tear test specimen.

In order to determine the work-hardening parameters of the materials, finite element simulations of the tensile test on the smooth specimen are run in Abaqus/Explicit combined with the non-linear optimization software LS-OPT [44]. The parameters of Equation (14) are calibrated by minimising the mean squared error between the stress-strain curves up to failure from the finite element simulation and the experimental tests. During this calibration, the material is assumed to have zero porosity (i.e., $f = 0$). The work-hardening parameters of the water-quenched material have previously been determined, and the reader is referred to Frodal et al. [43] for further details on the calibration process. Table 6 presents the resulting initial yield stress and the work-hardening parameters, where the parameter set has been adjusted to account for the minor softening introduced by the initial porosity calibrated below (i.e., $f = f_0$).

Table 6: Initial yield stress and parameters of the work-hardening rule.

Material	σ_0 (MPa)	θ_1 (MPa)	Q_1 (MPa)	θ_2 (MPa)	Q_2 (MPa)	θ_3 (MPa)	Q_3 (MPa)
6082.25-AC	99.6	2824.3	78.8	153.1	90.8	–	–
6082.25-WQ	302.1	489.1	30.1	474.5	28.7	50.4	281.8

The damage parameters of the porous plasticity model, including the initial porosity f_0, the critical porosity f_c, and the porosity at complete material failure f_F, are here calibrated using a similar approach as with the initial yield strength and the work-hardening parameters. Simulations of tensile tests on the smooth and V-notch specimens are performed in Abaqus/Explicit, and the distance between the point of maximum true stress (i.e., the true stress at incipient strain softening) is minimized simultaneously for both tests by means of the LS-OPT software. This ensures that the point of failure is precisely captured for both the tensile tests on the smooth and V-notch specimens. The resulting porous plasticity parameters are given in Table 7.

Table 7: Porous plasticity parameters, including initial porosity f_0, critical porosity f_c, and porosity at complete material failure f_F.

Material	f_0	f_c	f_F
6082.25-AC	$1.20 \cdot 10^{-3}$	$8.39 \cdot 10^{-3}$	$2.12 \cdot 10^{-1}$
6082.25-WQ	$1.30 \cdot 10^{-3}$	$8.38 \cdot 10^{-3}$	$6.08 \cdot 10^{-2}$

The stress-strain curves from the finite element simulations of the tensile tests of the smooth and V-notch specimens are shown in Figure 7 and Figure 8, respectively. A good agreement is found between the numerical and experimental results up to fracture for both the smooth and V-notch specimens, and the point of maximum true stress is well captured. In the tests of the smooth tensile specimens, the stress level drops abruptly after reaching the point of maximum true stress. Similarly, the stress level drops rapidly for the water-quenched material in the finite element simulation, whereas the decrease is less swift in the simulation of the air-cooled material. In the tests of the V-notch tensile specimens, accelerated damage induced softening is observed and the stress level decreases after the point of maximum true stress before a sudden drop of the stress level occurs. The same trends are seen in the numerical simulations, but the sudden drop in stress level is somewhat delayed. Thus, more energy is dissipated in the simulations than in the experiments before the material has lost all of its load-carrying capacity, i.e., the tensile ductility is somewhat overestimated in the simulations. It should however be noted that predictions of crack propagation by element deletion are mesh dependent and more accurate results might possibly have been obtained with an even finer mesh.

The resulting force-displacement curves from the simulations of the Kahn tear tests are presented in Figure 9. The peak force is slightly underestimated in the simulations for both the water-quenched and air-cooled materials, and the drop in the load level is not as steep after the peak force as observed in the experiments. In view of the results obtained in the simulations of the V-notch specimen subjected to tensile loading, it is reasonable to attribute the lower slope of the numerical force-displacement curves and the

higher energy dissipation during crack propagation to the more ductile failure mode of the finite element model. In addition, errors in the calibrated yield surface may become apparent for this loading condition. However, the differences observed experimentally between the water-quenched and air-cooled materials are well captured in the simulations, i.e., the predicted load level for the water-quenched material drops below that of the air-cooled material when the displacement increases.

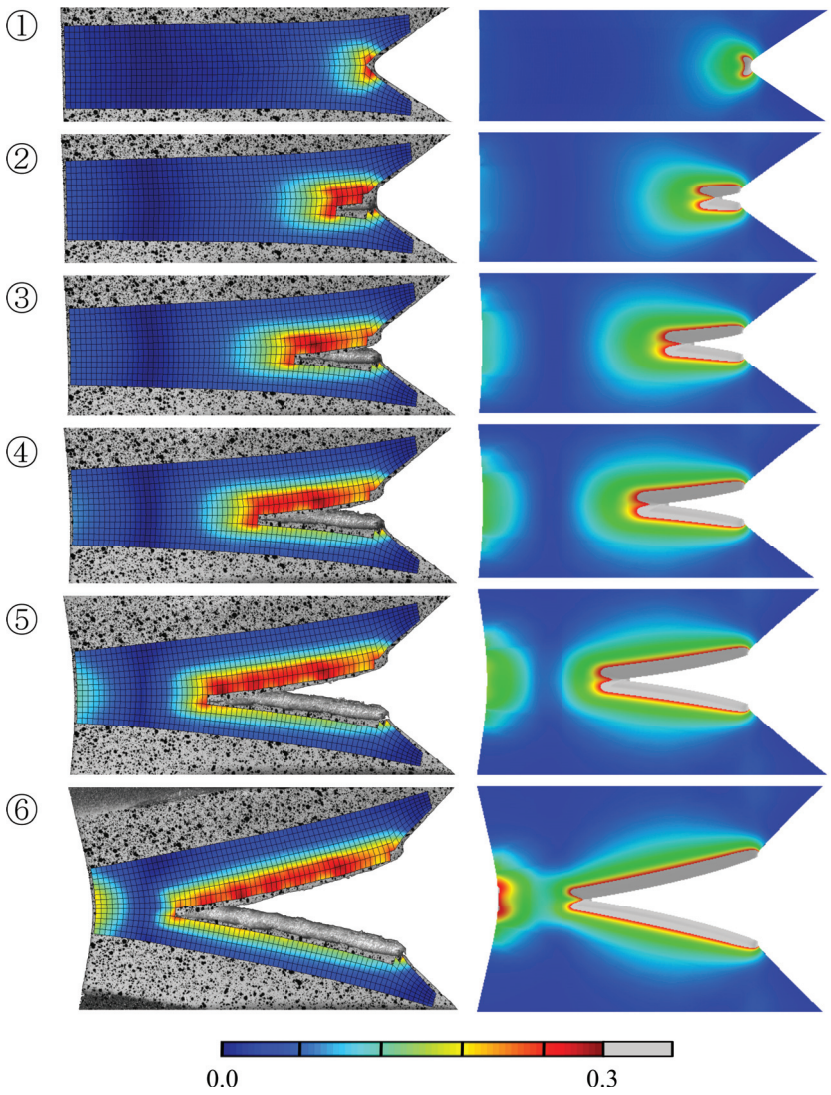

Figure 16: Contour plot of equivalent von Mises strain during crack propagation in the Kahn tear test of the air-cooled 6082.25 alloy loaded along ED: (left) experiment and (right) finite element analysis. Extracted images from the experiment and finite element analyses at the same crack opening displacement, see Figure 17.

Figure 16 depicts contours of the equivalent von Mises strain at failure initiation and during crack propa-

gation in the Kahn tear tests from the experiment and the finite element simulation of the air-cooled 6082.25 alloy loaded along ED. In the experiment, the strain field was calculated based on full-field measurements of the surface displacement field using digital image correlation (DIC). The strain fields from the experiment and the simulation are in relatively good agreement. Highly localized deformation is observed close to the notch and crack tip, where the equivalent strain is the highest. At peak force ①, "butterfly wing" shaped contours are seen close to the notch and further away from the notch tip the contours are more circular. As the crack progresses through the alloy, ②-⑥, the "butterfly wing" shaped contours persist in front of the crack tip. Figure 17 depicts the corresponding image locations on the force-displacement curve for the air-cooled 6082.25 alloy loaded along ED.

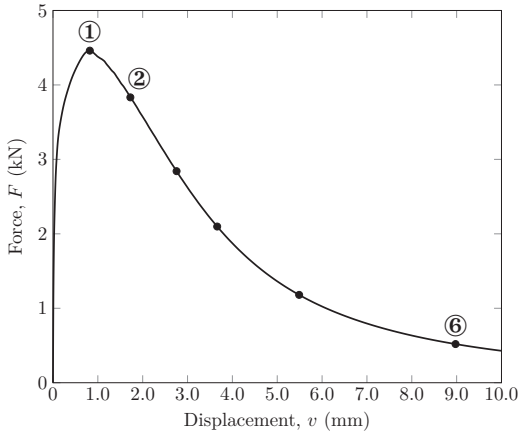

Figure 17: Force-displacement curve from the finite element analysis of the Kahn tear test with the air-cooled 6082.25 alloy loaded along ED. Markers correspond to the images in Figure 16.

6. Discussion

From the microstructural investigation in Section 4.1, it is evident that the precipitate structure is markedly influenced by the quench rate. A slower quench rate, i.e., air-cooling, gives a reduced volume fraction of strengthening precipitates within the grains, and wider PFZs at the grain boundaries and around the dispersoids. The influence of quench rate on the number density, cross-sectional area and length of the precipitates depends on the alloy. The lean 6060 alloy has a lower number density of precipitates after air-cooling and the precipitates have a larger cross-section area and length. The air-cooling is detrimental to the precipitate structure of the 6082.25 alloy, which has a fibrous grain structure with flat, elongated grains and small sub-grains, and results in an inhomogeneous microstructure where entire grains are free of strengthening precipitates. Precipitation in the 6082.50 alloy also becomes inhomogeneous after air-cooling, consisting of strong regions with dense precipitation resembling the water-quenched state and relatively large soft regions around dispersoids (due to PFZs around dispersoids).

The reduced number density of precipitates in the air-cooled 6060 alloy is most likely due to diffusion of solute and vacancies to GBs and other inhomogeneities in the microstructure. In the 6082.25 alloy, the inhomogeneous precipitation observed is due to overlapping PFZs from GBs and dispersoids. PFZs around dispersoids are also the reason for the inhomogeneous precipitate microstructure observed in the 6082.50 alloy. The physical origin of the increased precipitation outside these PFZs compared to the water-quenched state of this alloy has not been established. This particular aspect is outside of the scope of the current article, but should be of interest for future studies.

Albeit the width of the PFZs increases if air-cooling is used instead of water-quenching in all the three alloys, the relative increase depends on the alloy and is largest for the high-strength 6082 alloys. The reason for this observation is the very narrow PFZs in these alloys after water-quenching due to the increased precipitation potential of high-solute alloys. If one considers the absolute change in PFZ widths instead, the PFZs in the 6060 alloy widen more than those in the 6082.50 alloy. However, it should be mentioned here that there are some challenges in measuring PFZ widths in the dense alloys. In the 6082.25 alloy, precipitates were rarely observed, and in the 6082.50 alloy, few grain boundaries could be found in the TEM specimens due to the large grains.

In the following, the physically based model NaMo is used to predict the effect of different cooling conditions, grain structures and PFZ widths on the resulting yield strength after the final ageing heat treatment. NaMo is a combined precipitation, yield strength and work hardening model for 6xxx alloys. The model predicts the evolution of the precipitate structure for each time step during a non-isothermal heat treatment based on user-defined inputs including the alloy composition. The relevant parameters from the precipitate module of NaMo are used to calculate the yield stress and the work hardening rate through dislocation mechanics, and a complete stress-strain curve at room temperature can be predicted. The model has previously been outlined in several publications, see, e.g., [45, 46, 47, 48], and the readers are referred to these for a comprehensive description of the underlying theory and mathematical framework of NaMo. In the present article, only some special characteristics of the model, which are related to quench sensitivity, are described in more details, to explain how the model handles the different grain structures and PFZ widths for the alloys in the present investigation.

The model assumes that the alloy consists of two different materials, i.e., PFZ material that forms adjacent to grain boundaries and dispersoids, and matrix material that forms outside the PFZs. NaMo estimates the yield stress in each of these zones as well as the overall volume fraction of PFZs in the alloy based on grain structure data, dispersoid density data and PFZ widths. In the present study, the dispersoid density data of the two 6082 alloys has been determined using the Alstruc model [49, 50]. The estimated dispersoid number densities are $4.6{\cdot}10^{19}$ #/m^3 and $1.0{\cdot}10^{19}$ #/m^3, and the average dispersoid diameters are 54 nm and 84 nm for the 6082.25 and 6082.50 alloy, respectively. Figure 18 shows how the volume fraction of PFZs is estimated for the different materials in the present work. For large elongated recrystallized grains, like the ones in the 6082.50 alloy, the grain structure is illustrated in Figure 18a, where d_1 and d_3 are average grain sizes along the extrusion direction (ED) and thickness direction (ND), respectively. The grain size d_2 in the transverse direction (TD) is not shown in the two-dimensional figure, but for the 6082.50 alloy, it is about the same size as d_1. The volume fraction of PFZ, i.e., f_{PFZ}, for this type of grain structure can be estimated as follows

$$f_{\mathrm{PFZ}} = 1 - \frac{(d_1 - \delta)(d_2 - \delta)(d_3 - \delta)}{d_1 d_2 d_3} \tag{19}$$

Here, δ is the total PFZ width, i.e. on both sides of the grain boundary, and it is assumed that δ is the same in all the three directions ED, TD, and ND.

The recrystallized grains in the 6060 alloy are assumed to be equiaxed like the one schematically illustrated in Figure 18b. In this case, f_{PFZ} can be calculated by substituting d_1, d_2 and d_3 in Equation (19) by an average grain size d, which gives

$$f_{\mathrm{PFZ}} = 1 - \frac{(d - \delta)^3}{d^3} \tag{20}$$

Equation (20) is not restricted to recrystallized grains, but can also be used to estimate the volume fraction of PFZs associated with the equiaxed subgrain structure of the 6082.25 alloy based on the measured average subgrain-size.

NaMo also calculates the volume fraction of PFZ associated with dispersoids by assuming that each particle is encircled by a spherical PFZ. The volume fraction is then simply given as the volume of PFZ for each particle multiplied by the particle number density N_v as described by the following equation

$$f_{\mathrm{PFZ}} = \frac{4}{3}\pi \left[(r + \Delta r)^3 - r^3 \right] N_v \tag{21}$$

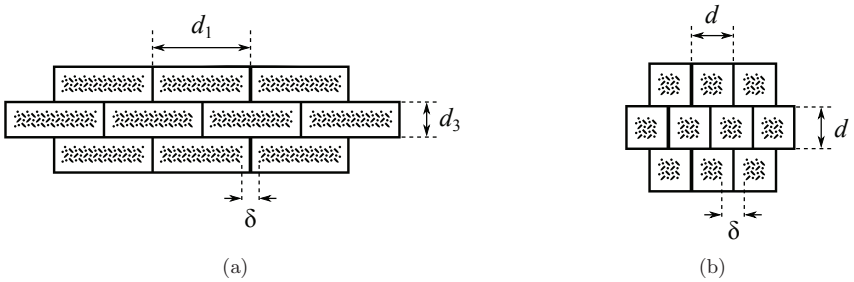

Figure 18: Schematic diagram showing the assumed PFZs in the different materials. The hatched regions illustrate precipitates that form within the matrix material after ageing, while the white regions are PFZs: (a) elongated grains, and (b) equiaxed grains.

Here r and Δr are the radius of the particle and the width of the PFZ adjacent to the particle surface, respectively. Note that in the following calculations, the contribution from PFZs around dispersoids is neglected as the PFZ width around these particles has not been determined in the present work.

In the estimation of the yield stress of the PFZ regions, it is simply assumed that this material does not respond to any ageing. This means that there is no nucleation of particles in these zones. The yield stress is therefore given by the solid solution concentrations of the different elements after the water-quenching or air-cooling described in Figure 1, as calculated by NaMo. For the matrix material, NaMo calculates the precipitation and resulting yield stress during the subsequent artificial ageing without any modifications of the model. In both the PFZ and matrix material, NaMo accounts for the negative effect of the dispersoids on the resulting yield strength due to coarse β'-type of particles that may nucleate at dispersoids during cooling [51]. In the PFZ material, this lowers the solid solution strengthening due to reduced solid solution concentrations of Mg and Si that are consumed to form these non-hardening particles during the cooling stage. In the matrix material, this reduction in Mg and Si lowers the hardening potential of the alloy, which in turn leads to a reduction in yield stress after artificial aging [51].

Finally, when the volume fraction of PFZs and the yield stress in each of the two zones, i.e., matrix and PFZ, are known, the resulting yield stress σ_0 is simply calculated as follows

$$\sigma_0 = (1 - f_{\mathrm{PFZ}})\sigma_{\mathrm{M}} + f_{\mathrm{PFZ}} \cdot \sigma_{\mathrm{PFZ}} \tag{22}$$

Here, σ_{M} and σ_{PFZ} are the yield stress of the matrix material and the PFZ material, respectively. Equation (22) is obviously a crude approximation of the integrated effect of the two individual materials on the resulting yield stress. In reality, σ_0 depends not only on the individual volume fractions of PFZ material and matrix material, but also on the spatial distribution and size of the individual PFZs.

Table 8: Calculated volume fractions of PFZs from grains, subgrains, dispersoids, and the total volume fraction, and calculated yield stresses, where σ_{M}, σ_{PFZ} and σ_0 are the yield stress of the matrix material, the PFZ material and the overall yield stress, respectively.

Material	f_{PFZ} (%)			σ_{M} (MPa)	σ_{PFZ} (MPa)	σ_0 (MPa)
	grains	subgrains	total			
6060-AC	2.2	-	2.2	166	90	164
6060-WQ	0.7	-	0.7	191	42	190
6082.25-AC	3.6	42.0	45.6	187	129	161
6082.25-WQ	0.7	8.9	9.6	327	132	308
6082.50-AC	< 0.1	-	< 0.1	164	107	164
6082.50-WQ	< 0.1	-	< 0.1	348	129	348

Table 8 shows the calculated volume fractions of PFZs for the six different combinations of alloy and cooling rate, and the corresponding yield stresses of the matrix material, the PFZ material, and the overall yield stress. Figure 19 shows a comparison between the calculated yield stresses σ_0 from Table 8, and the corresponding measured values given in Table 3. It is evident that the agreement between simulation results and measurements is good, and NaMo seems to capture the effect of alloy composition, grain structure, PFZ widths and cooling rate on the resulting yield stress with a good degree of accuracy.

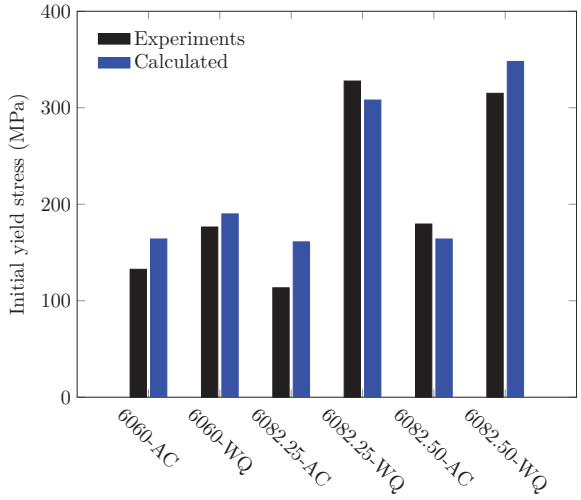

Figure 19: Comparison between the measured (Table 3) and calculated (Table 8) yield stress for the different alloys and cooling conditions.

The predictions of yield stress from NaMo are very close to the experimental values for all the alloys and heat treatments. In the 6060 alloy, NaMo predicts an overall reduction in precipitate strengthening upon air-cooling, and the effect of PFZs is low. In the 6082.25 alloy, the dramatic increase in PFZ volume fraction is responsible for the much lower yield stress of the air-cooled alloy compared to the water-quenched alloy. For the 6082.50 alloy, NaMo predictions are also good. In this case, NaMo predicts an overall lower number density of precipitates in the air-cooled alloy compared to the water-quenched alloy, which is responsible for the reduction in yield stress, as the volume fraction of PFZs are estimated to be relatively low. The TEM investigations indicated, however, that σ_M should be relatively similar for both the air-cooled and water-quenched states of this alloy, and that the inhomogeneous precipitate microstructure observed after air-cooling should increase the volume fraction of PFZs. It appears that the complex precipitation behaviour of this alloy is not captured by NaMo, and that the inhomogeneous distribution of precipitates and PFZs around dispersoids leads to a state of complex yielding and plastic flow in the material. This complex microstructure will probably affect the response observed in the tensile tests, and may explain the greater work-hardening rate in the air-cooled state compared to the water-quenched state of the 6082.50 alloy. Because the precipitation in these two materials primarily differs with respect to PFZs around dispersoids, making the air-cooled microstructure quite inhomogeneous, the difference in work hardening may be related to storage of dislocations within soft PFZs around hard impenetrable particles. Kawabata and Izumi [52] showed that the initial yield stress and plastic deformation of materials can depend on the PFZs, and of the strength difference between precipitate strengthened regions and PFZs. In particular, they suggested that early strain localization can lead to a high initial work-hardening rate and that this effect can increase with increasing PFZ size. This is in agreement with our experimental findings, where a higher work-hardening rate is observed for the air-cooled materials.

In previous studies on various aluminium alloys, the tensile ductility has been found to decrease with

increasing yield strength for similar grain structure [53, 54, 55, 56]. Consistent findings are made in this study, i.e., the tensile tests on air-cooled smooth and V-notch specimens give higher failure strain than those on water-quenched specimens. A plausible explanation for this finding is that the higher yield strength of the water-quenched materials accelerates void nucleation at constituent particles [26]. In addition, the work-hardening rate is greater for the air-cooled than for the water-quenched materials, see Figure 7 and Table 6, which is typically observed when the yield strength is reduced. The higher work-hardening rate of the air-cooled materials contributes to distributing the plastic deformation over a larger area of the specimen which delays necking, plastic localization and ductile fracture [57].

The crack initiation energies (UIEs) for the 6060 and 6082.25 alloys are similar for the air-cooled and water-quenched materials, see Table 5. As the peak force of the Kahn tear tests is lower after air-cooling, see Figure 9, the displacement to fracture initiation is larger than after water-quenching. This is consistent with the observed higher tensile ductility after air-cooling from the smooth and V-notch specimens. In contrast, air-cooling gives a slightly reduced crack initiation energy for the 6082.50 alloy compared to water-quenching.

The crack propagation energies (UPEs) are significantly affected by the quench rate for all the three alloys. For the 6060 alloy, the energy required for crack propagation is lower for air-cooling, but the difference in UPE compared with water-quenching is of the same magnitude as the difference in UPE between loading along ED and TD. Thus, the effect of quench rate on the UPE is equally large as the effect of plastic anisotropy for this alloy. Albeit a significant amount of intercrystalline fracture is observed for loading along TD, see Figure 11, the UPE is higher than what was observed for loading along ED, where very little intercrystalline fracture was observed. This indicates that the plastic anisotropy, caused by the crystallographic texture, has a significant influence on the UPE for this alloy having equiaxed grains. While the UPE is reduced after air-cooling for the 6060 alloy, it is drastically increased after air-cooling for the 6082.25 alloy compared with water-quenching. This suggests that the microstructure of this alloy after air-cooling, comprised of precipitate-free regions spanning entire grains, is favourable for the tear resistance compared to the water-quenched condition where the material consists of hard precipitate-strengthened grains surrounded by thin PFZs. For the 6082.50 alloy, the UPE is lower for the air-cooled material when loaded along ED and markedly higher when loaded along TD compared with the water-quenched material. These findings can be linked to the amount of intercrystalline fracture observed on the fracture surfaces, see Figure 13, as the intercrystalline fracture reduces the UPE [21, 22, 23, 17]. When the water-quenched material is suseptible to intercrystalline fracture, as the 6082.50 alloy is when loaded in TD, air-cooling increases the UPE by decreasing the amount of intercrystalline fracture. This is likely due to the increased capacity of wider PFZs to alleviate stresses ahead of slip bands, as suggested by Kawabata and Izumi [52] and Ryum [58]. However, when the water-quenched material is not susceptible to intercrystalline fracture, i.e., when the 6082.50 alloy is loaded in ED, air-cooling reduces the UPE despite a lower yield stress, by promoting intercrystalline fracture instead. In this case, the increased amount of intercrystalline fracture may be related to strain localization and preferential deformation in the wider PFZs, or the increased number of large particles (precipitates on dispersoids) that may act as void nucleation sites [59].

The porous plasticity model is capable of describing the plastic flow and failure initiation in the tensile tests on smooth and V-notch specimens with good accuracy, while the crack propagation speed is underestimated, i.e., the stress level in the simulations drops more gradually than in the experiments. The failure initiation is well predicted also for the Kahn tear test specimen, although the peak force is slightly underestimated, most probably due to inaccuracies in the calibrated yield surface. During crack propagation, the predicted force level is higher than that observed experimentally and the dissipated energy due to plastic deformation is overestimated. In the numerical simulations, the crack propagation is predicted by element deletion, and as such the crack tip radius is governed by the element size, rendering the crack propagation highly mesh dependent. As a result, the adopted failure modelling approach, i.e., combining porous plasticity with element erosion, is best suited for situations where the mechanisms of damage evolution and fracture are not as localized as in the Kahn tear test. However, it is assumed that the results could be improved by further decreasing the mesh size and thus increase the crack propagation speed in the simulations, see e.g. Besson [60] for a detailed discussion of mesh size sensitivity in finite element simulation of ductile fracture.

7. Concluding remarks

The role of quench rate after the solution heat-treatment on the plastic flow and fracture of three aluminium alloys was studied by conducting tensile tests on smooth and V-notched specimens as well as Kahn tear tests. The three AlMgSi alloys considered, i.e., 6060, 6082.25 and 6082.50, had different grain structure, grain size and crystallographic texture. The alloys were differently affected by the quench rate, as obtained by water-quenching or air-cooling. The TEM study showed that air-cooling is detrimental for precipitation in all alloys. In lean alloys, like the 6060 alloy, the detrimental effect is due to an overall reduction in precipitate number density and slightly coarser precipitates. In dense alloys that contain dispersoids, like the 6082 alloys, PFZs around the dispersoids become much wider after air-cooling. If the density of dispersoids is high and the grain size is small, such as in the 6082.25 alloy, the PFZs of adjacent dispersoids overlap, and due to the small grain and subgrain size in this material, entire grains can become free of precipitates. If the density of dispersoids is low and the grain size is relatively large, as in the 6082.50 alloy, PFZs around dispersoids do not necessarily overlap, resulting in an inhomogenous microstructure consisting of strong regions of dense preciptiation a certain distance from dispersoids that are surrounded by wide PFZs. Air-cooling gave consistently larger precipitate free zones around both GBs and dispersoids in the three alloys than water-quenching.

The changes in the precipitatate microstructure affects the initial yield stress, and air-cooling gave a lower yield stress for all three alloys. These changes were captured by the nanostructure model NaMo with good accuracy. In all materials, NaMo was able to predict correct precipitation and strengthening contributions, except for the air-cooled 6082.50 alloy where a homogeneous reduced precipitation was predicted. In this material, the microstructure is highly complex and inhomogeneous, which is not easily captured by such models. The plastic behaviour of this material is possibly linked to a complex interplay between the soft PFZs and hard precipitate strengthened regions.

In the Kahn tear tests, the displacement to crack initiation was larger for the air-cooled materials, as the crack initiation energies were similar for different quench rates, but the peak force was drastically reduced. The crack propagation energy was markedly affected by the quench rate after the solution heat-treatment, but the effect was different for the different alloys. Compared with water-quenching, air-cooling led to lower crack propagation energy for the 6060 alloy and higher crack propagation energy for the 6082.25 alloy, where entire grains are free of strengthening precipitates due to the slow cooling. For the 6082.50 alloy, the influence of quench rate on the crack propagation energy was different for the two loading directions, i.e., either along the extrusion direction or along the transverse in-plane direction, and can be linked to the amount of intercrystalline fracture observed on the fracture surface, as intercrystalline fracture reduces the crack propagation energy.

The anisotropic porous plasticity model used in the finite element simulations was able to precisely capture the fracture initiation in all the specimen geometries for the 6082.25 alloy. Albeit the dissipated energy due to plastic deformation was overestimated during crack propagation, the overall response was well captured, and the porous plasticity model was able to account for the influence of quench rate. The 6060 and 6082.50 alloys demonstrated effects and properties that the porous plasticity model was unable to describe. Thus, there is a need for more advanced physically-based models which are able to account for both the complex anisotropy of textured aluminium alloys and intercrystalline fracture due to the grain boundary PFZs in these materials.

Acknowledgements

The financial support of this work from the Centre for Advanced Structural Analysis (CASA), Project No. 237885, Centre for Research-based Innovation (CRI) at the Norwegian University of Science and Technology (NTNU), is gratefully acknowledged.

References

[1] A. L. Dons, O. Lohne, Quench Sensitivity of AlMgSi-Alloys Containing Mn or Cr, MRS Proceedings 21 (1983) 723.

[2] K. Strobel, M. D. H. Lay, M. A. Easton, L. Sweet, S. Zhu, N. C. Parson, A. J. Hill, Effects of quench rate and natural ageing on the age hardening behaviour of aluminium alloy AA6060, Materials Characterization 111 (2016) 43 – 52.
[3] K. Strobel, M. A. Easton, L. Sweet, M. J. Couper, J.-F. Nie, Relating quench sensitivity to microstructure in 6000 series aluminium alloys, Materials Transactions 52 (2011) 914–919.
[4] K. Strobel, M. A. Easton, M. D. H. Lay, P. A. Rometsch, S. Zhu, L. Sweet, N. C. Parson, A. J. Hill, Quench Sensitivity in a Dispersoid-Containing Al-Mg-Si Alloy, Metallurgical and Materials Transactions A 50 (2019) 1957–1969.
[5] M. Conserva, P. Fiorini, Interpretation of quench-sensitivity in Al-Zn-Mg-Cu Alloys, Metallurgical Transactions 4 (1973) 857–862.
[6] B. Milkereit, M. J. Starink, Quench sensitivity of Al–Mg–Si alloys: A model for linear cooling and strengthening, Materials & Design 76 (2015) 117 – 129.
[7] A. Deschamps, G. Texier, S. Ringeval, L. Delfaut-Durut, Influence of cooling rate on the precipitation microstructure in a medium strength Al–Zn–Mg alloy, Materials Science and Engineering: A 501 (2009) 133 – 139.
[8] M. S. Remøe, K. Marthinsen, I. Westermann, K. Pedersen, J. Røyset, C. Marioara, The effect of alloying elements on the ductility of Al-Mg-Si alloys, Materials Science and Engineering: A 693 (2017) 60 – 72.
[9] B. Milkereit, C. Schick, O. Kessler, Continuous cooling precipitation diagrams depending on the composition of aluminum-magnesium-silicon alloys, in: Proceedings of the 12th International Conference on Aluminium Alloys, Yokohama, Japan, 2010, pp. 407–412.
[10] A. Falahati, P. Lang, E. Kozeschnik, Precipitation in Al-alloy 6016 – the role of excess vacancies, Materials Science Forum 706 (2012) 317–322. Trans Tech Publications.
[11] M. Werinos, H. Antrekowitsch, T. Ebner, R. Prillhofer, P. J. Uggowitzer, S. Pogatscher, Hardening of Al–Mg–Si alloys: Effect of trace elements and prolonged natural aging, Materials & Design 107 (2016) 257 – 268.
[12] J. W. Evancho, J. T. Staley, Kinetics of precipitation in aluminum alloys during continuous cooling, Metallurgical Transactions 5 (1974) 43.
[13] H. Seyedrezai, D. Grebennikov, P. Mascher, H. S. Zurob, Study of the early stages of clustering in Al–Mg–Si alloys using the electrical resistivity measurements, Materials Science and Engineering: A 525 (2009) 186 – 191.
[14] P. N. T. Unwin, G. W. Lorimer, R. B. Nicholson, The origin of the grain boundary precipitate free zone, Acta Metallurgica 17 (1969) 1363 – 1377.
[15] O. Lohne, O. J. Naess, The Effect of Dispersoids and Grain Size on Mechanical Properties of AlMgSi Alloys, in: P. Haasen, V. Gerold, G. Kostorz (Eds.), Strength of Metals and Alloys, Pergamon, 1979, pp. 781 – 788.
[16] J. M. Dowling, J. W. Martin, The influence of MN additions on the deformation behaviour of an Al-Mg-Si alloy, Acta Metallurgica 24 (1976) 1147 – 1153.
[17] T. F. Morgeneyer, M. J. Starink, S. C. Wang, I. Sinclair, Quench sensitivity of toughness in an Al alloy: Direct observation and analysis of failure initiation at the precipitate-free zone, Acta Materialia 56 (2008) 2872 – 2884.
[18] M. Khadyko, C. D. Marioara, I. G. Ringdalen, S. Dumoulin, O. S. Hopperstad, Deformation and strain localization in polycrystals with plastically heterogeneous grains, International Journal of Plasticity 86 (2016) 128 – 150.
[19] Y. Chen, K. O. Pedersen, A. H. Clausen, O. S. Hopperstad, An experimental study on the dynamic fracture of extruded AA6xxx and AA7xxx aluminium alloys, Materials Science and Engineering: A 523 (2009) 253 – 262.
[20] E. Christiansen, C. D. Marioara, K. Marthinsen, O. S. Hopperstad, R. Holmestad, Lattice rotations in precipitate free zones in an Al-Mg-Si alloy, Materials Characterization 144 (2018) 522 – 531.
[21] D. Dumont, A. Deschamps, Y. Brechet, On the relationship between microstructure, strength and toughness in AA7050 aluminum alloy, Materials Science and Engineering: A 356 (2003) 326 – 336.
[22] D. Dumont, A. Deschamps, Y. Brechet, A model for predicting fracture mode and toughness in 7000 series aluminium alloys, Acta Materialia 52 (2004) 2529 – 2540.
[23] D. Dumont, A. Deschamps, Y. Bréchet, C. Sigli, J. C. Ehrström, Characterisation of precipitation microstructures in aluminium alloys 7040 and 7050 and their relationship to mechanical behaviour, Materials Science and Technology 20 (2004) 567–576.
[24] M. De Haas, J. T. M. De Hosson, On the effects of thermomechanical processing on failure mode in precipitation-hardened aluminium alloys, Journal of Materials Science 37 (2002) 5065–5073.
[25] R. T. Shuey, M. Tiryakioğlu, G. H. Bray, J. T. Staley, Toughness after interrupted quench, in: Aluminium Alloys 2006 - ICAA10, volume 519 of *Materials Science Forum*, Trans Tech Publications, 2006, pp. 1017–1022.
[26] A. Pineau, A. A. Benzerga, T. Pardoen, Failure of metals I: Brittle and ductile fracture, Acta Materialia 107 (2016) 424 – 483.
[27] E. Maire, S. Zhou, J. Adrien, M. Dimichiel, Damage quantification in aluminium alloys using in situ tensile tests in X-ray tomography, Engineering Fracture Mechanics 78 (2011) 2679 – 2690.
[28] H. Toda, H. Oogo, K. Horikawa, K. Uesugi, A. Takeuchi, Y. Suzuki, M. Nakazawa, Y. Aoki, M. Kobayashi, The True Origin of Ductile Fracture in Aluminum Alloys, Metallurgical and Materials Transactions A 45 (2013) 765–776.
[29] A. L. Gurson, Continuum theory of ductile rupture by void nucleation and growth: Part I—Yield criteria and flow rules for porous ductile media, Journal of Engineering Materials and Technology 99 (1977) 2–15.
[30] V. Tvergaard, Influence of voids on shear band instabilities under plane strain conditions, International Journal of Fracture 17 (1981) 389–407.
[31] V. Tvergaard, A. Needleman, Analysis of the cup-cone fracture in a round tensile bar, Acta Metallurgica 32 (1984) 157 – 169.
[32] D. Steglich, H. Wafai, J. Besson, Interaction between anisotropic plastic deformation and damage evolution in Al 2198 sheet metal, Engineering Fracture Mechanics 77 (2010) 3501 – 3518.
[33] L. E. B. Dæhli, J. Faleskog, T. Børvik, O. S. Hopperstad, Unit cell simulations and porous plasticity modelling for strongly

anisotropic FCC metals, European Journal of Mechanics - A/Solids 65 (2017) 360 – 383.
[34] B. H. Frodal, K. O. Pedersen, T. Børvik, O. S. Hopperstad, Influence of pre-compression on the ductility of AA6xxx aluminium alloys, International Journal of Fracture 206 (2017) 131–149.
[35] M. Khadyko, S. Dumoulin, T. Børvik, O. S. Hopperstad, An experimental–numerical method to determine the work-hardening of anisotropic ductile materials at large strains, International Journal of Mechanical Sciences 88 (2014) 25 – 36.
[36] ASTM, ASTM B871-01 Standard Test Method for Tear Testing of Aluminum Alloy Products, https://doi.org/10.1520/B0871-01, 2001.
[37] S. J. Andersen, Quantification of the Mg2Si β" and β' phases in AlMgSi alloys by transmission electron microscopy, Metallurgical and Materials Transactions A 26 (1995) 1931–1937.
[38] C. D. Marioara, S. J. Andersen, H. W. Zandbergen, R. Holmestad, The influence of alloy composition on precipitates of the Al-Mg-Si system, Metallurgical and Materials Transactions A 36 (2005) 691–702.
[39] M. Khadyko, S. Dumoulin, T. Børvik, O. S. Hopperstad, Simulation of large-strain behaviour of aluminium alloy under tensile loading using anisotropic plasticity models, Computers & Structures 157 (2015) 60 – 75.
[40] F. Barlat, H. Aretz, J. Yoon, M. Karabin, J. Brem, R. Dick, Linear transfomation-based anisotropic yield functions, International Journal of Plasticity 21 (2005) 1009 – 1039.
[41] Abaqus, Version 6.14, Dassault Systemès Simulia Corporation, 2014. Providence, Rhode Island, USA.
[42] M. Fourmeau, T. Børvik, A. Benallal, O. G. Lademo, O. S. Hopperstad, On the plastic anisotropy of an aluminium alloy and its influence on constrained multiaxial flow, International Journal of Plasticity 27 (2011) 2005 – 2025.
[43] B. H. Frodal, L. E. B. Dæhli, T. Børvik, O. S. Hopperstad, Modelling and simulation of ductile failure in textured aluminium alloys subjected to compression-tension loading, International Journal of Plasticity 118 (2019) 36 – 69.
[44] N. Stander, W. Roux, A. Basudhar, T. Eggleston, T. Goel, K. Craig, LS-OPT user's manual, Livermore Software Technology Corporation, 2015. Livermore, California, USA.
[45] O. R. Myhr, Ø. Grong, K. O. Pedersen, A Combined Precipitation, Yield Strength, and Work Hardening Model for Al-Mg-Si Alloys, Metallurgical and Materials Transactions A 41 (2010) 2276–2289.
[46] O. R. Myhr, Ø. Grong, C. Schäfer, An Extended Age-Hardening Model for Al-Mg-Si Alloys Incorporating the Room-Temperature Storage and Cold Deformation Process Stages, Metallurgical and Materials Transactions A 46 (2015) 6018–6039.
[47] O. R. Myhr, Ø. Grong, S. J. Andersen, Modelling of the age hardening behaviour of Al–Mg–Si alloys, Acta Materialia 49 (2001) 65 – 75.
[48] H. Granum, O. R. Myhr, T. Børvik, O. S. Hopperstad, Nanostructure-based finite element analyses of aluminium profiles subjected to quasi-static axial crushing, Thin-Walled Structures 131 (2018) 769 – 781.
[49] A. L. Dons, E. K. Jensen, Y. Langsrud, E. Trømborg, S. Brusethaug, The alstruc microstructure solidification model for industrial aluminum alloys, Metallurgical and Materials Transactions A 30 (1999) 2135–2146.
[50] A. L. Dons, The alstruc homogenization model for industrial aluminum alloys, Journal of Light Metals 1 (2001) 133 – 149.
[51] O. R. Myhr, O. Engler, J. R. Leinum, H. J. Brinkman, T. Furu, Modelling the effect of cooling rate on tensile properties of 6xxx series aluminium alloys for automotive applications, 2nd Conference & Exhibition on Light Materials (2017). November 8-10, Bremen, Germany.
[52] T. Kawabata, O. Izumi, Ductile fracture in the interior of precipitate free zone in an Al-6.0%Zn-2.6%Mg alloy, Acta Metallurgica 24 (1976) 817 – 825.
[53] D. J. Lloyd, The scaling of the tensile ductile fracture strain with yield strength in Al alloys , Scripta Materialia 48 (2003) 341 – 344.
[54] I. Westermann, K. O. Pedersen, T. Furu, T. Børvik, O. S. Hopperstad, Effects of particles and solutes on strength, work-hardening and ductile fracture of aluminium alloys , Mechanics of Materials 79 (2014) 58 – 72.
[55] K. O. Pedersen, I. Westermann, T. Furu, T. Børvik, O. S. Hopperstad, Influence of microstructure on work-hardening and ductile fracture of aluminium alloys , Materials & Design 70 (2015) 31 – 44.
[56] F. Hannard, T. Pardoen, E. Maire, C. L. Bourlot, R. Mokso, A. Simar, Characterization and micromechanical modelling of microstructural heterogeneity effects on ductile fracture of 6xxx aluminium alloys, Acta Materialia 103 (2016) 558 – 572.
[57] B. H. Frodal, D. Morin, T. Børvik, O. S. Hopperstad, On the effect of plastic anisotropy, strength and work hardening on the tensile ductility of aluminium alloys, Submitted for journal publication (2019).
[58] N. Ryum, The influence of a precipitate-free zone on the mechanical properties of an Al-Mg-Zn alloy, Acta Metallurgica 16 (1968) 327 – 332.
[59] A. K. Vasudévan, R. D. Doherty, Grain boundary ductile fracture in precipitation hardened aluminum alloys, Acta Metallurgica 35 (1987) 1193–1219.
[60] J. Besson, Continuum models of ductile fracture: A review, International Journal of Damage Mechanics 19 (2010) 3–52.

Part III

Conclusion and Outlook

Chapter 5

Conclusion and outlook

Advanced TEM techniques have been used to characterise aluminium alloys after deformation. SPED has been a very widely applied technique due to its sensitivity, versatility, and ability to quantitatively study larger areas than traditional TEM techniques, but HRTEM and atomic resolution STEM have also been used for detailed studies. The results of the thesis can be divided into two main parts; study of PFZs and study of dislocation-precipitate interactions in Al-Mg-Si alloys. These two parts are connected due to their coupling in terms of localisation of stress and strain, and ultimately are two important parts of ductile failure mechanisms. In this chapter, conclusions from these two studies are drawn, and suggestions for further work are discussed.

5.1 Precipitate Free Zones

The deformation mechanisms in PFZs are varied and complex, and depend on a number of factors. Paper 1 showed that the dislocation density in PFZs of the particular alloy is usually low, but that various features can develop [88]. Some of these features consist of dislocation accumulation at the transition region between PFZ and grain interior, which results in a misorientation between the PFZ as a whole and the grain interior. However, some PFZs can develop subgrains of high misorientation $\sim 20^{\circ}$ relative to the grain interior. These subgrains are likely a result of strain localisation in the particular PFZs during deformation, and is therefore a strain gradient effect phenomena. Instead of storing individual geometrically necessary or statistical dislocations, a form of recovery and strain induced recrystallisation occurs. This might strengthen the particular PFZ by a Hall-Petch mechanism [41], [42]. This strengthening mechanism will likely halt strain localisation and prevent further refinement of the sub grain structure. However, it is also

possible that further plasticity is achieved by grain boundary sliding between the PFZ subgrains. Furthermore, if the subgrain structure interacts with dislocations during deformation in a manner similar that seen in other pure metals [78], it is possible that voids may nucleate at the subgrain structures by a vacancy condensation mechanism. The consequence of the observed PFZ features with regards to ductile fracture is still unknown, and further work is needed. For instance, only PFZs of one alloy and heat treatment have been studied, and it will be beneficial to establish whether the features that form are dependent on the width of the PFZs. In addition, because PFZ strain localisation depends on the relative strength difference between the grain interior and the PFZ strength, different alloys and tempers should also be studied. This is particularly interesting considering the possibility of Hall-Petch strengthening in PFZs where strain localises, and it might be possible for even finer subgrain structures to form in PFZs of alloys with a stronger grain interior. *In situ* deformation experiments of thick specimens in high-voltage TEMs may be very useful in order to investigate the formation mechanisms of PFZ subgrain structures in various alloys.

The importance of PFZs has also been shown in relation to quench sensitivity of Al-Mg-Si alloys [129]. PFZs around GBs and dispersoids can become very wide if a slow quench rate from solution heat treatment is applied. If the density of GBs and dispersoids is high, the PFZs may overlap and lead to PFZs that span entire grains. The effect of this is that the alloy effectively becomes dramatically overaged for the same ageing time it takes to peak age it (if a fast water quench was applied instead). For alloys where the dispersoid content is low, the PFZs around dispersoids don't overlap, but they can still reduce the strength of the alloy. This softening occurs despite very dense precipitation away from the dispersoids. As such, the presence of wide PFZs inside strong precipitate strengthened regions are very detrimental to the material strength. The dispersoid PFZs also seem to increase work hardening. These findings are important in order to further develop simulation tools, such as NaMo [58], that can be used in a multi-scale simulation framework. There are numerous possible avenues for further work with regards to the quench sensitivity of Al-Mg-Si alloys and how it can be modelled, but only two are suggested here. First of all, establishing models for early clustering behaviour and precipitation is important, as this is required to predict eventual precipitation inhomogeneities. Secondly, the role of the dispersoid PFZs should be determined, for example by studying air cooled alloys after deformation. It will be particularly interesting to apply the same techniques that were applied to study the GB PFZ deformation mechanisms discussed in the previous paragraph, in order to investigate dislocation structures and eventual subgrain formation within the dispersoid PFZs. As a final note on the role of PFZs, it seems that wide GB PFZs (in slowly cooled state) increase ductility if the material is susceptible to intergranular ductile failure

with a narrower GB PFZ (in rapidly cooled state). If the material is not susceptible to intergranular ductile failure with a narrow PFZ, the wider GB PFZ in the slowly cooled state may promote intergranular ductile fracture and reduce the ductility in stead. Hence, GB PFZs are important for the ductility of age-hardenable aluminium alloys, but their effects can vary greatly depending on the microstructure of the material.

5.2 Shearing of β" precipitates

This thesis has shown that β" precipitates are most likely sheared by single steps of matrix Burgers vectors, distributed along the precipitate lengths [63], [122]. While most published literature seems to agree that these precipitates are sheared [62], [130], [131], there are some works that considers them as impenetrable precipitates that are looped by dislocations [61], [132]. Our work has shown that they must undergo some structural change during deformation, and we propose that this is due to planar defects inside the precipitates introduced by shearing. Of course the precipitates may, in principle, be looped by one or even two dislocations initially, but they must eventually be sheared. It has been a theoretical possibility that β" precipitates are sheared by a vector that is compatible with the precipitate crystal structure, and that the difference between this shearing vector and the Burgers vector of the matrix could be absorbed as elastic strain around the precipitates. However, we now know that the internal precipitate structure becomes disrupted by the shearing, and that they are therefore most likely sheared by the Burgers vector of the matrix. We also suggest that this shearing creates a local disruption of the crystal structure on the shearing plane. We observe several shearing planes, which suggests that the precipitates are sheared several times in more than one location. Based on this, and the fact that no big steps could be observed on the precipitate surfaces, it seems likely that the planar defects on the shearing planes makes it harder for repeated shear in the same plane. Hence, while these precipitates are shearable, they are not necessarily responsible for eventual strain localisation in these alloys, supporting earlier studies by Poole, Wang, Lloyd and Embury [130]. Based on multislice image simulations, the spacing between the shear planes must be about $10\ \mathrm{nm}$ in order to produce images similar to experimentally obtained ones [122]. Given a certain precipitate needle length, in the present case $\sim 40\ \mathrm{nm}$, this requires about 5 shearing events distributed along the precipitates. If these shearing events are due to the passage of one Burgers vector or several is not clear. However, if several Burgers vectors glide on the same plane, the local strain must be very high in order to shear precipitates so that they produce TEM images like the ones observed. Furthermore, the first shearing event (below the entrance surface of the thin foils) can not lie too close to the surface for atomic resolution to be obtained in STEM experiments. The sheared segments below

this first segment must be $\sim 10\ \mathrm{nm}$ thick. Finally, for the shadow-like regions observed close to precipitates seen in experimental STEM images to form, the lower segments cannot be too thick or shifted too far relative to the initial segment. The TEM image simulations in Paper 3 therefore support the experimental results and conclusions from Paper 2. In combination, the experimental work and the image simulations provide valuable knowledge and input to models of strength and work hardening. Applying this knowledge directly to a multi-scale modelling framework is challenging, however, and future studies are required.

Future work with respect to the shearing of β" precipitates can be divided in two groups: experiments and simulations. Future experimental work is needed to investigate how the aspect ratio of β" precipitates influences the shearing process, and how precipitates of different lengths appear after deformation. In addition, studies that investigate the same precipitate from different directions (by flipping the thin foil for instance) with several techniques would give detailed insight into the nature of the planar defects. If a thin needle-like specimen could be manufactured with a $[100]$ orientation, precipitates oriented along $[010]$ and $[001]$ could be investigated both parallel and perpendicular to their lengths. Tomography and 3D imaging of precipitates in deformed alloys will also be useful, especially if the results can be related to *in situ* deformation experiments and Burgers vector analysis. Future simulation work would benefit from this, as the distribution of slip along the needles could be determined with greater accuracy. Such simulations could consist of both *ab initio* simulations and molecular dynamics simulations. Energy barriers for successive slip on the same plane could be calculated from *ab initio* and be compared with the observed geometry of needles in experimental findings. MD simulations might provide insight into the atomic arrangement within the planar defects, and the energy required to form them. Coupling molecular dynamics simulations and *ab initio* simulations with TEM image simulations provides a way of validated the results from such simulations, and thus provide physically based estimates of the strengthening contribution from β" precipitates. Such models may be connected to models further up in scale and provide more accurate predictions of strength, work hardening, and ductile fracture of aluminium alloys.

References

[1] I. Polmear, *Light Alloys*, 4th ed. Oxford: Butterworth-Heinemann, 2005.

[2] G. Djukanovic, *Latest trends for aluminium demand in automotive industry*, Spotlightmetal, Ed., 24th2018. (visited on 23/06/2019).

[3] J. W. Martin, *Micromechanisms in particle-hardened alloys*, ser. Cambridge Solid State Science Series. Cambridge UK: Cambridge University Press, 1980.

[4] R. B. Nicholson, G. Thomas and J. Nutting, "The interaction of dislocations and precipitates", *Acta Metallurgica*, vol. 8, no. 3, pp. 172–176, 1960.

[5] P. B. Hirsch, A. Howie, R. B. Nicholson, D. W. Pashley and M. J. Whelan, *Electron Microscopy of thin crystals*, 1st ed. Butterworths, 1965.

[6] D. B. Williams and B. C. Carter, *Transmission Electron Microscopy*. Springer, 2009.

[7] G. Van Tendeloo, S. Bals, S. Van Aert, J. Verbeeck and D. Van Dyck, "Advanced Electron Microscopy for Advanced Materials", *Advanced Materials*, vol. 24, no. 42, pp. 5655–5675, 2012. DOI: 10.1002/adma.201202107.

[8] H. G. F. Wilsdorf and J. Schmitz, "The Observation and Interpretation of Dislocation Tangles in the Easy Glide Range of Aluminum", *Journal of Applied Physics*, vol. 33, no. 5, pp. 1750–1754, 1962. DOI: 10.1063/1.1728823.

[9] R. N. Gardner, T. C. Pollock and H. G. F. Wilsdorf, "Crack initiation at dislocation cell boundaries in the ductile fracture of metals", *Materials Science and Engineering*, vol. 29, no. 2, pp. 169–174, 1977. DOI: 10.1016/0025-5416(77)90123-9.

[10] F. R. N. Nabarro, Ed., *Dislocations in Solids*, ser. Dislocations in Metallurgy. Amsterdam, Netherlands: North-Holland Publishing Company, 1979, vol. 4.

[11] K. Jagannadham and H. G. F. Wilsdorf, "Spatially varying crack tip stress fields and low energy dislocation substructures", *International Journal of Fracture*, vol. 34, no. 4, pp. 297–307, 1987. DOI: 10.1007/BF00013084.

[12] M. J. Whelan, "The development and early applications of the weak-beam technique", *Philosophical Magazine*, vol. 90, no. 35-36, pp. 4611–4622, 2010. DOI: 10.1080/14786430903581312.

[13] M. F. Ashby, "The deformation of plastically non-homogeneous materials", *Philosophical Magazine A*, vol. 21, no. 170, pp. 399–424, 1970.

[14] ——, "The deformation of plastically non-homogeneous alloys", in *Strengthening Methods in Crystals*, ser. Elsevier Materials Science Series, A. Kelly and R. B. Nicholson, Eds., Amsterdam, Netherlands: Elsevier Publishing Company LTD, 1971, pp. 137–190.

[15] N. A. Fleck, G. M. Muller, M. F. Ashby and J. W. Hutchinson, "Strain gradient plasticity: Theory and experiment", *Acta Metallurgica et Materialia*, vol. 42, no. 2, pp. 475–487, 1994. DOI: 10.1016/0956-7151(94)90502-9.

[16] M. Langseth, *Casa project description*, 2014.

[17] E. Nembach, *Particle Strengthening of metals and alloys*. New York USA: Wiley, 1997.

[18] J. T. Fourie and H. G. F. Wilsdorf, "Production of Dislocation Loops by a Combined Climb and Glide Mechanism", *Journal of Applied Physics*, vol. 31, no. 12, pp. 2219–2223, 1960. DOI: 10.1063/1.1735525.

[19] A. H. Cottrell, *Dislocations and Plastic Flow in Crystals*, ser. The International Series of Monographs in Physics. Oxford UK: Clarendon Press, 1958.

[20] B. Clausen, T. Lorentzen and T. Leffers, "Self-consistent modelling of the plastic deformation of f.c.c. polycrystals and its implications for diffraction measurements of internal stresses", *Acta Materialia*, vol. 46, no. 9, pp. 3087–3098, 1998. DOI: 10.1016/S1359-6454(98)00014-7.

[21] F. J. Humphreys and M. Hatherly, *Recrystallization and related annealing phenomena*. Elsevier, 2004.

[22] S. Pogatscher, H. Antrekowitsch, H. Leitner, D. Pöschmann, Z. L. Zhang and P. J. Uggowitzer, "Influence of interrupted quenching on artificial aging of Al-Mg-Si alloys", *Acta Materialia*, vol. 60, no. 11, pp. 4496–4505, 2012. DOI: 10.1016/j.actamat.2012.04.026.

[23] T. Saito, E. A. Mørtsell, S. Wenner, C. D. Marioara, S. J. Andersen, J. Friis, K. Matsuda and R. Holmestad, "Atomic Structures of Precipitates in Al-Mg-Si Alloys with Small Additions of Other Elements", *Advanced Engineering Materials*, vol. 20, no. 7, 1800125, 2018. DOI: 10.1002/adem.201800125.

[24] C. D. Marioara, H. Nordmark, S. J. Andersen and R. Holmestad, "Post-β" phases and their influence on microstructure and hardness in 6xxx Al-Mg-Si alloys", *Journal of Materials Science*, vol. 41, no. 2, pp. 471–478, 2006. DOI: 10.1007/s10853-005-2470-1.

[25] G. A. Edwards, K. Stiller, G. L. Dunlop and M. J. Couper, "The precipitation sequence in Al–Mg–Si alloys", *Acta Materialia*, vol. 46, no. 11, pp. 3893–3904, 1998. DOI: 10.1016/S1359-6454(98)00059-7.

[26] C. D. Marioara, S. J. Andersen, J. Jansen and H. W. Zandbergen, "Atomic model for GP-zones in a 6082 Al–Mg–Si system", *Acta Materialia*, vol. 49, no. 2, pp. 321–328, 2001. DOI: 10.1016/S1359-6454(00)00302-5.

[27] J. H. Chen, E. Costan, M. A. van Huis, Q. Xu and H. W. Zandbergen, "Atomic pillar-based nanoprecipitates strengthen AlMgSi alloys.", *Science*, vol. 312, no. 5772, pp. 416–419, 2006. DOI: 10.1126/science.1124199.

[28] S. J. Andersen, H. W. Zandbergen, J. Jansen, C. Træholt, U. Tundal and O. Reiso, "The crystal structure of the β" phase in Al–Mg–Si alloys", *Acta Materialia*, vol. 46, no. 9, pp. 3283–3298, 1998. DOI: 10.1016/S1359-6454(97)00493-X.

[29] H. S. Hasting, A. G. Frøseth, S. J. Andersen, R. Vissers, J. C. Walmsley, C. D. Marioara, F. Danoix, W. Lefebvre and R. Holmestad, "Composition of β" precipitates in Al–Mg–Si alloys by atom probe tomography and first principles calculations", *Journal of Applied Physics*, vol. 106, no. 12, 123527, 2009. DOI: 10.1063/1.3269714.

[30] R. Vissers, M. A. van Huis, J. Jansen, H. W. Zandbergen, C. D. Marioara and S. J. Andersen, "The crystal structure of the β' phase in Al–Mg–Si alloys", *Acta Materialia*, vol. 55, no. 11, pp. 3815–3823, 2007. DOI: 10.1016/J.ACTAMAT.2007.02.032.

[31] S. J. Andersen, C. D. Marioara, R. Vissers, A. Frøseth and H. W. Zandbergen, "The structural relation between precipitates in Al–Mg–Si alloys, the Al-matrix and diamond silicon, with emphasis on the trigonal phase U1-MgAl2Si2", *Materials Science and Engineering: A*, vol. 444, no. 1-2, pp. 157–169, 2007. DOI: 10.1016/J.MSEA.2006.08.084.

[32] S. J. Andersen, C. D. Marioara, A. Frøseth, R. Vissers and H. W. Zandbergen, "Crystal structure of the orthorhombic U2-Al4Mg4Si4 precipitate in the Al–Mg–Si alloy system and its relation to the β' and β" phases", *Materials Science and Engineering: A*, vol. 390, no. 1-2, pp. 127–138, 2005. DOI: 10.1016/J.MSEA.2004.09.019.

[33] R. Vissers, C. D. Marioara, S. J. Andersen and R. Holmestad, in *Aluminium Alloys*, International Conference on Aluminium Alloys (22nd–26th Sep. 2008), J. Hirsch and B. Skrotzki, Eds., vol. 2, Aachen: Weinheim : Wiley-VCH, 2008, pp. 1263–1269.

[34] T. Hahn, Ed., *International tables for crystallography: Space-group symmetry*, 5th ed. Dordrecht: Published for the International Union of Crystallography by Springer, 2002, vol. A.

[35] D. Hull and D. J. Bacon, *Introduction to dislocations*, 5th ed. Butterworth-Heinemann, 2011. DOI: 10.1016/C2009-0-64358-0.

[36] A. J. Ardell, "Precipitation hardening", *Metallurgical Transactions A*, vol. 16, no. 12, pp. 2131–2165, 1985. DOI: 10.1007/BF02670416.

[37] L. M. Brown and R. K. Ham, "Dislocation-particle interactions", in *Strengthening Methods in Crystals*, ser. Elsevier Materials Science Series, A. Kelly and R. B. Nicholson, Eds., Amsterdam, Netherlands: Elsevier Publishing Company LTD, 1971, pp. 12–129.

[38] J. D. Embury, "Strengthening by dislocation substructures", in *Strengthening Methods in Crystals*, ser. Elsevier Materials Science Series, A. Kelly and R. B. Nicholson, Eds., Amsterdam, Netherlands: Elsevier Publishing Company LTD, 1971, pp. 333–334.

[39] W. Chrominski and M. Lewandowska, "Mechanisms of plastic deformation in ultrafine-grained aluminium – In-situ and ex-post studies", *Materials Science and Engineering: A*, vol. 715, pp. 320–331, 2018. DOI: 10.1016/J.MSEA.2017.12.083.

[40] A. Lasalmonie and J. L. Strudel, "Influence of grain size on the mechanical behaviour of some high strength materials", *Journal of Materials Science*, vol. 21, no. 6, pp. 1837–1852, 1986. DOI: 10.1007/BF00547918.

[41] E. O. Hall, "The Deformation and Ageing of Mild Steel: III Discussion of Results", *Proceedings of the Physical Society. Section B*, vol. 64, no. 9, pp. 747–753, 1951. DOI: 10.1088/0370-1301/64/9/303.

[42] R. Armstrong, I. Codd, R. M. Douthwaite and N. J. Petch, "The plastic deformation of polycrystalline aggregates", *Philosophical Magazine*, vol. 7, no. 73, pp. 45–58, 1962. DOI: 10.1080/14786436208201857.

[43] C. S. Pande, R. A. Masumura and R. W. Armstrong, "Pile-up based hall-petch relation for nanoscale materials", *Nanostructured Materials*, vol. 2, no. 3, pp. 323–331, 1993. DOI: 10.1016/0965-9773(93)90159-9.

[44] F. Mompiou, M. Legros, A. Sedlmayr, D. S. Gianola, D. Caillard and O. Kraft, "Source-based strengthening of sub-micrometer Al fibers", *Acta Materialia*, vol. 60, no. 3, pp. 977–983, 2012. DOI: 10.1016/j.actamat.2011.11.005.

[45] A. Rajabzadeh, M. Legros, N. Combe, F. Mompiou and D. A. Molodov, "Evidence of grain boundary dislocation step motion associated to shear-coupled grain boundary migration", *Philosophical Magazine*, vol. 93, no. 10-12, pp. 1299–1316, 2013. DOI: 10.1080/14786435.2012.760760.

[46] N. Combe, F. Mompiou and M. Legros, "Shear-coupled grain-boundary migration dependence on normal strain/stress", *Physical Review Materials*, vol. 1, no. 3, 033605, 2017. DOI: 10.1103/PhysRevMaterials.1.033605.

[47] C. S. Pande and K. P. Cooper, "Nanomechanics of Hall–Petch relationship in nanocrystalline materials", *Progress in Materials Science*, vol. 54, no. 6, pp. 689–706, 2009. DOI: 10.1016/J.PMATSCI.2009.03.008.

[48] E. L. Huskins, B. Cao and K. T. Ramesh, "Strengthening mechanisms in an Al–Mg alloy", *Materials Science and Engineering: A*, vol. 527, no. 6, pp. 1292–1298, 2010. DOI: 10.1016/j.msea.2009.11.056.

[49] A. Loucif, R. B. Figueiredo, T. Baudin, F. Brisset, R. Chemam and T. G. Langdon, "Ultrafine grains and the Hall–Petch relationship in an Al–Mg–Si alloy processed by high-pressure torsion", *Materials Science and Engineering: A*, vol. 532, pp. 139–145, 2012. DOI: 10.1016/J.MSEA.2011.10.074.

[50] W. Chrominski, S. Wenner, C. D. Marioara, R. Holmestad and M. Lewandowska, "Strengthening mechanisms in ultrafine grained Al-Mg-Si alloy processed by hydrostatic extrusion – Influence of ageing temperature", *Materials Science and Engineering: A*, vol. 669, pp. 447–458, 2016. DOI: 10.1016/J.MSEA.2016.05.109.

[51] E. Orowan, "Discussion", in *Symposium on Internal Stresses in Metals and Alloys*, Institute of Metals Monograph and Report Series (15th–16th Oct. 1948), London: The Institute of Metals, 1948, pp. 451–453.

[52] D. Broek, "The role of inclusions in ductile fracture and fracture toughness", *Engineering Fracture Mechanics*, vol. 5, no. 1, pp. 55–66, 1973. DOI: 10.1016/0013-7944(73)90007-6.

[53] M. Z. Butt and P. Feltham, "Solid-solution hardening", *Journal of Materials Science*, vol. 28, no. 10, pp. 2557–2576, 1993. DOI: 10.1007/BF00356192.

[54] P. Haasen, "Solution hardening in f.c.c. metals", in *Dislocations in Solids*, ser. Dislocations in Metallurgy, F. R. N. Nabarro, Ed., vol. 4, Amsterdam, Netherlands: North-Holland Publishing Company, 1979, pp. 155–190.

[55] A. Deschamps and Y. Brechet, "Influence of predeformation and ageing of an Al–Zn–Mg alloy—II. Modeling of precipitation kinetics and yield stress", *Acta Materialia*, vol. 47, no. 1, pp. 293–305, 1998. DOI: 10.1016/S1359-6454(98)00296-1.

[56] O. R. Myhr, Ø. Grong and S. J. Andersen, "Modelling of the age hardening behaviour of Al–Mg–Si alloys", *Acta Materialia*, vol. 49, no. 1, pp. 65–75, 2001. DOI: 10.1016/S1359-6454(00)00301-3.

[57] A. Simar, Y. Bréchet, B. de Meester, A. Denquin and T. Pardoen, "Sequential modeling of local precipitation, strength and strain hardening in friction stir welds of an aluminum alloy 6005A-T6", *Acta Materialia*, vol. 55, no. 18, pp. 6133–6143, 2007. DOI: 10.1016/J.ACTAMAT.2007.07.012.

[58] O. R. Myhr, O. S. Hopperstad and T. Børvik, "A Combined Precipitation, Yield Stress, and Work Hardening Model for Al-Mg-Si Alloys Incorporating the Effects of Strain Rate and Temperature", *Metallurgical and Materials Transactions A*, vol. 49, no. 8, pp. 3592–3609, 2018. DOI: 10.1007/s11661-018-4675-3.

[59] N. M. F. Nabarro, "Diffusion and precipitation in alloys", in *Symposium on Internal Stresses in Metals and Alloys*, Institute of Metals Monograph and Report Series (15th–16th Oct. 1948), London: The Institute of Metals, 1948, pp. 237–249.

[60] K. Banizs, "Dislocation structures caused by plastic deformations in an aged AlMgSi alloy", *Materials Science and Engineering*, vol. 41, no. 1, pp. 17–24, 1979. DOI: 10.1016/0025-5416(79)90039-9.

[61] P. Donnadieu, G. F. Dirras and J. Douin, "An approach of precipitate/dislocation interaction in age-hardened al-mg-si alloys: Measurement of the strain field around precipitates and related simulation of the dislocation propagation", in *Aluminium Alloys 2002 - ICAA8*, ser. Materials Science Forum, vol. 396, Trans Tech Publications Ltd, 2002, pp. 1019–1024. DOI: 10.4028/www.scientific.net/MSF.396-402.1019.

[62] K. Misumi, K. Kaneko, T. Nishiyama, T. Maeda, K. Yamada, K.-i. Ikeda, M. Kikuchi, K. Takata, M. Saga and K. Ushioda, "Three-dimensional characterization of interaction between β" precipitate and dislocation in Al–Mg–Si alloy", *Journal of Alloys and Compounds*, vol. 600, pp. 29–33, 2014. DOI: 10.1016/J.JALLCOM.2014.02.059.

[63] E. Christiansen, C. D. Marioara, B. Holmedal, O. S. Hopperstad and R. Holmestad, "Nano-scale characterisation of sheared β" precipitates in a deformed Al-Mg-Si alloy", *Submitted*, 2019.

[64] P. N. T. Unwin, G. W. Lorimer and R. B. Nicholson, "The origin of the grain boundary precipitate free zone", *Acta Metallurgica*, vol. 17, no. 11, pp. 1363–1377, 1969.

[65] Y. Q. Chen, D. Q. Yi, Y. Jiang, B. Wang and H. Q. Liu, "Concurrent formation of two different type precipitation-free zones during the initial stage of homogenization", *Philosophical Magazine*, vol. 93, no. 18, pp. 2269–2278, 2013. DOI: 10.1080/14786435.2013.766371.

[66] T. Ogura, S. Hirosawa and T. Sato, "Quantitative characterization of precipitate free zones in Al-Zn-Mg(-Ag) alloys by microchemical analysis and nanoindentation measurement", *Science and Technology of Advanced Materials*, vol. 5, no. 4, pp. 491–496, 2004. DOI: 10.1016/j.stam.2004.02.007.

[67] V. Radmilovic, C. Taylor, Z. Lee, A. Tolley, D. Mitlin and U. Dahmen, "Nanoindentation properties and the microstructure of grain boundary precipitate-free zones (PFZs) in an AlCuSiGe alloy", *Philosophical Magazine*, vol. 87, no. 26, pp. 3905–3919, 2007. DOI: 10.1080/14786430601153414.

[68] T. Ogura, A. Hirose and T. Sato, "Effect of pfz and grain boundary precipitate on mechanical properties and fracture morphologies in al-zn-mg(ag) alloys", in *THERMEC 2009*, ser. Materials Science Forum, vol. 638, Trans Tech Publications Ltd, 2010, pp. 297–302. DOI: 10.4028/www.scientific.net/MSF.638-642.297.

[69] A. K. Vasudévan and R. D. Doherty, "Grain boundary ductile fracture in precipitation hardened aluminum alloys", *Acta Metallurgica*, vol. 35, no. 6, pp. 1193–1219, 1987. DOI: 10.1016/0001-6160(87)90001-0.

[70] N. Ryum, "The influence of a precipitate-free zone on the mechanical properties of an Al-Mg-Zn alloy", *Acta Metallurgica*, vol. 16, no. 3, pp. 327–332, 1968. DOI: 10.1016/0001-6160(68)90018-7.

[71] W. F. Smith and N. J. Grant, "The effect of multiple-step aging on the strength properties and precipitate-free zone widths in Al-Zn-Mg alloys", *Metallurgical Transactions*, vol. 1, no. 4, pp. 979–983, 1970. DOI: 10.1007/BF02811781.

[72] T. Kawabata and O. Izumi, "Ductile fracture in the interior of precipitate free zone in an Al-6.0%Zn-2.6%Mg alloy", *Acta Metallurgica*, vol. 24, no. 9, pp. 817–825, 1976. DOI: 10.1016/0001-6160(76)90048-1.

[73] P. Schwellinger, "Investigation of the Mechanisms of Ductile Intergranular Fracture in Al-Mg-Si Alloys with Special Reference to Void Formation", *Zeitschrift für Metallkunde*, vol. 71, no. 8, pp. 520–524, 1980.

[74] L. Zhen and S. B. Kang, "Deformation and fracture behavior of two Al-Mg-Si alloys", *Metallurgical and Materials Transactions A: Physical Metallurgy and Materials Science*, vol. 28, no. 7, pp. 1489–1497, 1997.

[75] C. Watanabe, R. Monzen and K. Tazaki, "Effects of Al3Sc particle size and precipitate-free zones on fatigue behavior and dislocation structure of an aged Al–Mg–Sc alloy", *International Journal of Fatigue*, vol. 30, pp. 635–641, 2008. DOI: 10.1016/j.ijfatigue.2007.05.010.

[76] M. Abe, K. Asano and A. Fujiwara, "Influence of the precipitate-free zone width on the tensile properties of an Al-6 Wt pct Zn-1.2 Wt pct Mg alloy", *Metallurgical Transactions*, vol. 4, no. 6, pp. 1499–1505, 1973. DOI: 10.1007/BF02668000.

[77] D. Baither, T. Krol and E. Nembach, "Dislocation processes in precipitate-free zones in NIMONIC PE16 studied by in situ transmission electron microscopy", *Materials Science and Engineering A*, vol. 387-389, no. 1–2, pp. 163–166, 2004. DOI: 10.1016/j.msea.2004.01.072.

[78] P. Noell, J. Carroll, K. Hattar, B. Clark and B. Boyce, "Do voids nucleate at grain boundaries during ductile rupture?", *Acta Materialia*, vol. 137, pp. 103–114, 2017. DOI: 10.1016/j.actamat.2017.07.004.

[79] P. Schwellinger, "On the mechanism of ductile intergranular fracture in Al-Mg-Si alloys", *Scripta Metallurgica*, vol. 12, no. 10, pp. 899–901, 1978. DOI: 10.1016/0036-9748(78)90178-3.

[80] P. Schwellinger, "Investigation of the Mechanisms of Ductile Intergranular Fracture in Al-Mg-Si Alloys with Special Reference to Void Formation", *Zeitschrift für Metallkunde*, vol. 71, no. 8, pp. 520–524, 1980.

[81] T. Pardoen, D. Dumont, A. Deschamps and Y. Brechet, "Grain boundary versus transgranular ductile failure", *Journal of the Mechanics and Physics of Solids*, vol. 51, no. 4, pp. 637–665, 2003. DOI: 10.1016/S0022-5096(02)00102-3.

[82] T. F. Morgeneyer, M. J. Starink, S. C. Wang and I. Sinclair, "Quench sensitivity of toughness in an Al alloy: Direct observation and analysis of failure initiation at the precipitate-free zone", *Acta Materialia*, vol. 56, no. 12, pp. 2872–2884, 2008. DOI: 10.1016/j.actamat.2008.02.021.

[83] T. Pardoen and T. J. Massart, "Interface controlled plastic flow modelled by strain gradient plasticity theory", *Comptes Rendus Mecanique*, vol. 340, pp. 247–260, 2012. DOI: 10.1016/j.crme.2012.02.008.

[84] M. Fourmeau, C. D. Marioara, T. Børvik, A. Benallal and O. S. Hopperstad, "A study of the influence of precipitate-free zones on the strain localization and failure of the aluminium alloy AA7075-T651", *Philosophical Magazine*, vol. 95, no. 28-30, pp. 3278–3304, 2015. DOI: 10.1080/14786435.2015.1040099.

[85] M. Khadyko, C. D. Marioara, I. G. Ringdalen, S. Dumoulin and O. S. Hopperstad, "Deformation and strain localization in polycrystals with plastically heterogeneous grains", *International Journal of Plasticity*, vol. 86, pp. 128–150, 2016. DOI: 10.1016/j.ijplas.2016.08.005.

[86] M. Styczyńska and W. Łojkowski, "Grain boundaries as dislocation sources in a material with precipitate-free zones", *Scripta Metallurgica*, vol. 19, no. 12, pp. 1409–1413, 1985. DOI: 10.1016/0036-9748(85)90141-3.

[87] M. Jain, "TEM study of microstructure development during low-cycle fatigue of an overaged Al-Mg-Si alloy", *Journal of Materials Science*, vol. 27, no. 2, pp. 399–407, 1992. DOI: 10.1007/BF00543929.

[88] E. Christiansen, C. D. Marioara, K. Marthinsen, O. S. Hopperstad and R. Holmestad, "Lattice rotations in precipitate free zones in an Al-Mg-Si alloy", *Materials Characterization*, vol. 144, pp. 522–531, 2018. DOI: 10.1016/j.matchar.2018.08.002.

[89] R. Erni, *Aberration-corrected imaging in transmission electron microscopy : an introduction*, 2nd ed. Imperial College Press, 2010.

[90] C. J. Humphreys, "The scattering of fast electrons by crystals", *Reports on Progress in Physics*, vol. 42, no. 11, pp. 1825–1887, 1979. DOI: 10.1088/0034-4885/42/11/002.

[91] P. D. Nellist and S. J. Pennycook, "The principles and interpretation of annular dark-field Z-contrast imaging", *Advances in Imaging and Electron Physics*, vol. 113, pp. 147–203, 2000. DOI: 10.1016/S1076-5670(00)80013-0.

[92] E. J. Kirkland, *Advanced Computing in Electron Microscopy*, 2nd ed. Springer, 2010. DOI: 10.1007/978-1-4419-6533-2.

[93] M. L. Prydderch, N. J. Waltham, R. Turchetta, M. J. French, R. Holt, A. Marshall, D. Burt, R. Bell, P. Pool, C. Eyles and H. Mapson-Menard, "A 512×512 CMOS Monolithic Active Pixel Sensor with integrated ADCs for space science", *Nuclear Instruments and Methods in Physics Research Section A: Accelerators, Spectrometers, Detectors and Associated Equipment*, vol. 512, no. 1-2, pp. 358–367, 2003. DOI: 10.1016/S0168-9002(03)01914-4.

[94] A. R. Faruqi, R. Henderson, M. Pryddetch, P. Allport and A. Evans, "Direct single electron detection with a CMOS detector for electron microscopy", *Nuclear Instruments and Methods in Physics Research Section A: Accelerators, Spectrometers, Detectors and Associated Equipment*, vol. 546, no. 1-2, pp. 170–175, 2005. DOI: 10.1016/J.NIMA.2005.03.023.

[95] G. McMullan, D. M. Cattermole, S. Chen, R. Henderson, X. Llopart, C. Summerfield, L. Tlustos and A. R. Faruqi, "Electron imaging with Medipix2 hybrid pixel detector", *Ultramicroscopy*, vol. 107, no. 4-5, pp. 401–413, 2007. DOI: 10.1016/J.ULTRAMIC.2006.10.005.

[96] G. McMullan, S. Chen, R. Henderson and A. R. Faruqi, "Detective quantum efficiency of electron area detectors in electron microscopy", *Ultramicroscopy*, vol. 109, no. 9, pp. 1126–1143, 2009. DOI: 10.1016/J.ULTRAMIC.2009.04.002.

[97] L. Jin, A.-C. Milazzo, S. Kleinfelder, S. Li, P. Leblanc, F. Duttweiler, J. C. Bouwer, S. T. Peltier, M. H. Ellisman and N.-H. Xuong, "Applications of direct detection device in transmission electron microscopy", *Journal of Structural Biology*, vol. 161, no. 3, pp. 352–358, 2008. DOI: 10.1016/J.JSB.2007.10.007.

[98] A.-C. Milazzo, G. Moldovan, J. Lanman, L. Jin, J. C. Bouwer, S. Klienfelder, S. T. Peltier, M. H. Ellisman, A. I. Kirkland and N.-H. Xuong, "Characterization of a direct detection device imaging camera for transmission electron microscopy", *Ultramicroscopy*, vol. 110, no. 7, pp. 741–744, 2010. DOI: 10.1016/J.ULTRAMIC.2010.03.007.

[99] C. Ophus, P. Ercius, M. Sarahan, C. Czarnik and J. Ciston, "Recording and Using 4D-STEM Datasets in Materials Science", *Microscopy and Microanalysis*, vol. 20, no. S3, pp. 62–63, 2014. DOI: 10.1017/S1431927614002037.

[100] H. Yang, L. Jones, H. Ryll, M. Simson, H. Soltau, Y. Kondo, R. Sagawa, H. Banba, I. MacLaren and P. D. Nellist, "4D STEM: High efficiency phase contrast imaging using a fast pixelated detector", *Journal of Physics: Conference Series*, vol. 644, no. 1, 012032, 2015. DOI: 10.1088/1742-6596/644/1/012032.

[101] D. Zhang, P. Oleynikov, S. Hovmöller and X. Zou, "Collecting 3D electron diffraction data by the rotation method", *Zeitschrift für Kristallographie*, vol. 225, no. 2-3, pp. 94–102, 2010. DOI: 10.1524/zkri.2010.1202.

[102] R. Vincent and P. A. Midgley, "Double conical beam-rocking system for measurement of integrated electron diffraction intensities", *Ultramicroscopy*, vol. 53, no. 3, pp. 271–282, 1994. DOI: 10.1016/0304-3991(94)90039-6.

[103] A. S. Eggeman, R. Krakow and P. A. Midgley, "Scanning precession electron tomography for three-dimensional nanoscale orientation imaging and crystallographic analysis", *Nature Communications*, vol. 6, no. 1, 7267, 2015. DOI: 10.1038/ncomms8267.

[104] J. K. Sunde, C. D. Marioara, A. T. J. van Helvoort and R. Holmestad, "The evolution of precipitate crystal structures in an Al-Mg-Si(-Cu) alloy studied by a combined HAADF-STEM and SPED approach", *Materials Characterization*, vol. 142, pp. 458–469, 2018. DOI: 10.1016/j.matchar.2018.05.031.

[105] I. Ghamarian, Y. Liu, P. Samimi and P. C. Collins, "Development and application of a novel precession electron diffraction technique to quantify and map deformation structures in highly deformed materials - As applied to ultrafine-grained titanium", vol. 79, pp. 203–215, 2014. DOI: 10.1016/j.actamat.2014.06.063.

[106] J.-L. Rouviere, A. Béché, Y. Martin, T. Denneulin and D. Cooper, "Improved strain precision with high spatial resolution using nanobeam precession electron diffraction", *Applied Physics Letters*, vol. 103, no. 24, 241913, 2013. DOI: 10.1063/1.4829154.

[107] M. P. Vigouroux, V. Delaye, N. Bernier, R. Cipro, D. Lafond, G. Audoit, T. Baron, J. L. Rouvière, M. Martin, B. Chenevier and F. Bertin, "Strain mapping at the nanoscale using precession electron diffraction in transmission electron microscope with off axis camera", *Applied Physics Letters*, vol. 105, no. 19, 191906, 2014. DOI: 10.1063/1.4901435.

[108] C. Mahr, K. Müller-Caspary, R. Ritz, M. Simson, T. Grieb, M. Schowalter, F. F. Krause, A. Lackmann, H. Soltau, A. Wittstock and A. Rosenauer, "Influence of distortions of recorded diffraction patterns on strain analysis by nano-beam electron diffraction", *Ultramicroscopy*, vol. 196, pp. 74–82, 2019. DOI: 10.1016/J.ULTRAMIC.2018.09.010.

[109] J. S. Barnard, D. N. Johnstone and P. A. Midgley, "High-resolution scanning precession electron diffraction: Alignment and spatial resolution", *Ultramicroscopy*, vol. 174, pp. 79–88, 2017. DOI: 10.1016/j.ultramic.2016.12.018.

[110] G. S. Liu and I. M. Robertson, "Three-dimensional visualization of dislocation-precipitate interactions in a Al–4Mg–0.3Sc alloy using weak-beam dark-field electron tomography", *Journal of Materials Research*, vol. 26, no. 4, pp. 514–522, 2011. DOI: 10.1557/jmr.2010.83.

[111] J. S. Barnard, A. S. Eggeman, J. Sharp, T. A. White and P. A. Midgley, "Dislocation electron tomography and precession electron diffraction – minimising the effects of dynamical interactions in real and reciprocal space", *Philosophical Magazine*, vol. 90, no. 35-36, pp. 4711–4730, 2010. DOI: 10.1080/14786430903581338.

[112] S. S. Ruvimov and K. Scheerschmidt, "Burgers vector determination in TEM by using the dislocation parity analysis", *Physica Status Solidi (a)*, vol. 141, no. 2, pp. 269–284, 1994. DOI: 10.1002/pssa.2211410204.

[113] S. van Aert, P. Geuens, D. van Dyck, C. Kisielowski and J. Jinschek, "Electron channelling based crystallography", *Ultramicroscopy*, vol. 107, no. 6-7, pp. 551–558, 2007. DOI: 10.1016/J.ULTRAMIC.2006.04.031.

[114] D. van Dyck and J. H. Chen, "Towards an exit wave in closed analytical form", *Acta Crystallographica Section A Foundations of Crystallography*, vol. 55, no. 2, pp. 212–215, 1999. DOI: 10.1107/S0108767398011337.

[115] Q. Xu, D. van Dyck and H. W. Zandbergen, "From thickness dependent exit waves to projected potential: Thickness derivative approach", *Ultramicroscopy*, vol. 110, no. 5, pp. 535–542, 2010. DOI: 10.1016/J.ULTRAMIC.2009.10.008.

[116] S. J. Pennycook and D. E. Jesson, "High-resolution Z-contrast imaging of crystals", *Ultramicroscopy*, vol. 37, no. 1-4, pp. 14–38, 1991. DOI: 10.1016/0304-3991(91)90004-P.

[117] S. Hillyard, R. F. Loane and J. Silcox, "Annular dark-field imaging: Resolution and thickness effects", *Ultramicroscopy*, vol. 49, no. 1-4, pp. 14–25, 1993. DOI: 10.1016/0304-3991(93)90209-G.

[118] S. Hillyard and J. Silcox, "Thickness effects in ADF STEM zone axis images", *Ultramicroscopy*, vol. 52, no. 3-4, pp. 325–334, 1993. DOI: 10.1016/0304-3991(93)90043-W.

[119] D. O. Klenov and S. Stemmer, "Contributions to the contrast in experimental high-angle annular dark-field images", *Ultramicroscopy*, vol. 106, no. 10, pp. 889–901, 2006. DOI: 10.1016/j.ultramic.2006.03.007.

[120] G. T. Martinez, K. H. W. van den Bos, M. Alania, P. D. Nellist and S. van Aert, "Thickness dependence of scattering cross-sections in quantitative scanning transmission electron microscopy", *Ultramicroscopy*, vol. 187, pp. 84–92, 2018. DOI: 10.1016/J.ULTRAMIC.2018.01.005.

[121] S. Hillyard and J. Silcox, "Detector geometry, thermal diffuse scattering and strain effects in ADF STEM imaging", *Ultramicroscopy*, vol. 58, no. 1, pp. 6–17, 1995. DOI: 10.1016/0304-3991(94)00173-K.

[122] E. Christiansen, C. D. Marioara, I. G. Ringdalen, R. Bjœrge and R. Holmestad, "Multislice image simulations of sheared needle-like precipitates in an Al-Mg-Si alloy", *To be submitted*, 2019.

[123] L.-M. Peng, G. Ren, S. L. Dudarev and M. J. Whelan, "Debye–Waller Factors and Absorptive Scattering Factors of Elemental Crystals", *Acta Crystallographica Section A Foundations of Crystallography*, vol. 52, no. 3, pp. 456–470, 1996. DOI: 10.1107/S010876739600089X.

[124] I. Lobato and D. van Dyck, "MULTEM: A new multislice program to perform accurate and fast electron diffraction and imaging simulations using Graphics Processing Units with CUDA", *Ultramicroscopy*, vol. 156, pp. 9–17, 2015. DOI: 10.1016/J.ULTRAMIC.2015.04.016.

[125] F. de la Peña, V. T. Fauske, P. Burdet, E. Prestat, P. Jokubauskas, M. Nord, T. Ostasevicius, K. E. MacArthur, M. Sarahan, D. N. Johnstone, J. Taillon, A. Eljarrat, V. Migunov, J. Caron, T. Furnival, S. Mazzucco, T. Aarholt, M. Walls, T. Slater, F. Winkler, B. Martineau, G. Donval, R. McLeod, E. R. Hoglund, I. Alxneit, I. Hjorth, T. Henninen, L. F. Zagonel, A. Garmannslund and A. Skorikov, *Hyperspy/hyperspy v1.4.1*, 2018. DOI: 10.5281/ZENODO.1469364.

[126] D. N. Johnstone, P. A. Crout, B. Martineau, S. Høgås, J. Laulainen, S. Collins, S. Smeets, J. Morzy, T. Doherty, E. Prestat, T. Ostasevicius, T. Bergh and H. Ånes, "pyxem/pyxem: pyXem 0.7.1", 2019. DOI: 10.5281/ZENODO.2650296.

[127] F. Bachmann, R. Hielscher and H. Schaeben, "Grain detection from 2d and 3d EBSD data—Specification of the MTEX algorithm", *Ultramicroscopy*, vol. 111, no. 12, pp. 1720–1733, 2011. DOI: 10.1016/j.ultramic.2011.08.002.

[128] L. Jones, H. Yang, T. J. Pennycook, M. S. J. Marshall, S. van Aert, N. D. Browning, M. R. Castell and P. D. Nellist, "Smart Align—a new tool for robust non-rigid registration of scanning microscope data", *Advanced Structural and Chemical Imaging*, vol. 1, no. 1, p. 8, 2015. DOI: 10.1186/s40679-015-0008-4.

[129] B. H. Frodal, E. Christiansen, O. R. Myhr and O. S. Hopperstad, "The role of quench rate on the plastic flow and fracture of three aluminium alloys with different grain structure and texture", *To be submitted*, 2019.

[130] W. J. Poole, X. Wang, D. J. Lloyd and J. D. Embury, "The shearable-non-shearable transition in Al-Mg-Si-Cu precipitation hardening alloys: Implications on the distribution of slip, work hardening and fracture", *Philosophical Magazine*, vol. 85, no. 26-27, pp. 3113–3135, 2005. DOI: 10.1080/14786430500154935.

[131] Ø. Ryen, B. Holmedal, K. Marthinsen and T. Furu, "Precipitation, strength and work hardening of age hardened aluminium alloys", in *IOP Conference Series: Materials Science and Engineering*, vol. 89, 2015. DOI: 10.1088/1757-899X/89/1/012013.

[132] Z. Zhu and M. J. Starink, "Age hardening and softening in cold-rolled Al–Mg–Mn alloys with up to 0.4 wt% Cu", *Materials Science and Engineering: A*, vol. 489, no. 1-2, pp. 138–149, 2008. DOI: 10.1016/J.MSEA.2007.12.019.